

UNCLASSIFIED

ELECTROMAGNETIC PROBING OF THE
MARTIAN IONOSPHERE AND
ATMOSPHERE FROM AN ORBITING PAIR

FINAL REPORT

ON

CONTRACT NAS 8-21222

(JUNE 19, 1967 TO DECEMBER 19, 1967)

R67-4537

DECEMBER 19, 1967

GPO PRICE \$ _____

CSFTI PRICE(S) \$ _____

Hard copy (HC) _____

Microfiche (MF) _____

ff 653 July 65

RAYTHEON

RAYTHEON COMPANY

SPACE AND INFORMATION SYSTEMS DIVISION

FACILITY FORM 602

N 68-36468

(ACCESSION NUMBER)

217

(PAGES)

CR-98001

(NASA CR OR TMX OR AD NUMBER)

(THRU)

(CODE)

30

(CATEGORY)

**ELECTROMAGNETIC PROBING OF THE
MARTIAN IONOSPHERE AND
ATMOSPHERE FROM AN ORBITING PAIR**

FINAL REPORT

ON

CONTRACT NAS 8-21222

(JUNE 19, 1967 TO DECEMBER 19, 1967)

R67-4537

DECEMBER 19, 1967

PREPARED FOR

**NATIONAL AERONAUTICS AND SPACE ADMINISTRATION
GEORGE C. MARSHALL SPACE FLIGHT CENTER
HUNTSVILLE, ALABAMA 35812**

PREPARED BY

**RAYTHEON COMPANY
SPACE AND INFORMATION SYSTEMS DIVISION
SUDBURY, MASSACHUSETTS 01776**

ABSTRACT

Electromagnetic probing of a planetary ionosphere and atmosphere from an orbiting pair is a method capable of providing unambiguous determination of three-dimensional ionospheric and atmospheric density profiles.

Refractivity, transmission absorption spectroscopy and radiometric measurements at suitable wavelengths, with the instrumentation accommodated in a dual-spacecraft configuration, provide a convenient experimental approach.

Two Voyagers or equivalent spacecraft, orbiting the planet Mars at the same time, offer a suitable platform for conducting a comprehensive survey, encompassing spacecraft-to-spacecraft and spacecraft-to-sun occultation measurements, complemented by radiometric probings.

The method is potentially a tool of general use for planetary research.

FOREWORD

This report was prepared by Raytheon Co., Space and Information Systems Division, Sudbury, Mass., under contract NAS 8-21222, entitled "Electromagnetic Probing of the Martian Ionosphere and Atmosphere from an orbiting pair".

The date of contract award was June 19, 1967 and the period of performance was six months. The contracting Agency was the George C. Marshall Space Flight Center of the National Aeronautics and Space Administration.

The work was administered under the technical direction of the Space Sciences Laboratory of the George C. Marshall Space Flight Center.

ACKNOWLEDGEMENTS

The fundamental concept of the mother/daughter method of the probing of planetary atmospheres and ionospheres, the object of this report, was formulated by Prof. J. V. Harrington, Director of MIT Space Research Center and Consultant to Raytheon Company. He and Dr. Mario D. Grossi, who served as Project Director, led the effort reported here. Mr. Robert S. Riddell, as Assistant Project Director, coordinated the engineering study activity in its system and equipment aspects. Mr. John L. Fritz, Manager of Space Science Programs, had management cognizance of the project. Mr. Charles A. Baugher, of the NASA-MSFC Space Sciences Laboratory, Huntsville, Alabama, was the Technical Monitor of the Project.

Individual contributors were the following:

Prof. A. H. Barrett	-Surface radiometry (microwave and IR)
Dr. Perry Miles	-Atmospheric radiometry (IR)
Prof. P.P. Lombardini	-Transmission absorption spectroscopy (microwave, IR and UV)
Dr. R.J. Doviak	
Dr. J. Goldhirsh	
Mrs. B.M. Langworthy	-Analysis of refractivity measurements and generation of profile inversion algorithms
Mr. R.W. Goff	-Orbital mechanics analysis
Mr. E.L. Genest	-Overall system synthesis
Mr. W.A. Fordon	-Refractivity system analysis, doppler error and phase loop analysis
Dr. J.J. Stiffler	
Mr. F. Ricciardi	-Laboratory tests on equipment phase stability
Mr. J. Hopkins	
Mr. H.M. Weinstein	-Antenna analysis and measurements.

CONTENTS

<u>Section</u>	<u>Page</u>
1 SUMMARY OF THE PROBING METHOD	1-1
2 EXPERIMENT OBJECTIVES AND MAJOR REQUIREMENTS . . .	2-1
3 BACKGROUND AND JUSTIFICATION FOR THE CONDUCT OF THE EXPERIMENT	3-1
4 TECHNICAL APPROACH	4-1
4.1 Experiment Concept and Mission	4-1
4.1.1 The Basic Experiment	4-1
4.1.2 Secondary Experiments	4-3
4.2 Orbital Requirements	4-3
4.3 Refractivity Experiment	4-4
4.3.1 General Experiment Description	4-4
4.3.2 Orbital Mechanics Analysis	4-5
4.3.3 Simulated Mission Investigations . . .	4-11
4.3.4 Range Rate and Position Determination .	4-25
4.3.5 Phase Measurement Accuracy	4-26
4.3.6 Refractivity Experiment System Requirements	4-37
4.3.7 Equipment Design	4-48
4.3.8 Interface Requirements	4-53
4.3.9 Telemetry Requirements	4-54
4.3.10 Command Functions	4-55
4.3.11 Summary of Weight, Size, Primary Power Requirements for Refractivity Experiment	4-56
4.4 Transmission Absorption Spectroscopy Experiment	4-57
4.4.1 Model Atmosphere of Mars	4-57

CONTENTS (CONTINUED)

<u>Section</u>	<u>Page</u>
4.4.2 Microwave Spectroscopy Considerations	4-63
4.4.3 IR Absorption Computations for the Assumed Model	4-69
4.4.4 Design Considerations for the IR Spectrometer System	4-86
4.4.5 Ultraviolet Spectroscopy	4-111
4.4.6 Physical Parameters of the IR and UV Instrumentation	4-127
4.5 Bandpass Radiometric Experiments	4-128
4.5.1 Outline	4-128
4.5.2 Equipment Description - Summary	4-134
4.5.3 Pointing Requirement - Summary	4-134
4.5.4 Telemetry Requirements	4-134
4.5.5 Command Functions	4-136
4.6 Summary of Weight, Volume and Primary Power Requirements for Overall Experiment System	4-136
5 DATA REDUCTION REQUIREMENTS	5-1
5.1 Refractivity Data Processing	5-1
5.1.1 Collecting Experiment Data	5-1
5.1.2 Data Reduction	5-2
5.2 Spectroscopic Data Processing	5-26
5.3 Radiometric Data Processing	5-26
6 CONCLUSIONS AND RECOMMENDATIONS	6-1
7 REFERENCES	7-1
A APPENDIX A	A-1
B APPENDIX B	B-1

ILLUSTRATIONS

<u>Figure</u>	<u>Page</u>
3-1 Occultation Scheme Used before Space Age	3-2
3-2 Occultation Concepts Usable with Flyby or Single Orbiter Configurations	3-4
3-3 Dual Flyby and Dual Orbiter Occultation Schemes . .	3-6
4-1 Block Diagram of the Interrelationships among Measured Quantities	4-2
4-2 Geometry of the Probing Link	4-6
4-3 Coverage History (Path Offset Excursions with Voyager to Voyager Link	4-10
4-4 Path Length versus Time	4-12
4-5 Path Offset versus Time	4-13
4-6 Temperature of Martian Atmosphere (Mean Model). . .	4-16
4-7 Pressure of Martian Atmosphere (Mean Model)	4-17
4-8 Positional Error	4-19
4-9 Laboratory Tests, Setup	4-29
4-10a Frequency Response Curve of the BP Filter and the WB Amplifier	4-30
4-10b Frequency Response Curve of the BP Filter Used in the Laboratory Tests	4-30
4-11 Output Phase vs. Input Amplitude	4-31
4-12 Output Phase vs. Temperature	4-32
4-13 Contributions to the Phase Instability Due Separately to the Filter and the Amplifier	4-33
4-14 Differential Phase vs. Temperature Behavior of the Assembly Filter/Amplifier	4-34
4-15 Gain (db) versus Temperature	4-36
4-16 Azimuth Pattern of One-Wavelength Helical Antenna Horizontally Polarized	4-38

ILLUSTRATIONS (CONTINUED)

<u>Figure</u>	<u>Page</u>
4-17 Vertical Pattern of One-Wavelength Helical Antenna Horizontally Polarized	4-39
4-18 Measured Vertical for a Two- λ Helical Antenna . . .	4-40
4-19 Typical Measured Horizontal Pattern for a Two- λ Helical Antenna	4-41
4-20 Voyager Scale Model with the Helical Antenna . . .	4-42
4-21 Helical Antenna (Scale Model) 5 Wavelengths Long, 2 Wavelengths per Turn	4-43
4-22 Voyager Scale Model Used for Antenna Studies in Anechoic Chamber	4-44
4-23 Overall Refractivity Experiment System Block Diagram	4-45
4-24 Dual Orbiter Operating Modes	4-47
4-25 Block Diagram of Mother Equipment	4-50
4-26 Block Diagram of Daughter Equipment	4-51
4-27 Constituent Abundances of CO ₂ , CO, and O in Martian Atmosphere	4-59
4-28 Temperature Profile of Martian Atmosphere	4-64
4-29 Profiles of Pressure and CO ₂ Density Variation in Martian Atmosphere	4-65
4-30 Microwave Spectroscopy Experiment Configuration . .	4-66
4-31 Configuration Depicting the IR Ray Paths Passing through the Atmosphere of Mars during Occultations (h ₁ , h ₂ , etc. are the Corresponding Target Heights)	4-71
4-32a Equivalent Absorptive Path Length of CO ₂ on Mars as a Function of Altitude (0-40 km)	4-77
4-32b Equivalent Absorptive Path Length of CO ₂ on Mars as a Function of Altitude (40-65 km)	4-78

ILLUSTRATIONS (CONTINUED)

<u>Figure</u>	<u>Page</u>
4-32c Equivalent Absorptive Path Length of CO ₂ on Mars as a Function of Altitude (65-90 km)	4-79
4-33 Absorption Display Over the Spectral Interval 2-20 Microns at Different Tangent Heights for CO ₂ and H ₂ O	4-80
4-34 Absorption vs. Tangent Height at Frequencies in the 15 μ Region	4-81
4-35 Absorption vs. Tangent Height at Frequencies in the 4 μ Region	4-82
4-36 Spherically Symmetric Atmosphere of Mars Divided into Concentric Intervals	4-84
4-37 IR Spectrometer System	4-87
4-38 Approximate Sun-Mars Satellite Configuration when Sun-Satellite Path Passes through Martian Atmos- phere (Centers of Sun, Satellite, and Mars are in same Plane)	4-89
4-39 Michelson Type Interference Spectrometer	4-94
4-40 Illustrative Example of Absorption Line	4-103
4-41 Absorption Coefficients in CO ₂	4-114
4-42 Absorption Coefficients in CO	4-115
4-43 Absorption Coefficients in Nitrogen	4-116
4-44 Photionization Cross-Section of Atomic Oxygen as a Function of the Wavelength of the Incident Radiation	4-117
4-45 A Survey of Absorption Coefficients in Oxygen	4-118
4-46 Photoionization Cross-Sections in Helium, Neon, and Argon	4-119
4-47 The Ultraviolet Spectrometer	4-123
4-48 Angular Spread of Diffracted Rays in Interval 800 Å-1300 Å ($\alpha = 86^\circ$)	

ILLUSTRATIONS (CONTINUED)

<u>Figure</u>		<u>Page</u>
4-49	Emissivity vs. Angle of Incidence	4-129
4-50	Geometry of the Radiometric Measurements	4-131
4-51	Optical Schematic for Bandpass Radiometry Experiment	4-135
5-1	Recovered Refractivity vs. Height ($f = 2000$ MHz).	5-4
5-2	Recovered Refractivity vs. Height ($f = 600$ MHz)	5-5
5-3	Recovered Refractivity vs. Height with Horizontal Gradient of Figure 5-4 ($f = 600$ MHz)	5-6
5-4	High-Steepness Model for Horizontal Gradient ($F_2 N_{\max}$ vs. Longitude)	5-7
5-5	Recovered Refractivity vs. Height with Horizontal Gradient of Figure 5-6 ($f = 2000$ MHz).	5-8
5-6	Adopted Model for Horizontal Gradient ($F_2 N_{\max}$ vs. Longitude) with Realistic Steepness	5-9
5-7	Probing Link Geometry	5-11
5-8	Geometry of the Mother/Daughter Ray	5-15
5-9	Geometry of the Profile Inversion along Many Vertices Simultaneously by Abel Transform	5-21

TABLES

<u>Number</u>		<u>Page</u>
4-1	Refractivity Errors Versus Phase Delay Perturbations (F = 600 MHz, Max. Err. = 0.005 cycles)	4-20
4-2	Absolute Errors in Ionospheric Density and Atmospheric P/T Ratios	4-24
4-3	System Performance	4-48
4-4	Weight, Volume, and Primary Power	4-56
4-5	Summary of the Constituent Abundances in the Martian Atmosphere	4-61,4-62
4-6	Comparison of Minimum Detectable Constituent Densities (or Reduced Path Lengths) with Their Maximum Expected Values for the Microwave Spectroscopy Experiment	4-70
4-7	Intensities in Solar XUV-Spectrum at a Distance of 1 A.U. (July, 1963)	4-113
4-8	Summary of Weight, Volume, and Primary Power Requirements for the Overall Experiment System .	4-136
5-1	Data Reduction Methods	5-2

1. SUMMARY OF THE PROBING METHOD

The method's objectives are the unambiguous three-dimensional mapping of the Martian atmosphere and ionosphere using two orbiters to perform remote electromagnetic probing.

The two orbiters are terminals of a two-frequency probing link capable of providing integrated columnar measurements of the dispersive and nondispersive refractive properties of the medium under investigation. If a slight velocity differential exists between the two terminals, the line of sight along which columnar measurements are performed, changes its position with respect to the planet, penetrating the planet's ionosphere and atmosphere from orbital heights down to surface levels as occultation eventually occurs.

By processing the columnar measurements belonging to the same set, i.e., those measurements normal to a planetary radial line at various distances from the surface, radial refractivity profiles can be reconstructed. These profiles lead directly to ionospheric three-dimensional maps (electron content vs. height, longitude, latitude) and to atmospheric three-dimensional refractivity profiles.

The averaging features of the columnar probing impose limits on the steepness of the detectable horizontal gradients. However, for a planet in which the height extension of the neutral and ionized atmosphere is a small fraction of the planet's radius (approx. 1 to 10), horizontal gradients of realistic steepness can be mapped accurately.

Although refractivity measurements in their atmospheric and ionospheric aspects are the basis of the method the interpretation of the atmospheric refractivity profiles in terms of atmospheric density, pressure, and temperature requires the addition to the experiment of spectroscopic and radiometric features.

Transmission absorption spectroscopy measurements in the UV and IR bands, using the Sun as a source, are therefore included as part of the experiment. They constitute a complement to the

refractivity measurements. Having the line of sight from the Sun to one or both orbiters descending through the planet's atmosphere from orbital heights down to surface levels (occultation) permits the construction of profiles of the constituents (primary data provided by these measurements) as well as the temperature and pressure profiles (secondary data). Here again columnar data can be transformed into radial profiles by the same processing applied to the refractivity data.

By knowing the constituents, the scale height of the refractivity profile can be interpreted in terms of temperature vs. height (under assumption of an exponential atmosphere) and the refractivity itself in terms of pressure vs. height.

The addition of IR radiometric instrumentation permits the mapping of the surface temperature, thus providing a useful comparison point for the temperature of the lower atmosphere. In addition the same instrumentation provides another source of temperature profiling of the atmosphere.

2. EXPERIMENT OBJECTIVES AND MAJOR REQUIREMENTS

A dual Voyager orbiter or equivalent spacecraft configuration constitutes a suitable platform for the conduct of the mother/daughter experiment.

Some of the basic requirements for the performance of the major experimental tasks are easily met by essentially any pair configuration considered by NASA's mission planners. For instance, the UV and IR transmission absorption spectrometer must be aimed constantly along the line between the Sun and the spacecraft, and this direction usually is already one of the spacecraft stabilization axes; the IR radiometer must aim at the surface of the planet, and usually an optical axis, (TV camera, etc.) already points in this direction.

Other requirements are not met by provisionally defined Mars dual-orbiter configurations. However, in this case it appears feasible to change certain of these configurations in order to better fit the experiment. For instance, in the case of a dual-Voyager scheme, the two orbital planes could be chosen as coincident, and passing through the radial axis of the diurnal bulge expected to exist in the Martian atmosphere and characterized by a longitudinal lag of approximately 30° with respect to the subsolar point. The relative velocity between Voyagers could be chosen in the 10 m/sec range. This mission configuration would provide the coverage of practically all the resolution cells (300 km x 300 km x 1 km at the surface) along a complete great circle in a plane containing the axis of the atmospheric bulge. Even if a vital spacecraft function would cease at this point, the data collected would be sufficient to describe fully the planet's atmosphere and ionosphere, assuming cylindrical symmetry around the bulge axis.

The remaining life span could be utilized to cover different portions of the Martian atmosphere, because of the motion of the nodal line due to the planet's oblateness. The impact of the cylindrical symmetry assumption could be therefore progressively eliminated and second order features of the planet's atmosphere and ionosphere adequately covered.

In order to obtain transmission absorption spectroscopy measurements using the Sun as a source, it is necessary to achieve periodic orbiter-to-Sun occultations. With some Voyager orbits, occultation occur too infrequently and alterations of these orbits would be required to provide at least one Sun occultation every week (3 occultations in the first 20 days of orbital life). Only short-period occultation are necessary. With other orbits that are also achievable, occultation could occur more frequently, up to orbital rates. Even with this recommendation, Voyager-Sun occultations would provide only sample measurements, separated in time.

This may be overcome, however; and continuous, although less accurate, monitoring of the planet atmosphere's temperature and pressure profiles may be accomplished using multicolor radiometric measurements of the atmospheric emission in the optically dense 15μ CO₂ band. Transmission absorption spectroscopy using the Sun as a source provides certainly superior accuracy and the few absorption observations during the mission lifetime would be vital in determining the corrections for the data gathered by the continuous-duty multi-color radiometer. A continuous-duty multi-color radiometer would also provide the mapping of the planet's surface temperature, and the enslaving of its field of view to the one of the TV cameras would permit correlation of surface features and isothermal line patterns.

In conclusion, a Voyager-to-Voyager or a configuration involving an equivalent spacecraft pair provide desirable alternatives among several schemes considered for a mother/daughter experiment.

For the Voyager case, a possible requirement that both Voyagers be fully interchangeable would be easily complied with by installing mother and daughter equipment in both. Each Voyager can act as mother or daughter, achieving full reciprocity and redundancy with only minor increase in complexity.

An alternate configuration has been investigated during the study here reported, since a mother/daughter refractivity experiment could not be performed if only one Voyager (or equivalent spacecraft) achieved orbit. A subsatellite installed in each spacecraft would increase the reliability of operation through further redundancy and would provide an experiment capability even if a single spacecraft mission would eventually be implemented. Various configurations have been briefly studied, the results of which are incorporated in Appendix B to this report. Since

this configuration is obviously more complex and expensive, it has been selected as second choice alternative. The satellite needs carry only the daughter portion of the refractivity experiment and provisions for Earth communication, in order to determine position and range rate with respect to the mother terminal. The sub-satellite described in the Appendix B is a coplanar vehicle, spin stabilized, with the spin axis normal to the plane of the ecliptic after being separated from the main spacecraft at approximately 10 meters/second.

3. BACKGROUND AND JUSTIFICATION FOR THE CONDUCT OF THE EXPERIMENT

Before the space age, occultation methods for the study of planetary atmospheres and ionospheres were limited to earth-based observations of the absorption and refraction effects imposed by these media upon the electromagnetic radiation from a star chosen for the experiment (Figure 3-1).

The difficulties and pitfalls of the method were such that very few successful occultation observations were made, and even in these cases the interpretation of the data remains questionable. We recall the occultation experiment of σ Arietis by Jupiter (Ref. 1), of the Crab Nebula by the Moon (Ref. 2), of Regulus by Venus (Ref. 3).

The problems resulting from these experiments, and which will be referred to hereafter, were the following:

1. poor signal-to-noise ratio
2. rarity of usable occultations
3. ratio of the scale height of the planet's atmosphere to the planet/Earth distance too small
4. probing confined to the upper layer of the atmosphere under investigation
5. decrease in measurement accuracy due to the effects of the Earth's own atmosphere and ionosphere
6. limitation of the probing to only two regions of the planet's atmosphere
7. nonrepetitive measurements
8. sensitivity to sudden change in the refractive and absorptive characteristics of the interplanetary medium.

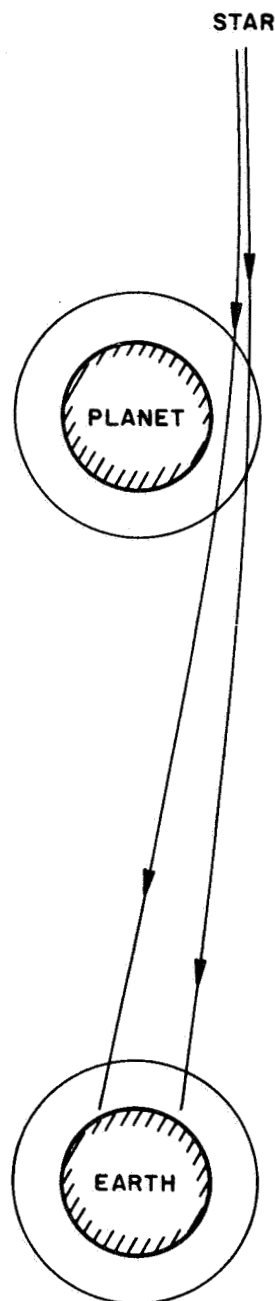


Figure 3-1 Occultation Scheme Used Before Space Age

The development of space technology made possible significant improvements of the scheme that have removed many of its limitations (Ref. 4).

Even in the case of a single space platform, two new concepts emerge. One concept involves a controllable radiator installed in the space platform that either orbits or flies by a planet using a detector installed on the Earth's surface. The Mariner IV radio occultation experiment (Ref. 5) is the pioneering experiment using the concept wherein the space vehicle flew past a target planet. Figure 3-2a depicts this configuration. This concept eliminated all the problems previously discussed with the traditional occultation experiments except Problems 5, 6 and 7. If the space vehicle had been an orbiter, Problem 7 also would have been eliminated. An example of this configuration, but with the Sun in place of the planet, is the MIT Sunblazer experiment, which probes the solar atmosphere (Ref. 6).

Figure 3-2b shows the second concept that uses a star or the sun as the radiator of electromagnetic energy while the detector is installed in an orbiting or flyby spacecraft. This concept has already been used in the following satellite missions:

a) NRL-1964-01-D and NRL-1965-16-D satellite, which measured the density of the Earth's upper atmosphere from the attenuation of the solar X-rays (44 to 60, 8 to 14, 8 to 12 Å) taking place along the line of sight between the satellite and the sun, while this line was descending through the Earth's upper atmosphere at the occultation entry and exit (Ref. 7).

b) OSO III Satellite, which measured in March 1967 the upper atmospheric density of the earth from the attenuation of the 630 Å and 430 Å Sun radiation while again the line of sight, Sun-to-Satellite, was cutting through the earth's atmosphere (Ref. 8).

c) OSO IV Satellite, which is performing at present UV measurements of the Sun radiation and which is scheduled to perform occultation measurements when the correct geometrical relationships will take place (Ref. 9)

The concept of Figure 3-2b eliminated all the problems of the traditional experiments except those identified as 6 and 7. If an orbiter is used, Problem 7 vanishes.

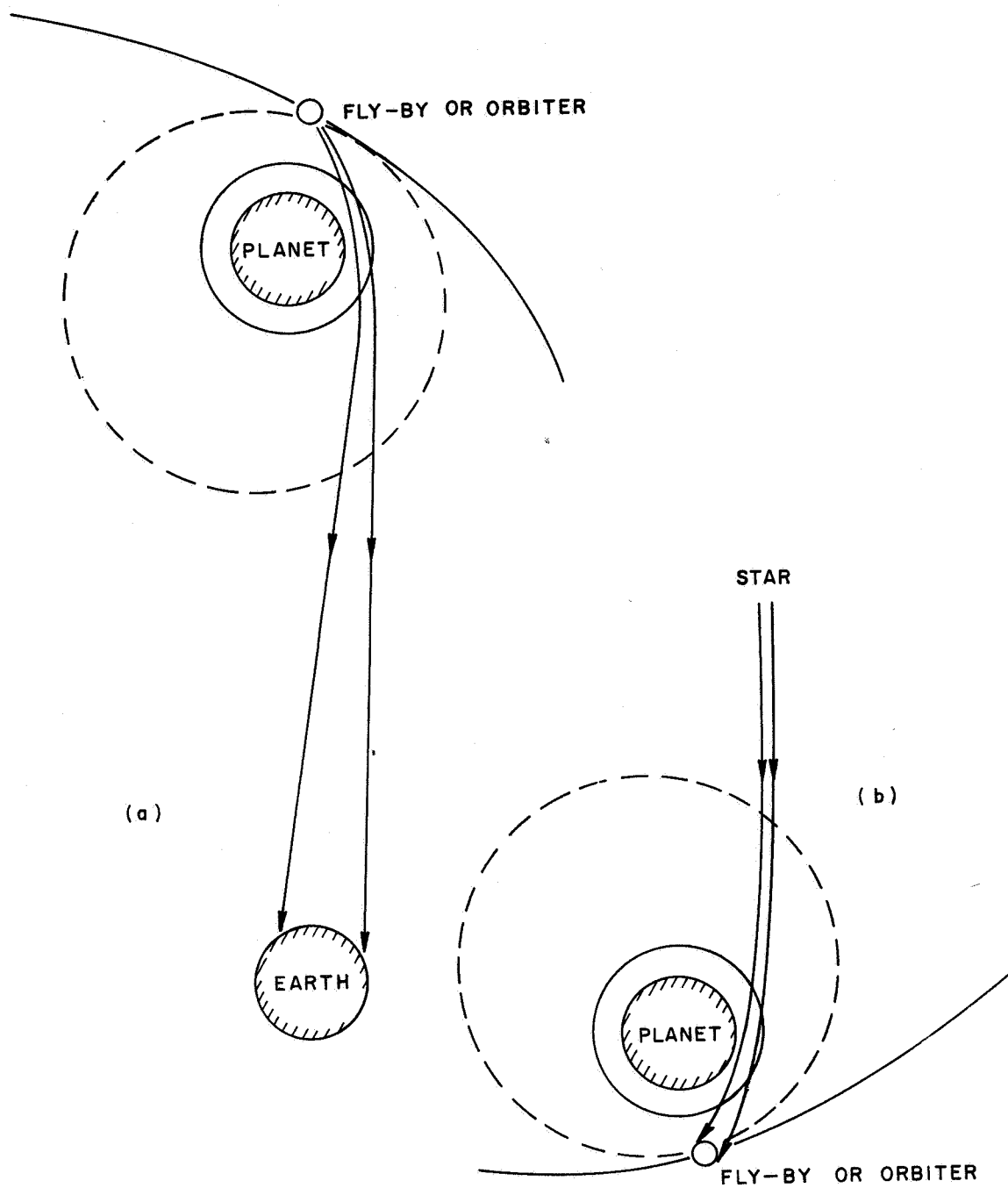


Figure 3-2 Occultation Concepts Usable with Flyby or Single Orbiter Configurations.

When two space platforms are available, it is possible to replace the natural noncoherent electromagnetic source with a known coherent transmitter and, at the same time, substitute the Earth-bound detector with a receiver also placed in the vicinity of the planet under study (Figure 3-3).

The dual flyby scheme (Ref.11) belongs to this category (Figure 3-3a). This configuration provides significant advantages. However, Problems 6 and 7 of the traditional experiment still remain unsolved, since only two regions of the planet's atmosphere are probed and the measurements are not repetitive.

These limitations are eliminated if both space platforms orbit the planet as shown in Figure 3-3b. Thus, the dual-orbiter configuration appears to be the first choice for occultation experiments to probe the atmospheres and ionospheres of the planets.

Recognizing these merits, the Raytheon Company initiated an in-house research effort in 1965 (Ref.11). Additional research activity was devoted to the possibility of identifying constituents such as water vapor using an active mother/daughter millimetric wave absorption spectroscopy link (Ref. 12). These activities confirmed the potential use of the mother/daughter occultation scheme in planetary research and defined problem areas requiring further efforts.

The limitations of occultation methods other than the mother/daughter scheme were studied in detail and the ambiguity of single-frequency probings was pointed out, particularly in reference to past experiments such as the Mariner IV (Ref. 13). The analysis showed how large errors can be incurred when inferring atmospheric pressures from single-frequency total refractivity measurements along paths involving both neutral and ionized atmospheres.

Finally, the feasibility and practicality of the orbiting pair scheme for use in atmospheric and ionospheric probing of Mars was investigated under the contract here reported. From the results obtained, both the practicality and feasibility of the method for the probing of the Martian atmosphere and ionosphere appear ascertained.

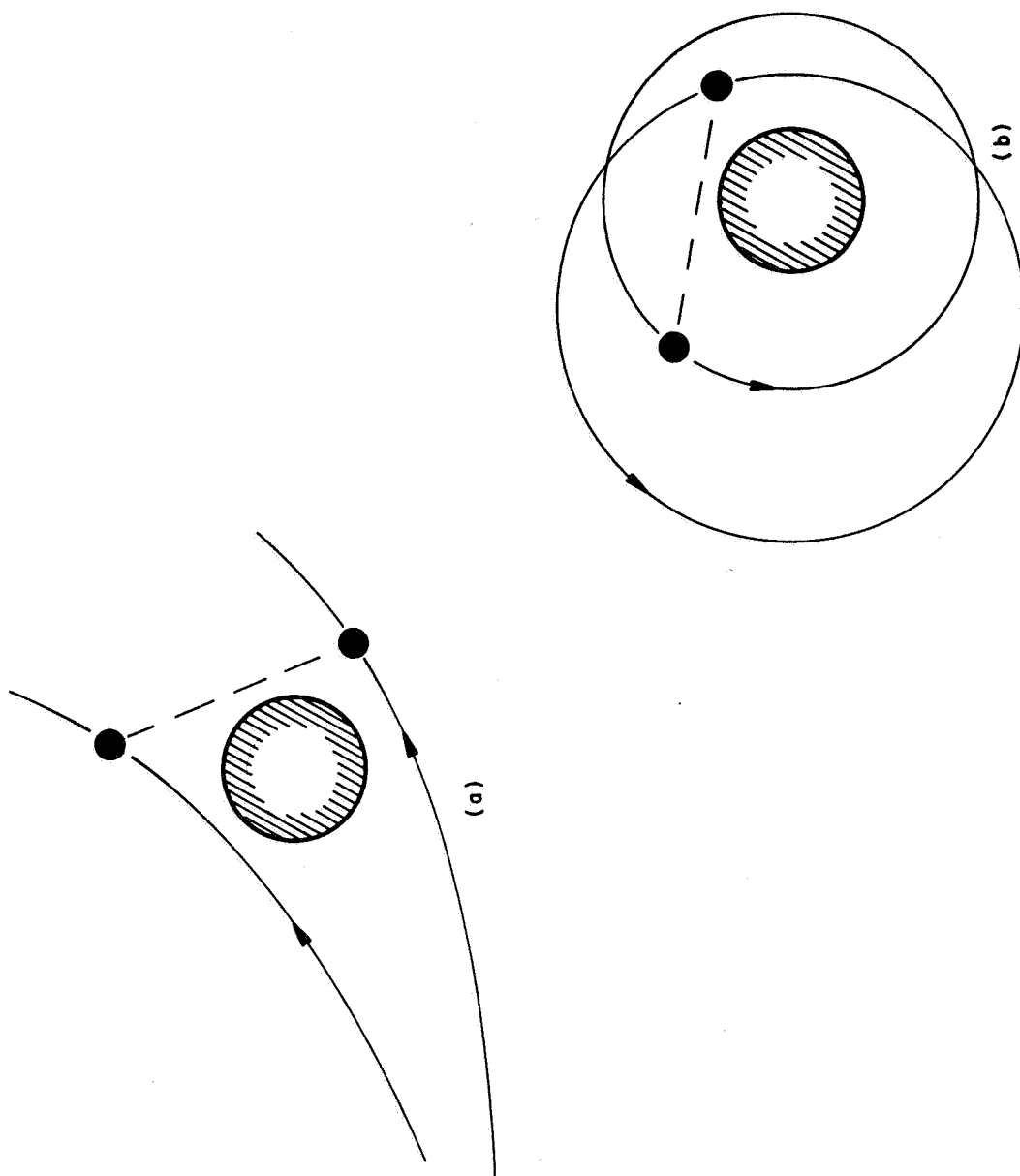


Figure 3-3 Dual Flyby and Dual Orbiter Occultation Schemes

4. TECHNICAL APPROACH

4.1 EXPERIMENT CONCEPT AND MISSION

4.1.1 THE BASIC EXPERIMENT

Refractivity, spectroscopy and radiometry data constitute a slightly redundant set of measurements in providing an unambiguous description of the neutral and ionized atmosphere of a planet.

Their interrelationship is depicted in Figure 4-1.

The dispersive component of the refractivity profile is obtained by a dual-frequency method, and yields the ionospheric electron density directly for a planet like Mars.

The nondispersive components of overall refractivity measurements made in planetary atmospheres require that the refractivity measurements be considered in context with other measured data to yield pressure, temperature, and density profiles.

The addition of measurements defining atmospheric constituents' profiles obtained by transmission absorption spectroscopy allows the derivation of pressures from the refractivity measurements, under the assumption of an exponential atmosphere. The scale height of the refractivity curve yields in fact the temperature when the mean molecular weight is known through the absorption spectroscopy measurements. Pressure remains, therefore, the sole unknown in the refractivity formula. However, the occurrence of Sun-to-Voyager occultations necessary for the absorption spectroscopy are rare events for certain Voyager orbital orientation, and multicolor radiometric measurements can be used to yield the surface temperature, and a low-accuracy but continuous probing of the atmospheric temperature and pressure.

When Sun occultations take place, the radiometric measurements can be calibrated with the high-accuracy transmission absorption spectroscopy data.

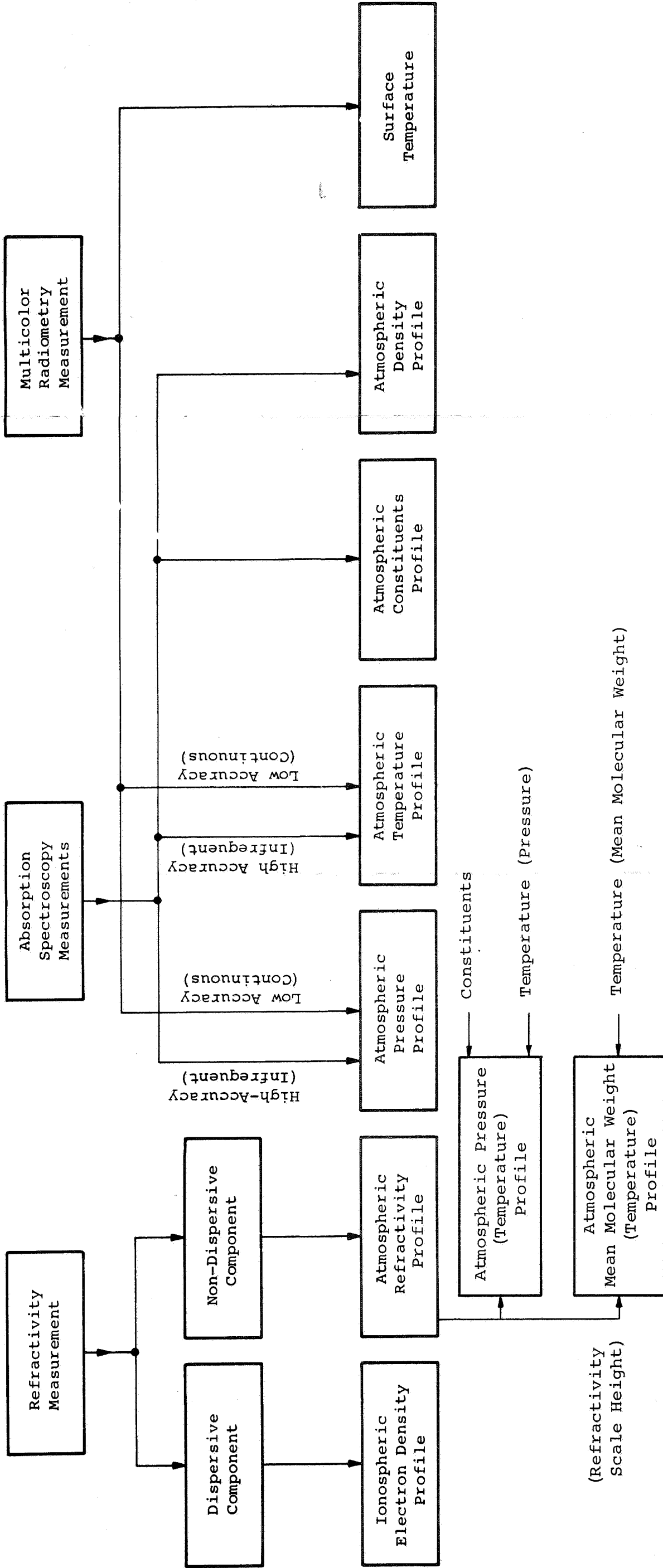


Figure 4-1 Block Diagram of the Interrelationships Among Measured Quantities

When combined with the refractivity measurements, all these data, owing to their redundancy, allow the evaluation of weighted error averages and, ultimately, the achievement of a better overall measurement accuracy.

4.1.2 SECONDARY EXPERIMENTS

The availability of the instrumentation for the basic experiment provides an opportunity to carry on additional measurements on a noninterference basis, both during the flight of the two spacecraft to Mars and during their orbiting around the planet.

While the two spacecraft move from the Earth orbit to the Mars orbit, the availability of a two-frequency probing link between them gives the opportunity of attempting the measurement of perturbations in the columnar electron densities in the interplanetary medium, while the links with the Earth allows the same measurement from each spacecraft to Earth (Ref. 14).

When the two spacecraft are in orbit around the planet, two secondary experiments are feasible: the measurement of the harmonics in the planet's gravitational field and the observations of aerosol particles in the planet's atmosphere.

Another possibility is to perform radio occultation measurements of the solar atmosphere by the radio link spacecraft-to-Earth in situations of planet conjunction.

4.2 ORBITAL REQUIREMENTS

The orbits that are currently postulated for the 1973 Voyager-Mars mission are satisfactory for the conduct of a refractivity experiment. If Voyager will be replaced in the NASA plans by an equivalent spacecraft, the orbit's choice is likely to be such that the following requirements are met. The two spacecraft orbits should be coplanar with approximately coincident lines-of-apsides. This common orbital plane should be oriented to contain the axis-of-symmetry of the Martian atmospheric bulge. The two orbits must differ in energy by an amount that would allow spacecraft separation at a rate providing one 360 degree cycle of relative rotation in a time period of 20 days or less. No specific initial relative positioning in the orbits is required. A discussion of the experiment coverage attainable using a pair of orbiters that meet these requirements is contained in Section 4.3.2.

Some currently postulated Voyager orbits are not optimal with respect to the obtainment of transmission absorption spectroscopy data during Sun occultations. The experiment requires an orbital inclination such that short-period Sun occultations occur at least once a week and more often if possible.

The relative doppler data between the two spacecraft, in addition to satisfying the basic experiment requirements, can be used to enhance the orbit determination process using stereo doppler techniques. A by-product of this orbit determination enhancement might be an increase in the accuracy of determining the Martian gravitational coefficients. This would require the development of an orbit determination program that utilizes the spacecraft-to-spacecraft doppler as one of the observation parameters. A preliminary program of this type has been developed already by JPL (Ref. 15).

4.3 REFRACTIVITY EXPERIMENT

4.3.1 GENERAL EXPERIMENT DESCRIPTION

A phase-coherent dual-frequency probing link established between the two orbiting terminals is affected by a doppler shift characterized by the following components:

(a) A geometric component due to the relative motion (range rate) of the two link terminals. This component acquires a value at each one of the probing frequencies proportional to the frequency itself ($\Delta f_1/\Delta f_2 = f_1/f_2$). When the radio path between the mother and daughter terminals is entirely in free space, this component represents the total doppler shift, and its measurement, when suitably processed, provides an effective tool for the determination of the motion of the two orbiting spacecraft.

(b) A dispersive component due to ray propagation in the ionosphere, for which $\Delta f'_1/\Delta f'_2 \neq f_1/f_2$. The method was originated by Carl Seddon (Ref. 16).

(c) A nondispersive component due to ray propagation in the planet's atmosphere. For this component, $\Delta f''_1/\Delta f''_2 = f_1/f_2$; it is indistinguishable, therefore, from true range-rate doppler, unless the latter rate is independently determined.

The two quantities that are basic to the refractivity measurements are the dispersive and nondispersive doppler components;

they can be obtained by removing the range-rate doppler contributions from the total doppler. Therefore, range rate must be known with an accuracy of a small fraction of a cm/sec to keep the error in refractivity measurements down to a few percent.

When geometric dopplers are extracted and the doppler residuals obtained, the columnar refractivity measurements can be derived and converted to desired radial profiles. The conversion can be performed using the classical Abel transform (see Ref. 11) or by the application of model matching methods (Ref. 17).

The columnar measurements are integral measurements and will not resolve horizontal gradients in the planet's atmosphere and ionosphere when these gradients are too sharp. Fortunately for Mars, at ground surface, the requirement for low gradient necessitates essentially uniform densities over a planet-centered angle of a few degrees and this is adequate to resolve the expected day-side/night-side gradients, that are significant over 10's of degrees.

4.3.2 ORBITAL MECHANICS ANALYSIS

4.3.2.1 General

The selection of orbital parameters for the two spacecraft requires consideration of the various mission constraints. A two-Voyager configuration is the basic alternative submitted to analysis in this section. Mission constraints can be grouped into trajectory constraints, which arise due to the characteristics of the interplanetary transfer trajectory; engineering constraints which are necessary for the efficient operation of the spacecraft systems and involve such items as avoiding Sun and star occultations; and scientific constraints imposed by the design of the scientific experiments.

The scope of the investigation of the orbital requirements for the refractivity experiment was reduced by disregarding the scientific constraints imposed by other experiments and, also, by disregarding the engineering constraints except for the approximate size of the Voyager orbits as they are presently known. For the assumed Voyager orbital size, the experiment coverage was assessed, and desirable orbital orientations were investigated. The results are presented here for the refractivity experiment as well as for the spectroscopic and radiometric experiments, in the form of orbital requirements. These requirements can be used by NASA mission

planners in conjunction with the other mission and experimental constraints and requirements, in order to design the final Voyager orbits, or the orbits of an equivalent spacecraft, if the Voyager program will not be executed.

4.3.2.2 Orbital Requirements for the Refractivity, Spectroscopic and Radiometric Experiment

Successful refractive probing of the neutral and ionized atmosphere of Mars requires that the path offset point as defined in Figure 4-2 pass through enough resolution cells to define the medium completely. For our purposes, a resolution cell is defined as 300 km in latitude, 300 km in longitude, and 1 km in height.

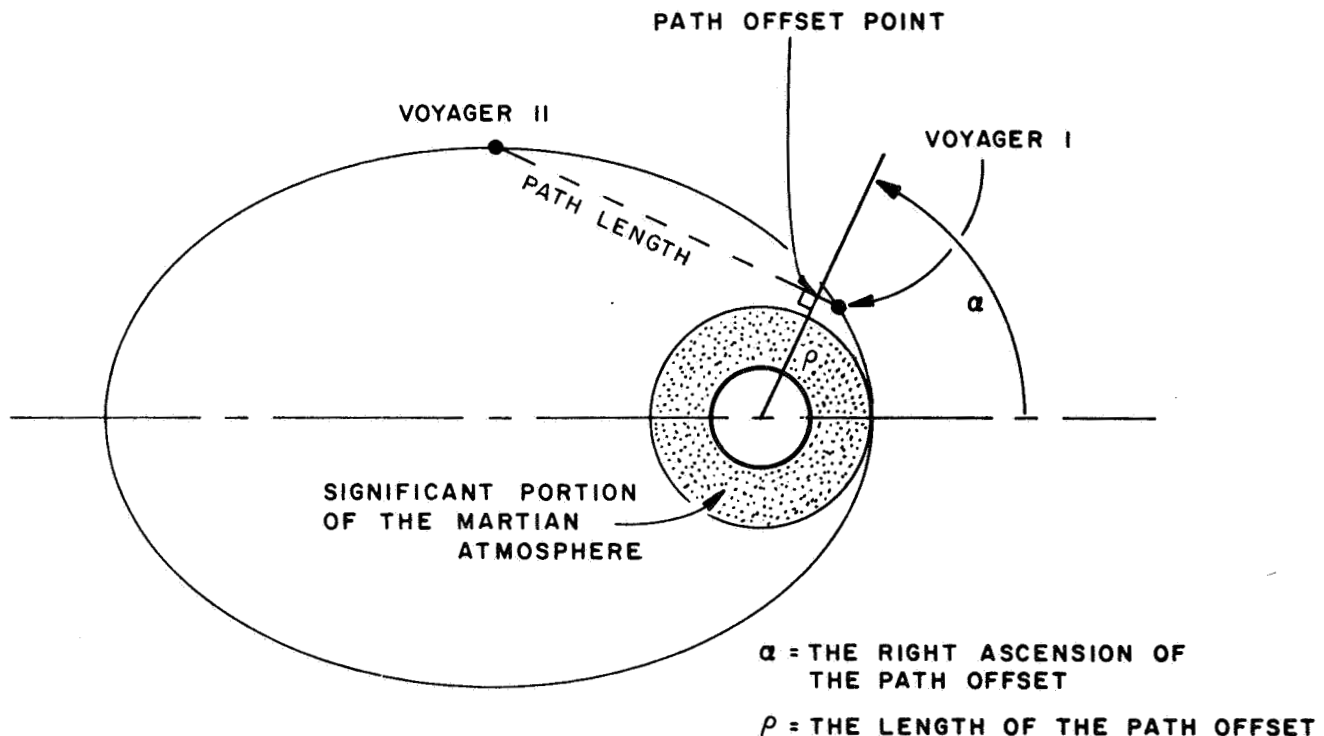


Figure 4-2 Geometry of the Probing Link

In an ideal experiment, the path offset point would move in a short period of time radially from the surface to the maximum desired probing altitude (1000 km), move then to an adjacent column of cells and repeat.

Under the actual conditions of this refractivity experiment, the probing link is established using two Voyager spacecraft as terminals and therefore the motion of the path offset is governed by the assumed orbit.

In order to investigate the coverage using realistic Voyager orbits, the following assumptions were made: The two Voyager orbits have the same orientation (inclination and argument of periapsis) and the same periapsis height, but differ slightly in the length of their semimajor axes. The latter causes a difference in mean motion resulting in relative motion between the two spacecraft.

Since the two Voyager spacecraft are in coplanar orbits, the offset point also moves in the orbital plane, which raises the following question: Can the three-dimensional characteristics of the Martian neutral and ionized atmosphere be defined when the path offset point moves in a plane? The answer to this question is affirmative, provided that the Martian atmosphere is first rotationally symmetric during the time period required to take data; second, that the axis of atmospheric symmetry lies in the plane of the Voyager orbiters; and third, that the oblateness perturbations causing rotation of the major axis and nodal line are small during the time required to take data.

The atmosphere of Mars is assumed to have a solar bulge much the same as the Earth, fixed relative to the Mars-Sun line and whose maximum lags the subsolar point in longitude by a small angle (approximately 30 degrees, as in the case of the Earth).

The refractivity experiment requires that the Voyager orbiters be coplanar and that their common orbital plane pass through a point approximately 30 degrees in longitude away from the subsolar point in the direction of planet rotation. This does not appear to be a serious experimental constraint as a family of orbits of varying inclination exist satisfying this requirement that hopefully will also satisfy the other Voyager engineering and experimental requirements.

The oblateness of Mars will cause rotations of the orbital line-of-apsides and line-of-nodes. For an orbit with a 1000 kilometer periapsis height and a 20,000 kilometer apoapsis height at an inclination (i) these perturbations amount to:

Line-of-Apsides

$$\frac{d\omega}{dt} = 0.2(1-5 \cos^2 i), \text{ deg/day}$$

Line-of-Nodes

$$\frac{d\Omega}{dt} = - 0.4 \cos i, \text{ deg/day}$$

Rotation of the line-of-apsides has no significant effect on the refractivity experiment coverage since it corresponds to a rotation of the orbital major axis in the orbital plane. However, rotation of the line-of-nodes causes the orbital plane to shift away from the principal axis of the atmosphere's bulge, unless the orbit is at the particular inclination at which the nodal perturbation just equals the rotation of the bulge axis in inertial space due to Martian motion about the Sun. Since the latter is unlikely, we can assume that the orbital plane will gradually shift away from the atmosphere's axis of symmetry. For the assumed orbit, the maximum rate of this shift is approximately 0.9 degree/day in longitude (0.4 degree due to oblateness and 0.5 degree due to planet motion about the Sun) and over the time required to complete one cycle of coverage (approximately 20 days) the relative motion in longitude will be 18 degrees. Since the angle between the bulge axis and the orbital plane changes by a fraction of this amount, the assumption that data be taken in a fixed plane passing through the bulge axis is almost satisfied.

The advantage of having nodal motion is that subsequent cycles of coverage are all taken with respect to different slices through the atmospheric bulge. This enables the complete three-dimensional characteristics of the atmosphere to be determined in time.

Another desirable, although not completely necessary orbital requirement is that the orbital plane be perpendicular to the day-night transition line (terminator). However, this latter constraint would completely fix the orbital orientation, since it requires the orbital plane to contain both the Mars-Sun line and the Mars-bulge line, and should be considered only if it does not conflict with other requirements.

The size of the Voyager orbit assumed for investigating the refractivity experiment coverage has a periapsis height of 1000 km and an apoapsis height of 20,000 km. This orbit was investigated as it represents the largest Voyager orbit size postulated, resulting in the greatest orbital period, and, therefore, the most pessimistic orbit from the standpoint of minimizing the coverage

time. If adequate coverage-time characteristics are attainable with this orbital size, they should be improved with a reduction in apoapsis height.

In Figure 4-2 the Voyager orbits were assumed to be equatorial; this enables the offset point to be located in inertial space by its right ascension, (α), and length from the Martian center (ρ).

To obtain relative motion between the two Voyager spacecraft, they were assumed to be coplanar with slightly different semimajor axis and, for computational purposes, the same periapsis height. The major axis difference was computed on the basis of having a differential mean motion between the two Voyagers resulting in one 360 degree cycle of relative rotation in approximately 21 days. This requires a major axis differential between the two spacecraft of approximately 250 km. Although a major axis difference greater than this is acceptable, the difference cited is consistent with a reasonable coverage time.

The coverage history obtained using the above orbits (considering separation to begin from periapsis) is shown in Figure 4-3. It requires a few days before the two spacecraft separate enough for the coverage pattern to become systematic. After this initial time interval, the offset point makes the excursions shown beginning in the lower left-hand corner of the figure at 2.28 days from separation. The offset point, following the contour of the orbit, continues up to apoapsis heights and then decays to zero at 2.8 days at which time it briefly reappears on the opposite side of the planet; the first of which is indicated by a time mark at 2.48 days. This pattern continues with the upper curves shifting downwards and the lower curves shifting upwards until after approximately ten days the two coverage patterns merge (not shown for clarity) at which time one-half of the coverage cycle is complete. This condition corresponds to having one spacecraft at periapsis while the second is at apoapsis of its orbit. Subsequently (from 10 to 21 days) the lower and upper curves intersperse providing additional coverage continuing until a full cycle is completed in approximately 21 days.

As shown, the offset point moves almost vertically through the altitude band of interest ($h = 0$ to 1000 kilometers) four times per orbit. The resolution cell width is approximately five degrees, and therefore more than adequate density of coverage is provided over much of the field. Those portions not adequately covered are partially accounted for by the symmetrical characteristics of the atmosphere.

The behaviour of the path length and the path offset length are shown as a function of time in Figures 4-4 and 4-5 respectively. For the orbit investigated, the path offset moves very rapidly through the altitude band of interest moving at a rate approaching 2 kilometers/second. An obvious disadvantage of the postulated Voyager orbit size and shape, apparent from Figure 4-5, is the large apoapsis height which results in considerable wasted time between subsequent passes through the coverage zone.

The results of this study suggest the following orbital requirements for the refractivity experiment.

- Orbital Size (1) A 1000 kilometer periapsis height by 20,000 kilometer apoapsis height is acceptable, although 1000 by 10,000 would reduce coverage time.
- (2) The two Voyager orbits should have slightly different major axis in order to provide relative motion.

- Orbital Orientation (1) The two Voyager orbits should have approximately the same inclination, and argument of periapsis.
- (2) The orbital planes should initially pass through the Martian atmosphere's axis of symmetry.

The orbital requirements for the radiometric and spectroscopic experiments are easily delineated.

For the spectroscopic experiment, the only requirement is that occultations of the Sun by Mars occur at least 5-10 times during the experiment's lifetime. For the radiometric experiment, no special requirement must be imposed, in the final approach adopted by the investigators of this experiment in the course of the study here reported.

4.3.3 SIMULATED MISSION INVESTIGATIONS

In order to gain a better understanding of the refractive portion of the electromagnetic probing experiment necessary for a more accurate experiment design, the Martian atmosphere and ionosphere were simulated and the transmission through them was analyzed by means of a double precision ray tracing program, which

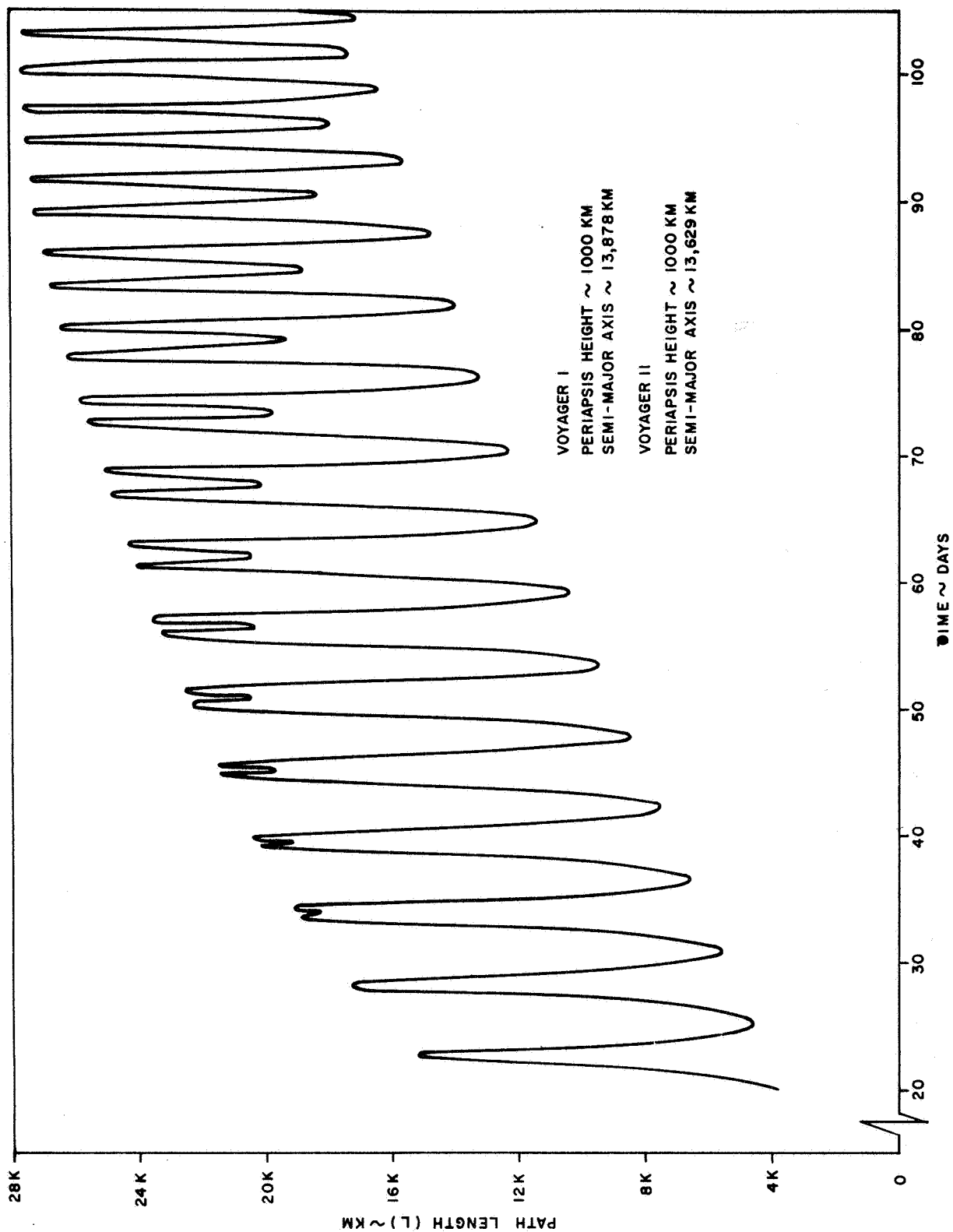


Figure 4-4 Path Length versus Time

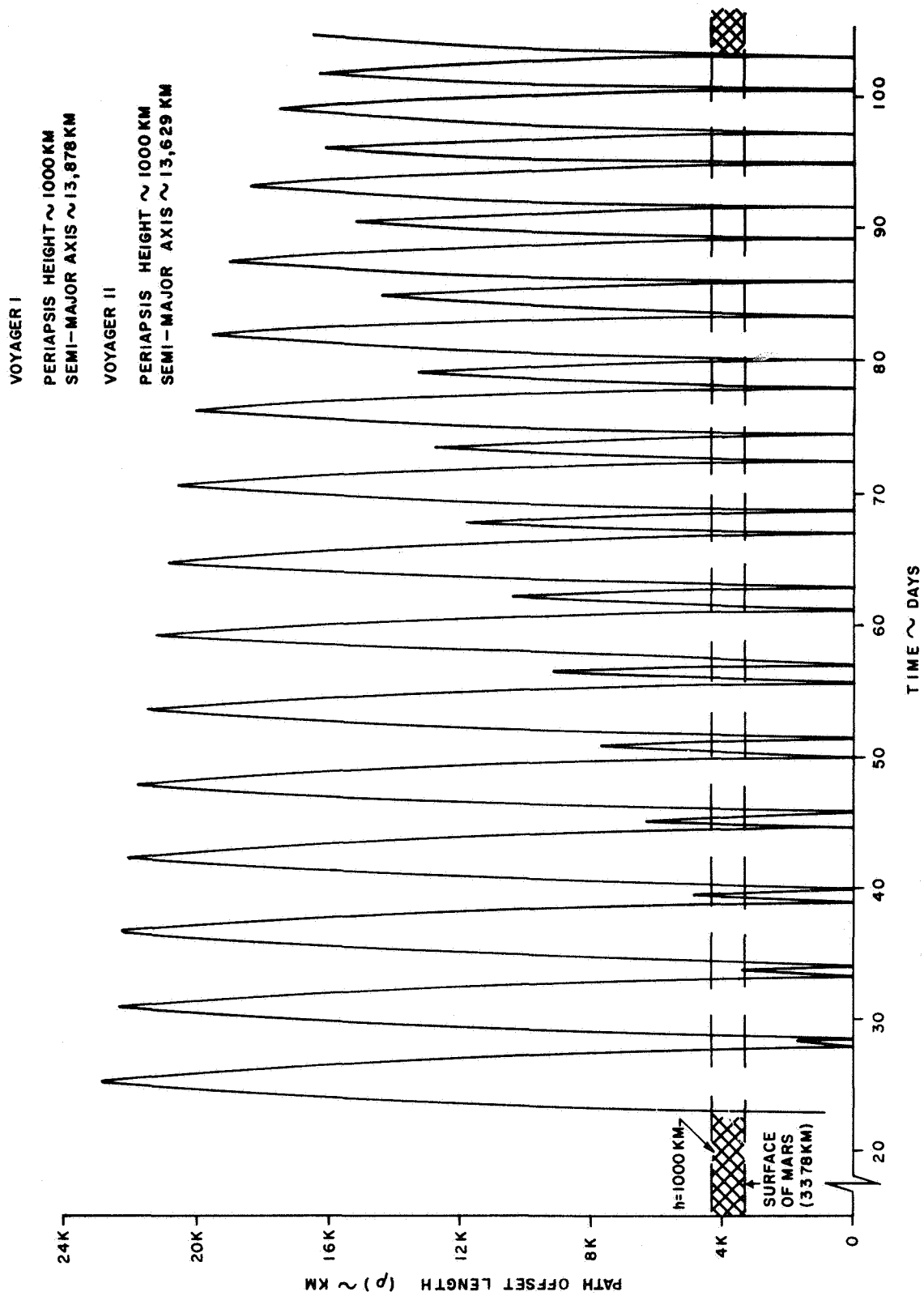


Figure 4-5 Path Offset versus Time

includes the effect of electron density of the ionosphere, and the effects of pressure and temperature of the atmosphere.

Models of the Martian temperature and pressure profiles were constructed by mathematical curve fits to the mean models published by NASA (Ref. 18). The equations are given below and the accuracy of the fits can be seen in Figures 4-6 and 4-7.

For the Mars Pressure profile, we adopted the following fit:

$$P = \exp \left[a_1 h + a_2 + a_3 \sin \left(\frac{\pi}{100} h \right) \right], \text{ mb}$$

$$\frac{\partial P}{\partial h} = P \left[a_1 + \frac{a_3 \pi}{100} \cos \left(\frac{\pi}{100} h \right) \right]$$

where

$$a_1 = -.109064$$

$$a_2 = 2.07946$$

$$a_3 = 0.575645$$

h = height above surface of Mars, km

For the Mars temperature profile, the fit was as follows:

For

$$0 \leq h \leq 40 \text{ km}$$

$$T = b_2 (h + b_1)^2 + b_3, \text{ } ^\circ\text{K}$$

$$\frac{\partial T}{\partial h} = 2b_2 (h + b_1)$$

where

$$b_1 = -40$$

$$b_2 = 0.06125$$

$$b_3 = 132$$

For $h > 40$ km

$$T = 132^{\circ} \text{ K}$$

$$\frac{\partial T}{\partial h} = 0$$

The Mars electron density model was taken from the literature (Ref. 19) except that the D-layer was removed. This curve was fit with a Chapman double exponential profile.

$$N = N_{\max} \exp \left\{ \left[1 + w - \exp(w) \right] / 2 \right\}$$

where

$$w = \frac{h_{\max} - h}{11}$$

and h is the height above the planet surface, N_{\max} is the density of the F₂-layer, and h_{\max} is the height at which N_{\max} occurs.

N_{\max} and h_{\max} are made to vary with latitude and longitude to model horizontal gradients.

Models were taken to be spherically symmetric for initial investigations and then perturbed in a systematic fashion to evaluate the effects of sharp horizontal gradients on the inversion techniques developed.

For the mean model of the Martian atmosphere, the composition was assumed to be 75% CO₂ and 25% N₂.

4.3.3.1 Frequency Selection for the Refractivity Experiment

Using the simulated atmosphere and ionosphere, we were able to select the frequencies of transmission according to the following criteria.

- (1) The two frequencies must be such that each of the two radio paths passing between the two spacecraft must have their point of minimum altitude in the same 1 km x 300 km x 300 km resolution cell.
- (2) At least one of the frequencies should be high enough so that the effects of the atmosphere play a dominant role.

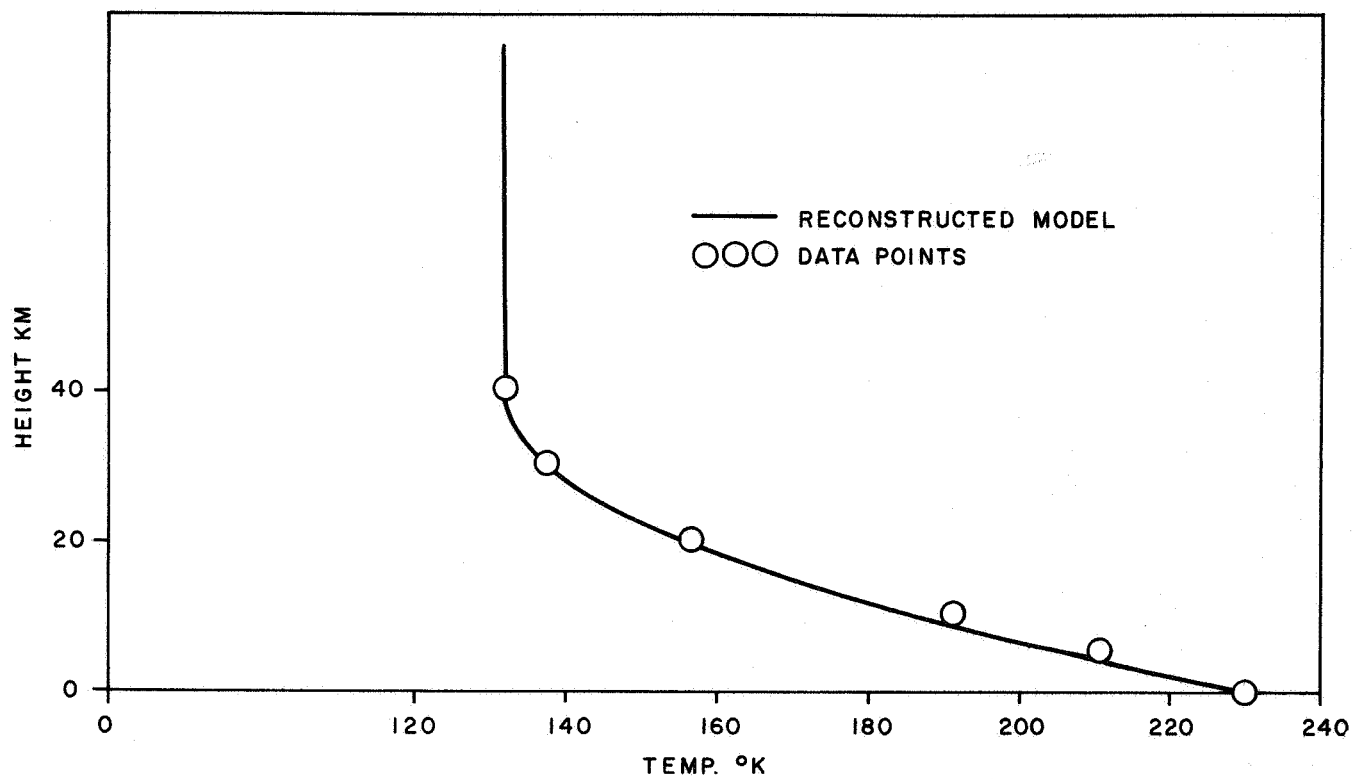


Figure 4-6 Temperature of Martian Atmosphere (Mean Model)

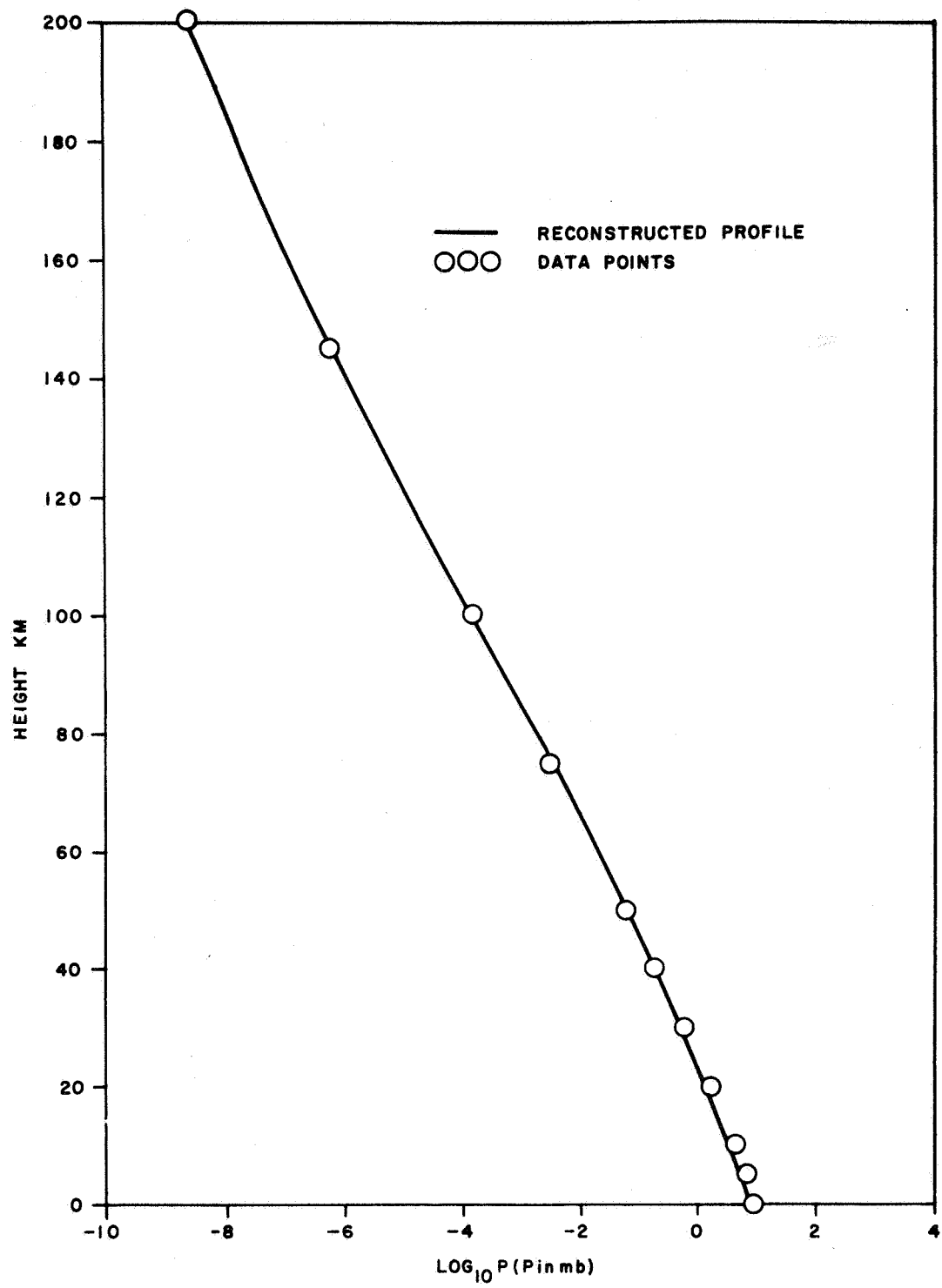


Figure 4-7 Pressure of Martian Atmosphere (Mean Model)

- (3) The frequencies must be separated widely enough to provide the wanted accuracy when separating dispersive and nondispersive refractivity.

Rays were traced at frequencies of 50, 100, 200, 400, 600, 800, 1000, and 2000 MHz. For each frequency three rays were traced with miss distance 0, 75, 150 km from the planet surface (ray traveling on a straight line). To satisfy condition (1) the height of the minimum points of the rays must not vary from the intended minimum by more than 0.5 km.

Phase delay data at the 0 km miss distance must be of the same order of magnitude and opposite in sign to the maximum delay caused by the F-layer to satisfy condition (2). Condition (3) was tested by taking values of refractivity along the rays of one frequency and comparing them to values at the same altitude for another frequency. Having two values of refractivity at a given height and two different frequencies, we can separate the dispersive from the nondispersive refractivity. Since we know the refractivity at a given height from our atmospheric and ionospheric models, we can evaluate the error in separating the elements. For frequencies which satisfy conditions (1) and (2) we then select the pair which gives the minimum error in condition (3).

By condition (1) frequencies must be greater than 100 MHz. The highest frequency was chosen to be 2000 MHz in order to satisfy condition (2). For condition (3), 400, 600, and 800 MHz gave similar errors. For simulation purposes we have selected 600 MHz but the choice of the second frequency can vary between 400 and 800 MHz depending on system requirements.

4.3.3.2 Positioning Accuracy Requirements

In order to ensure that the radio path passes through a given cell, we must know the position of each spacecraft within a given tolerance. The problem was in staying inside the 1 km height of the resolution cell. The following approach was used.

For a particular minimum point in the ray path, rays were traced from points along the perimeter of a 0.5 km circle about the minimum point. All rays were assumed to be traveling horizontally at these points (see Figure 4-8).

The locations found to be critical in keeping the point determined in a 1 km x 300 km x 300 km box were the points 1 and 2 above and below the actual minimum.

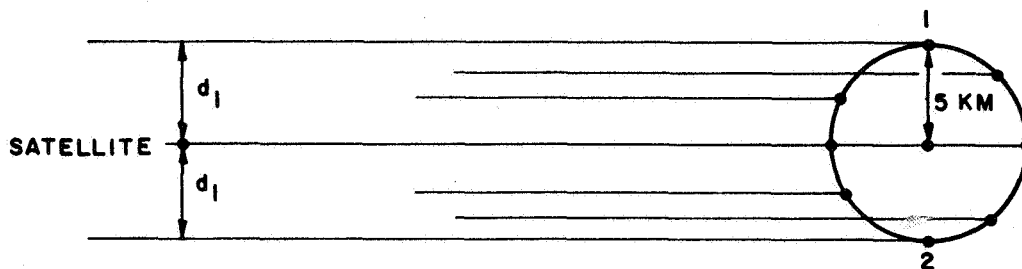


Figure 4-8 Positional Error

It was found that to ensure that the midway position would be within a circle of radius 0.5 km, we need to know the satellite position to within 0.5 km.

4.3.3.3 Range Rate Accuracy

To determine the allowable error in range rate determination, 600 and 2000 MHz rays were traced through a model ionosphere yielding two profiles of height versus phase delay (cycles). This data was converted by an Abel transform program (see Subsection 5.1) to refractivity versus height. These refractivity profiles were then used to examine the deviation in refractivity when the phase delay was perturbed by additive random errors with a Gaussian distribution of zero mean and various standard deviations. The perturbed phase delay was then converted to refractivity by Abel transform and the perturbed refractivity was examined. An example is given below (Table 4-1) for $f = 600$ MHz with the error standard deviation of 0.005 cycles. For this case we can see that the error which is given in percentage is less than 2 percent except where the refractivity is small. The difference between the perturbed and original refractivity has an unbiased mean of -1.80×10^{-5} and a standard deviation of 0.008 N-units.

TABLE 4-1

Refractivity Errors Versus Phase Delay Perturbations
(F = 600 MHz, Max. Err. = 0.005 cycles)

Height (km)	Perturbed Refractivity (N units)	Original Refractivity (N units)	Difference (N units)	Relative Error %
5	2.42517	2.4357	0.010533	0.432444
10	1.64941	1.6292	-2.02058 E-2	-1.24023
20	0.768318	0.77186	3.54227 E-3	0.458926
30	0.339886	0.3454	5.51381 E-3	1.59636
40	0.167851	0.15683	-1.10212 E-3	-7.02751
50	0.130968	0.13566	4.69169 E-3	3.45842
70	8.76163 E-2	0.09194	4.32375 E-3	4.70279
80	0.164949	0.1654	4.50957 E-4	0.272647
90	0.408443	0.4106	2.15708 F-3	0.525348
100	-1.10911	-1.114	-4.89346 E-3	0.439269
110	-7.00521	-7.0052	1.21966 E-5	-1.74108 E-4
115	-9.8666	-9.8655	1.10450 E-3	-1.11956 E-2
120	-11.2007	-11.2013	-6.42747 E-4	5.73814 E-3
125	-11.1251	-11.1374	-1.23354 E-2	0.110757
130	-10.1367	-10.1227	1.40057 E-2	-0.138359
140	-7.35352	-7.3521	1.42436 E-3	-1.93735 E-2
150	-4.92716	-4.9293	-2.13659 E-3	4.33447 E-2
160	-3.20426	-3.1955	8.75658 E-3	-0.274029
170	-2.03337	-2.0359	-2.52644 E-3	-0.124095
180	-1.21845	-1.2142	4.24659 E-3	-0.349744
200	-0.472181	-0.47438	-2.19937 E-3	0.463631
225	-0.159433	-0.16463	-5.19718 E-3	3.15688
250	0	0	0	5.78960 E 76

In order to meet the criterion of 5 percent accuracy in refractivity measurements, it was found that the errors in the phase delay must have a standard deviation of less than 0.01 cycles for $f = 2000$ MHz and less than 0.005 cycles for $f = 600$ MHz. The reason for higher requirements on 600 MHz is that the effects of the atmosphere are smaller, relatively speaking, at this frequency than the ionospheric ones and can be obscured by the errors affecting these last.

This translates to the requirement that the rms "noise" in the doppler residuals be smaller than 0.018 Hz at 2000 MHz and 0.009 Hz at 600 MHz, assuming an integration time of 1/2 sec, which is compatible with the established resolution cell structure and terminals' orbits.

Consequently, the affordable errors in overall doppler measurements and in range rate measurement must each be within $1/\sqrt{2}$ of the above quantities.

4.3.3.4 Recovery Inaccuracies when Dispersive Nondispersive Effects are Separated

Once we have found the refractivity profiles for two frequencies, we must separate them into dispersive and nondispersive components. This is done in the following manner. The quantities we begin with are:

$$\text{Combined refractivity at } f = f_1: N_1(f_1) = (\mu_1 - 1) \times 10^6$$

$$\text{Combined refractivity at } f = f_2: N_2(f_2) = (\mu_2 - 1) \times 10^6$$

We wish to find N_e and N_A where

N_e = Electron Density in electrons/cc., and

N_A = Atmosphere refractivity (not frequency dependent)

In addition we will define

$$\begin{aligned} N_I &= \text{Ionosphere refractivity at } f_1 = M_I/f_1^2, \text{ where } M_I \\ &= -1/2 \frac{N_e}{12400} \quad (\text{in absence of magnetic field}) \end{aligned}$$

$$\begin{aligned} N_I' &= \text{Ionosphere refractivity at } f_2 = M_I/f_2^2, \text{ where } M_I \\ &= -1/2 \frac{N_e}{12400} \end{aligned}$$

The indexes of refraction for f_1 and f_2 are given by:

$$\mu_1^2 = \frac{1 + 2 (A_1 + B_1)}{1 - (A_1 + B_1)}$$

where

$$A_1 = \frac{2 N_I \times 10^{-6}}{3 + 2 N_I \times 10^{-6}}$$

$$B_1 = \frac{(1 + 10^{-6} N_A)^2 - 1}{(1 + 10^{-6} N_A)^2 + 2}$$

$$\mu_2^2 = \frac{1 + 2 (A_2 + B_2)}{1 - (A_2 + B_2)}$$

where

$$A_2 = \frac{2 N_I' \times 10^{-6}}{3 + 2 N_I' \times 10^{-6}}$$

$$B_2 = B_1$$

Using the above equations we can write them as:

$$A_1 + B_1 = \frac{\mu_1^2 - 1}{2 + \mu_1^2} \approx \frac{2 N_1 (f_1) \times 10^{-6}}{3} \quad \text{for } N_1 (f_1) \ll 1 \quad (1)$$

$$A_2 + B_2 = \frac{\mu_2^2 - 1}{2 + \mu_2^2} = \frac{2 N_2 (f_2) \times 10^{-6}}{3} \quad \text{for } N_2 (f_2) \ll 1 \quad (2)$$

but

$$A_1 \approx \frac{2}{3} N_I \times 10^{-6} = \frac{2}{3} \frac{M_I}{f_1^2} \times 10^{-6}$$

$$A_2 \approx \frac{2}{3} N_I' \times 10^{-6} = \frac{2}{3} \frac{M_I}{f_2^2} \times 10^{-6}$$

$$A_1 - A_2 = \frac{2}{3} M_I \times 10^{-6} \left(\frac{1}{f_1^2} - \frac{1}{f_2^2} \right)$$

Subtracting (2) from (1)

$$A_1 - A_2 = \frac{2}{3} \left(N_1 (f_1) - N_2 (f_2) \right) \times 10^{-6}$$

$$M_I = \frac{(N_1 (f_1) - N_2 (f_2))}{\frac{1}{f_1^2} - \frac{1}{f_2^2}} = \frac{1}{2} \frac{N_e}{12400}$$

from which the electron density N_e is obtained. We can solve then for N_A using (1)

$$B_1 = \frac{2}{3} N_1 (f_1) \times 10^{-6} - \frac{1}{6} \frac{M_I}{f_1^2} \times 10^{-6}$$

$$= \frac{2}{3} \left(N_1 (f_1) - \frac{M_I}{f_1^2} \right) \times 10^{-6}$$

but

$$B_1 = \frac{(1 + 10^{-6} N_A)^2 - 1}{(1 + 10^{-6} N_A)^2 + 2} \approx \frac{2 \times 10^{-6} N_A}{3 + 2 \times 10^{-6} N_A}$$

$$N_A = \frac{3 B_1}{2 \times 10^{-6} (1 - B_1)}$$

The errors in the refractivity profiles will translate to electron density and atmospheric density errors. We must now determine what kind of accuracy we need in our refractivity profiles so that our errors in ionospheric and atmospheric profiles are tolerable. We can no longer usefully speak of relative errors since the electron density and atmospheric density are zero over large portions of the profile (space between atmosphere and ionosphere). Absolute errors must therefore be considered.

Gaussian errors of zero mean and standard deviation σ were applied to the refractivity profiles, and they were separated into electron density (electrons per cc) and atmospheric P/T ratios (dynes/cm²/°K).

Table 4-2 gives the standard deviation of: 1) the electron density and 2) the atmospheric P/T ratio for various values of σ , the standard deviation of the input refractivity profile.

The requirements stated in Subsection 4.3.3.3 impose that we have a differential phase standard deviation of 0.01 cycles for $f = 2000$ MHz and 0.005 cycles for $f = 600$ MHz. In refractivity units, this leads to $\sigma = 0.005$ N-units for $f = 2000$ MHz, and $\sigma = 0.0075$ N-units for $f = 600$ MHz.

TABLE 4-2
ABSOLUTE ERRORS IN IONOSPHERIC DENSITY AND
ATMOSPHERIC P/T RATIOS

f = 2000 MHz \ f = 600MHz	$\sigma = 0.05$	$\sigma = 0.1$
$\sigma = 0.005$	1) 511.15 el/cc 2) 0.14242 dynes cm ⁻² °K ⁻¹	1) 609.56 el/cc 2) 0.172002 dynes cm ⁻² °K ⁻¹
$\sigma = 0.01$	1) 524.218 el/cc 2) 0.210855 dynes cm ⁻² °K ⁻¹	1) 630.7 el/cc 2) 0.243348 dynes cm ⁻² °K ⁻¹

4.3.4 RANGE RATE AND POSITION DETERMINATION

A recent analysis (Ref. 20) conducted at the Jet Propulsion Laboratory indicates the capability of determining satellite orbits around Mars with extremely high accuracy. The uncertainty in the periapsis altitude, for example, after one orbit, was found to vary from a sigma of 0.4 meter to one of 40 meters depending upon the particular orbital characteristics. Similarly, the uncertainty in the period was discovered to be at most on the order of 40 milliseconds. On the basis of this study, it can be concluded that range rate accuracies on the order of 0.15 cm/sec are well within reason. The relative uncertainty in the position and velocity of the two satellites relative to each other will therefore be on the same order of magnitude (greater by at most a factor of $\sqrt{2}$, if the separate position and velocity errors are independent). This error is larger than the maximum acceptable, but it should be emphasized that these results are based on two-way doppler measurements only; in particular, they make no use of the doppler link between the two satellites. D.W. Curkendall (Ref. 15) has shown that this link can be particularly effective in the determination of the relative orbits of two satellites. Effort is being made to include these data in future orbit determination programs. Another approach being investigated involves a direct extrapolation of the intersatellite doppler data to estimate the geometric doppler when the transmission path includes the Martian atmosphere.

Finally, it should also be noted that the direct range measurements, which will presumably be available during the Voyager flight, also have not been used in these satellite position determination programs. These data, too, could conceivably be used to improve the accuracy of the results, although at present this does not seem to be necessary.

It is therefore concluded that the required range rate rms error of approximately 0.18 cm/sec does not appear infeasible, when all the observations are utilized to their fullest.

4.3.5 PHASE MEASUREMENT ACCURACY

4.3.5.1 General

Three separate doppler measurements are to be used in the experiment; viz:

1. The two-way doppler in the Earth-Voyager I link.
2. The two-way doppler between the two spacecraft (two frequencies). (Since the Voyager I VCO will be phase-locked to the signal received from Earth, this measure will also include the one-way Earth-Voyager I doppler.)
3. The "stereo" doppler in the Earth-Voyager I-Voyager II-Earth link.

It is shown in Section 4.3.6, that the threshold signal-to-noise ratio at this loop input is nominally 25 db in a 20 Hz bandwidth. This implies a phase error standard deviation of 0.04 radian in the 20 Hz receiver phase-locked loop bandwidth. If 1/2 second averages are used to determine the doppler rate, this corresponds to a doppler frequency error of approximately 0.013 Hz at 2000 MHz. The task of obtaining an error of 0.0065 Hz in the 600 MHz link is of lesser difficulty. The doppler errors in link (3) of course will be slightly greater than this value due to the error contributions of the other phase-locked loops. Since these bandwidths can be made less than the 20 Hz bandwidth of the final loop, and since these other loops operate at higher signal-to-noise ratios, these additional contributions are not likely to be significant. For the same reasons, the tracking accuracies of the other doppler links will be somewhat greater than that of link (3).

To review in more detail, the behaviour of phase locked loops when connected in series, let's consider the block diagram of the experiment (see Figure 4-23, Section 4.3.6.2) and let's analyze the PLL tandem. Three loops in tandem are involved in the measurement-one for the Earth-Voyager I link, the second for Voyager I-Voyager II and the third for Voyager II-Earth (or Voyager II-to-Voyager I) link. Identical, critically-dampened, second-order loops were assumed at each terminal. The phase variance was derived due to noise at the input of each loop. The Signal/Noise ratio at the input of each loop was assumed to be high enough to ensure that the loops are operating in the linear region.

The total output phase variance (σ_ϕ^2) due to the thermal noise at the loop inputs is

$$\sigma_\phi^2 = \frac{N_1}{2A_1^2} \int_{-\infty}^{\infty} |H(\omega)|^6 \frac{d\omega}{2\pi} + \frac{N_2}{2A_2^2} \int_{-\infty}^{\infty} |H(\omega)|^4 \frac{d\omega}{2\pi} + \frac{N_3}{2A_3^2} \int_{-\infty}^{\infty} |H(\omega)|^2 \frac{d\omega}{2\pi} \quad (1)$$

where N_i is the single-sided noise spectral density and A_i the signal amplitude at the input to the i th loop, $H(\omega)$ is the loop transfer function,

$$H(s) = \frac{Ks + K^2/4}{s^2 + Ks + K^2/4} \quad (s = j\omega) \quad (2)$$

and K the loop gain. Expressed in terms of the noise bandwidth B_{L+L} of a single loop ($B_L = 5K/16$), σ_ϕ^2 becomes

$$\sigma_\phi^2 = \frac{483}{5 \times 10^7} \frac{N_1 B_L}{A_1^2} + \frac{29}{40} \frac{N_2 B_L}{A_2^2} + \frac{N_3 B_L}{A_3^2} \quad (3)$$

Assuming all three loop inputs simultaneously attain their threshold values, $\frac{N_1}{A_1^2} = \frac{1}{2.09 \times 10^4}$, $\frac{N_2}{A_2^2} = \frac{1}{3.09 \times 10^3}$, $\frac{N_3}{A_3^2} = \frac{1}{3.31 \times 10^2}$

the phase error variance would be $\sigma_\phi^2 = (3.29 \times 10^{-3}) B_L$. (4)

This, in turn, yields a phase-error variance of

$$\sigma_\phi^2 = (6.58 \times 10^{-2}) \text{ rad}^2. \quad (5)$$

when the three loops all have 20 Hz noise bandwidths. This represents a 9% increase over the variance contributed by the third loop alone.

With 1/2-second integration time, twenty independent phase samples can be obtained, with reduction of the variance to $3.25 \times 10^{-3} \text{ rad}^2$.

The small percentage increase is, of course, a consequence of the fact that the third link in this configuration is by far the most critical one. In contrast, the phase-error variance in the Earth-Voyager I-Voyager II-Voyager I link is nearly double (1.22×10^{-2} vs. $0.64 \times 10^{-2} \text{ rad}^2$) the value it would have were only the last loop involved. Even so, this tracking error is considerably smaller than that of the preceeding link and is well below the maximum acceptable variance. The phase-error variance in the third configuration of concern, the Earth-Voyager I-Earth link, is also attainable from Equation (3) by equating N_1 to zero (since only two loops are involved). In this case, since the up-link is so much stronger than the down-link the total variance is virtually entirely due to the latter link alone, ($\sigma_\phi^2 = 6.05 \times 10^{-2} \text{ rad}^2$).

As the relative positions of the three terminals change, these conclusions as to the percentage increase in the phase-error caused by the multiple-loop configuration may be altered. Nevertheless, the total variance should never exceed those values derived above, since these were determined under the assumption of nominal threshold conditions at all three (or two) loop inputs.

A more difficult problem is to optimize simultaneously the three loop transfer functions. The configuration utilizing identical critically-damped loops was chosen more for historical connotation and mathematical convenience. Simultaneous optimization would probably yield a superior design, and in any case would establish a standard to which a practical system could be compared.

4.3.5.2 Equipment Phase Stability

The refractivity measurements require overall rms errors in the doppler residuals within 0.013 Hz at 2000 MHz and 0.0065 Hz at 600 MHz. This in turn requires that the components used in the system have negligible phase changes as a function of temperature and signal amplitude. In order to obtain direct information on the phase stability of typical building blocks of the refractivity measurement instrumentation, laboratory tests were conducted within the scope of the present program.

Figure 4-9 depicts the laboratory tests setup. The two blocks under test were a bandpass filter and a standard wide-band amplifier suitable for use either for IF or video frequencies.

Figure 4-10a provides the pass-band curve of the filter, Figure 4-10b the frequency response of the amplifier.

Figure 4-11 shows the variation in output phase vs input amplitude. It shows the remarkable feature of a sole 2° phase rotation across 60 db dynamic range.

Figure 4-12 indicates output phase changes vs amplifier and filter temperature.

Again it can be noticed how small phase rotations accompany very large temperature excursions.

Figure 4-13 provides more details on the separate contributions to the phase instability due separately to the filter and the amplifier.

Figure 4-14 illustrates differential phase behaviours of the assembly filter/amplifier when temperature changes. There is no detectable variation in this parameter.

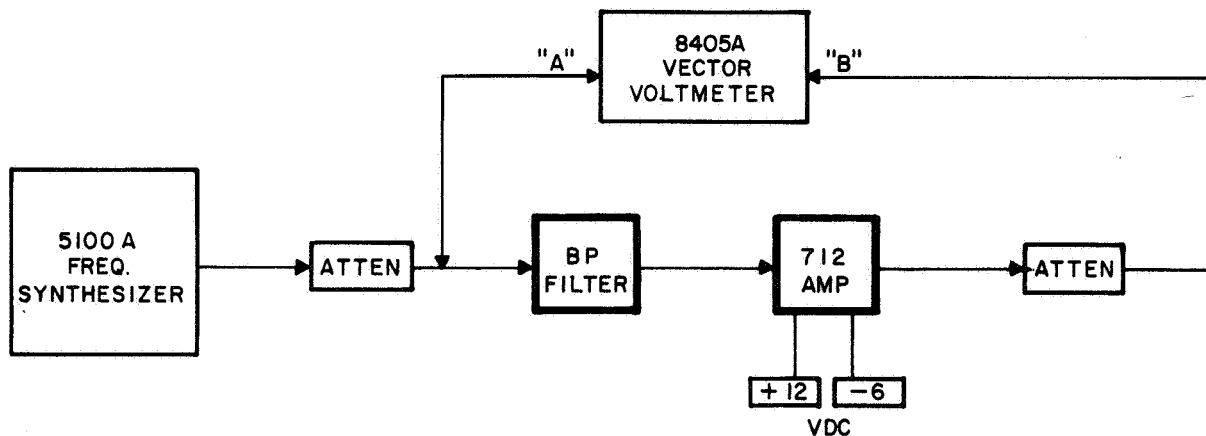


Figure 4-9 Laboratory Tests, Setup

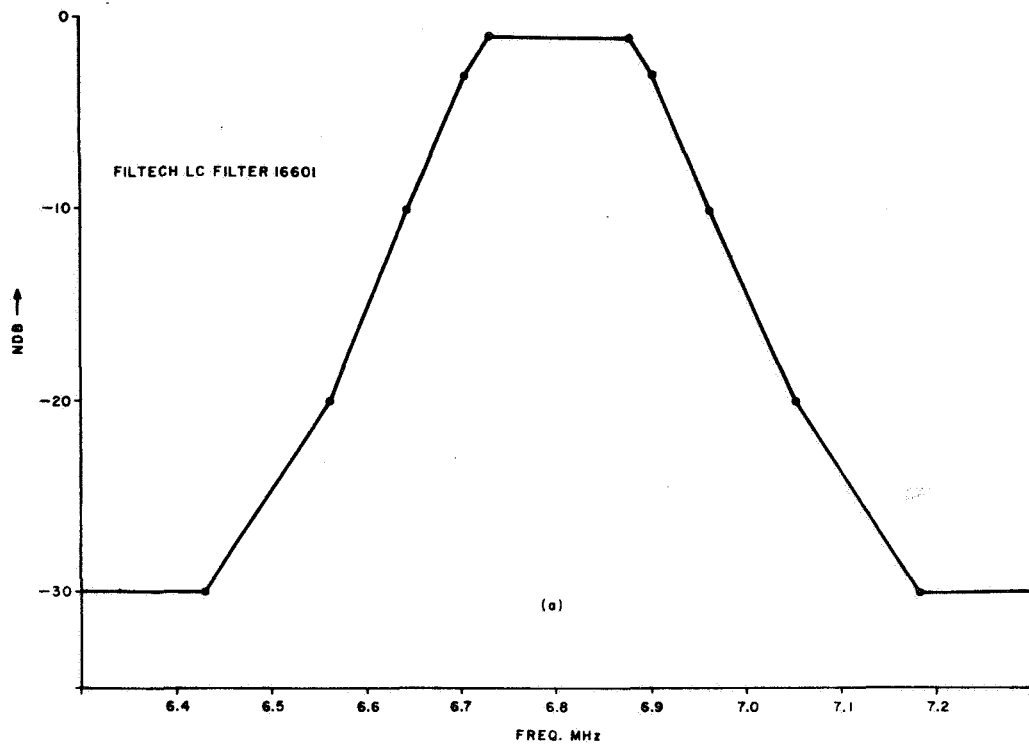


Figure 4-10a Frequency Response Curve of the BP Filter and the WB Amplifier

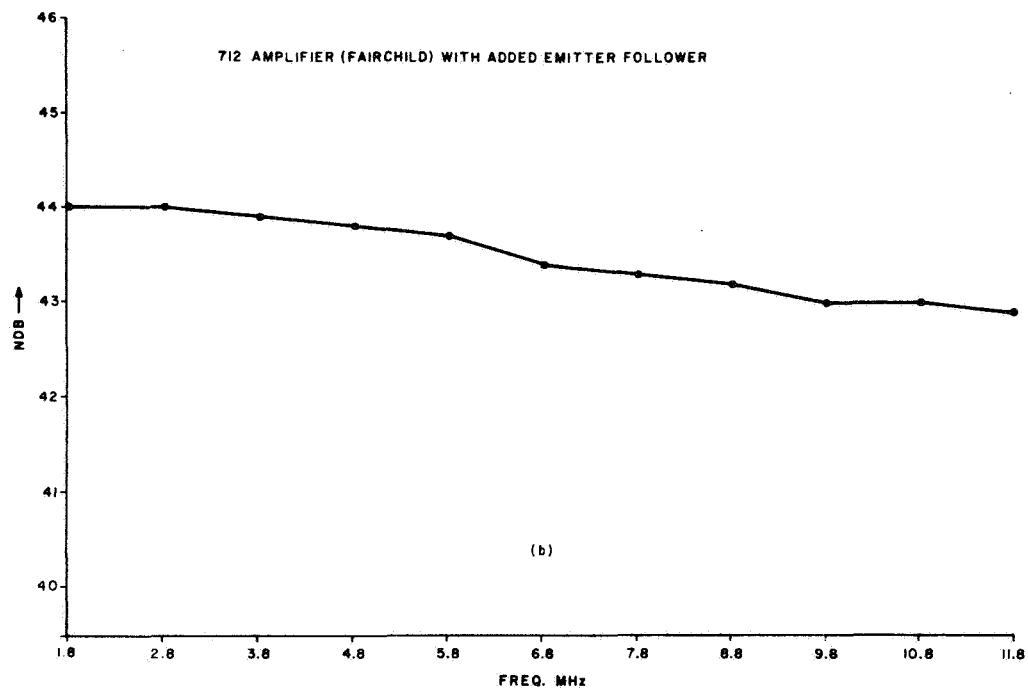


Figure 4-10b Frequency Response Curve of the BP Filter used in the Laboratory Tests

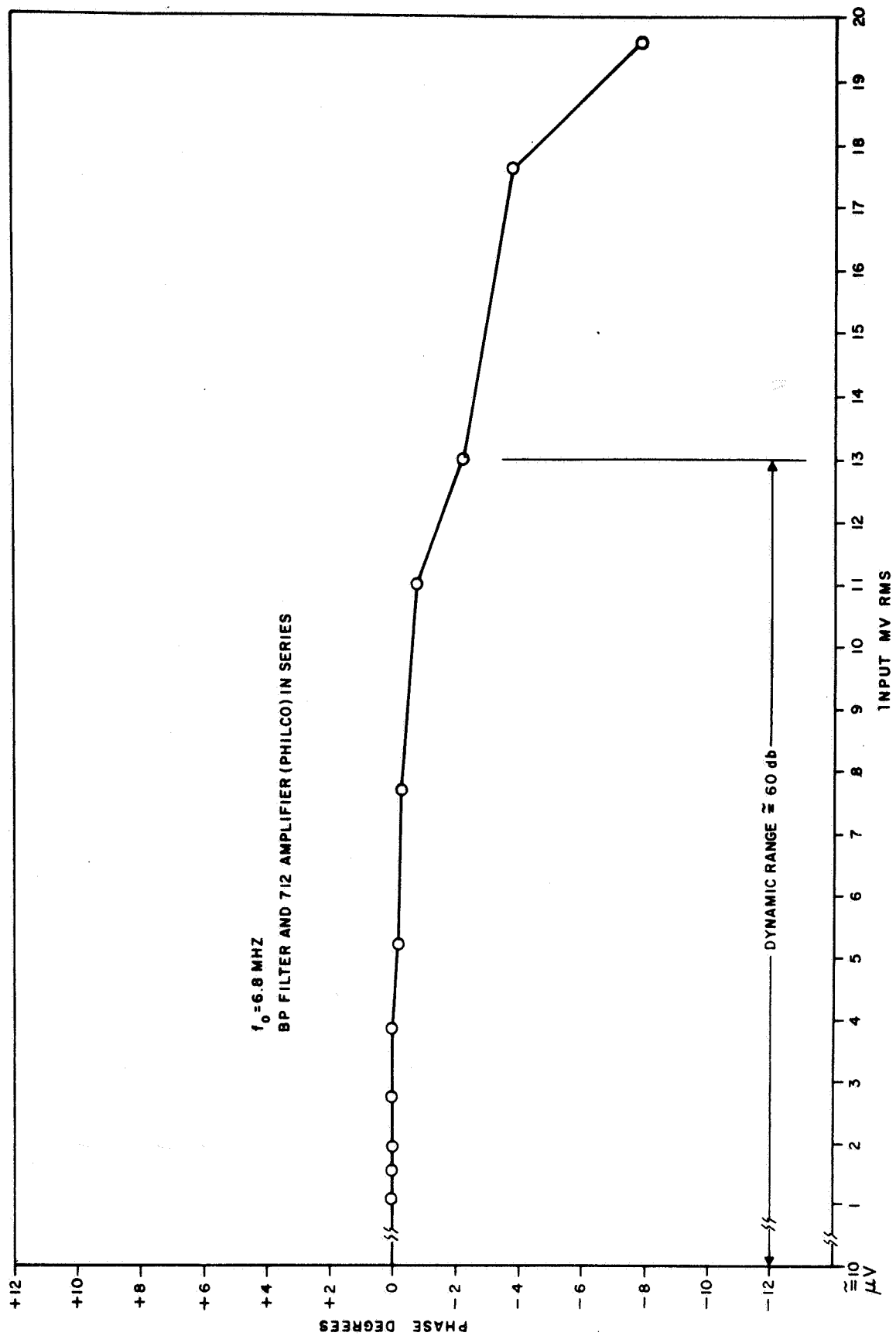


Figure 4-11 Output Phase vs Input Amplitude

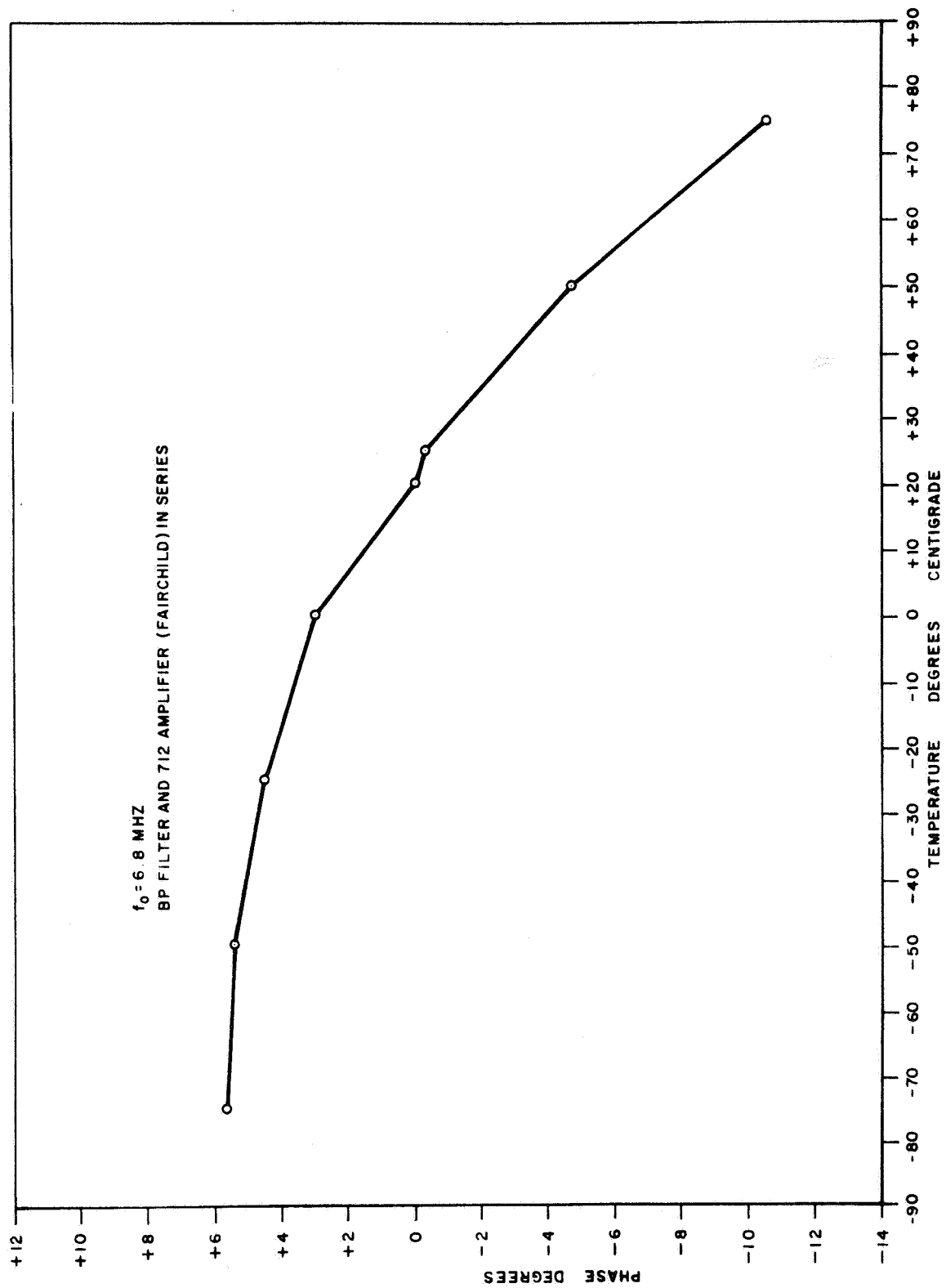


Figure 4-12 Output Phase vs Temperature

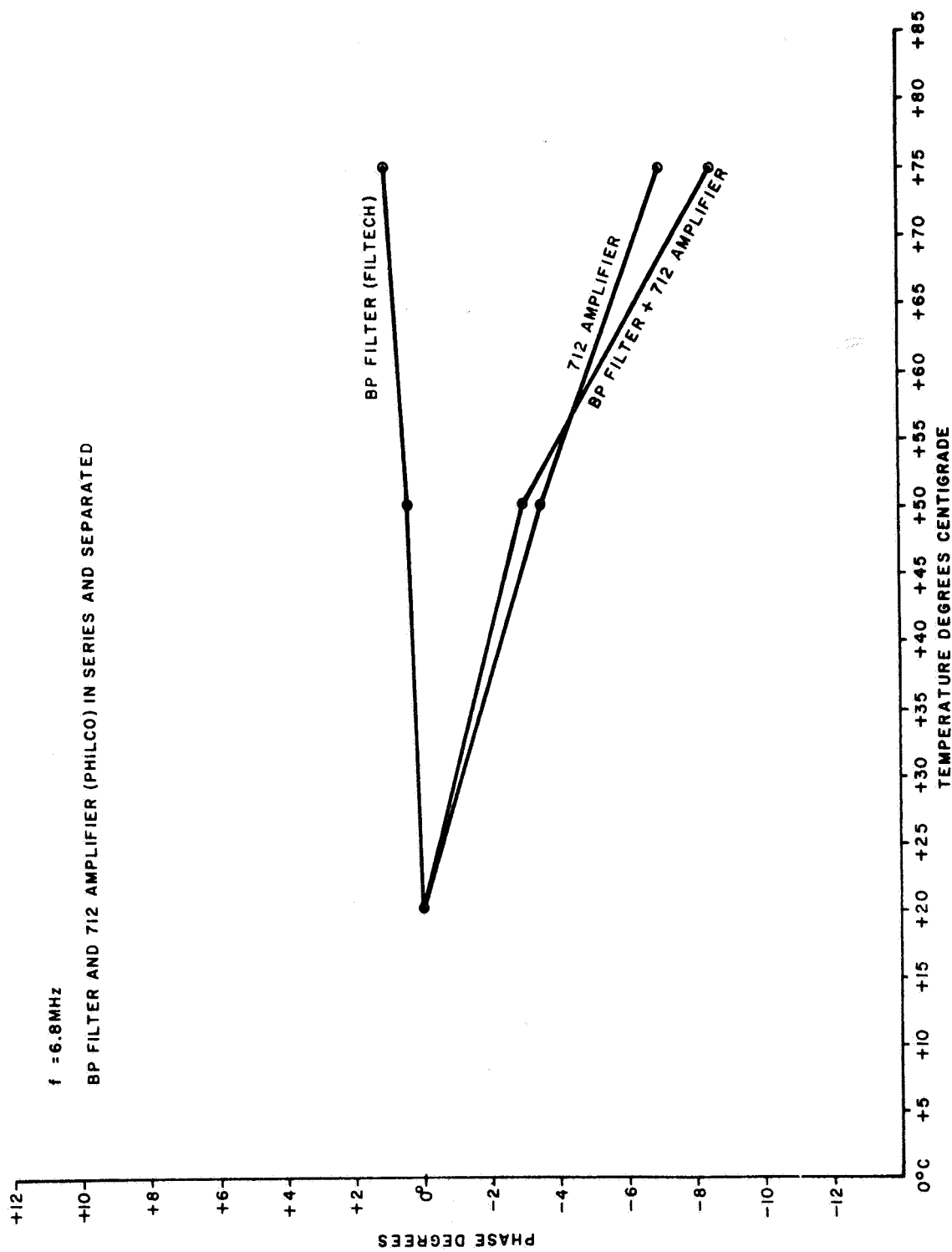


Figure 4-13 Contributions to the Phase Instability Due Separately to the Filter and the Amplifier

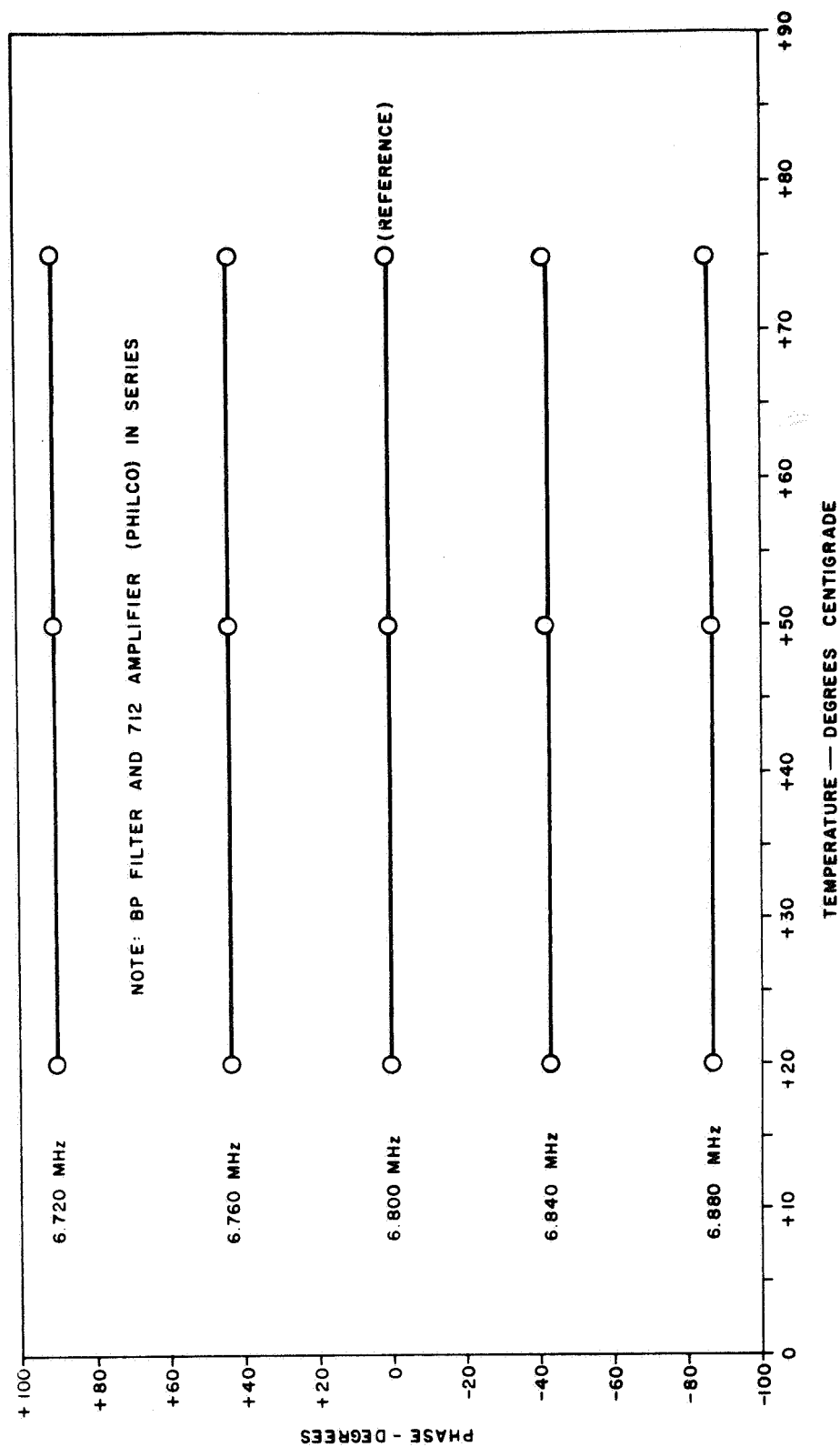


Figure 4-14 Differential Phase vs Temperature Behavior of the Assembly Filter/Amplifier

Figure 4-15 finally indicates how the gain of the assembly changes when temperature drifts. Again the smallness of these changes in the large temperature range -75°C to $+75^{\circ}\text{C}$ is conspicuous.

As it is known, doppler instability is given by the ratio $\Delta\phi/\Delta t$, where Δt is the time interval during which the phase change $\Delta\phi$ materializes. The irrelevance of the $\Delta\phi$'s which stem from the laboratory tests can be easily proven.

In order to cause, for instance, a 0.001 Hz doppler noise, the temperature change of 150°C that Figure 4 indicates as capable of producing a 16° phase rotation should take place in an unrealistically short 5-minute time interval.

It is concluded therefore, that present state-of-art electronic blocks are fully adequate to guarantee the phase stability necessary for the desired refractivity measurement accuracy.

4.3.5.3 Antenna Requirements and Phase Problems

The type of antenna best suited for refractivity measurements of the Martian neutral and ionized atmosphere is dependent upon the configuration of the mission that uses two orbiters, 3 axes stabilized, and in coplanar orbit. An Earth-oriented S-band link already on the Voyagers will be available for receipt of a reference signal and for telemetry of experimental data to Earth.

Under these assumptions, no major antenna problems exist. Two signals are generated in Voyager I in phase coherency with the reference signal coming from the Earth. A reference at 2000 MHz is then transmitted to the other orbiter. At Voyager Orbiter #2, the 2000 MHz signal, received from Voyager #1, is used to generate two phase coherent signals at 500 MHz and 2160 MHz, both of which are transmitted back to Voyager Orbiter #1.

The requirements for Voyager #1 can be accommodated by only one additional antenna capable of transmitting at 2000 MHz, receiving at 2160 MHz, and receiving at 500 MHz. Their response must be omnidirectional in the plane of the Voyager orbits. It is desirable and feasible to add some gain to this antenna in the plane perpendicular to the orbital plane.

The requirements for the antenna in Voyager #2 are similar except for a reversal of the transmit-receive function.

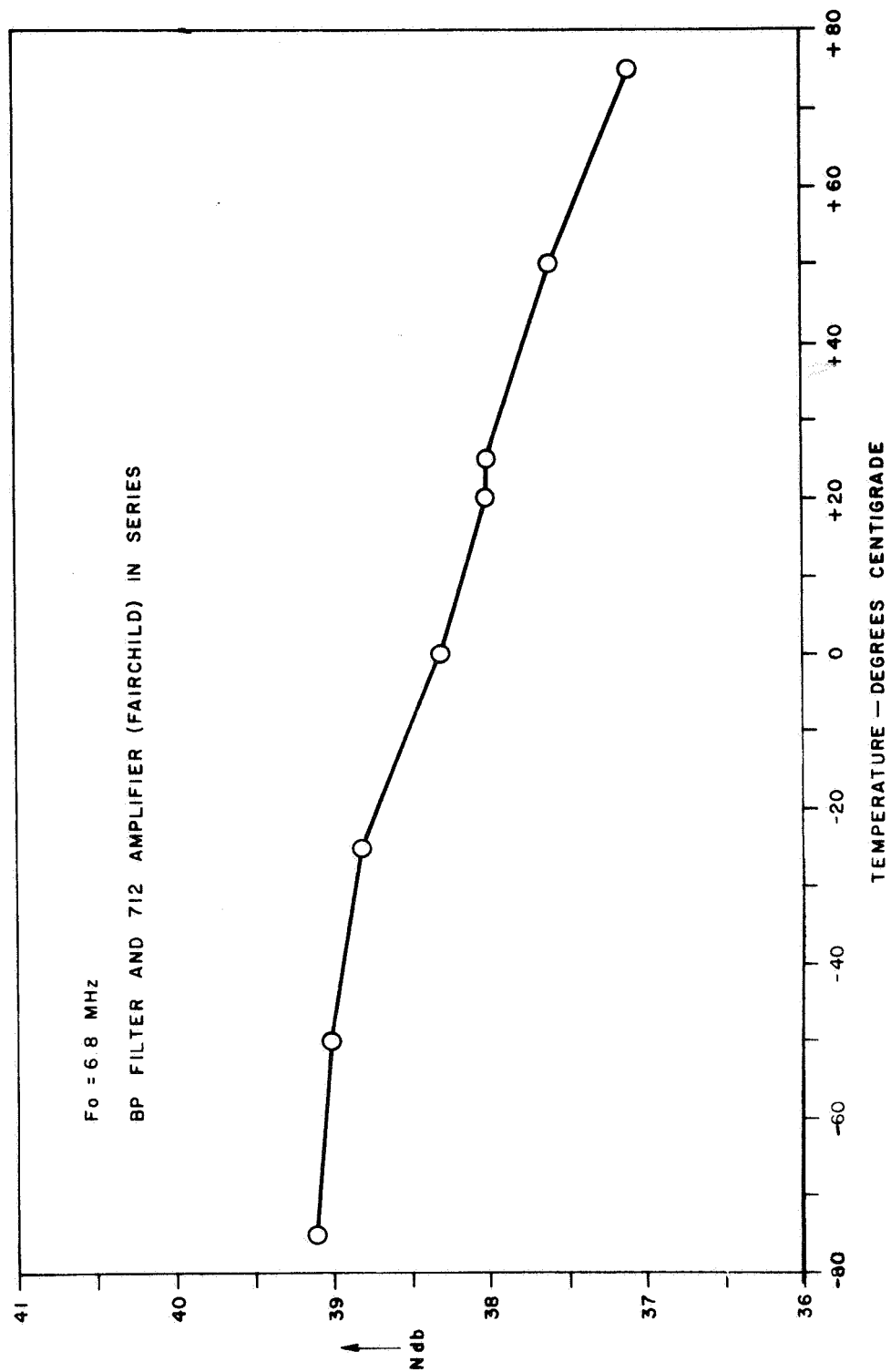


Figure 4-15 Gain (db) Versus Temperature

A precaution must be taken since, if the radiation patterns have nulls, each time that the Voyager-to-Voyager radio path line passes through one of them, a 180° phase shift results. Based on a helical antenna approach, two types of designs have been investigated: the one wavelength per turn and two wavelengths per turn configurations. The former is smaller in diameter and yields a greater variation in the azimuth pattern. The latter has better omnidirectional characteristics. Patterns for a single way one-wavelength antenna are depicted in Figures 4-16 and 4-17. Patterns for the two-wavelength circumference antenna are depicted in Figures 4-18 and 4-19. The overall length of the antenna in both cases is five wavelengths. Figures 4-20 and 4-21 are photographs of such an antenna on a scale model of the Voyager vehicle. Figure 4-12 shows the anechoic chamber set-up used in the pattern measurements.

The gain of this antenna over a dipole is approximately 7 db (for an overall gain of 9.1 db) including the losses due to cross polarization. This gain is sufficient for the 500 MHz antenna and is marginal for S-band. By increasing the length of the array the extra db needed can be achieved.

4.3.6 REFRACTIVITY EXPERIMENT SYSTEM REQUIREMENTS

4.3.6.1 General

An overall refractivity experiment system block diagram is shown in Figure 4-23. The experiment will be compatible with and will utilize the telemetering and command systems that will be a part of standard Voyager equipment. The refractivity experiment will make phase comparisons between the Earth-to-Voyager reference signal and the two Voyager-to-Voyager signals.

In order to make the phase measurement, each received frequency must be phase-locked to a common frequency and then phase detected to provide the differential phase measurement. The entire process of phase-locking the various frequencies requires that a certain integer relation between frequencies be maintained in order that a common frequency in each phase locked loop be obtained. Actually, any combinations of frequencies between Earth ground stations and the two Voyagers are possible providing that they are within the bandwidths of the various units. However, frequencies can be selected in which the harmonics are of lower order and therefore more easily obtained with conventional circuits. The proposed design (see Figure 4-23) can accomodate any frequency accessible to the telemetering and command system.

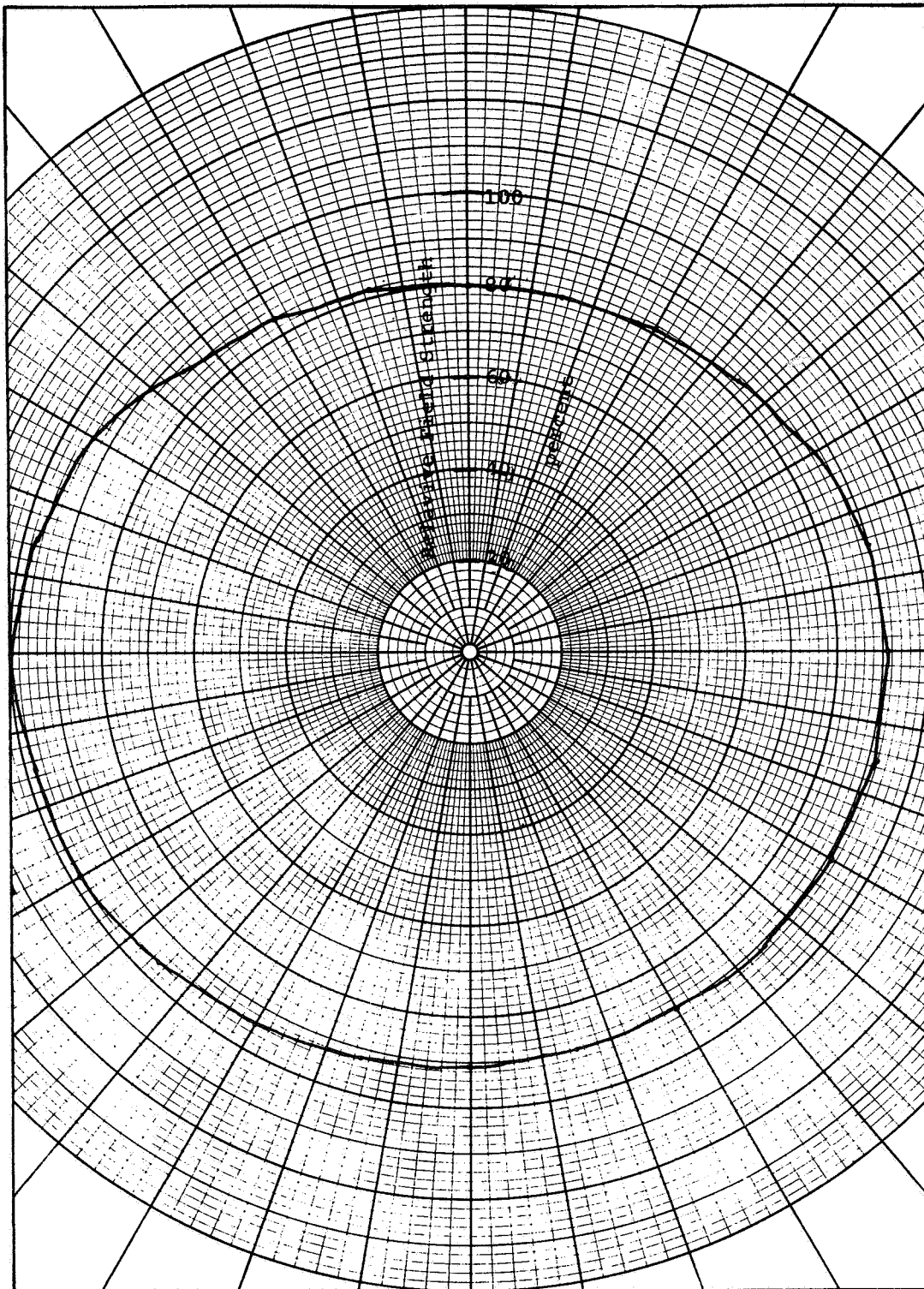


Figure 4-16 Azimuth Pattern of One-Wavelength Helical Antenna Horizontally Polarized

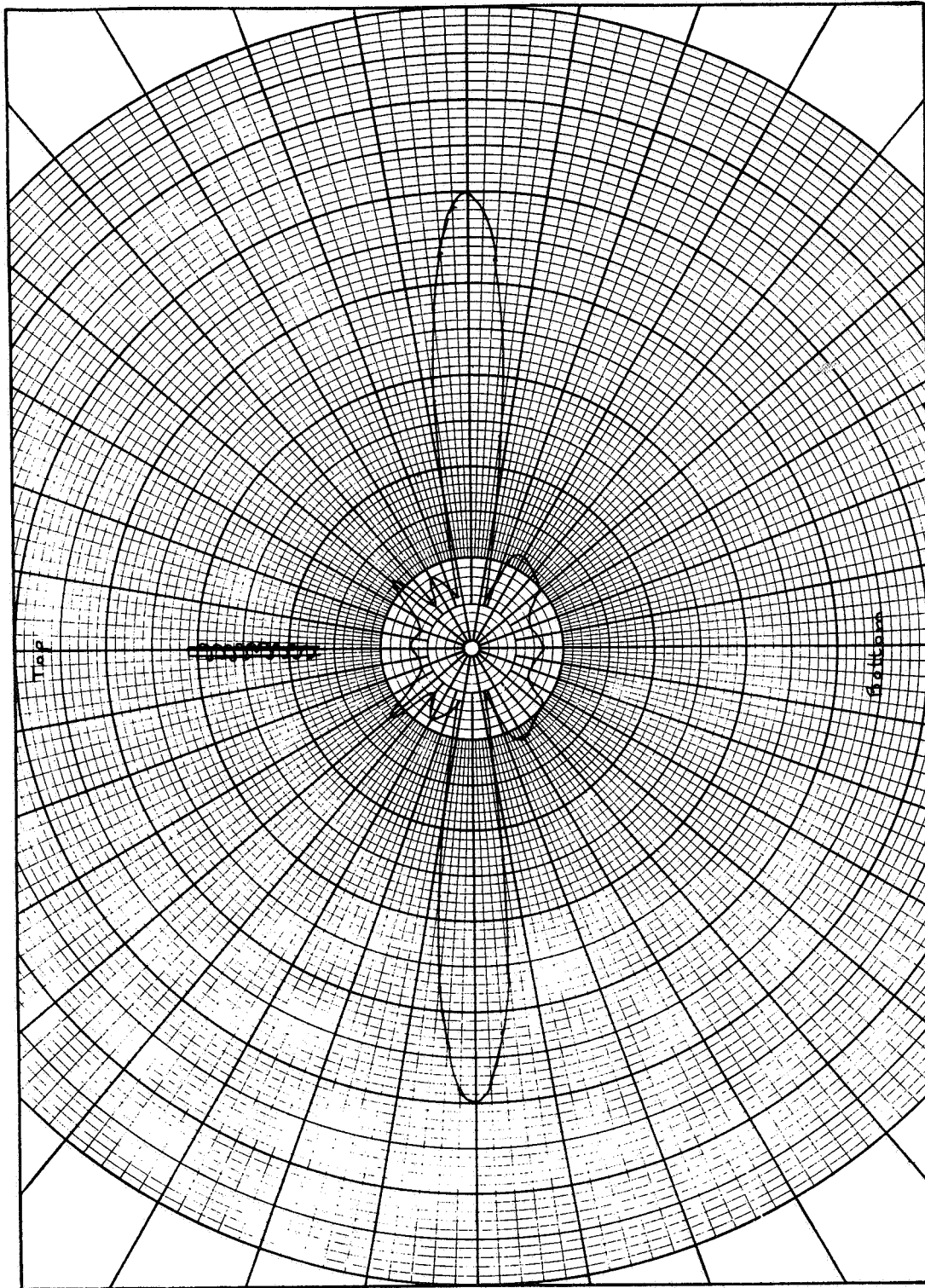


Figure 4-17 Vertical Pattern of One-Wavelength Helical Antenna Horizontally Polarized

POWER GAIN 5 (6.99 db)

SOLID CURVE --- RELATIVE FIELD INTENSITY

DOTTED CURVE --- RELATIVE POWER

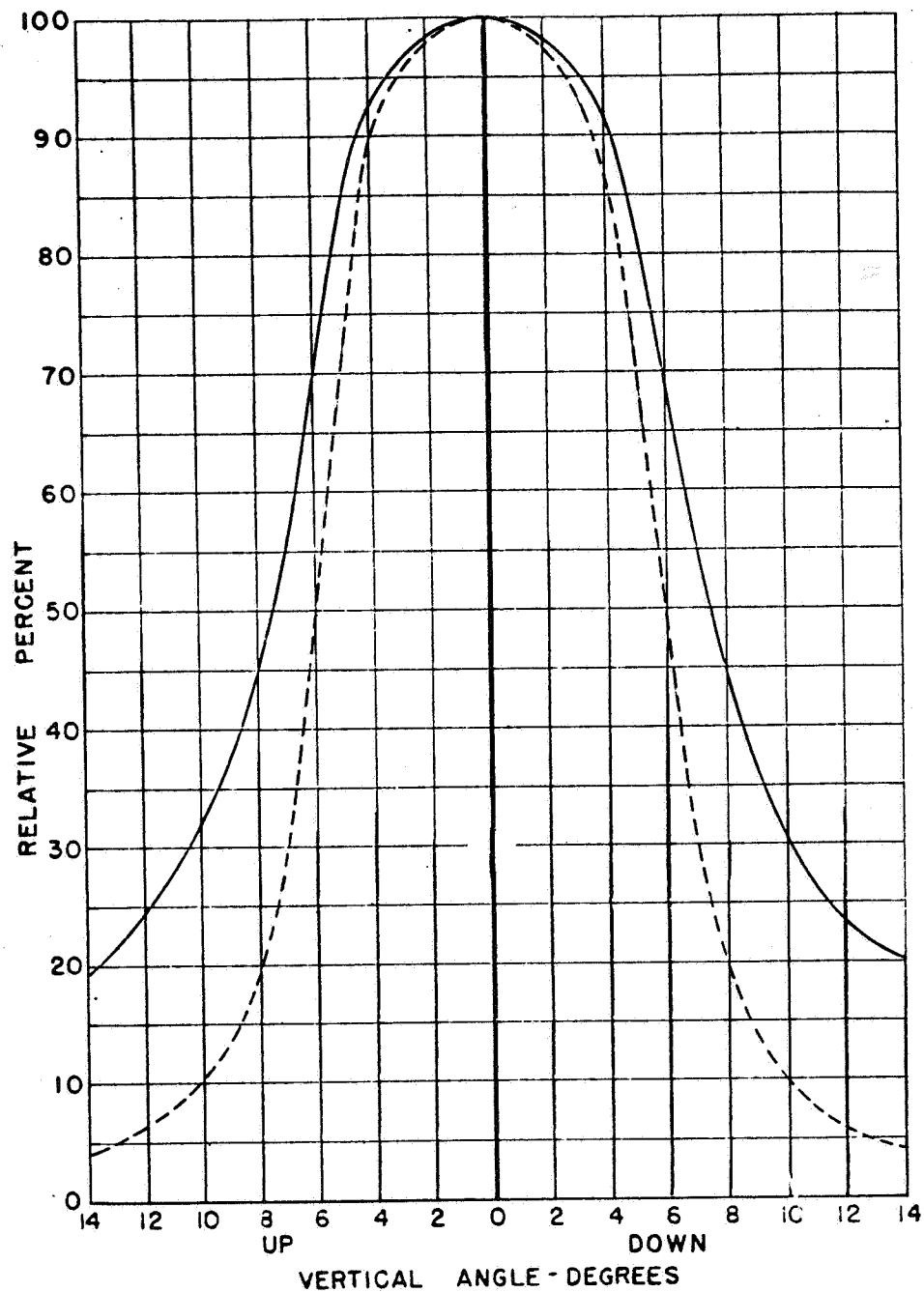


Figure 4-18 Measured Vertical for a Two- λ Helical Antenna

ANTENNA FEEDPOINT LOCATED AT 0°

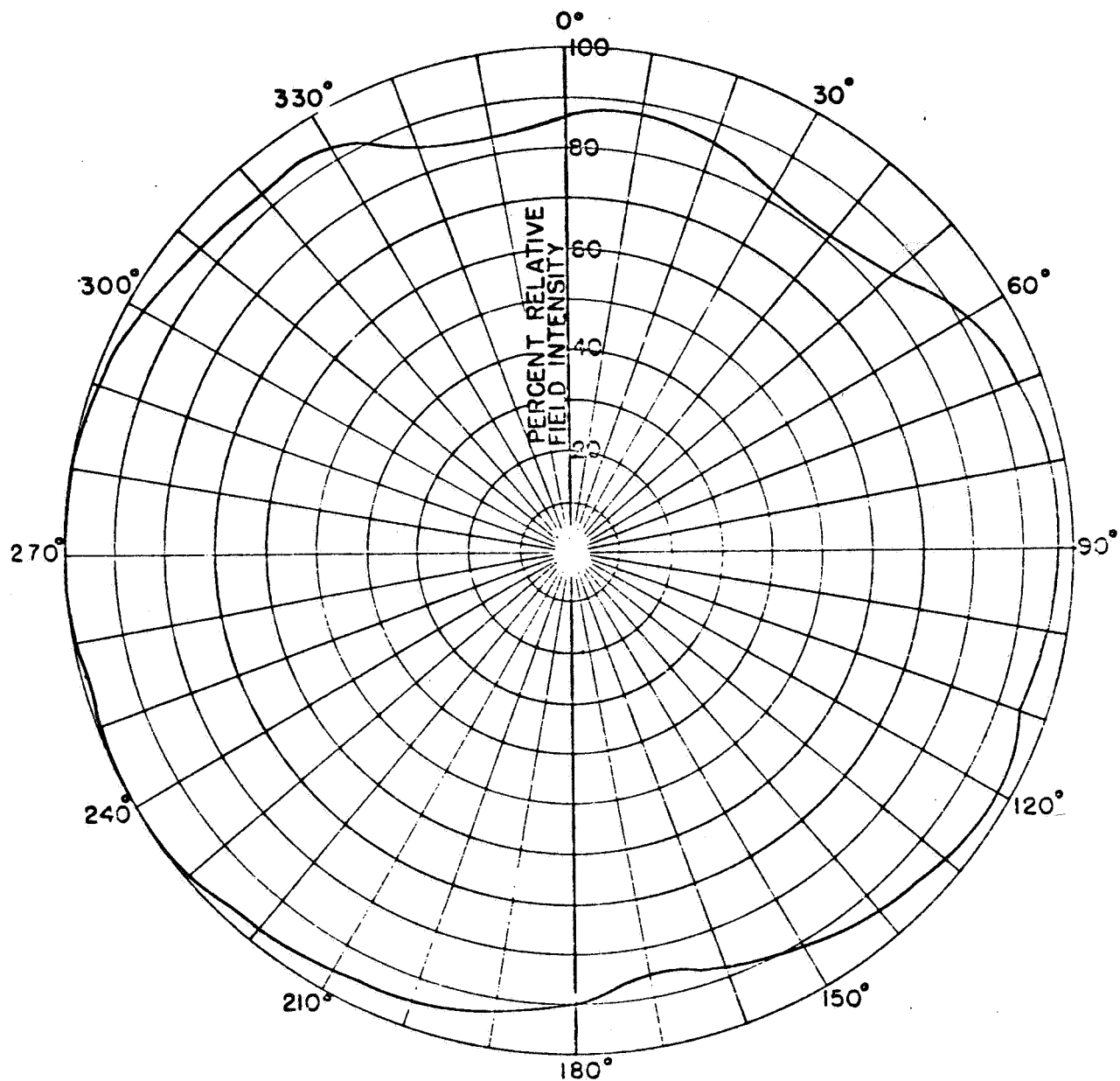


Figure 4-19 Typical Measured Horizontal Pattern for a Two- λ Helical Antenna

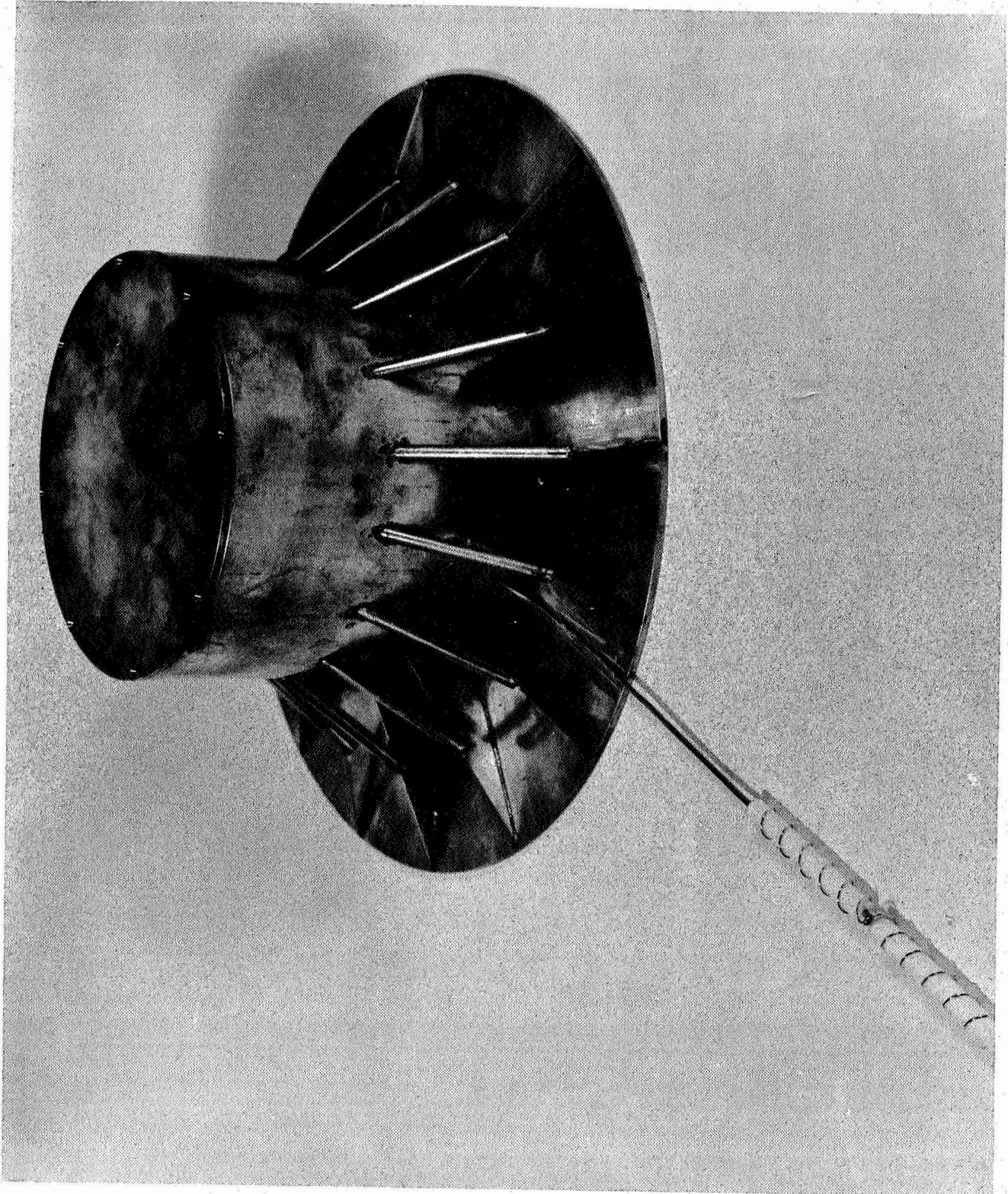


Figure 4-20 Voyager Scale Model with the Helical Antenna

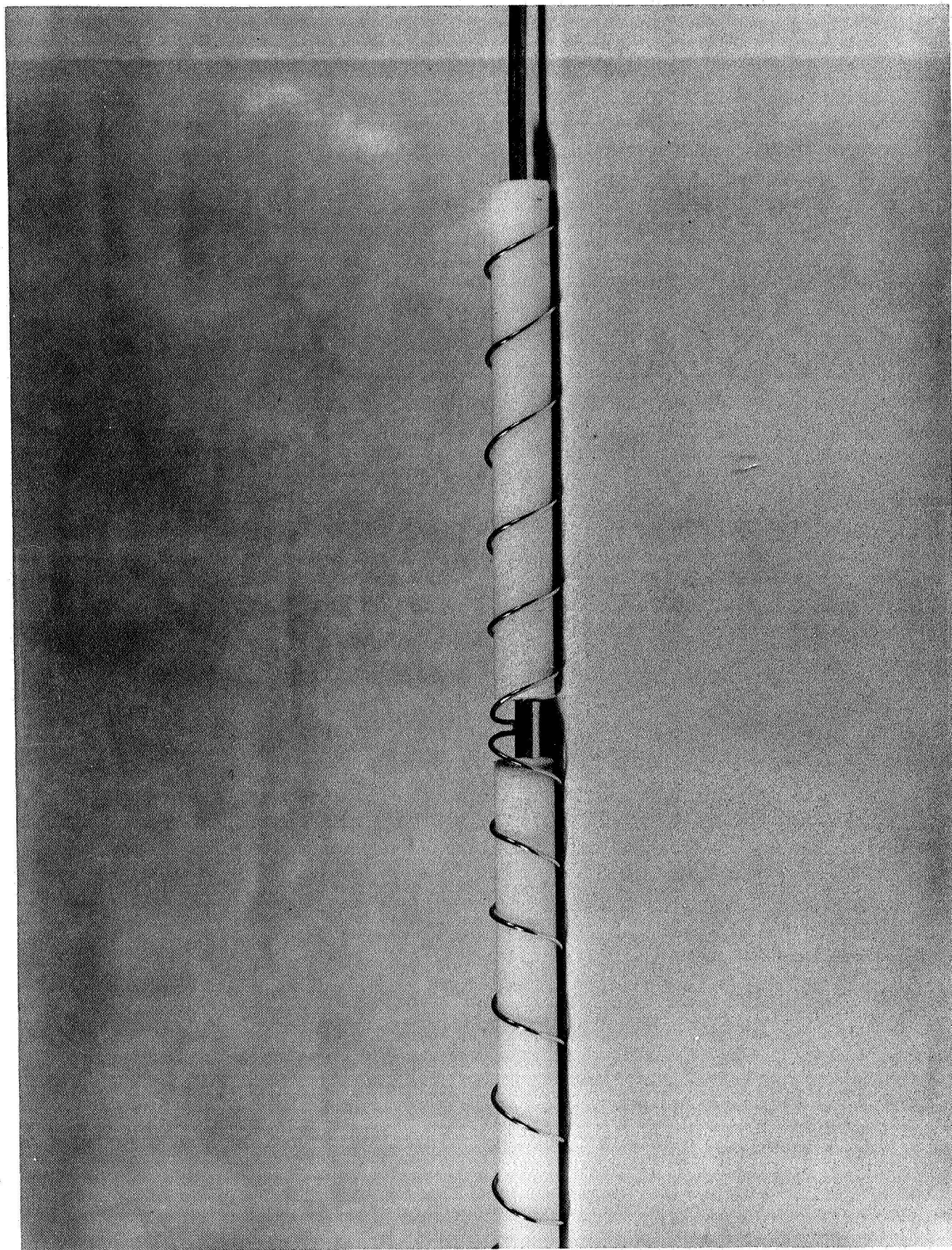


Figure 4-21 Helical Antenna (Scale Model) 5 Wavelengths
Long, 2 Wavelengths Per Turn

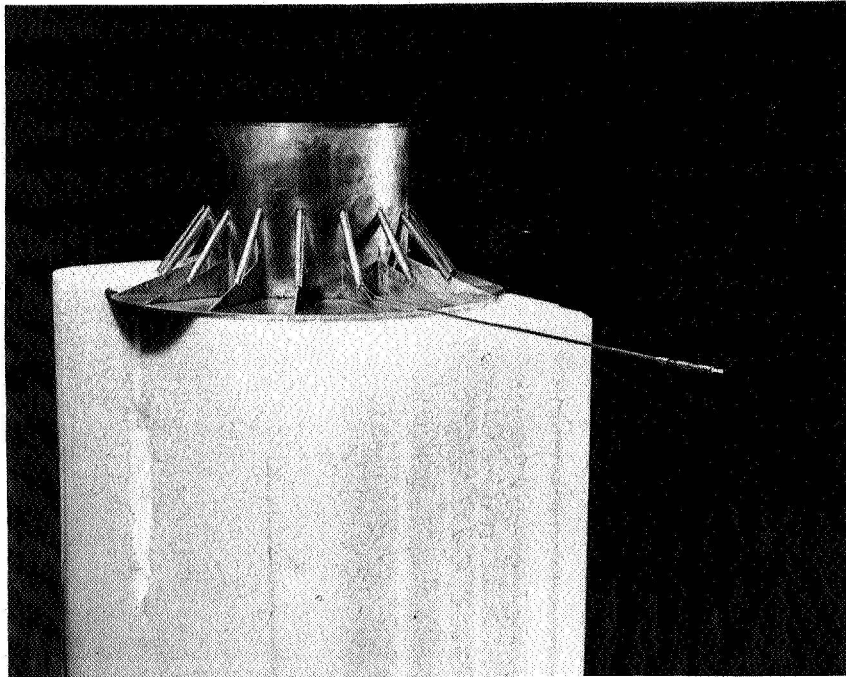


Figure 4-22 Voyager Scale Model Used for Antenna Studies in Anechoic Chamber

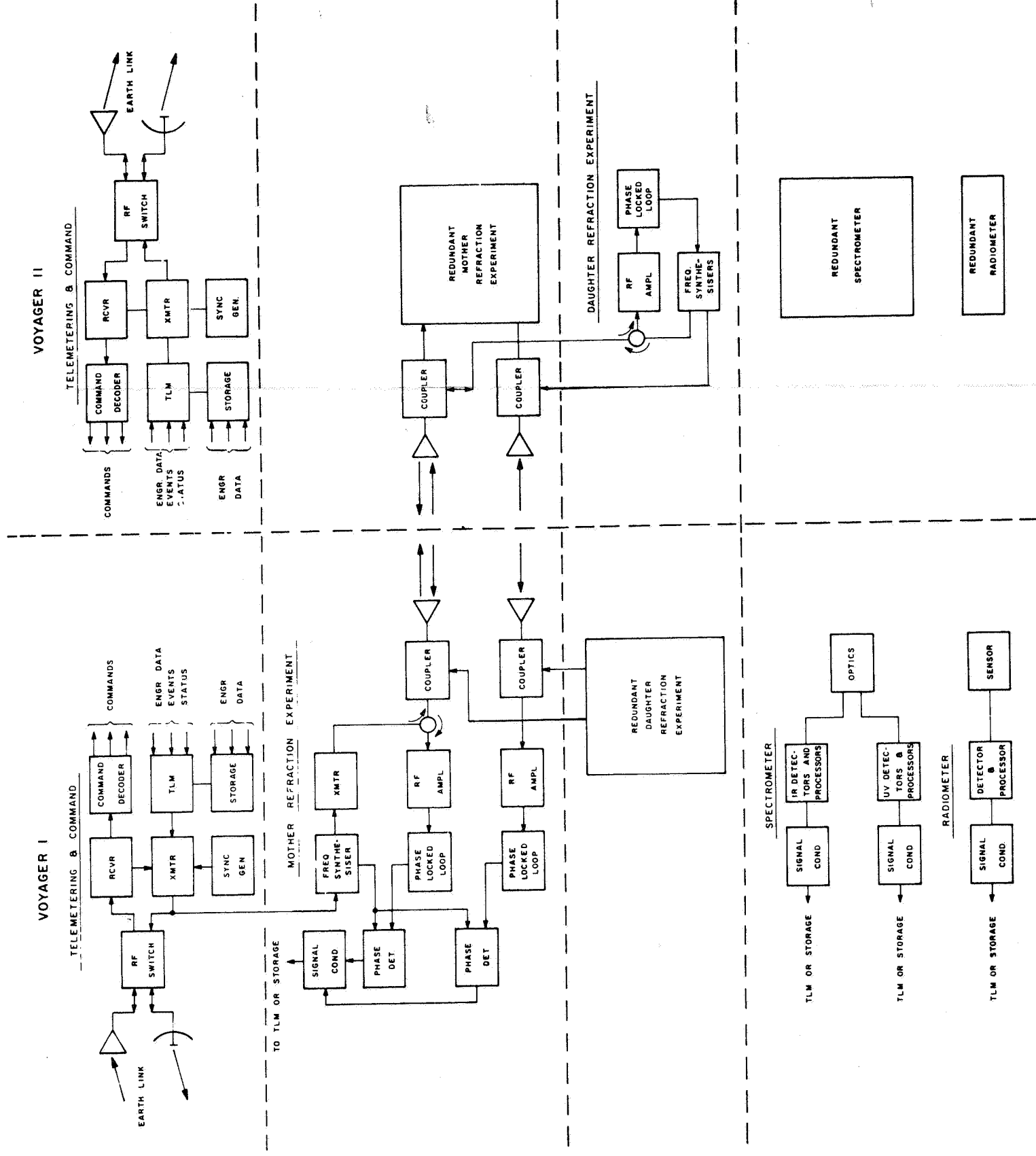


Figure 4-23 Overall Refractivity Experiment System Block Diagram

The refractivity experiment has been designed to provide the maximum flexibility, permitting measurements under most orbital situations. In order to provide this flexibility, a mother/daughter subsystem is contained in each Voyager spacecraft. The operating modes are shown in Figure 4-24. In the normal mode (Fig. 4-24a) transmission is from Voyager I to Voyager II and the mother subsystem of Voyager I is activated. When Voyager II is occulted (Fig. 4-24b), operation between Voyagers is the same, but the telemetering and command information to Voyager II must be relayed through Voyager I. When Voyager I and II are occulted from each other (Fig. 4-24d), no refractivity measurements are possible.

This design, in addition to providing the flexibility of measurement, will also permit increased reliability because in the normal mode the daughter subsystem of Voyager I and the mother subsystem of Voyager II comprise a complete redundant system for making the refractivity measurements. The system block diagram of Figure 4-23 represents the normal mode with the redundant subsystem.

4.3.6.2 System Performance

The refractivity system performance from Voyager-to-Voyager will be considered here. Link's performance between Voyager and the Earth station has been adequately covered in the literature (Ref. 21), and it is assumed that a similar system is planned for Voyager.

The proposed refractivity experiment will transmit from mother to daughter at approximately 2000 MHz and from daughter to mother at approximately 2160 and 500 MHz. Because the 2160 and 2000 MHz frequencies are so close, only the 2000 and 500 MHz paths need to be considered.

Table 4-3 lists the system performance parameters that will provide a 25 db signal-to-noise ratio in a 20 Hz noise bandwidth. This allows for degradation in the performance parameters. Some tradeoff in terms of increased antenna gain and decreased transmitter power may be possible if the orbits of the two Voyagers and the stabilization of Voyagers within their orbits can be controlled to permit the higher gain. No antenna stabilization is planned at this time.

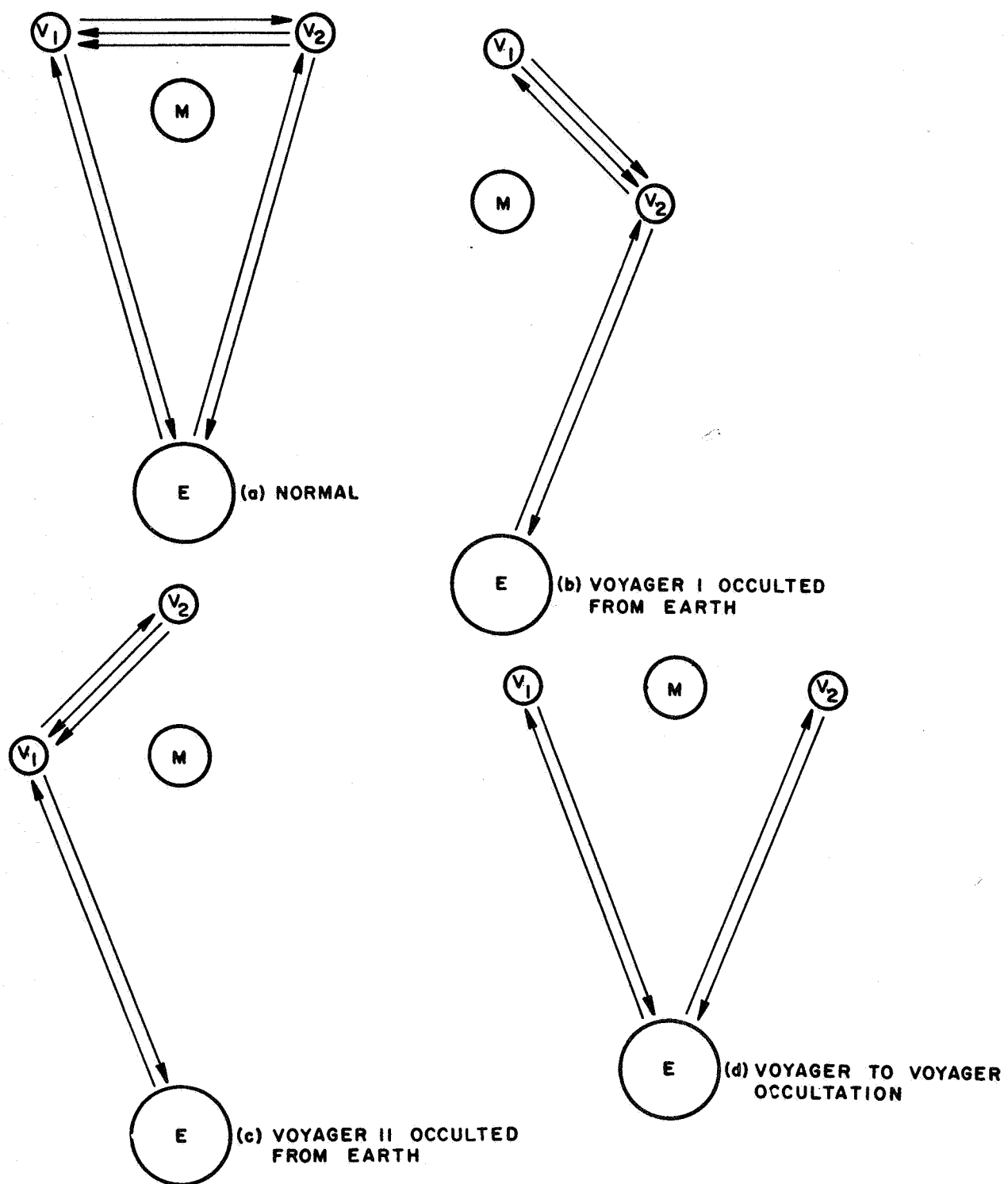


Figure 4-24 Dual Orbiter Operating Modes

TABLE 4-3
SYSTEM PERFORMANCE

Frequency	2000 or 2250 MHz	500 MHz
Xmtr Power	44 dbm	44 dbm
Ant. Gain-Total	20 db	10 db
Modulation Losses	-3 db	-3 db
System Losses	-3 db	-3 db
Path Losses (17,000 km)	-185 db	-173 db
KT _B (T = 2700°)* (B = 20 Hz)	152 dbm	152 dbm
Min S/N	25 db	27 db

*Where T is the effective system noise temperature and includes noise figure, Ant Temp, and Waveguide losses.

4.3.7 EQUIPMENT DESIGN

4.3.7.1 General

The need to preserve phase information and the low signal powers available dictate the use of phase-locked receivers. The refractivity experiment block diagram (Figure 4-23) shows that there are three phase-locked loops (PLL) in the mother orbiter and one in the daughter. Included in these are the necessary transmitter and frequency synthesis components as well as the normal low level PLL circuitry. The choice of frequencies is somewhat limited by the possibility of unwanted crosstalk. In particular, the three voltage-controlled oscillators (VCO's) in the mother must be at the same frequency in order to make valid comparisons between the transmitted and received phases. There are however, other sets of frequencies that will also fulfill all these requirements.

4.3.7.2 Block Diagram Description

Complete block diagrams of the mother and daughter equipment required for the refractivity experiment are contained in Figures 4-25 and 4-26. Since the circuitry is almost identical, however, only the daughter equipment (Figure 4-26) will be explained in detail.

An RF amplifier is used to establish a low receiver noise figure and provide enough selectivity to reject the other carriers. A tunnel diode amplifier was chosen for this requirement along with a limiter to prevent saturation. The received signal is mixed with the 108th harmonic of the VCO to provide a 20 MHz IF frequency, which is amplified in a high gain IF chain. The resultant signal is mixed with a lower harmonic of the VCO to form a second IF frequency, which is compared with the VCO in a phase detector. The DC output is filtered and fed back to control the VCO.

The VCO is then multiplied by 216 and 50 respectively, to form the frequencies to be transmitted back to the mother. Prior to transmission, both are amplified to their final power signal levels.

4.3.7.3 Parameter Evaluation

A loop S/N on the order of 25 db is desirable in order to guarantee maintenance of lock in a PLL. This loop S/N (SNR_L) determines the phase error due to noise and the loop bandwidth. Thus:

$$\theta_{no} = \left[\frac{1}{2 (SNR_L)} \right]^{1/2} = 0.04 \text{ radians}$$

which exceeds the required phase accuracy.

The loop bandwidth (B_L) can be expressed as:

$$B_L = \frac{(SNR_O) (B_O)_L}{SNR_L}$$

Where: B_O = receiver predetection bandwidth

SNR_O = predetection SNR

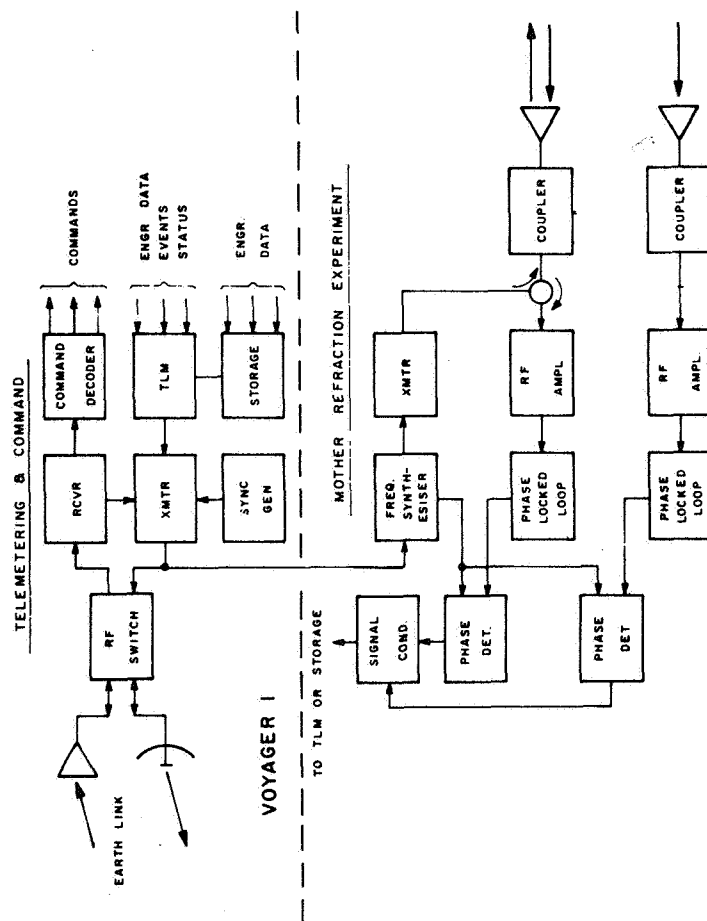


Figure 4-25 Block Diagram of Mother Equipment

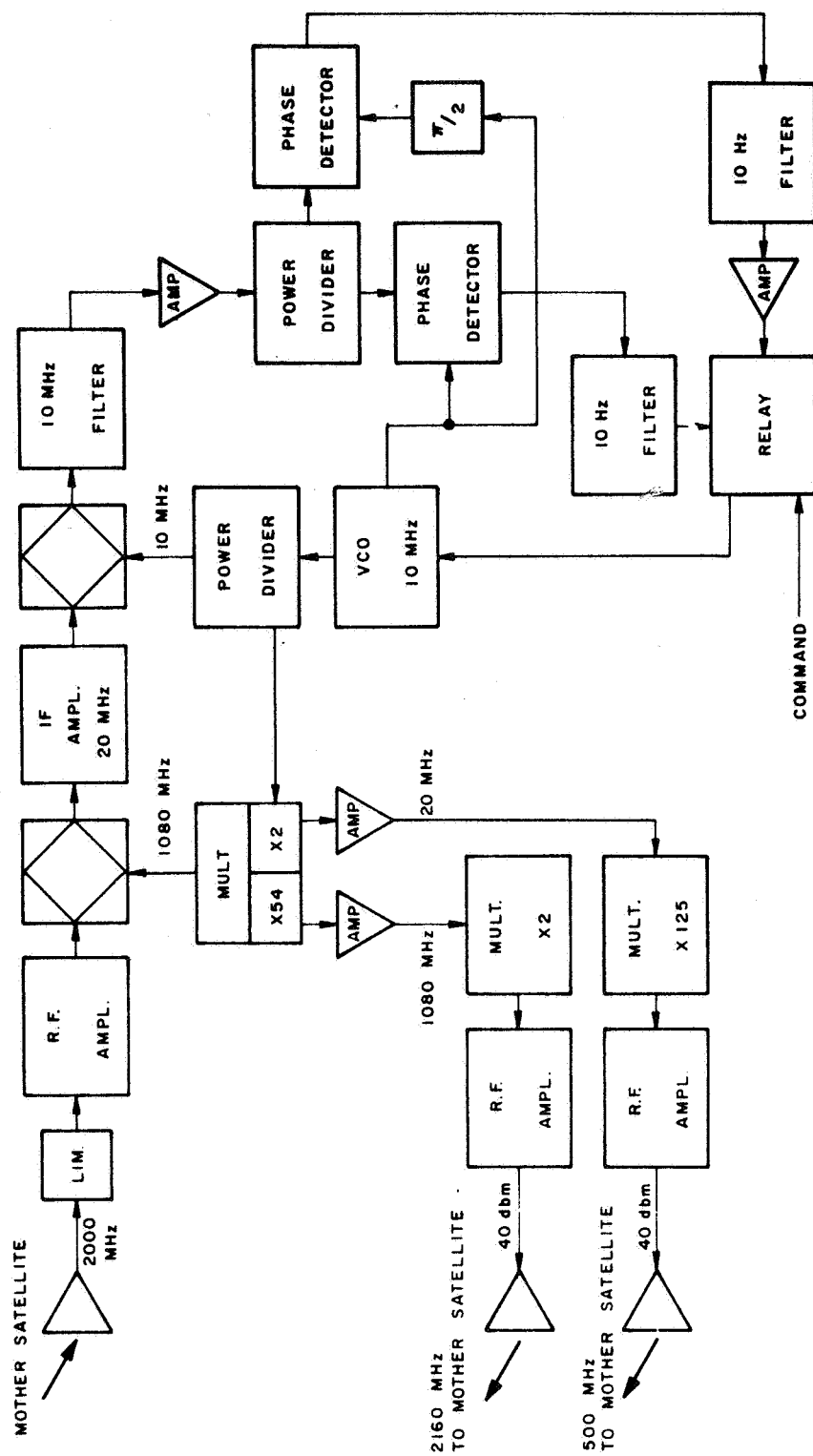


Figure 4-26 Block Diagram of Daughter Equipment

Assuming $B_o = 50$ KHz (a simple quartz crystal filter centered at the second IF frequency):

$$SNR_o = \frac{P_r}{KTB_o F}$$

Where P_r = power received $v = -127$ dbm (worst case)

$$FKT = -165 \text{ dbm/Hz}$$

$$\text{or: } SNR_o = -9 \text{ db}$$

$$\text{and: } B_L = 20 \text{ Hz}$$

The natural loop frequency (ω_n) and the loop bandwidth are related by the equation:

$$B_L = \frac{\omega_n}{2} \left(\Gamma + \frac{1}{4\Gamma} \right) \text{ Hz (Ref. 22, p. 30)}$$

For a damping factor of $\Gamma = 0.5$

$$\omega_n = 40 \text{ radians/second}$$

With a narrow bandwidth system such as this, signal acquisition time can become a problem, especially just after occultation when it is desirable to obtain data immediately. The doppler shift can be as much as 5 KHz removed from its former (pre-occultation) value. One common acquisition method would require sweeping the VCO.

In order to maintain lock, the loop cannot sweep at a rate exceeding ω_n^2 (Ref. 22, p. 36). Thus the maximum sweep rate is 1600 rad/sec/sec or 250 Hz/second; and 20 seconds would be required to acquire the signal under the conditions outlined.

In order to avoid this difficulty, the VCO will be positioned from the earth to a value adjusted for the expected doppler shift.

Other parameters of the loop are:

- 1) Max. doppler rate of change

$$\Delta f = \frac{\theta \omega_n^2}{2\pi} \quad (\text{Ref. 22, p. 30})$$

Where θ_a = phase error.

Therefore:

$$\dot{\Delta f} \approx 5 \text{ Hz/second maximum}$$

2) Loop gain

Loop gain and static phase error are related by:

$$\theta_v = \frac{\Delta\omega}{K_v}$$

Where θ_v = phase error

$\Delta\omega$ = doppler bandwidth

$K_v = A K_d N K_o$ = loop gain

A = DC voltage gain

K_d = phase detector characteristic = 3 V/radian

K_o = VCO characteristic = 1 KHz/volt

N = Local oscillator multiplication factor = 210

Therefore:

$$K_v = 47 \times 10^6$$

$$\text{and: } A = \frac{K_v}{K_d N K_o} = 12$$

Thus, little or no DC gain will be required in the loop.

4.3.8 INTERFACE REQUIREMENTS

No special interface requirements are anticipated at this time. Power requirements are indicated in Table 4-4. Engineering data can be conditioned for video storage and present recording rates and storage capacity available on Voyager are expected

to be adequate. The Voyager transmission rates are 15,000 BPS, and expected data rates for the refractivity experiment will be less than 1000 BPS: therefore, their direct transmission is possible. However, the large amount of data to be collected when integrated with other telemetry and command data for the overall experiment is best handled by the provided storage facilities, there being no requirement for real time processing. Storage requirements are expected to be less than 10 percent of the available storage capacity.

The physical interfaces, weight, size, and temperature, will be controlled using configuration management methods to assure compatibility. The expected weight and size for all of the proposed equipment are indicated in Table III. Operation within a temperature environment of a 32°F to 165°F is anticipated, and the proposed equipment will generate approximately 40 watts of thermal power.

4.3.9 TELEMETRY REQUIREMENTS

The parameters that will be monitored and telemetered for the refractivity experiment are:

- Phase Differences
- VCO Frequencies
- Phase Lock Loop Status

In addition, various signals to command the erection of antenna and the positioning of VCO frequencies will be required. It is expected that provisions will be made in the Voyager itself for numerous monitoring of temperature, pressure power supply voltages, and various status signals indicating events.

No special requirements for telemetry are anticipated because data rates for the above are considerably lower than available data rates. The engineering data can be time multiplexed using commutators, then converted into binary words and stored. Phase shift keying of the binary data to a subcarrier frequency and then the summing of this signal with necessary synch signals for telemetering to the ground station is anticipated as in the Mariner program. Telemetering of the information from Voyager to Voyager will also be possible using the existing carrier frequencies. This will

permit flexibility during occultations between earth and Voyager or Voyager-to-Voyager. It will also introduce redundancy for increased reliability.

4.3.10 COMMAND FUNCTIONS

The command functions required for the refractivity experiment will add the following requirements to the existing Voyager command subsystems:

- Refractivity Experiment Antenna Erection
- Phase Lock Frequency Adjustment
- Start/Stop Command Experiment
- Redundant Change in Components
- Subassemblies
- Mother/Daughter Interchange

As an aid to performing the erection of the antennas, the status of the erection will be monitored and telemetered. The phase lock frequency adjustment can be made entirely by adjusting the DSN transmitted frequency until the phase locked loops from both Voyagers are locked up. This procedure will be used for initial lock up of the loops and, as an aid to performing this operation, the variable controlled oscillator (VCO) and lock indication of each phase lock loop (PLL) will be monitored and telemetered back to the DSN ground station.

The loss of lock due to occultation is a problem that deserves special attention if acquisition after occultation is to be effected in a short period of time (less than a second). The narrow bandwidths of the phase locked loops preclude their self acquisition in such short times and necessitate use of programmed auxiliary oscillators or a programmed signal drive to the VCO to effect the PLL lock-up in short time (about 1/10 of a second).

The proposed method calls for determining at the DSN ground station from ephemeris data the time of expected occultation and the time and expected doppler frequency when coming out of occultation. A command signal setting the VCO, or an auxiliary oscillator to the expected frequency when coming out of occultation, would permit operation of the phase lock loops within the one second requirement. The times of occultation and associated doppler frequencies could be determined after an ephemeris of the orbits of Voyager has been obtained. A determination of the doppler frequency to within 500 Hz would be adequate to provide a phase lock within one second.

As in the telemetering subsystem, the command signals may be encoded, modulated with a subcarrier, and transmitted from Voyager to Voyager as well as from Voyager to Earth. This will permit a flexibility that will allow for various combinations of occultations and also increased reliability because of the redundancy.

4.3.11 SUMMARY OF WEIGHT, SIZE, PRIMARY POWER REQUIREMENTS FOR REFRACTIVITY EXPERIMENT

The summary of the main physical parameters of the equipment involved in the refractivity experiment is provided in Table 4-4.

TABLE 4-4
WEIGHT, VOLUME, AND PRIMARY POWER

	Power (W)	Weight (kg)	Volume (m ³)
Mother	62	8	0.013
Daughter	50	5.4	0.0067
Antenna	-	2.2	0.0038
Telemetering & Command	5	2.2	0.0067

4.4 TRANSMISSION ABSORPTION SPECTROSCOPY EXPERIMENT

4.4.1 MODEL ATMOSPHERE OF MARS

For purposes of providing guidelines and establishing possible design limitations for the various absorption experiments under study (e.g., microwave, IR, UV) for Mars, a model atmosphere is necessary. In the following paragraphs, a short survey of the constituent abundances is given, and a specific model atmosphere is selected that is believed to represent a most recent consensus among investigators. One of the more comprehensive surveys of the atmosphere of Mars is presented by Brooks (Ref.23), which is believed to supersede earlier surveys such as those reported by Rea (Ref.24), and Van Tassel and Salisbury (Ref.25). Another prominent work appears to be that due to Evans et al. (Ref.26), who have presented data giving profiles for temperature, pressure, and density in the atmosphere of Mars for several assumed models of constituent abundances.

4.4.1.1 A Survey of the Constituents on the Martian Atmosphere

4.4.1.1.1 Carbon Dioxide

Both the Mariner IV occultation observations in July 1965 and Earth-based spectroscopic measurements suggest that CO₂ is the major constituent of the Martian atmosphere (Ref.42, 28, 29). Spectroscopically, CO₂ abundances were determined by an investigation of the radiative absorption in weak unsaturated CO₂ lines. From data obtained during the March 1965 opposition of Mars, abundance values of 65 ± 20 m-atm (Ref.36), 68 ± 26 m-atm (Ref.28), and 90 ± 27 m-atm (Ref.29) were obtained. The Mariner IV observations suggest that the Martian atmosphere consists mainly of CO₂ with abundances closer to the smaller values suggested by the previous investigations (Ref.30). Under the assumption of an atmosphere of pure CO₂, a number density of $1.9 \pm .1 \times 10^{17}$ mol/cm³ (at a pressure of $4.9 \pm .8$ mb) has been deduced, based on the immersion of Mariner IV into occultation (Ref.35, 42).

4.4.1.1.2 Carbon Monoxide

Carbon monoxide is suggested as a possible constituent of the upper atmosphere of Mars. Carbon dioxide, for example, may undergo photodissociation at altitudes 70 to 80 km by solar

ultraviolet radiation giving $\text{CO}_2 \rightarrow \text{CO} + \text{O}$ (Ref. 31). These latter constituents may again recombine to form CO_2 (Ref. 32). Carbon monoxide may also be produced by CO_2 joining with atomic oxygen, giving $\text{CO}_2 + \text{O}^+ \rightarrow \text{CO} + \text{O}_2^+$. The abundance of CO produced from CO_2 by the aforementioned processes is about .2 cm-atm (Ref. 33). In Figure 4-27 are profile models indicating CO_2 , O, and CO as a function of the Martian altitude, where the process $\text{O}^+ + \text{CO}_2 \rightarrow \text{CO} + \text{O}_2^+$ is assumed to be the main loss process in the ionosphere (Ref. 42).

4.4.1.1.3 Nitrogen

Nitrogen was formerly believed to be the main constituent of the Martian atmosphere based on the assumption that the surface pressure was considerably higher than that suggested by the Mariner IV occultation experiment (Ref. 42, 24). The results derived from the Mariner occultation, however, indicate that nitrogen represents a minor constituent in the Martian atmosphere. Cosmic abundance considerations suggest that the partial pressure of N_2 at the Martian surface should be about 1 mb (Ref. 34), which suggests an atmospheric model having up to 20% of N_2 by volume (Ref. 42).

4.4.1.1.4 Nitric Oxides

Although there are many possible oxides that may be produced in the Martian atmosphere (Ref. 35), their predicted abundances are extremely low (smaller than $5 \times 10^{-6}\%$ by volume). Since no NO_2 absorption has been observed in the spectra of the Martian atmosphere, upper limits on its abundance confirm the predicted extremely low values (Ref. 36).

4.4.1.1.5 Neon

Gross et al. (Ref. 34), using the concept of cosmic abundances indicates that neon should exist in the Martian atmosphere and have a partial pressure of at least 2 mb.

4.4.1.1.6 Argon

Argon has been surmised in the Martian atmosphere to account for the atmospheric density where the spectroscopically determined amount of CO_2 is insufficient to supply the total surface pressure (Ref. 24, 37). A model atmosphere has been developed that assumes that argon may exist up to 20% by volume, while other models exist that assume 50% of argon (Ref. 42), corresponding to 60 m-atm of CO_2 and a surface pressure of 10 mb, while 84% concentration may exist with a surface pressure as high as 19.6 mb (Ref. 38, 39).

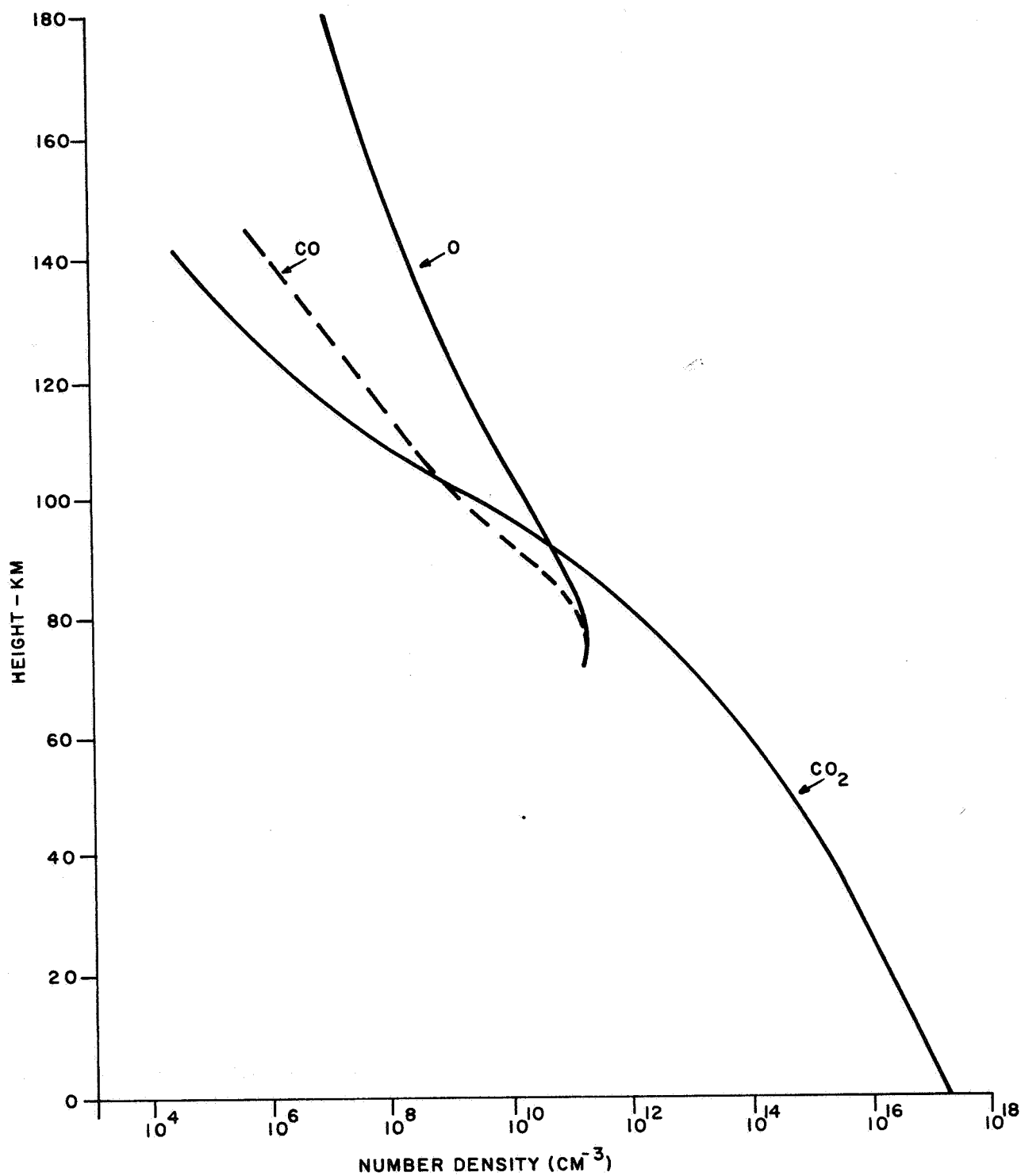


Figure 4-27 Constituent Abundances of CO₂, CO, and O in Martian Atmosphere

4.4.1.1.7 Oxygen

Both atomic and molecular oxygen are likely to exist at high altitudes in the Martian atmosphere. Assuming a pure CO_2 atmosphere, the relative abundance of atomic oxygen with CO_2 and CO is illustrated in Figure 4-27 (Ref. 42). An upper limit of the atomic oxygen abundance has been placed at 250 cm-atm by Marmo et al (Ref. 32). An upper limit of the O_2 concentration was set at 2 cm-atmosphere by Rea (Ref. 24).

4.4.1.1.8 Ozone

Marmo et al. (Ref. 32) indicate that no evidence exists for a theoretical ozone concentration peak at some altitude above the Martian surface, but that only a monotonic decrease of O_3 concentration with increasing height probably exists. An upper limit of 4×10^{-4} cm-atm has been placed on O_3 concentration by Rea (Ref. 24) based on a 2 cm-atm concentration of O_2 .

4.4.1.1.9 Water Vapor

Spectroscopic observations indicate that Mars has a trace of water, most of which is probably on or under the surface. The atmosphere may contain a small fraction, amounting to 10 to 20 microns of precipitable water (Ref. 40). Spinrad (Ref. 29) for example, suggests 15 microns, while Öpik (Ref. 30) suggests 14 microns of precipitable H_2O .

Although water vapor on Mars has been determined spectroscopically from Earth, these observations are confined only to certain regions with favorable local meteorological conditions. For example, Spinrad (Ref. 29) has observed spectroscopically water vapor migration away from a dwindling polar cap.

4.4.1.1.10 Summary of the Gaseous Composition

In Table 4-5 is a summary indicating abundances of the aforementioned constituents.

TABLE 4-5
SUMMARY OF THE CONSTITUENT ABUNDANCES
IN THE MARTIAN ATMOSPHERE

Constituent	Concentration	Investigators
CO ₂	65 ± 20 m-atm	Owen, 1966b; Öpik, 1966; Fjeldbo et al, 1966a (Ref. 36, 30, 42)
	68 ± 26 m-atm	Belton and Hunten, 1966a (Ref. 28)
	90 ± 27 m-atm	Spinrad et al, 1966a (Ref. 29)
	44 to 97% by volume	Evans et al, 1967 (Ref. 26)
CO	.2 cm-atm	Shimizu, 1966 (Ref. 33)
N ₂	up to 20%	Fjeldbo et al, 1966a (Ref. 42)
	3 to 52%	Evans et al, 1967 (Ref. 26)
NO ₂	smaller than 5 x 10 ⁻⁶ %	
Ne	2 mb	Gross et al, 1966 (Ref. 34)
Argon	20%	Fjeldbo et al, 1966a (Ref. 42)
	50%	Gray, 1966a (Ref. 38)
	84%	Gray, 1966b (Ref. 39)
	.6 to 25%	Evans et al, 1967 (Ref. 26)

TABLE 4-5 (Continued)
SUMMARY OF THE CONSTITUENT ABUNDANCES
IN THE MARTIAN ATMOSPHERE

Constituent	Concentration	Investigators
O ₂	smaller than 2 cm-atm	Rea, 1965 (Ref. 24)
	smaller than 70 cm-atm	Evans et al, 1967 (Ref. 26)
O	smaller than 250 cm-atm	Marmo et al, 1965 (Ref. 32)
O ₃	4 x 10 ⁻⁴ cm-atm	Rea, 1965 (Ref. 24)
H ₂ O	15 x 10 ⁻⁴ prec-cm	Spinrad, 1966a (Ref. 29)
	14 x 10 ⁻⁴ prec-cm	Öpik, 1966 (Ref. 30)
	10-20 x 10 ⁻⁴ prec-cm	Otterman et al, 1966 (Ref. 40)
	14 ± 7 x 10 ⁻⁴ prec-cm	Evans et al, 1967 (Ref. 26)

According to Brooks (Ref. 23), the gases and vapors can be grouped in three classes according to estimates of their abundance:

- (1) CO₂, Ar, Ne, N₂ comprise 100 m-atm or 99.95% by volume.
- (2) O, O₂, H₂O, CO comprise 5 cm-atm or .05% by volume.
- (3) O₃, NO, NO₂, N₂O₄ and others comprise 5 x 10⁻⁴ cm-atm or 5 x 10⁻⁶% by volume.

4.4.1.2 Selected Model of the Atmosphere of Mars

Since CO₂ is generally believed to represent a dominant constituent in the atmosphere of Mars, the model atmosphere that will be selected here is that given by Evans et al (Ref. 26) in which CO₂ comprises 97% of the volume and N₂ approximately 3%, with

existing traces of the other constituents as suggested in the previous section. In Figures 4-28 and 4-29 are given altitude profiles of CO₂ density, pressure, and temperature for the Martian atmosphere corresponding to the above suggested atmospheric constituent abundances. In examining the absorption due to other constituents in the atmosphere of Mars (especially near the surface) we shall assume uniform mixing in the computation of their density distributions. Thus, their density profile may be obtained by the proportionality,

$$N_X = \frac{N(\text{CO}_2) \times X(\%)}{97} \quad (4.4-1)$$

where X(%) corresponds to the volume percentage of the minor constituent, N(CO₂) corresponds to the density of CO₂, and N_X is the density of the minor constituent.

4.4.2 MICROWAVE SPECTROSCOPY CONSIDERATIONS

The possibility of performing a microwave spectroscopy experiment in the atmosphere of Mars is analyzed here for the configuration in which a high-gain transmitting antenna is located on the "mother satellite" as suggested by the configuration in Figure 4-30. Because of the limitation in output power in the present "state-of-art" microwave oscillator tubes at frequencies above 200 GHz, we have concentrated our analysis at frequencies below this value. Unfortunately, none of the expected predominantly existing constituents on Mars, such as CO₂, N₂, N, and A, absorb in this frequency range. Molecules that do absorb in this range, of which there are expected possible traces, are H₂O, O₂, CO, O₃ and NO₂. It has been suggested in Section 4.4.1 that these constituents combined comprise at most 5 cm-atm (STP) or 0.05% of the total density. The maximum density on the surface of Mars for the presently assumed model atmosphere described in Section 4.4.1 is 1.6 x 10¹⁷ cm⁻³. An upper limit of the molecular densities in the above latter group of constituents is then 5% of this value, which is

$$N_{\text{max}} = 8 \times 10^{13} \text{ (cm}^{-3}\text{)} \quad (4.4-2)$$

It may be noted that if the upper limit density is to correspond to a concentration of 5 cm-atm (Ref. 23), then N_{max} as given by 4.4-2 may be assumed uniformly distributed over an effective path length,

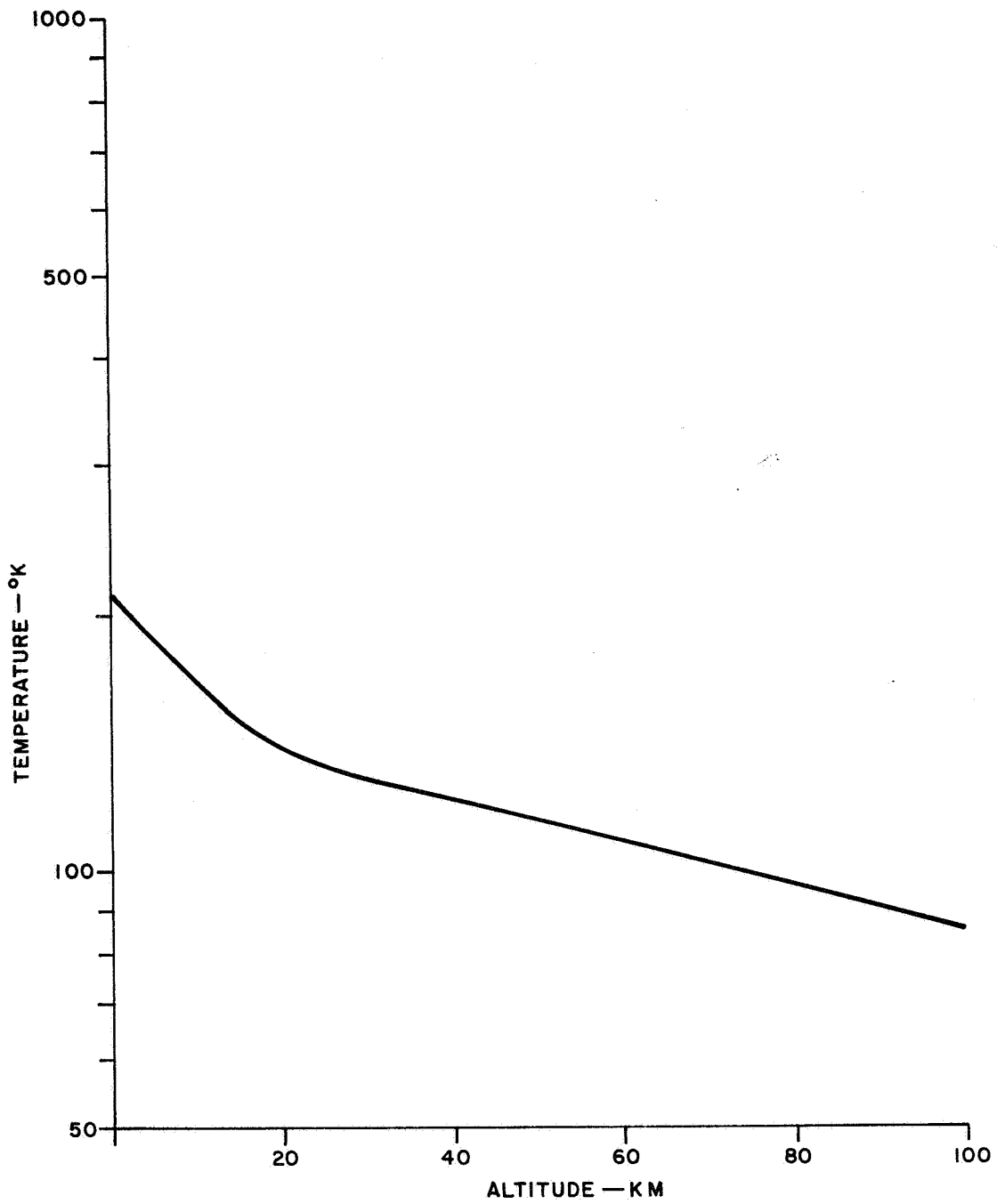


Figure 4-28 Temperature Profile of Martian Atmosphere

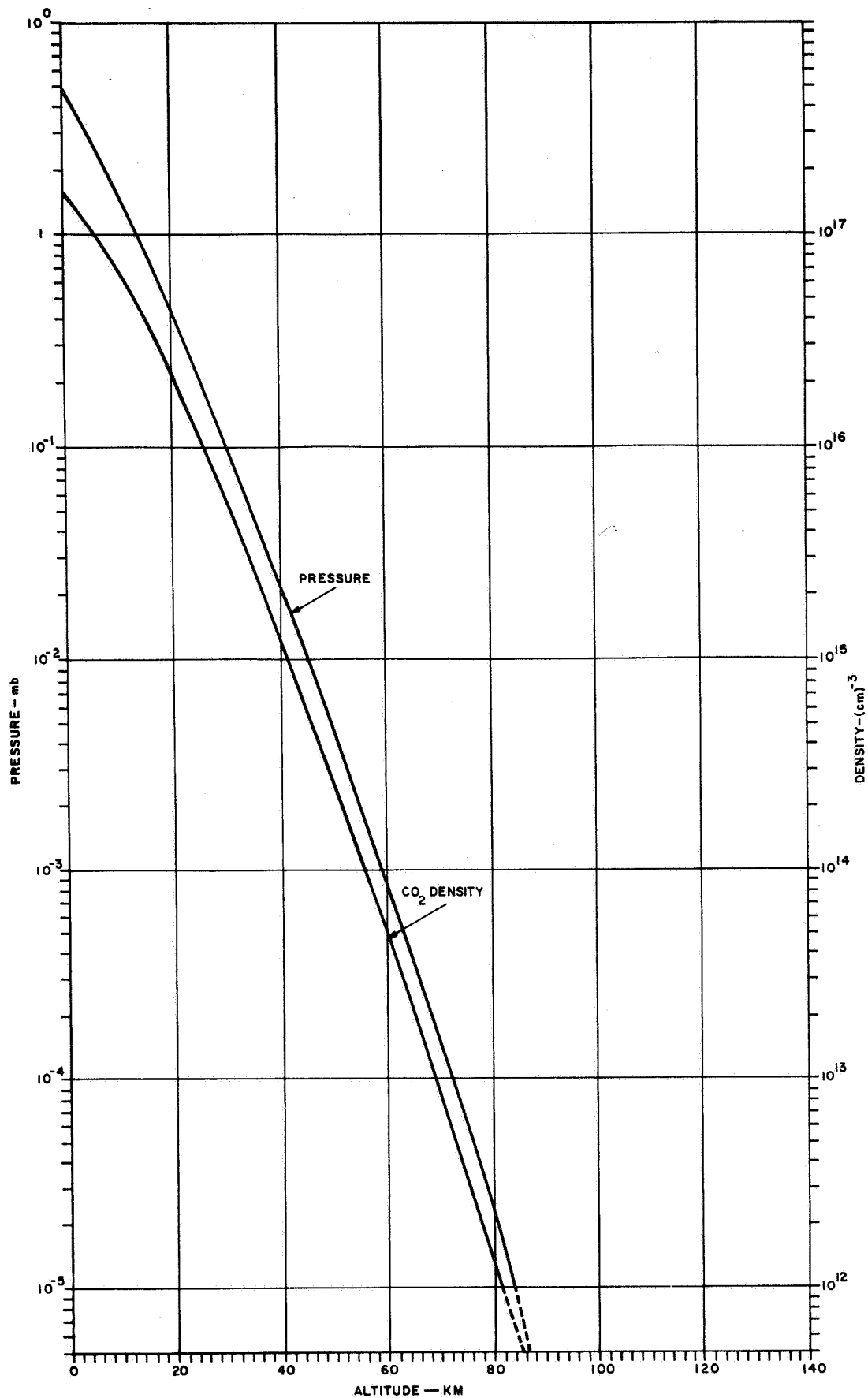


Figure 4-29 Profiles of Pressure and CO₂ Density Variation in Martian Atmosphere
4-65

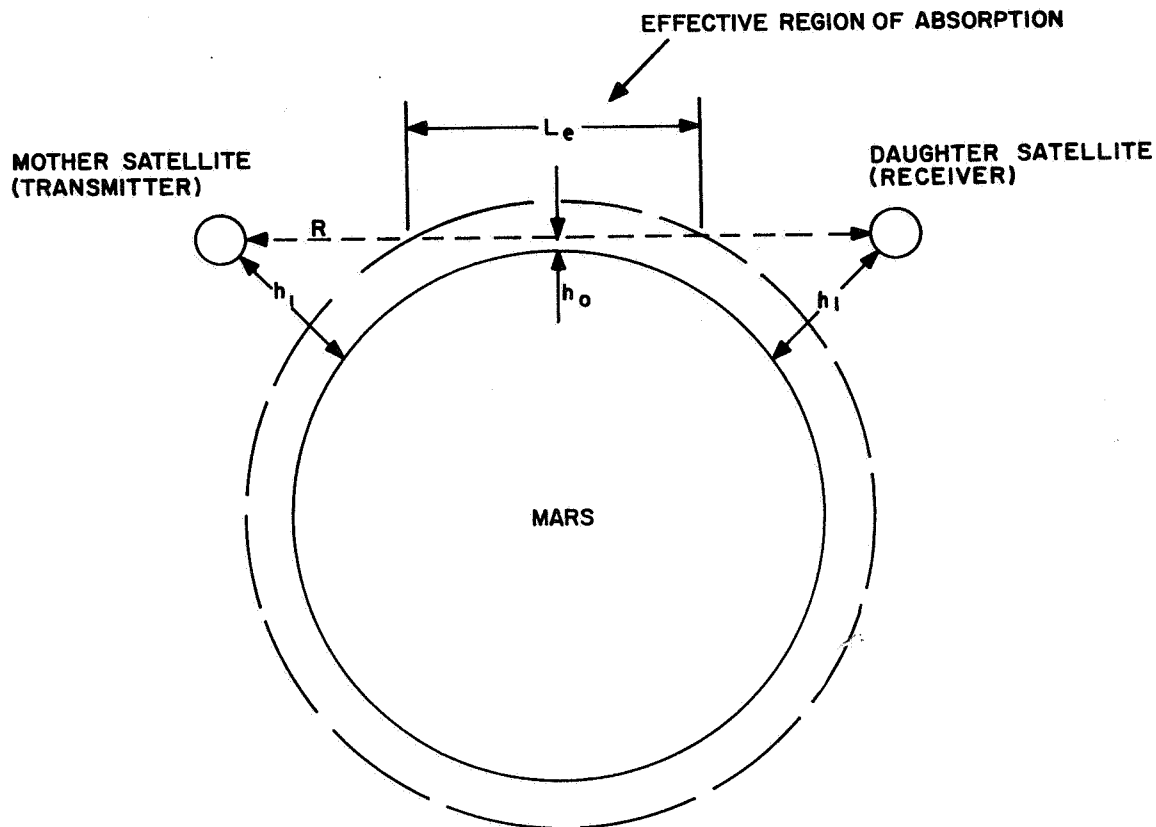


Figure 4-30 Microwave Spectroscopy Experiment Configuration

$$L_{\text{eff}} = \frac{[\text{Cm-atm (STP)}] \times N_0}{N_{\text{max}}} \approx 17 \text{ km} \quad (4.4-3)$$

where N_0 is the Loschmidt's number = $2.69 \times 10^{19} \text{ (cm}^{-3}\text{)}$.

It is apparent that the expected upper limit of the above mentioned constituents (equation 4.4-2) may be too small to obtain detectable absorption on Mars. We shall therefore determine independently the values of the constituent densities that do give rise to measurable absorptions and compare these values with the expected upper limit value (equation 4.4-2). It has been demonstrated by Lombardini et al. (Ref. 45) that the measurable absorption of electromagnetic energy over a propagation path, L , that a receiver may detect (under idealized conditions) is given by the relation,

$$\left[\int_{L \text{ (km)}} \alpha \text{ (db/km)} d\ell \right] \geq \frac{34.4}{(P_{\text{SO}}/P_{\text{NO}})^{1/2}} \text{ (db)} \quad (4.4-4)$$

where it is assumed that a frequency modulated carrier is transmitted, P_{SO} is the unabsorbed carrier power received, and P_{NO} is the noise power at the receiver input given by

$$P_{NO} = [F k T \Delta f] \quad (4.4-5)$$

where

F is the noise figure of the receiver
 k is the Boltzmann constant
 T is the ambient temperature
 Δf is the bandwidth.

The expression equation 4.4-4 reduces approximately to that derived by Gordy (Ref. 44), who considered propagation through a uniform gas contained in a cell. The unabsorbed carrier power is given by

$$P_{SO} = \frac{\lambda^2 P_T G_T G_R}{(4 \pi R)^2} \quad (4.4-6)$$

where

P_T = transmitted power at the mother satellite
 G_T, G_R = gains of transmitting and receiving antennas, respectively
 R = distance between satellites
 λ = free-space wavelength.

To obtain an indication of the measurable absorption (4.4-4) we shall assume a typical distance, R , between satellites and idealized parameters as follows:

$$R = 10^4 \text{ km (equivalent to 1 1/2 times the diameter of Mars)} \quad (4.4-7)$$

$$P_T = 10 \text{ watts} \quad (4.4-8)$$

$$G_T = G_R = 10^3 \quad (4.4-9)$$

$$F = 10 \quad (4.4-10)$$

$$T = 300^\circ\text{K} \quad (4.4-11)$$

$$\Delta f = 10 \text{ Hz} \quad (4.4-12)$$

Substituting the above parameters into equations 4.4-5 and 4.4-6 we obtain

$$P_{NO} = 4 \times 10^{-19} \text{ watts} \quad (4.4-13)$$

$$P_{SO} \approx 6 \times 10^{-10} \lambda^2 \text{ watts (where } \lambda^2 \text{ is in m}^2) \quad (4.4-14)$$

Substituting equations 4.4-13 and 4.4-14 into equation 4.4-4 results in the detectable absorption satisfying the relation,

$$\left[\int_{L(\text{km})} \alpha \text{ (db/km)} d\ell \right] \geq \frac{10^{-3}}{\lambda} \text{ db} \quad (4.4-15)$$

where λ is expressed in meters.

As a first approximation at microwave frequencies, equation 4.4-15 may alternately be expressed as

$$\int_L \alpha_o \frac{N}{N_o} d\ell \geq \frac{10^{-3}}{\lambda} \text{ db} \quad (4.4-16)$$

where N is the molecular density of the particular constituent in the Martian atmosphere, N_o is Loschmidt's number [$2.69 \times 10^{19} \text{ cm}^{-3}$], and α_o is the absorption coefficient at STP. The effective reduced path length at STP is given by

$$\int_L \frac{N}{N_o} d\ell \geq \frac{10^2}{\lambda(\text{m}) \alpha_o \text{ (db/km)}} \text{ (cm-atm)} \quad (4.4-17)$$

When the equality sign holds the right-hand side of equation 4.4-17 represents the "minimum" detectable reduced path length (STP) pertaining to the constituent density, N . This value may be compared with the maximum expected value of 5 cm-atm alternately if N is assumed distributed uniformly over an effective path length, L_{eff} , and equation 4.4-16 becomes

$$N_{\text{min}} = \frac{2.69 \times 10^{16}}{\alpha_o \text{ (db/km)} L_{\text{eff}} \text{ (km)} \lambda \text{ (m)}} \text{ (cm}^{-3}) \quad (4.4-18)$$

where the left-hand side represents the minimum detectable density.

Assuming the identical effective path length as equation 4.4-3 (reduced path length over which the homogeneous constituent density gives rise to the same absorption as the inhomogeneous density over the actual path length) and using values of α_0 (at STP) as provided by Ghosh and Edwards (Ref. 43), the corresponding values of equations 4.4-17 and 4.4-18 are tabulated in Table 4-6 and compared with their maximum expected values.

Comparing the minimum detectable values of the constituent densities (or the corresponding reduced path lengths) with their maximum expected values in Table 4-6 , we observe the former to exceed the latter. It may be concluded from our analysis that a microwave spectroscopy on Mars is not presently possible with the present power limitations on oscillator tubes, and emphasis should therefore be placed on IR and UV spectroscopy to detect and characterize the constituents in the Martian atmosphere.

4.4.3 IR ABSORPTION COMPUTATIONS FOR THE ASSUMED MODEL

The aim of this section is to present a model depicting the expected transmittances of the infrared radiation as the ray path to the satellite passes through the atmosphere of Mars, as illustrated in Figure 4-31. Specifically, we are interested in determining the transmittances versus the tangent altitude (altitude at which the ray path is tangent to a sphere concentric with Mars) over the frequency band of interest in the IR (namely from 2.5μ to 20μ). A knowledge of the expected transmittances over the various spectral bands as a function of tangent altitude will provide design criteria concerning required sensitivity and dynamic range of spectrometer. These results will also present notions as to which constituents may be identified and what their limiting altitudes are.

In determining the transmittance curves, we shall make use of the model atmosphere described in Section 4.4.1. As suggested by Plass (Ref. 46, 47, 67) and Stull et al. (Ref. 48), two basic methods exist to evaluate the transmittance through nonhomogeneous paths. The first method uses essentially theoretical quantities for this calculation. For this case, it is necessary to know the following information as a function of altitude for every band that contributed to absorption: (1) the intensity of every line; (2) the half-widths of every line; (3) the frequency of every line; (4) the line shape. The second method makes use of absorption data, either measured or calculated for homogeneous paths, along which the pressure and temperature are constant. By relating certain

TABLE 4-6

COMPARISON OF MINIMUM DETECTABLE CONSTITUENT DENSITIES (OR REDUCED PATH LENGTHS) WITH THEIR MAXIMUM EXPECTED VALUES FOR THE MICROWAVE SPECTROSCOPY EXPERIMENT

Constituent	Selected Lines		Absorption Coefficient α_o (db/km) (STP)	Minimum Detectable Density (cm^{-3})	Minimum Detectable cm-atm	Maximum Expected Density (cm^{-3})	Maximum Expected cm-atm
	f (GHz)	λ (m)					
H ₂ O	22.22	1.35×10^{-2}	39	3×10^{15}	190	8×10^{13}	5
O ₂	63.00	4.76×10^{-3}	15	2.2×10^{16}	1400		
O ₃	65.48	4.57×10^{-3}	4.34	8×10^{16}	5050		
NO ₂	78.87	3.8×10^{-3}	7.8×10^1	5.33×10^{15}	338		
CO	115.27	2.6×10^{-3}	2.08×10^1	2.92×10^{16}	1850		
H ₂ O	184.36	1.63×10^{-3}	3.52×10^3	2.76×10^{14}	17.4		

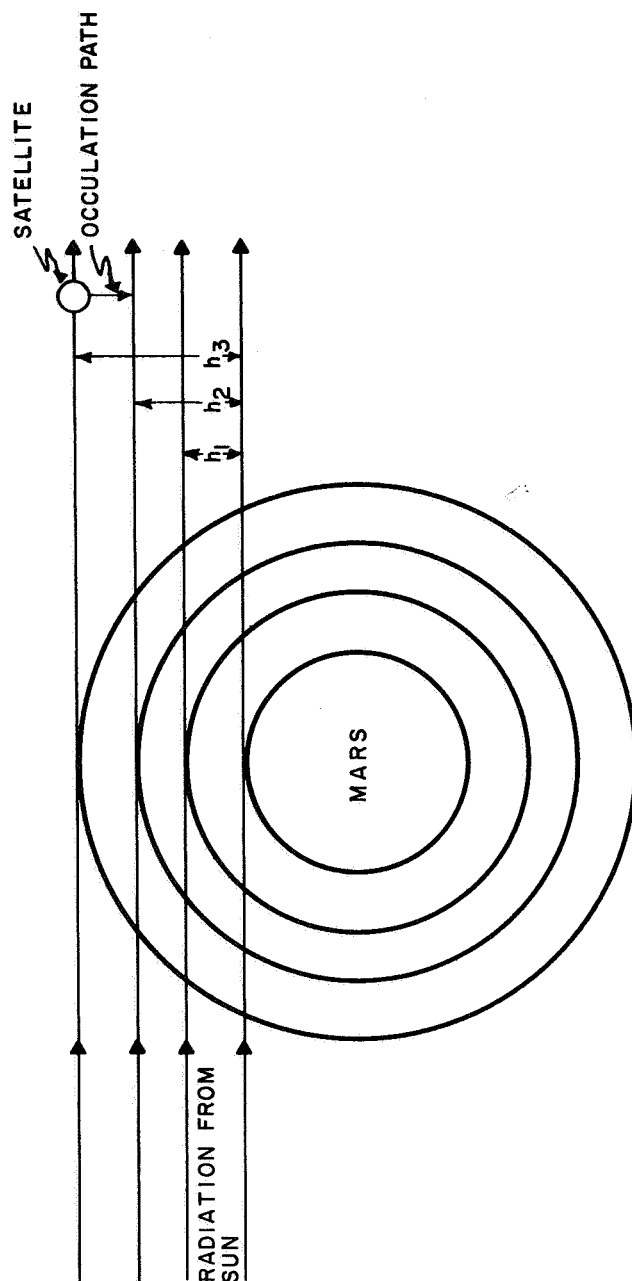


Figure 4-31 Configuration Depicting the IR Ray Paths Passing Through The Atmosphere of Mars During Occultations (h_1 , h_2 etc. are the corresponding target heights.)

fundamental physical quantities (such as pressure, temperature, density) for the inhomogeneous path case with the homogeneous path data, the transmittance may be deduced for the former. The basic idea is that there are fundamental quantities common to both the homogeneous and inhomogeneous cases that are multiplicative in nature and therefore cancel when their absorptions are related. In using the latter technique, a knowledge of the individual line shapes, half-widths, and spacing between the lines in the spectral interval in question is not necessary. Because of the comparative simplicity of the latter technique, we shall rely on it here to compute the expected transmittances for the proposed model. For purposes of completeness, the theory pertaining to this method is described in Appendix A.

4.4.3.1 Absorption Criteria

It has been demonstrated by Plass (Ref.47,67) (see Appendix A) that the absorption of infrared energy over an inhomogeneous path along which the pressure, density, and temperature vary is equivalent to the absorption over an equivalent homogeneous path having a uniform pressure, density, and temperature if the following relations are satisfied:

Strong Line Approximation

$$U_H^* = \frac{P_H^{-1} T_H^{1/2}}{n_O} \int_0^{\ell} s(T) N(\ell) P T^{-1/2} d\ell \quad (\text{atm-cm}) \quad (4.4-19)$$

Weak Line Approximation

$$U_H^* = \frac{1}{n_O} \frac{\sum_{i=1}^N \int_0^{\ell} S_i(\ell) d\ell}{\sum_{i=1}^N S_{iH}} \quad (\text{atm-cm}) \quad (4.4-20)$$

or

$$U_H^* = \frac{1}{n_O} \int_0^{\ell} N(\ell) s(t) d\ell \quad (\text{atm-cm}) \quad (4.4-21)$$

where U_H^* is the equivalent absorptive path length (expressed in atm-cm) and is given by

$$U_H^* = \frac{N_H L_H}{n_O} \quad (4.4-22)$$

where

N_H = density of homogeneous constituent

L_H = equivalent path length over which absorption is measured or calculated for homogeneous constituent

$n_O = 2.69 \times 10^{19} \text{ cm}^{-3}$ (Loschmidt's number)

P_H, T_H = the total pressure and temperature of homogeneous constituent

$N(\ell)$ = constituent density at specific location along inhomogeneous path

ℓ = total inhomogeneous path length

$P(\ell), T(\ell)$ = the total pressure and temperature at specific location along inhomogeneous path

$S_i(T)$ = the i^{th} line intensity in the given spectral interval at a point along the inhomogeneous path length

$S_{iH}(T_H)$ = the i^{th} line intensity measured at a temperature, T_H .

The function $s(T)$ may be calculated from the theory of molecular spectra and has been introduced in the derivation of equations 4.4-19 and 4.4-21 by assuming that each of the spectral line intensities in the spectral interval in question varies according to the same functional form of temperature. That is, if $S_i(T)$ represents the i^{th} line intensity at a temperature, T , in a spectral interval in which $i = 1, 2 \dots N$, then it is assumed that

$$S_i(T) = s(T) S_{iH}(T_H) \quad (4.4-23)$$

where $S_{iH}(T_H)$ is the i^{th} line intensity evaluated at an equivalent homogeneous temperature, T_H . Equation 4.4-23 is not valid when

large temperature differences occur along the slant path and the spectral lines have quite different intensities (Ref. 47).

Equation 4.4-19 is valid when the absorption of the incident radiation is virtually complete over frequency intervals at least several half-widths wide around the band centers of the strongest lines in the band and when these lines are largely responsible for the absorption over the given frequency interval. Equations 4.4-20 and 4.4-21 are valid when the absorption of each spectral line considered individually is small even near the line centers. It may be noted that equation 4.4-19 assumes the strong line approximation, a pressure broadened half-width, and the approximation of equation 4.4-23 to be valid. Otherwise, this relation is valid for any variation of line shape, line intensities, half-widths, and spacing between the lines in the spectral interval in question. Equations 4.4-20 and 4.4-21 assume the weak line approximation and these results are independent of the type of broadening (Lorentz and/or Doppler), half-widths, spacing between lines, and pressure.

The absorption calculated from the Lorentz shape alone is not changed appreciably by the Doppler effect for either weak or strong lines at heights up to 50 km on the Earth (Ref. 51). This corresponds to a pressure of 5.9×10^{-1} mm of Hg (Ref. 52), which is equivalent to an altitude of approximately 35 km on Mars, assuming the model of Section 4.4.1 . Since the predominant absorption occurs below this altitude, some form of Lorentz broadening is applicable here, thus justifying the use of equation 4.4-19.

For the present analysis we assume to know the density, pressure, and temperature along the inhomogeneous path and desire to determine the corresponding absorption. Assume for the moment that a set of tables exists giving the absorptions at various values of U_H^* , P_H , and T_H . It may be mentioned that such a set of tables has been prepared by Stull et al. (Ref.54,48) for CO_2 and by Wyatt et al. (Ref.55,56) for H_2O . Their results cover a frequency range 500 to 10,000 cm^{-1} at intervals as low as 2.5 cm^{-1} , for three temperatures (200, 250, 300°K), seven pressures (.01, .02, .05, .1, .2, .5, 1.0 atm), and fifteen amounts. For CO_2 these amounts range from .2 to 10,000 cm-atm, and for H_2O these amounts range from .001 to 50 prec-cm. If the strong line absorption approximation is valid, equation 4.4-19 suggests that the absorption over any inhomogeneous path may be deduced by computing the value of the integral and examining a set of tables for which the absorptance is tabulated at values of P_H , T_H , and U_H^* satisfying the equality of equation 4.4-19. Although a certain amount of arbitrariness exists

as to the selection of U_H , P_H , and T_H , only one value of absorption is possible as long as $(U_H P_H T_H^{1/2})$ is constant for the given path. Likewise, if the weak line approximation is valid, equation 4.4-20 suggests that the absorption may be deduced by evaluating the right-hand integral and examining any set of tables in which the absorption is tabulated as a function of U_H^* and T_H independent of pressure. (The function $S(T)$ is intrinsically related to T_H as a reference.) If neither the strong line nor the weak line approximation is valid over the spectral interval, a method of interpolation may be used to obtain the correct absorption as outlined in Appendix A.

4.4.3.2 Estimate of Expected Absorption for Various Constituents on Mars as a Function of Tangent Height

We shall here use the formulation presented in the previous section, in conjunction with transmittance tables of Stull et al. (Ref. 54, 48) and Wyatt et al. (Ref. 55, 56), as well as the model atmosphere of Section 4.4.1, to obtain curves describing the absorption of various constituents as a function of tangent height over spectral intervals of 50 cm^{-1} in the spectral range from 2 to 20μ . Because of the expected abundance of CO_2 as well as the existence of many CO_2 lines in this range, we have particularly concentrated on this constituent with some emphasis on H_2O .

Due to the unavailability of more extensive transmittance tables at the time of this report, certain simplifying assumptions have been made in the computation of the absorption curves for CO_2 and H_2O . These are: (1) the strong line approximation is assumed to be valid for CO_2 over the entire frequency interval considered; (2) the temperature is constant and equal to $T = 300^\circ\text{K}$. The absorption for CO_2 was then computed by equation 4.4-19 as the pressure and density were allowed to vary over the path lengths. The former assumption is considered to be for the most part valid for CO_2 since its abundance as well as the absorptive path lengths are large.

In order to obtain an estimated result here, the following other assumptions were made: (1) the radiation from the sun over the spectral interval used is considered to be constant during the occultation process; (2) a spherically symmetric atmosphere is assumed; and (3) refractive effects are neglected. With the receipt of more data and its numerical extension, assumptions (1) and (2) of the previous paragraph will be eliminated and the more general

situation of the mixed line strength and variations in temperature will be considered later. Furthermore, a spherically inhomogeneous model will also be considered later and refractive effects, especially at tangent heights near the surface of Mars, will be included. It may be mentioned that in the synthesis of the data, the refractive effects determined independently by the mother-daughter satellite experiment described elsewhere in this report will be used to identify the path more exactly.

Making use of the above assumptions, equation 4.4-19 becomes

$$U_H^* = \frac{P_H^{-1}}{n_0} \int_0^{\ell} N(\ell) P d\ell \quad \text{atm-cm} \quad (4.4-24)$$

The equivalent path length of equation 4.4-24 has been numerically integrated for CO₂, assuming the model atmosphere of Section 4.4.1 for different tangent heights, depicted in Figure 4-31. The results are plotted in Figure 4-32 for P_H = 1 atm. Comparing the results of this curve with the data in the tables by Stull et al. (Ref. 48) for CO₂ and Wyatt et al. (Ref. 56) for H₂O, leads to the corresponding equivalent absorption over the path lengths relative to the different tangent heights. In Figure 4-33 the absorption displays are plotted as a function of frequency over the spectral interval 2 to 20 microns for path lengths corresponding to different tangent heights. The absorption in db is here defined as 10 Log₁₀ I₀/I where I₀ and I are spectral intensities before and after absorption, respectively. The available absorption data had been computed at center frequencies located at spectral intervals of 50 cm⁻¹ and averaged over an interval of 50 cm⁻¹ for CO₂ and 100 cm⁻¹ for H₂O. In Figures 4-34 and 4-35 are plotted the absorptions as a function of tangent altitude for specific center frequencies in both the 15μ and 4μ interval. Assuming a 20 db dynamic range and a minimum detectable absorption of .5 db, it is apparent from Figures 4-34 and 4-35 that the absorption may continuously be monitored up to a tangent altitude of, at most, 50 km.

4.4.3.3 Synthesis of Absorption Data for the Determination of Pressure, Temperature, and Density

As an illustration of the technique that can be employed to synthesize the raw observed absorption data so that pressure,

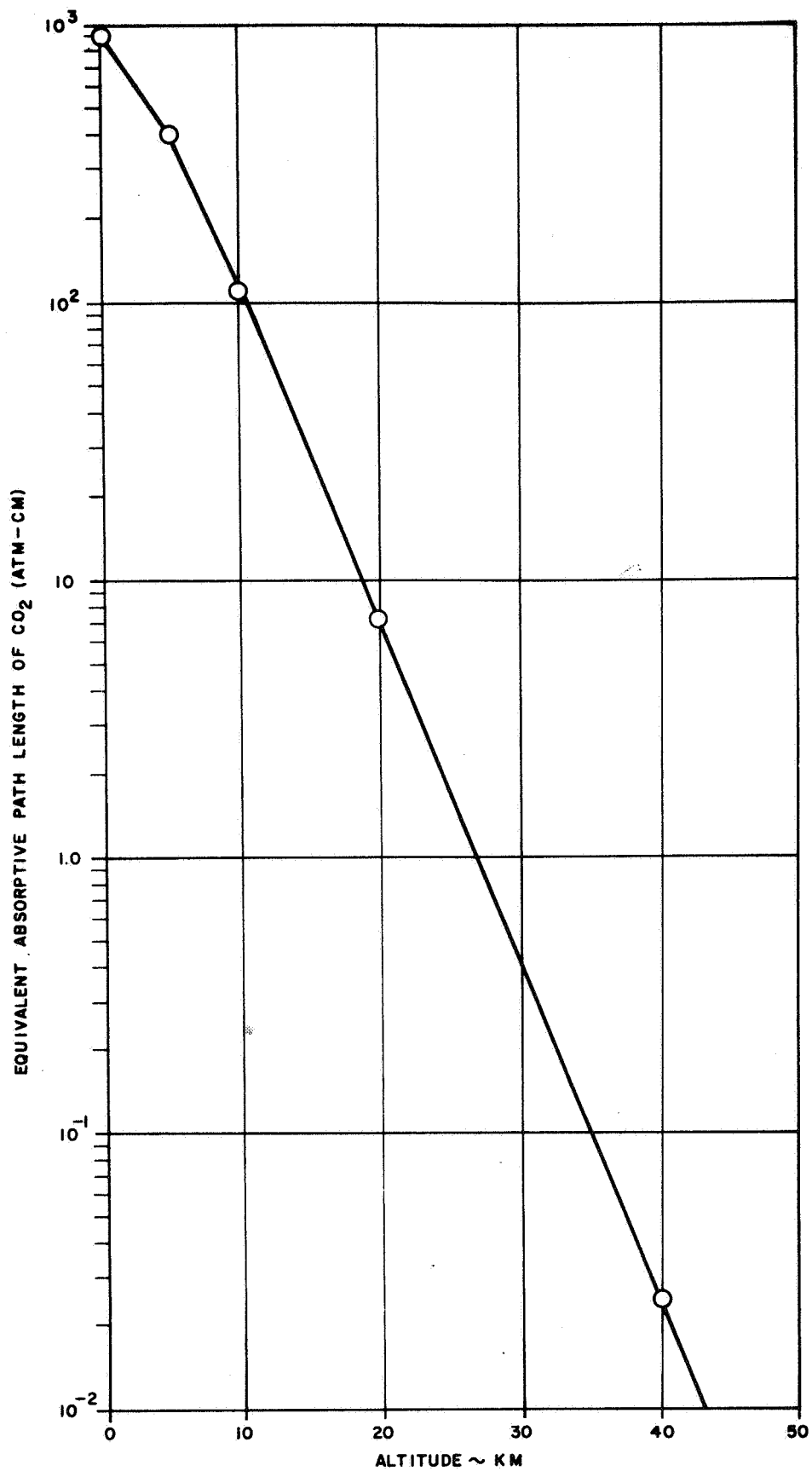


Figure 4-32a Equivalent Absorptive Path Length of CO₂ on Mars as a Function of Altitude (0-40 km)

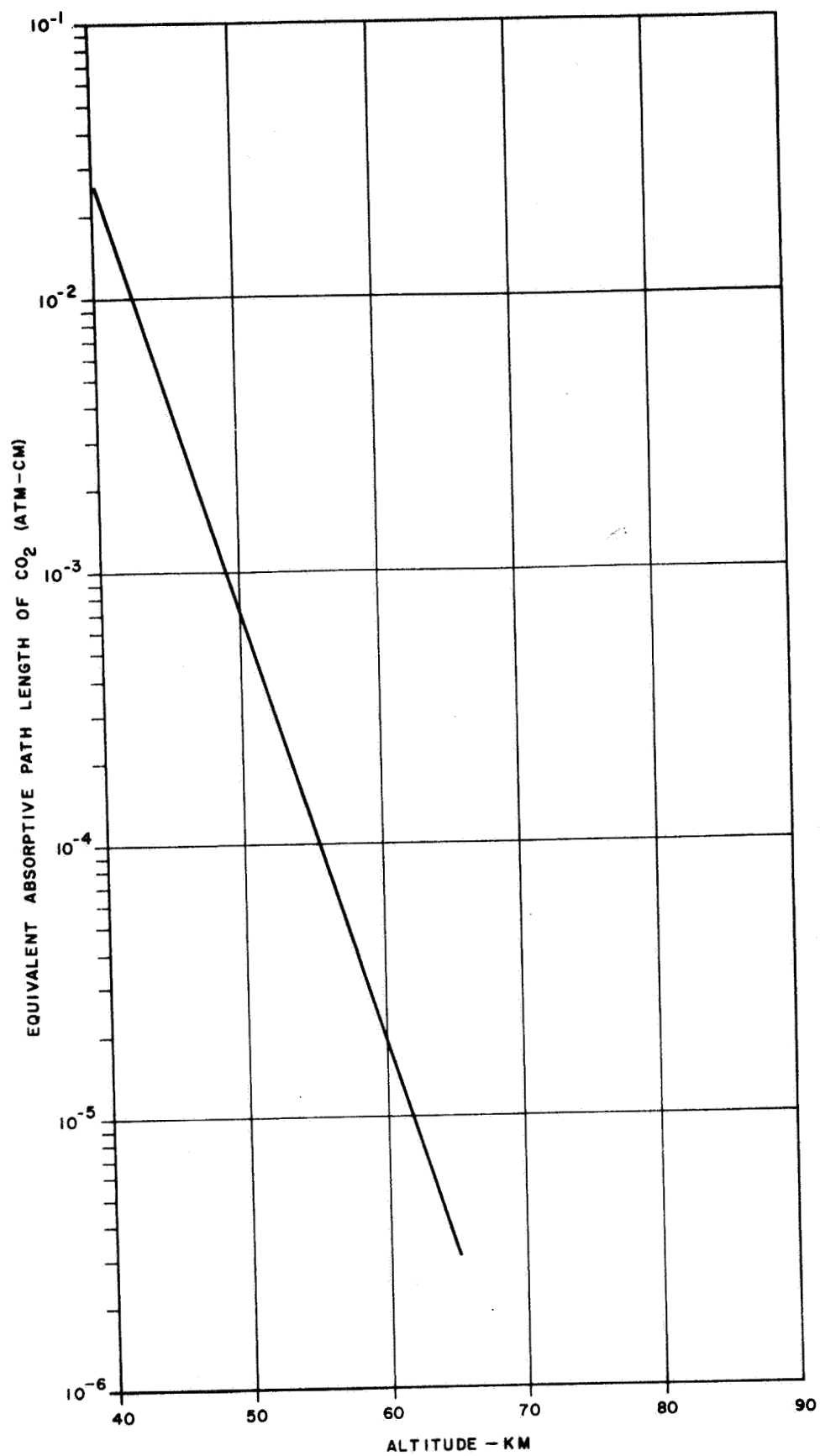


Figure 4-32b Equivalent Absorptive Path Length of CO₂ on Mars as a Function of Altitude (40-65 km)

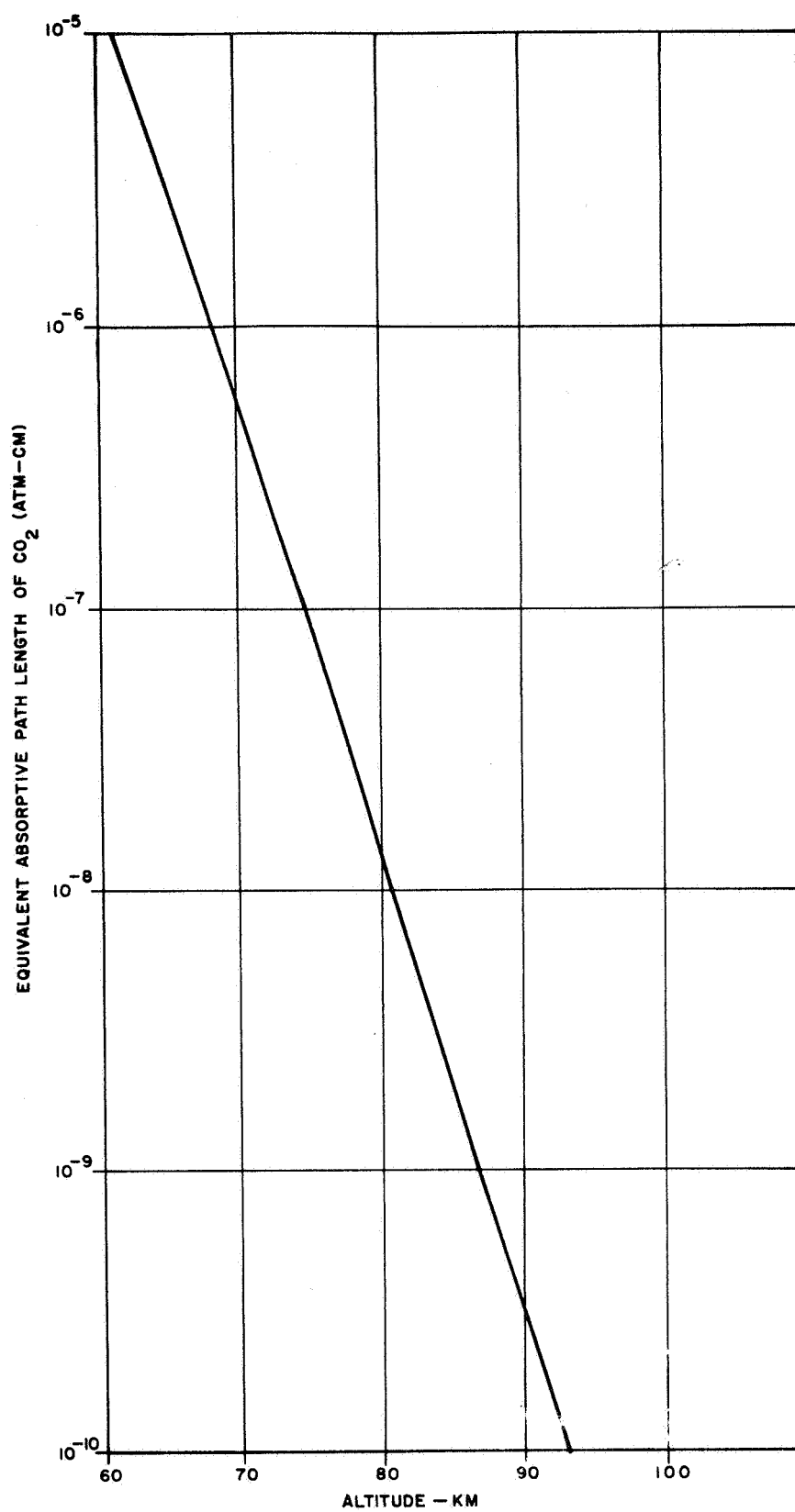


Figure 4-32c Equivalent Absorptive Path Length of CO₂ on Mars as a Function of Altitude (65-90 km)

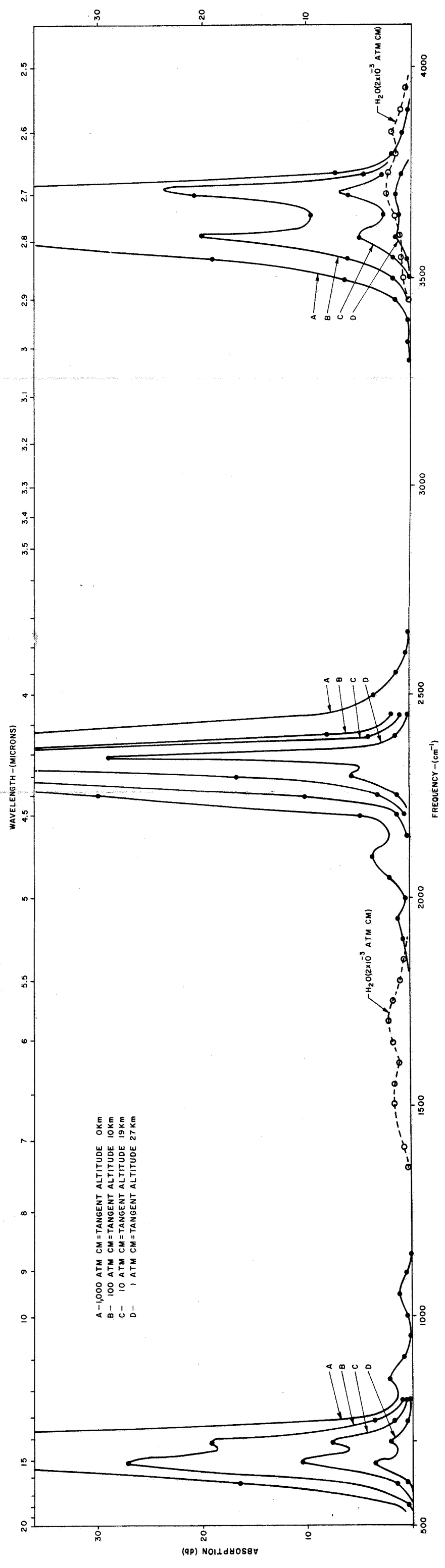


Figure 4-33 Absorption Display
Over the Spectral
Interval 2-20 Microns
at Different Tangent
Heights for CO₂ and H₂O

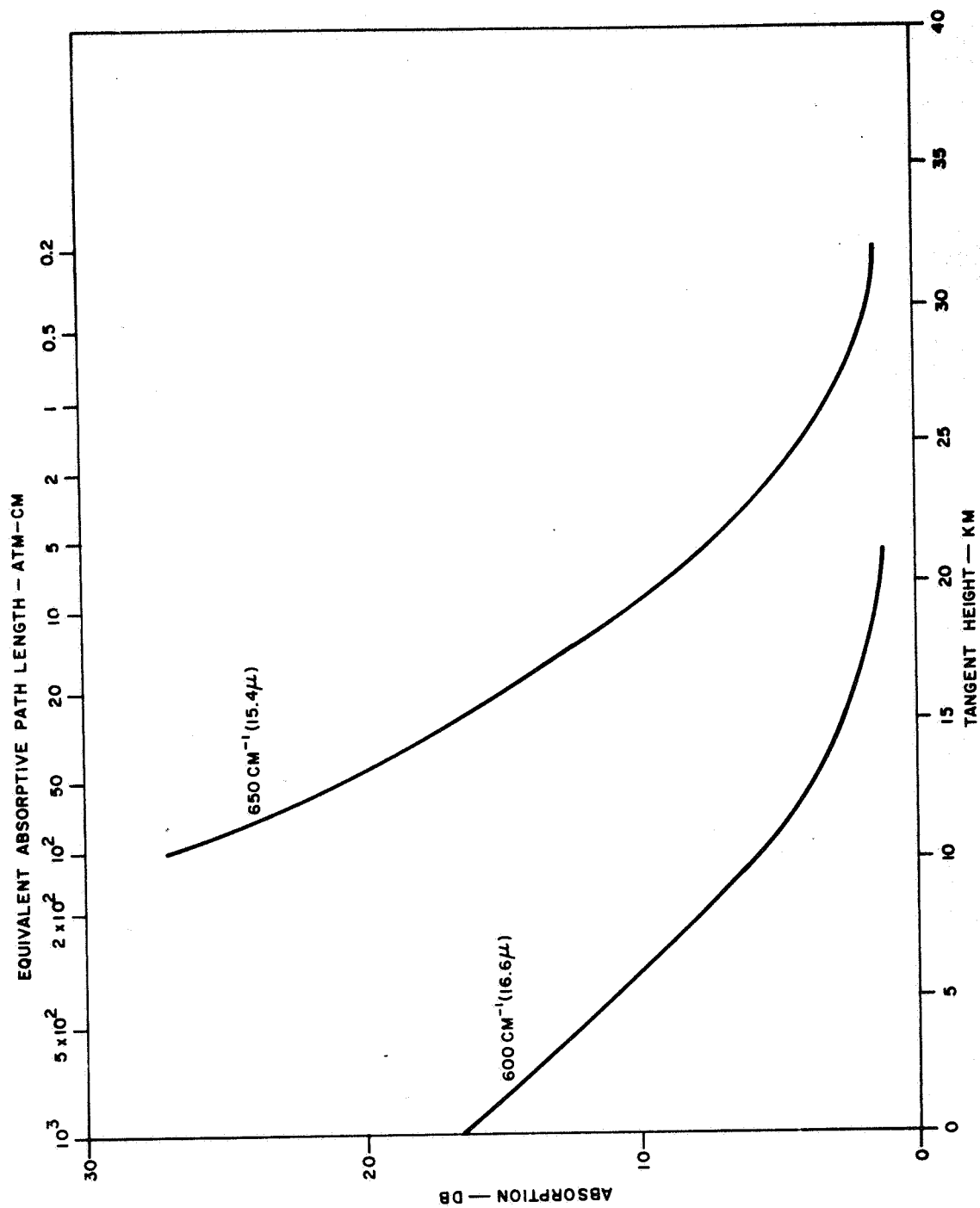


Figure 4-34 Absorption vs. Tangent Height at Frequencies in the 15 μ Region

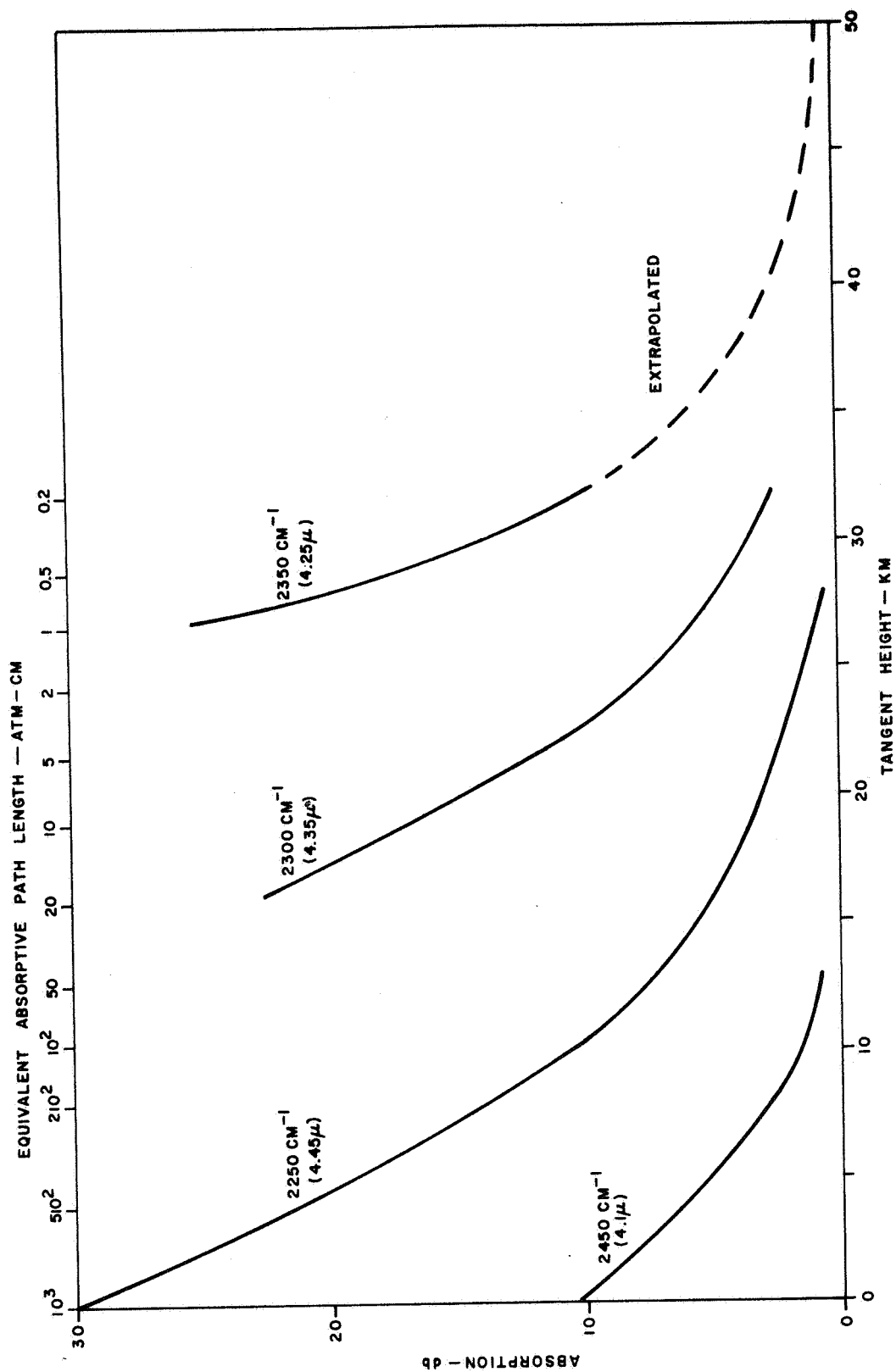


Figure 4-35 Absorption vs. Tangent Height at Frequencies in the 4μ Region

temperature, and gas constituent density can be determined, consider an idealized case of a spherically symmetric atmosphere of Mars divided into concentric intervals (e.g., 1 km intervals) as shown in the out-of-proportion sketch in Figure 4-36. The ray path traversing the tangent altitude is labeled path i ($i = 0, 1, 2, \dots$), where $i = 0$ represents the grazing ray path as shown. In the interval $(h_i - h_{i-1})$, the average values of pressure, temperature, and constituent density are denoted by P_i , T_i , and N_i , respectively.

Although the absorption throughout the frequency interval from 2.5μ to 20μ is to be measured, we shall, for the moment, consider two spectral intervals: one in which the weak line approximation is most probably valid, the other in which the strong line approximation is valid. For the weak line case, the integral in equation 4.4-21 may be expressed as a discrete summation over the approximated uniform path length intervals depicted in Figure 4-36. Considering N tangent paths, we may consider the following N equations:

$$U_{H1}^* = 2s(T_1) N(h_1) \Delta L_{11} + 2s(T_2) N(h_2) \Delta L_{12} + \dots + 2s(T_N) N(h_N) \Delta L_{1N}$$

$$U_{H2}^* = 0 + 2s(T_2) N(h_2) \Delta L_{22} + \dots + 2s(T_N) N(h_N) \Delta L_{2N}$$

.

.

.

$$U_{HN}^* = 0 + 0 + \dots + 2s(T_N) N(h_N) \Delta L_{NN}$$

(4.4-25)

where U_{Hj}^* is the equivalent absorptive length over the j^{th} tangent path, ΔL_{jp} is the p^{th} indicated interval (Figure 4-36) for the j^{th} path, $s(T_i) N(h_i)$ corresponds to the values at the i^{th} altitude. The experimental values of the absorptions over the different tangent paths dictate the values of U_{H1}^* , U_{H2}^* , ..., U_{HN}^* , which may be found from the transmittance tables for any value of P_H (the weak line approximations independent of pressure) and for a given reference temperature, T_H .

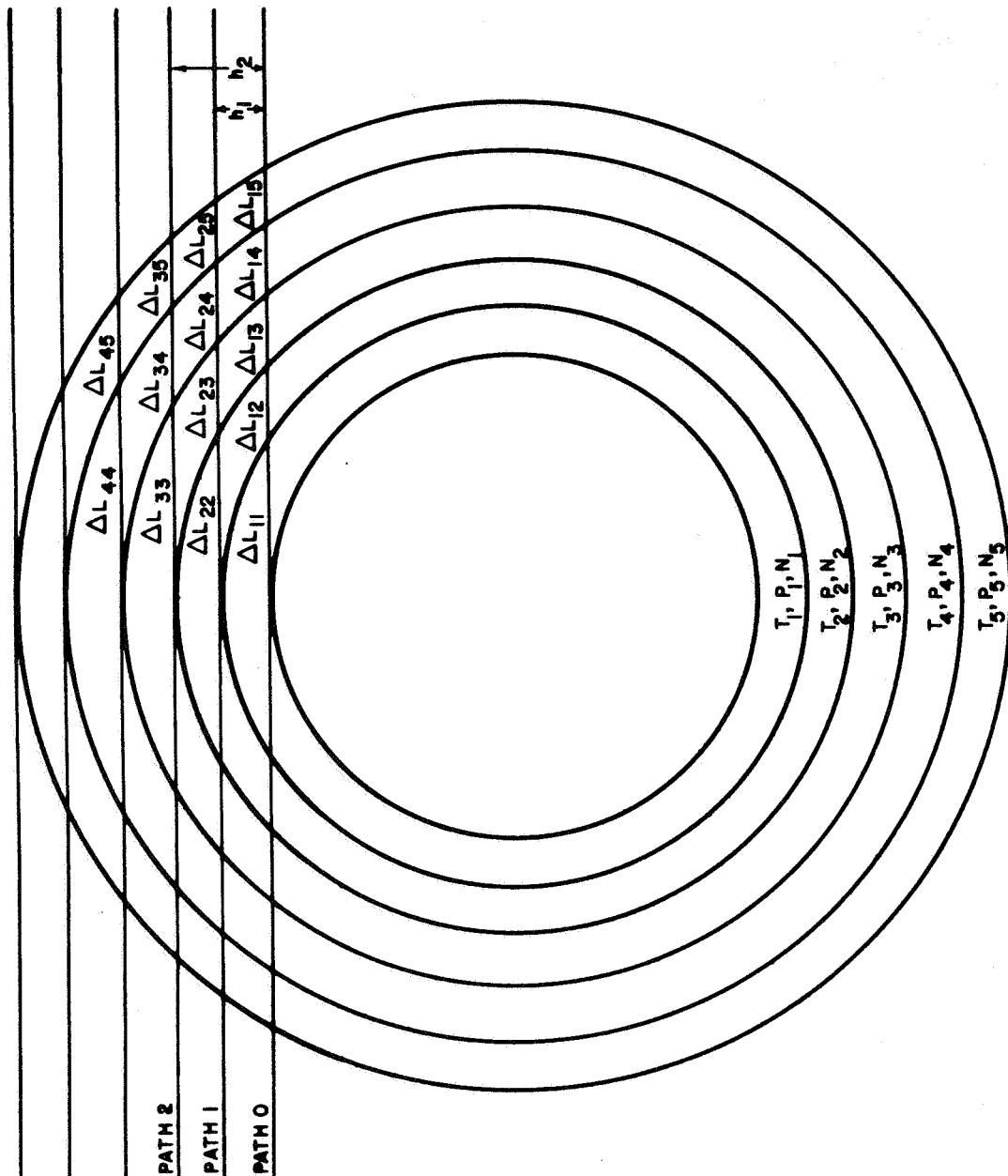


Figure 4-36 Spherically Symmetric Atmosphere of Mars Divided into Concentric Intervals

The equations in 4.4-25 represent N equations and N unknowns, from which we may obtain a curve relating $s(T) N(h)$ to altitude. Assuming that we may express this product relationship functionally by $f_i(h)$, then

$$s(T) N(h) = f_1(h) \quad (4.4-26)$$

Now consider a frequency interval over which the strong line approximation is most probable. Then equation 4.4-19 may be expressed in a form similar to equation 4.4-25, namely,

$$\begin{aligned} A_1 &= 2\alpha_1 \Delta L_{11} + 2\alpha_2 \Delta L_{12} + \dots + 2\alpha_N \Delta L_{1N} \\ A_2 &= 0 + 2\alpha_2 \Delta L_{22} + \dots + 2\alpha_N \Delta L_{2N} \\ &\cdot \\ &\cdot \\ &\cdot \\ A_N &= 0 + 0 + \dots + 2\alpha_N \Delta L_{NN} \end{aligned} \quad (4.4-27)$$

where

$$A_i = (P_H T_H^{-1/2} U_H)_i \quad (4.4-28)$$

and

$$\alpha_j = [s(T) p T^{-1/2} N]_j \quad (4.4-29)$$

where again the absorption over each tangent path dictates a specific value of A_i and the unknown coefficients correspond to α_j . The solution of the N simultaneous equations gives the dependence of α_j , an altitude that we assume to express functionally by

$$s(T) p T^{-1/2} N = f_2(h) \quad (4.4-30)$$

Assuming the perfect gas law to be valid,

$$p = k N T \quad (4.4-31)$$

Substituting equation 4.4-31 into equation 4.4-30, we arrive at

$$k s(T) T^{1/2} N^2 = f_2(h) \quad (4.4-32)$$

Squaring equation 4.4-26 and dividing the result by equation 4.4-32, we arrive at the transcendental equation,

$$s(T) T^{-1/2} = k \frac{f_1^2(h)}{f_2(h)} \quad (4.4-33)$$

from which the temperature variation as a function of altitude may be deduced. A knowledge of the T variations leads to the p and N variations by use of the other equations.

4.4.4 DESIGN CONSIDERATIONS FOR THE IR SPECTROMETER SYSTEM

4.4.4.1 Basic Spectrometer System

In view of the requirements of having a simple detector system that can operate at standard temperatures (e.g., 300°K) and be sensitive to radiation in the band 2.5μ to 20μ, a balometer detector is considered as the detecting element. In order that we have sufficient signal-to-noise ratio, computations are made here to determine the requirements on the collecting aperture for a given high resolution, Δh = 1 km, and for a selected type of spectrometer.

An interference spectrometer is suggested because a gain in the signal-to-noise ratio, S/N, is realized over that obtained with a dispersive type instrument (Ref. 61). A sketch of the system is depicted in Figure 4-37. A collector mirror of area, A, and focal length f forms an image of the sun on a plane in which a circular hole of diameter d_r is cut so that the proper height resolution (e.g., 1 km) is obtained. The portion of the image transmitted through the circular hole is incident upon the interferometer cube and the interferogram is obtained using a balometer whose output is subsequently reduced and recorded. In order to reduce smear due to the rapid passage of the sun-satellite path through the atmosphere of Mars, a complete scan of the 2.5μ to 20μ spectrum should be made in a time of 1 second or less.

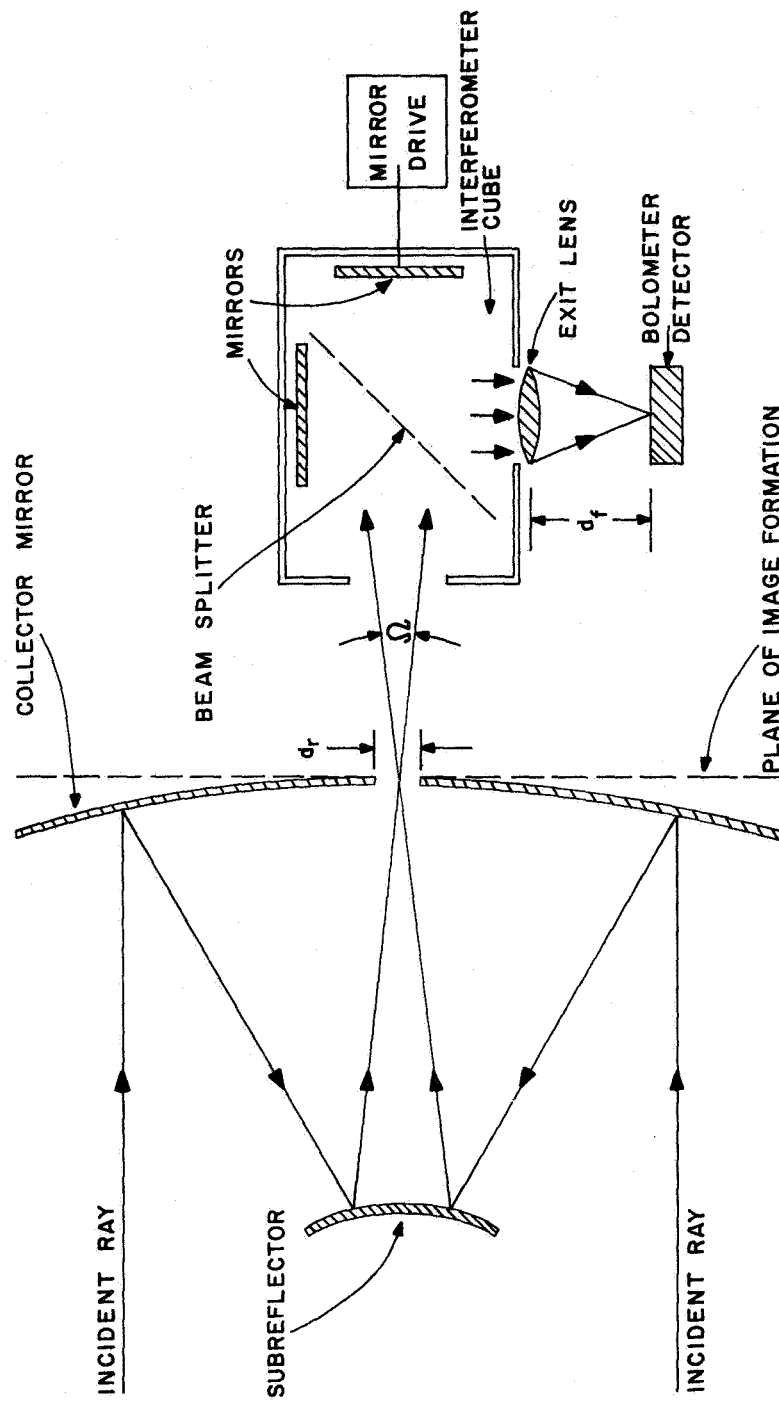


Figure 4-37 IR Spectrometer System

A spectrometer design of the type described above, having a spectral resolution $\Delta\nu$, of 20 cm^{-1} , is commercially available for satellite flights (Ref. 65).

In the following sections the specific design requirements of the IR spectrometer will be determined.

4.4.4.2 Relationship between the Sun's Image and the Orifice Size

In this section we shall examine the relation between the diameters of the orifice and the Sun in order to obtain for a given Mars-to-satellite distance a height resolution of 1 km. The Sun's diameter, D_S , and its average distance to Mars, D_{SM} (Figure 4-38) is given by

$$D_S = 1.4 \times 10^6 \text{ km} \quad (4.4-34)$$

$$D_{SM} \approx 2.2 \times 10^8 \text{ km} \quad (4.4-35)$$

The satellite subtends an angle θ_S (depicted in Figure 4-38), given by

$$\theta_S \approx 6 \times 10^{-3} \text{ rad} \quad (4.4-36)$$

At a Mars-satellite distance, d_{SM} , the height interval subtended by the Sun along a plane passing through the center of Mars is

$$\Delta h = 6 \times 10^{-3} d_{SM} \quad (4.4-37)$$

As an example, for a distance of $d_{SM} \approx 5000 \text{ km}$, Δh is 30 km. Thus, in order to achieve a 1 km height resolution, an orifice 1/20th of the diameter of the Sun's image must be used.

The size of the image is directly related to the focal length, f , of the collecting mirror by the relation,

$$d_S = f \theta_S = 6 \times 10^{-3} f \quad (4.4-38)$$

where

d_S = the image size of the Sun at the image plane;

f = focal length of collecting mirror.

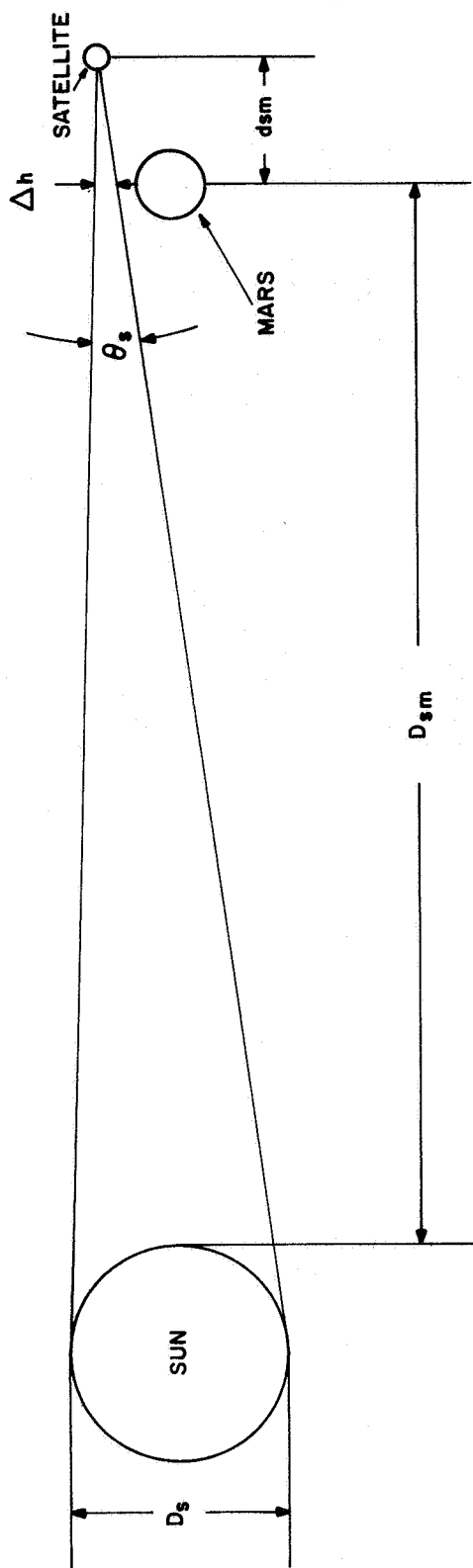


Figure 4-38 Approximate Sun-Mars Satellite Configuration when Sun-Satellite Path Passes through Martian Atmosphere (Centers of Sun, Satellite, and Mars are in same Plane)

Taking 1/30th of d_s , as given by equation 4.4-38, we obtain an orifice size,

$$d_r = 2 \times 10^{-4} f \quad (4.4-39)$$

As will be shown later, limitations must be placed upon d_r in order that the interferometer maintains its spectral resolution over the band. This limitation will then determine the focal length of the mirror.

4.4.4.3 Collecting Mirror Characteristics

We shall assume that the Sun radiates as a black body source having a uniform surface temperature (averaged) that subtends an angle, θ_s , at the receiver location that is larger than the angular beamwidth, θ_w , of the collecting mirror. If it is assumed that the angular beamwidth of the collecting mirror is diffraction limited, then

$$\theta_w \approx \lambda/D \quad (4.4-40)$$

where

λ = wavelength in spectral interval

D = aperture of collecting mirror.

The power received by a "point receiver" (e.g., one in which the orifice area is of the order of the focal area) is given by (Ref. 63)

$$\frac{d P_o(\nu)}{d \lambda} = \frac{2 C^2 h}{\lambda^3 (e^{Ch/\lambda KT} - 1)} \quad (\text{watts/m}) \quad (4.4-41)$$

where

C = speed of light (meter/sec)

λ = wavelength (meters)

h = Planck's constant = 6.6×10^{-34} joules/sec

K = Boltzmann's constant = 1.38×10^{-23} joules/°K

T = temperature of Sun $\approx 6 \times 10^3$ °K

In terms of the wavenumber $\nu = \lambda^{-1} > 4 \times 10^5 \text{ m}^{-1}$ (i.e., $\lambda > 2.5$ microns), equation 4.4-41 reduces to

$$\frac{d P_o(v)}{dv} = 2 K C T \quad (\text{watt/m}^{-1}) \quad (4.4-42)$$

It should be noted that equations 4.4-41 and 4.4-42 are independent of the diameter of the collecting mirror. An increase in the diameter of the mirror, therefore, does not increase the power flow into the focal area but only decreases the focal area itself, which is equivalent to increasing the resolution of the mirror (i.e., its ability to distinguish between two adjacent point sources). For our present case we do not have a point receiver, since the orifice diameter d_r will be much greater than the focal diameter, and hence the power received will be dependent upon the collector aperture area. The receiving area, A_r , given by

$$A_r = \frac{\pi d_r^2}{4} \quad (4.4-43)$$

effectively broadens the angular beamwidth of the collecting mirror and hence this beamwidth is no longer diffraction limited as suggested by equation 4.4-40. The effective beamwidth θ_e may be computed, using geometric optic theory and is given by

$$\theta_e \approx \frac{d_r}{f} \quad (4.4-44)$$

The orifice receives radiation from a larger area of the Sun than does the point receiver. From the above discussion, we may deduce that the orifice aperture can be considered to be a collection of point receivers of apertures equal to some effective focal area, A_{fi} . Each focal area, A_{fi} , collects radiation from a different area on the Sun, A_{Si} , given by

$$A_{Si} = \frac{\pi}{4} [D_{SM} \theta_w] \quad (4.4-45)$$

where D_{SM} is depicted in Figure 4-38 and θ_w is given by equation 4.4-40. If the radiation intensity in the focal plane were uniformly distributed over the effective focal area, this area would account for all the power, $\Delta P(v)$, collected by the mirror due to radiation from A_{Si} . Following the development of Born and Wolf (Ref. 64) we obtain an expression for A_{fi} given by

$$A_{fi} = \frac{4 \lambda^2}{\pi} (f/D)^2 \quad (4.4-46)$$

Thus, the total power, $\Delta P_r(\nu)$, received by the orifice, d_r , is equal to the power received through each effective focal area, A_{fi} , times the number N of focal areas contained in the orifice. That is,

$$d P_r(\nu) = d P_o(\nu) \times N \approx d P_o(\nu) \frac{A_r}{A_{fi}} \quad (4.4-47)$$

or

$$d P_r(\nu) = d P_o(\nu) \left(\frac{\pi}{4} \frac{d_r D}{\lambda f} \right)^2 \quad (4.4-48)$$

where $d P_o(\nu)$ is the power received by a point receiver (equation 4.4-42), A_r is given by equation 4.4-43 and A_{fi} by equation 4.4-46.

It should be remembered that equation 4.4-41 was derived under the assumption that the Sun is a uniform black body and that the focal area, A_{fi} , is constant for focus points away from the axis of the collecting mirror. Since the mirror has an overall efficiency, η , due to losses caused by imperfect reflections from its surface as well as diffraction losses, the power receiver $d P_r(\nu)$ would then be

$$d P_r(\nu) = \eta d P_o(\nu) \left(\frac{\pi}{4} \frac{d_r D}{\lambda f} \right)^2 \quad (4.4-49)$$

The power determined by equation 4.4-49 is that power which is delivered to the interferometer cube depicted in Figure 4-37 .

4.4.4.4 Interferometric Considerations

In this section, we shall give a brief analysis of the operation of a specific type of interference spectrometer of the kind depicted in Figure 4-39, namely the Michelson type, in order to later relate the minimum detectable atmospheric absorption coefficient, α_{\min} (See Section 4.4.4.6) to the specific interferometer characteristics. When the radiation from the Sun passes through the atmosphere of Mars, the power received by the orifice is no longer proportional to the $d P_r(\nu)$ as given by Equation 4.4-29. The absorption due to the constituents in the atmosphere will modify this relation and the power incident on the collecting mirror will be proportional to some new function $E_r(\nu)$, where $E_r(\nu)$ is the received spectral power density after the radiation has passed through the atmosphere. The power received by the orifice then takes the form,

$$d P_r(\nu) = \eta E(\nu) \left(\frac{\pi}{4} \frac{d_r}{\lambda} \frac{D}{f} \right)^2 d\nu \quad (4.4-50)$$

or

$$d P_r(\nu) = C(\nu) d\nu \quad (4.4-51)$$

where $C(\nu)$ is the collected spectral power density that is incident on the interferometer.

Consider an essentially monochromatic element of the spectrum $C(\nu)$ situated at a wave number ν . The power incident on the interferometer is given by Equation 4.4-51. When the movable mirror is located at the $x = 0$ position, the paths of the two beams, caused by the splitting of the incident beam, are equal and hence the power incident on the detector is maximum and equal to $1/2 C(\nu)d\nu$. The $1/2$ factor appears because $1/2$ of the power is reflected out of the interferometer along the path of the incident rays. Note that all spectral components in the spectrum will add in phase for this condition and hence the detector will have one half of all the collected spectral power incident on the orifice. As the mirror is moved either to the left or right, the path length of beam 2 changes with respect to the path of beam 1, causing the power incident on the detector to decrease. When $x = N\lambda$, the path lengths differ by a half wavelength, causing

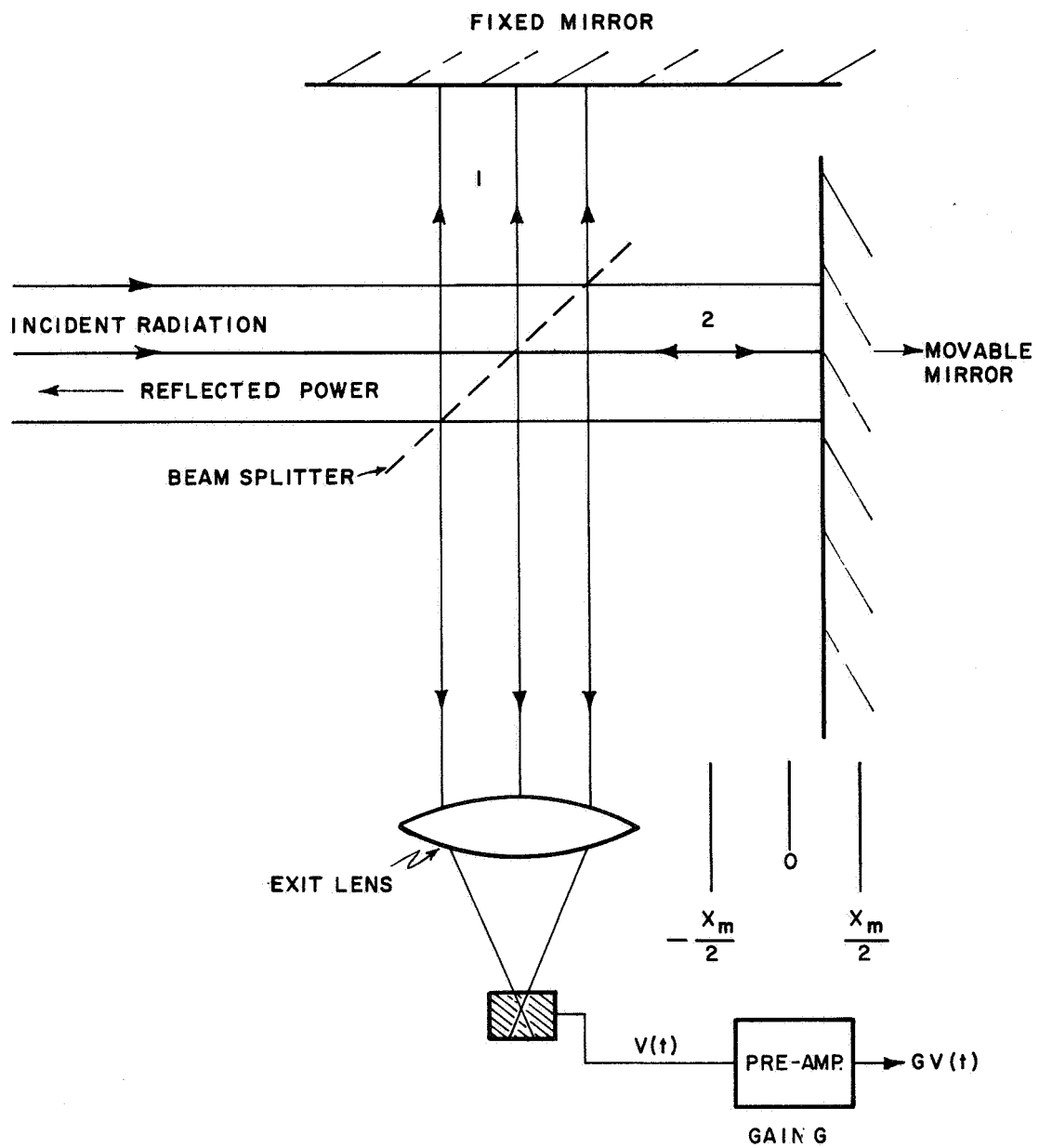


Figure 4-39 Michelson Type Interference Spectrometer

complete cancellation of the monochromatic power at the detector. Thus, the power incident on the detector will vary as

$$d P_r(\nu) = \frac{1}{2} C(\nu) \frac{\left[\cos \left(\frac{4\pi x}{\lambda} \right) + 1 \right]}{2} d\nu \quad (4.4-52)$$

where x = displacement of mirror from the reference.

If the mirror is moved at constant velocity from $-x_m/2$ to $+x_m/2$ the detected power will vary in a time $\left[-\frac{T_M}{2} \leq t \leq \frac{T_M}{2} \right]$ as

$$d P_r(t) = \frac{1}{4} C(\nu) \left[\cos \left(\frac{4\pi u}{\lambda} t \right) + 1 \right] d\nu \quad (4.4-53)$$

For a detector having a responsivity, R , the output voltage (depicted in Figure 4-39) has a time variation (Ref. 66),

$$dV(t) = \frac{R}{4} C(\nu) d\nu \cos(2\pi f t) \quad (4.4-54)$$

where the dc term has been omitted. The modulation frequency, which may be shown to be given by $f = 2\nu u$, is typically in the audio range (i.e., less than 1 kHz). It may be noted that the responsivity of a bolometer detector is relatively constant in the spectral band 2-20 μ . In all further developments we shall omit the dc term of Equation 4.4-52 since it does not contain information of the shape of the spectrum.

Assuming that the entire spectrum contains elements that lie entirely between the wave numbers from ν_a to ν_b , the time or distance dependence of the detector output would be

$$V(\gamma) = R P_r(\gamma) = \frac{R}{4} \int_{\nu_a}^{\nu_b} C(\nu) \cos[2\pi\gamma\nu] d\nu \quad (4.4-55)$$

where $\gamma = 2x - 2Vt$ is the total phase path change.

In order to retrieve the desired spectrum $C(\nu)$, one must perform an inverse Fourier operation on Equation 4.4-55. Such an inverse transform is given by

$$S(\nu') = 2R \int_{-\infty}^{\infty} P_r(\gamma) \cos(2\pi \nu' \gamma) d\gamma \quad (4.4-56)$$

Since the parameter, γ , varies from $-X_m$ to $+X_m$, the function $P_r(\gamma)$ will be assumed as zero outside this range. Making use of this fact plus the fact that $P_r(\gamma)$ is an even function, Equation 4.4-56 becomes

$$S(\nu') = R \int_{\nu_a}^{\nu_b} d\nu \int_0^{x_m} C(\nu) \cos(2\pi \gamma \nu) \cos(2\pi \gamma \nu') d\gamma \quad (4.4-57)$$

Since the parameter γ varies from $-X_m$ to $+X_m$, the function of $P_r(\gamma)$ will be assumed to be zero outside this range. Since $P_d(\gamma)$ is an even function, Equation 4.4-57 reduces to

$$S(\nu') = 4R \int_0^{x_m} P_d(\gamma) \cos 2\pi \nu' \gamma d\gamma \quad (4.4-58)$$

Substituting Equation 4.4-56 into 4.4-58 we have

$$S(\nu') = R \int_{\nu_a}^{\nu_b} d\nu \int_0^{x_m} C(\nu) \cos 2\pi \gamma \nu \cos 2\pi \gamma \nu' d\gamma \quad (4.4-59)$$

We shall now show that if X_m is sufficiently large (a value to be determined), the Fourier Transform $S(\nu')$ of $V(\gamma)$ is equivalent to the collected spectral power density $C(\nu)$.

In practice, one would perform the operation given by Equation 4.4-58 on $V(\gamma)$ using a digital computer or an electronic correlator.

Integrating the right-hand side of Equation 4.4-59 with respect to γ we obtain

$$S(\gamma') = \frac{R}{2} \int_{\gamma_a}^{\gamma_b} C(\gamma) \left[\frac{\sin 2\pi(\gamma - \gamma') X_m}{2\pi(\gamma - \gamma')} + \frac{\sin 2\pi(\gamma + \gamma') X_m}{2\pi(\gamma + \gamma')} \right] d\gamma \quad (4.4-60)$$

The function having the form $\left(\frac{\sin \alpha x}{\alpha} \right)$ is oscillatory, except in the vicinity of $\alpha = 0$. Since γ and γ' are positive constant, the second term of Equation 4.4-60 will contribute very little to the integral as the integration variable γ passes through γ' . Thus, we shall neglect this contribution and Equation 4.4-60 becomes:

$$S(\gamma') \approx \frac{R}{2} \int_{\gamma_a}^{\gamma_b} C(\gamma) \sin \frac{2\pi(\gamma - \gamma') X_m}{2\pi(\gamma - \gamma')} d\gamma \quad (4.4-61)$$

Case A - Slowly Changing Spectrum

If $C(\gamma)$ changes very slowly over the width, $\Delta\gamma_i$, given by

$$\Delta\gamma_i = (\gamma - \gamma') \equiv \frac{1}{2X_m} \quad (4.4-62)$$

then $C(\gamma)$ can be replaced with $C(\gamma')$ and be taken out of the integral to give

$$S(\gamma') = \frac{R C(\gamma')}{2} \int_{\gamma_a}^{\gamma_b} \frac{\sin 2\pi(\gamma - \gamma') X_m}{2\pi(\gamma - \gamma')} d\gamma \quad (4.4-63)$$

Since $\gamma_b - \gamma_a$ is assumed much larger than $\Delta\gamma_i$, upon integration, Equation 4.4-63 results in

$$S(\gamma') \approx \frac{C(\gamma') R}{4} \text{ volt-cm} \quad (4.4-64)$$

Thus, when the resolution, $\Delta\nu_i$, of the interferometer is sufficiently small, the approximate computed spectrum $S(\nu')$ is equal to the actual spectrum $C(\nu')$. The factor of 1/4 is present because one-half the power is lost in the interferometer and the other half is lost to the dc component.

Case B - Spectrum for Case $\Delta\nu < \Delta\nu_i$

In case the line width $\Delta\nu$ is less than the instrument resolution $\Delta\nu_i$ the recovered spectrum signal level, $S(\nu')$ will be less, where $S(\nu')$ is now given by

$$S(\nu') = \frac{1}{2} \int_{\nu_o - \frac{\Delta\nu}{2}}^{\nu_o + \frac{\Delta\nu}{2}} R C(\nu) \frac{\sin 2\pi(\nu - \nu')X_m}{2\pi(\nu - \nu')} d\nu \quad (4.4-65)$$

In Equation 4.4-65, we have assumed that the line shape is rectangular (of width $\Delta\nu$) in order to illustrate the form of $S(\nu')$. Thus,

$$S(\nu') = \frac{R}{2} C(\nu_o) X_m \int_{\nu_o - \frac{\Delta\nu}{2}}^{\nu_o + \frac{\Delta\nu}{2}} \frac{\sin 2\pi(\nu - \nu')X_m}{2\pi(\nu - \nu')X_m} d\nu \quad (4.4-66)$$

or

$$S(\nu') = \frac{R}{2} C(\nu_o) X_m \Delta\nu \frac{\sin 2\pi(\nu_o - \nu')X_m}{2\pi(\nu_o - \nu')X_m} \quad (4.4-67)$$

Thus the peak of the recovered line is

$$S(\nu_o) = \frac{R}{2} C(\nu_o) X_m \Delta\nu \quad (4.4-68)$$

When the instrument width $\Delta\nu_i$ is greater than the width $\Delta\nu$, the recovered spectrum peak intensity is reduced by a factor $\Delta\nu/\Delta\nu_i$.

If the instrument width $\Delta\nu_i$ is less than the $\Delta\nu$, then the recovered spectral intensity will be that given by Equation 4.4-64.

4.4.4.5 Signal-to-Noise Ratio of the Recovered Spectrum

The amount of input power required to increase the detected output voltage to twice the output noise voltage level is called the "noise equivalent power" (NEP). With this power, the noise voltage at the output of the detector changes by

$$V_N = R \text{ (NEP)} \quad (4.4-69)$$

The signal strength of the interferogram is

$$V(o) = R \int_{\nu_a}^{\nu_b} \frac{C(\nu)}{4} d\nu \quad (4.4-70)$$

and the signal-to-noise voltage ratio at the center of the interferogram is

$$\left(\frac{S}{N} \right)_I = \frac{\int_{\nu_a}^{\nu_b} \frac{C(\nu) d\nu}{4}}{\text{NEP}} \quad (4.4-71)$$

where the NEP is given by

$$\text{NEP} = \frac{(\text{BW})^{1/2} (A)^{1/2}}{D^*} \quad (4.4-72)$$

and where

A is the area of detector in cm

BW is the bandwidth that the output of the detector is subjected to

D^* is the specific detectivity of the detector.

Let us now focus our attention on a spectral element $C(\nu)\Delta\nu$, which produces a signal at the output terminals of the detector of

$$R C(v_o) \Delta v \text{ volts} \quad (4.4-73)$$

It will be assumed that the spectrum consists of a single line at strength $C(v_o)$ having a rectangular shape of width Δv . The signal strength of this element in the interferogram would be that given by (4.4-64). The signal-to-noise voltage ratio in the interferogram is for the case of a single line

$$\left(\frac{S}{N} \right)_i = \frac{C(v_o) \Delta v D^*}{(BW)^{1/2} A^{1/2}} \quad (4.4-74)$$

It is now our task to determine the signal-to-noise ratio in the processed spectrum denoted by $(S/N)_s$. As was shown in the previous section, when the resolution Δv_i of the instrument is greater than the spectral width of the line, the recovered spectral intensity is reduced by the ratio $\Delta v / \Delta v_i$. Thus the spectral energy density is (from Equation 4.4-68) given by

$$S(v_o) = \frac{R}{4} C(v_o) \left(\frac{\Delta v}{\Delta v_i} \right) \quad (4.4-75)$$

Parseval's relation yields the following for the noise power, N_s^2 , in the recovered spectrum (Ref.),

$$N_s^2 (v_b - v_a) = N_i^2 X_m \quad (4.4-76)$$

where N_i^2 = noise power density in the interferogram. The above equation assumes that the noise in the interferogram $N_i^2 X_m$ is uncorrelated with signal. Thus the noise in the processed spectrum is given by

$$N_s = \frac{N_i X_m^{1/2}}{(v_b - v_a)^{1/2}} \quad (4.4-77)$$

Now the noise N_i in the interferogram given by Equation 4.4-69 results in

$$N_s = \sqrt{\frac{X_m}{(v_b - v_a)}} V_N \text{ volt-cm} \quad (4.4-78)$$

Thus the signal-to-noise ratio in the recovered spectrum is

$$\left(\frac{S}{N} \right)_S = \frac{\frac{1}{4} C(\nu_o) \left(\frac{\Delta \nu}{\Delta \nu_I} \right) D^*}{\sqrt{\frac{X_m}{(\nu_b - \nu_a)} (BW)^{1/2} A^{1/2}}} \quad (4.4-79)$$

where

$$BW = 2 (\nu_b - \nu_a) \frac{X_m}{T_m} \quad (4.4-80)$$

Substituting Equation 4.4-80 into 4.4-79 we obtain

$$\left(\frac{S}{N} \right)_S = \frac{\sqrt{2}}{4} \frac{C(\nu_o) \Delta \nu D^* \sqrt{T_m}}{A^{1/2}} \quad (4.4-81)$$

In terms of NEP, Equation 4.4-81 becomes

$$\left(\frac{S}{N} \right)_S = \frac{\sqrt{2}}{4} C(\nu_o) \frac{\Delta \nu}{\Delta \nu_I} \frac{\sqrt{\Delta \nu_I (\nu_b - \nu_a)}}{NEP} \quad (4.4-82)$$

where

$$C(\nu_o) = \eta E(\nu_o) \left(\frac{\pi}{4} \frac{dr}{\lambda} \frac{D}{f} \right)^2$$

Since there is an inefficiency associated with the interferometer, Equation 4.4-81 should be multiplied by η_i , which is defined as the efficiency of the interferometer. Thus the signal-to-noise ratio is

$$\left(\frac{S}{N} \right)_S = \frac{\sqrt{2}}{4} \eta_i \frac{C(\nu_o) \Delta \nu D^* \sqrt{T_m}}{A^{1/2}} \quad (4.4-83)$$

4.4.4.6 Minimum Detectable Absorption

Since we are interested in observing the absorption lines of the atmospheric constituents, the signal we desire to discern would correspond to a differential decrease in the received spectrum of the Sun. We must be able to distinguish this change from any random changes due to noise. Assuming that the fluctuations are entirely due to noise in the thermal detector, we can obtain

an estimate of the minimum detectable absorption, α_{\min} . We define α_{\min} as that total absorption along the path which is required to cause a change in the recovered spectrum of level equal to the noise in this spectrum. Thus, without absorption the processed spectral distribution is

$$S_o(\nu_o) = \frac{R C_o(\nu_o)}{4} \quad (4.4-84)$$

where ν_o is the wave number at which absorption is to take place. In presence of absorption, the resultant processed spectrum will be reduced in magnitude by an amount $\Delta S(\nu_o)$. That is,

$$S(\nu_o) = S_o(\nu_o) - \Delta S(\nu_o) \quad (4.4-85)$$

Now the amount of change $\Delta S(\nu_o)$ that is obtained is a function both of the intensity of the absorption line and its effective width $\Delta\nu$. For example, the incoming collected spectrum may have the characteristics depicted in Figure 4-39.

In order to determine ΔS , let us consider the following argument. In Section 4.4.4.4 we had shown that for an emission line of width $\Delta\nu$ and peak strength $C(\nu_o)$, the processed spectrum had an amplitude,

$$S(\nu_o) = \frac{R C(\nu_o)}{4} \frac{\Delta\nu}{\Delta\nu_I} \quad (4.4-86)$$

and a width equal to the instrument width $\Delta\nu_i$. Thus a narrow spectral element is smoothed out by the limited response of the instrument. It appears, therefore, that an absorption line as shown in Figure 4-40 would also be smoothed out (e.g., the depression decreased in intensity). Thus, for absorption line of change ΔC we assume that

$$\Delta S(\nu_o) = \frac{\Delta C(\nu_o)}{4} \frac{\Delta\nu}{\Delta\nu_I} R \quad (4.4-87)$$

where

$$\Delta C(\nu_o) = C_o(\nu_o) - C(\nu_o) \quad (4.4-88)$$

Substituting Equation 4.4-87 and 4.4-88 into 4.4-85, we obtain that at the absorption line, ν_o , the processed spectrum has a magnitude given by

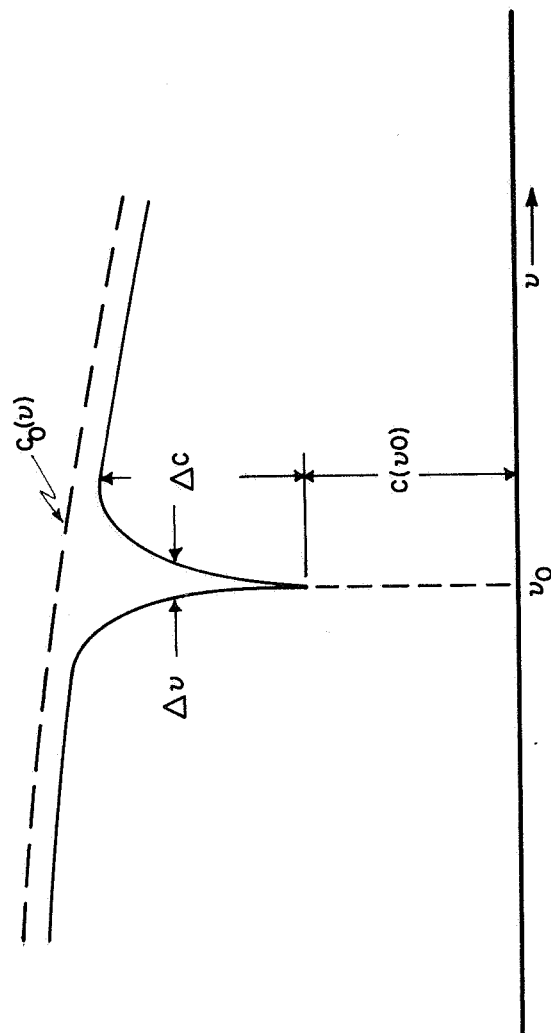


Figure 4-40 Illustrative Example of Absorption Line

$$S(\nu_o) = S_o(\nu_o) - \frac{[C_o(\nu_o) - C(\nu_o)]R}{4} \frac{\Delta \nu}{\Delta \nu_I} \quad (4.4-89)$$

In order to be able to detect the change $[S_o(\nu_o) - S(\nu_o)]$ in the processed spectrum, this change must be at least equal to the noise N_S . Thus,

$$S_o(\nu_o) - S(\nu_o) = N_S \quad (4.4-90)$$

Substituting Equations 4.4-89 and 4.4-77 into 4.4-90 we obtain

$$\frac{C_o(\nu_o)}{4} \frac{\Delta \nu}{\Delta \nu_I} - \frac{C(\nu_o)}{4} \frac{\Delta \nu}{\Delta \nu_I} = (\text{NEP}) \sqrt{\frac{X_m}{(\nu_b - \nu_a)}} \quad (4.4-91)$$

where $C_o(\nu_o)$ is the collected spectral power density in absence of absorption and is given by

$$C_o(\nu_o) = \eta \, 2K \, C \, T \left(\frac{\pi}{4} \frac{dr}{\lambda} \frac{D}{f} \right)^2 \quad (4.4-92)$$

Let us assume that in presence of an absorption line that $C(\nu_o)$ can be expressed as

$$C(\nu_o) = C_o(\nu_o) [1 - \alpha] \quad (4.4-93)$$

where α would be a measure of the total absorption along the entire path of the radiation centered at $\nu = \nu_o$. Substituting Equation 4.4-93 and 4.4-92 into 4.4-91 results in the following expression for α_{\min} :

$$\alpha_{\min} = \frac{\sqrt{2 \text{ NEP}}}{\eta \, \eta_i \, KCT} \sqrt{\frac{1}{\Delta \nu_I (\nu_b - \nu_a)}} \cdot \frac{\Delta \nu_I}{\Delta \nu} \frac{1}{\left(\frac{\pi}{4} \frac{dr}{\lambda} \frac{D}{f} \right)^2} \quad (4.4-94)$$

Substituting Equation 4.4-72 for NEP and Equation 4.4-80 for BW, we obtain

$$\alpha_{\min} = \frac{\sqrt{2} A^{1/2}}{\eta \eta_i KCT D^*} \frac{1}{\Delta \nu} \frac{1}{\left(\frac{\pi}{4} \frac{dr}{\lambda} \frac{D}{f} \right)^2} \frac{1}{\sqrt{T_m}} \quad (4.4-95)$$

where $\Delta \nu$ is the effective width of the line, T_m is the scan time, and T is the effective temperature of the Sun.

In order that the temperature fluctuations of the Sun do not cause fluctuations in the processed spectrum greater than the noise N_s , the temperature variation ΔT must satisfy the inequality,

$$\frac{\Delta T}{T} < \alpha_{\min} \quad (4.4-96)$$

The minimum absorption coefficient, α_{\min} , is directly related to $\left(\frac{S}{N} \right)_s$ and can be easily shown to be

$$\alpha_{\min} = \left(\frac{S}{N} \right)_s^{-1} \quad (4.4-97)$$

4.4.4.7 Limits on Resolution and Determination of Focal Length

The resolution of the interferometer is given by Equation 4.4-62, which shows that in order to achieve a better resolution a larger displacement of the movable mirror must be made. Typical resolutions of the order of 20 cm^{-1} can be achieved easily. However, because of differing path lengths for rays obliquely incident on the interferometer, the solid angle of acceptance for a given resolution $\Delta \nu_i$ (or conversely, the resolution for a given solid angle of the source) is limited by the equation (Ref. 67),

$$\Omega \leq \frac{2\pi \Delta \nu_i}{\nu} \quad (4.4-98)$$

The solid angle subtended at the orifice is

$$\Omega_r = \left(\frac{D}{2f} \right)^2 \quad (4.4-99)$$

In order to realize the full aperture of the collecting mirror and the resolution Δv_i , Ω_r must be

$$\Omega_r \leq \frac{2\pi \Delta v_i}{v} \quad (4.4-100)$$

Substituting Equation 4.4-99 into 4.4-100 results in

$$f \geq \frac{D}{2} \sqrt{\frac{v}{2\pi \Delta v_i}} \quad (4.4-101)$$

Selecting $\Delta v_i = 20 \text{ cm}^{-1}$ and the largest wave number $v = 5 \times 10^3 \text{ cm}^{-1}$ we obtain that

$$f \geq 10 D \quad (4.4-102)$$

Thus, the angle of rays incident on the interferometer is

$$\theta_r = \frac{D}{f} \leq 10^{-1} \text{ rad} \approx 6^\circ \quad (4.4-103)$$

4.4.4.8 Orifice Size

In order to obtain a fine height resolution (i.e., $\Delta h = 1 \text{ km}$), an orifice $1/30^{\text{th}}$ on the diameter of the sun image is required. The actual dimensions of the orifice is then determined by the image size, which is proportional to the focal length as shown by Equation 4.4-38. In order to be able to neglect diffraction effects of the orifice, the orifice diameter should be many times larger than the longest wavelength considered (e.g., 20μ). The angle of radiation due to diffraction effects is λ/d_r and this should be equal to or smaller than Equation 4.4-103. Thus,

$$d_r > \frac{\lambda f}{D} \quad (4.4-104)$$

Noting that d_r and f are related by Equation 4.4-39, that is,

$$d_r = 2 \times 10^{-4} f \quad (4.4-105)$$

we must, in solving Equation 4.4-105 for d_r , make sure Equation 4.4-104 is satisfied. If Equation 4.4-104 cannot be satisfied, it would be necessary to interpose a collimating lens between the orifice and the interferometer.

4.4.4.9 Dynamic Range

In order to realize the signal-to-noise ratio $(S/N)_S$ of the recovered spectrum, the recording system must have a dynamic range sufficiently large in order to contain the wide amplitude variations of the interferogram. The dynamic range is defined as the ratio,

$$N = \frac{V(o)}{V_N} \quad (4.4-106)$$

where $V(o)$ is the amplitude of the interferogram when all phase paths are equal, and this corresponds to the maximum level on the interferogram. V_N is given by Equation 4.4-69 and $V(o)$ is given by

$$V(o) = R \int_{\nu_a}^{\nu_b} C(\nu) d\nu \quad (4.4-107)$$

Substituting from Equation 4.4-51 for $C(\nu)$,

$$V(o) = \eta \left(\frac{\pi}{4} \frac{dr}{\lambda} \frac{D}{f} \right)^2 R \int_{\nu_a}^{\nu_b} E(\nu) d\nu \quad (4.4-108)$$

Since in absence of absorption we have the maximum value of $V(o)$, we shall solve Equation 4.4-108 for this case. Thus, replacing $E(\nu)$ with $2KCT$, we obtain

$$V(o) = \eta \left(\frac{\pi}{4} \frac{dr}{\lambda} \frac{D}{f} \right)^2 R 2KCT (\nu_b - \nu_a) \quad (4.4-109)$$

Substituting Equations 4.4-109 and 4.4-69 into Equation 4.4-106, we obtain

$$N = \frac{\eta \left(\frac{\pi}{4} \frac{dr}{\lambda} \frac{D}{f} \right)^2 2KCT (\nu_b - \nu_a)}{NEP} \quad (4.4-110)$$

The dynamic range can be expressed simply in terms of $(S/N)_S$ in absence of absorption by solving for $C(\nu_o)$ in Equation 4.4-82. Substituting this value into Equation 4.4-110 gives

$$N = \left(\frac{S}{N} \right)_S \frac{4}{\sqrt{2}} \sqrt{\frac{(\nu_b - \nu_a)}{\Delta\nu_I}} \quad (4.4-111)$$

Thus, for a $(S/N)_S = 10^2$, $(\nu_b - \nu_a) \cong 5 \times 10^3 \text{ cm}^{-1}$, $\Delta\nu_i \cong 20 \text{ cm}^{-1}$,

$$N \approx 5 \times 10^3 \quad (4.4-112)$$

4.4.4.10 Determination of Signal-to-Noise Ratio

In order to have a signal-to-noise ratio (in the reduced spectrum) that is sufficiently high (greater than 100), the collecting mirror area must have a sufficiently large area. According to Equation 4.4-97 the minimum detectable absorption is proportional to the inverse of the signal-to-noise ratio $(S/N)_S$ in the reduced spectrum. Assuming that an α_{\min} of 10^{-2} is desired, a collecting mirror diameter D , which will result in a $(S/N)_S = 10^2$, must be computed.

From Equation 4.4-81 we have for $(S/N)_S$,

$$\left(\frac{S}{N}\right)_S = \frac{\sqrt{2}}{4} \frac{C(\nu) \Delta\nu D^* \sqrt{T_m} \eta_i}{A^{1/2}} \quad (4.4-113)$$

where

$$C(\nu) = \eta E(\nu) \left(\frac{\pi}{4} \frac{d_r}{\lambda} \frac{D}{f} \right)^2 \quad (4.4-114)$$

$\Delta\nu$ is the spectral width of an absorption line.

In absence of absorption $E(\nu)$ is given by Equation 4.4-42,

$$E(\nu)_0 = \frac{dP}{d\nu} = 2KCT$$

Thus, in the absence of absorption,

$$\left(\frac{S}{N}\right)_S = \frac{\sqrt{2}}{4} \eta_o \frac{2KCT}{A^{1/2}} \Delta\nu \left(\frac{\pi}{4} \frac{d_r}{\lambda} \frac{D}{f} \right)^2 D^* \sqrt{T_m} \quad (4.4-115)$$

where $\eta_o = \eta_i$ η is the overall efficiency.

For an assumed Sun temperature of $T = 6 \times 10^3$ °K,

$$2KCT = 6.6 \times 10^{-9} \text{ watts-cm} \quad (4.4-116)$$

Considering a thermistor bolometer of area $A = (2.5 \times 10^{-2})^2 \text{ cm}^2$ and D^* given by (Ref. 66),

$$D^* = 8 \times 10^8 \text{ cm(sec)}^{1/2}/\text{watt} \quad (4.4-117)$$

Substituting Equations 4.4-116 and 4.4-117 into Equation 4.4-113 we obtain for $T_m = 1 \text{ sec.}$,

$$\left(\frac{S}{N}\right)_S = 13.2 \sqrt{2} \eta_o \left(\frac{\pi}{4} \frac{d_r}{\lambda} \frac{D}{f} \right)^2 \Delta\nu \quad (4.4-118)$$

Substituting Equation 4.4-39 into 4.4-118 and considering the spectral line width $\Delta\nu$ to be equal to $\Delta\nu_i = 20 \text{ cm}^{-1}$, Equation 4.4-118 becomes

$$\left(\frac{S}{N}\right)_S = 1.6 (\pi/2)^2 \times 10^{-5} (D/\lambda)^2 \eta_o \quad (4.4-119)$$

Solving for (D/λ) ,

$$(D/\lambda) = \frac{10^3}{4 \pi} \frac{1}{\eta_o} \left(\frac{S}{N}\right)_S^{1/2} \quad (4.4-120)$$

For an assumed value of $(S/N)_S = 10^2$ and $\eta_o = 10^{-1}$ at $\lambda = 2 \times 10^{-3} \text{ cm}$,

$$D = 16 \text{ cm} \quad (4.4-121)$$

4.4.4.11 Recapitulation of Design Parameters

Below is a recapitulation of the design parameters of the IR spectrometer necessary to achieve a $(S/N)_S \approx 10^2$.

- a. Mirror diameter (Equation 4.4-121)

$$D = 16 \text{ cm}, \text{ Area} = 5 \times 10^2 \text{ cm}^2$$

- b. Mirror focal length (Equation 4.4-102)

$$f = 10 \times D = 160 \text{ cm}$$

- c. Specific detectivity (bolometer) D^*

$$D^* = 8 \times 10^8 \frac{\text{cm}(\text{sec})^{1/2}}{\text{watt}}$$

- d. Detector area A_d

$$A_d = (2.5 \times 10^{-2})^2 \text{ cm}^2$$

- e. Orifice diameter d_r (Equation 4.4-39)

$$d_r = 2 \times 10^{-4} \times f = 3.2 \times 10^{-2} \text{ cm}$$

- f. Overall efficiency $\eta_o = 10^{-1}$
- g. Spectrometer resolution $\Delta\nu_i = 20 \text{ cm}^{-1}$
- h. Scan time $T_m = 1 \text{ sec.}$

4.4.5 ULTRAVIOLET SPECTROSCOPY

4.4.5.1 Introduction

The main purpose of the ultraviolet experiment on Mars is to identify and characterize constituents not possessing lines in the infrared region (e.g., O_2 , N_2 , A and Ne). Absorption of ultraviolet solar radiation by the terrestrial atmosphere has been observed with rockets and satellites (Ref. 68,69,70,71). However, in many of these measurements the attenuation of a "known" Earth atmosphere is studied in order to deduce an unknown solar radiation. In the present proposed experiment, on the contrary, the characteristics of an unknown Martian atmosphere are deduced from the absorption of the solar system, which is measured just before the occultation process.

A difficulty of the method arises from the fact that the Sun's radiation at wavelengths shorter than 1500 \AA no longer has the characteristics of a black body (as it does in the infrared and visible region), but rather involves a spectrum of sharp lines. For this reason, the envisaged apparatus consists of an array of monochromators (having about 2 \AA band) to receive selected spots of the solar spectrum.

Another difficulty derives from the incomplete knowledge of the ultraviolet absorption spectrum of most gases. While new experimental data are continuously being acquired, no band of the ultraviolet atmospheric absorption range can be predicted with satisfactory accuracy.

Finally, ultraviolet absorption takes place in regions where the atmospheric constituents are not mixed uniformly, but, on the contrary, are separated by photochemistry and gravitational diffusive equilibrium. Hence, height profiles are, in general, difficult to deduce.

4.4.5.2 Ultraviolet Absorption Spectra

Observations of the terrestrial atmosphere during occultations of the OSO III satellite have shown that solar radiation at 304 Å undergoes extinction for tangential altitudes of about 150 km (Ref. 8). At this altitude, the average number density in the Earth's atmosphere is of the order of 10^{10} cm^{-3} . In view of the fact that in this region of wavelength all gases display a continuum of absorption with comparable cross-sections, we may expect that extinction will occur in the Martian atmosphere for a tangential altitude having a similar number density, i.e., about 90 km.

The absolute intensity of the Sun's radiation for the region of ultraviolet of interest is presented in Table 4-7 (Ref. 72). The listed intensities of the various lines are relative to the radiation of the whole solar disk, and represent time averaged values. Their time variations, however, are small and may generally be considered constant within .5 db assuming a time interval of several minutes.

An illustration of the ultraviolet absorption cross-sections of the most probable constituents in the upper atmosphere of Mars is presented in Figures 4-41 through 4-46 (Ref. 73, 75). As it has been already pointed out, the details of these cross-sections are continuously revised by new experimental data. However, inspection of the figures justifies the choice of the band 1300-800 Å for the exploration of the Martian atmosphere, since this band is conveniently located between the absorption continuum of the considered gases and the intense black body radiation of the Sun in the near ultraviolet.

At the lower Martian altitudes (below 90 km), it is expected that CO₂ will cause the main absorption. Its spectrum, however, shows several "windows" in the 1300-800 Å band. Above the tangential height of 110 km, CO may become a prevailing constituent, together with oxygen (see Section 4.4.1). In all cases, since H₂O and O₃ are most probably confined near the planet's surface, oxygen and nitrogen, if existing, should become distinguishable in the upper atmosphere of Mars, through their characteristic absorption spectra.

Noble gases, like Argon and Neon, which might exist in the Martian atmosphere, offer no absorption lines in the 1500-800 Å

TABLE 4-7
 INTENSITIES IN SOLAR XUV-SPECTRUM AT A DISTANCE OF 1 A.U.
 (July, 1963)

<i>Wavelength or Range in Å</i>	<i>Identification</i>	$\Phi_0 / \frac{10^8 \text{ ph}}{\text{cm}^2 \text{ sec}}$	$I_0 / \frac{\text{erg}}{\text{cm}^2 \text{ sec}}$
1775-1325		2700	32
1325-1275		11.8	0.18
1275-1220		26	0.41
1215.7	H Ly- α	270	4.4
1206.5	Si III	4.3	0.071
1220-1200	excl. H Ly- α , Si III	7.4	0.121
1200-1180		5.5	0.092
1175.7	C III	2.5	0.042
1180-1130	excluding C III	5.8	0.100
1130-1090		4.4	0.079
1085.7	N II	0.48	0.009
1090-1040	excluding N II	4.2	0.078
1037.6	O VI	1.33	0.025
1031.9	O VI	1.89	0.036
1040-1027	excluding O VI	0.69	0.013
1325-1027	total	350	5.7
1025.7	H Ly- β	2.3	0.045
991.5	N III	0.33	0.007
1027- 990	excl. H Ly- β , N III	2.4	0.049
977.0	C III	4.0	0.081
972.5	H Ly- γ	0.55	0.011
990- 950	excl. C III, H Ly- γ	0.97	0.021
949.7	H Ly- δ	0.25	0.005
937.8	H Ly- ϵ	0.17	0.004
950- 920	excl. H Ly- δ , ϵ	1.07	0.022
920- 911		1.25	0.028
1027- 911	total	13.4	0.027
911-890	H Ly-continuum	4.0	0.089
890-860	H Ly-continuum	4.2	0.096
860-840	H Ly-continuum	2.0	0.047
832-835	O II, III	0.54	0.013
840-810	excluding O II, III	2.0	0.048
810-796		0.7	0.017
911-796	total	13.4	0.31

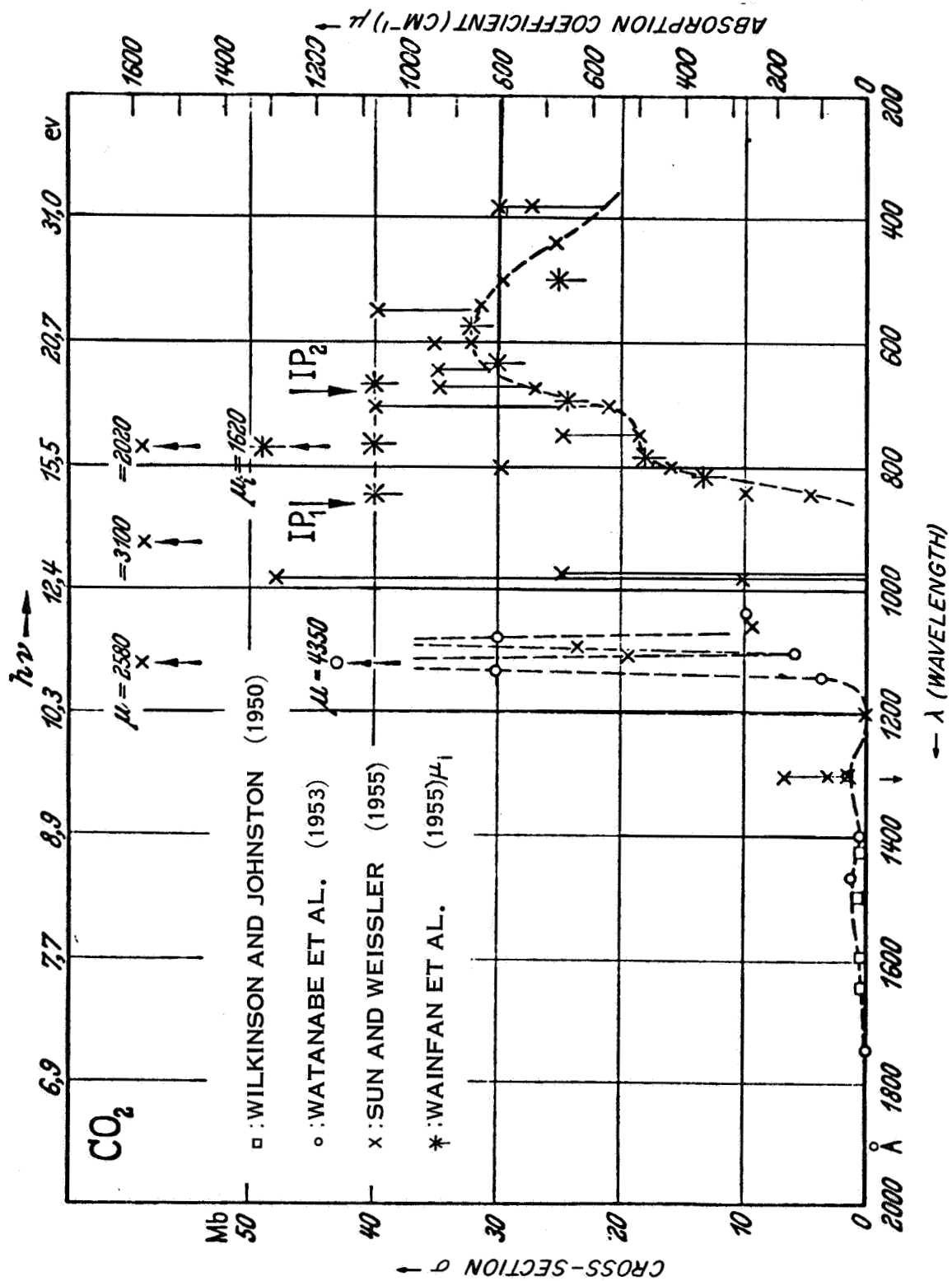


Figure 4-41 Absorption Coefficients in CO₂

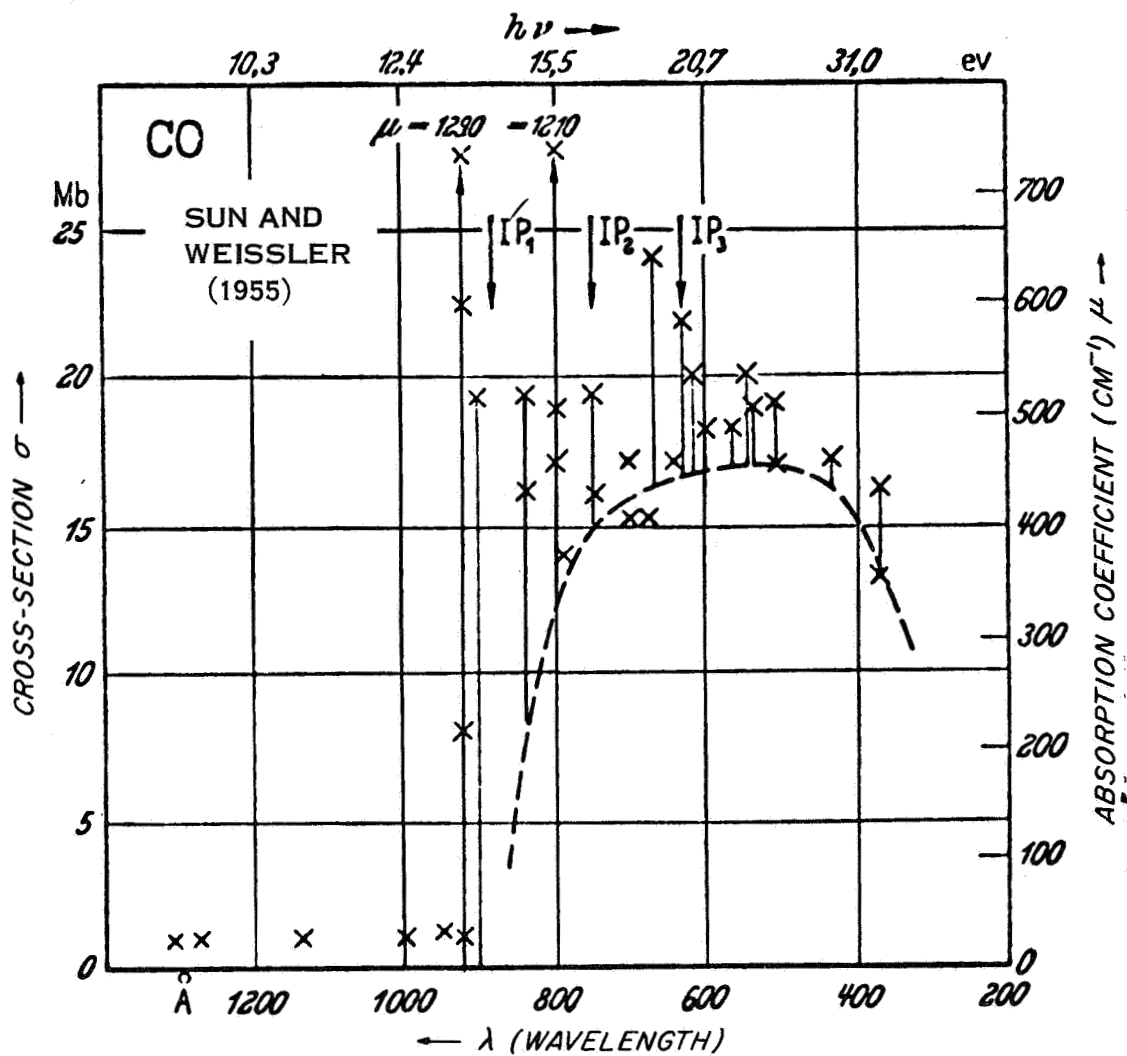


Figure 4-42 Absorption Coefficients in CO

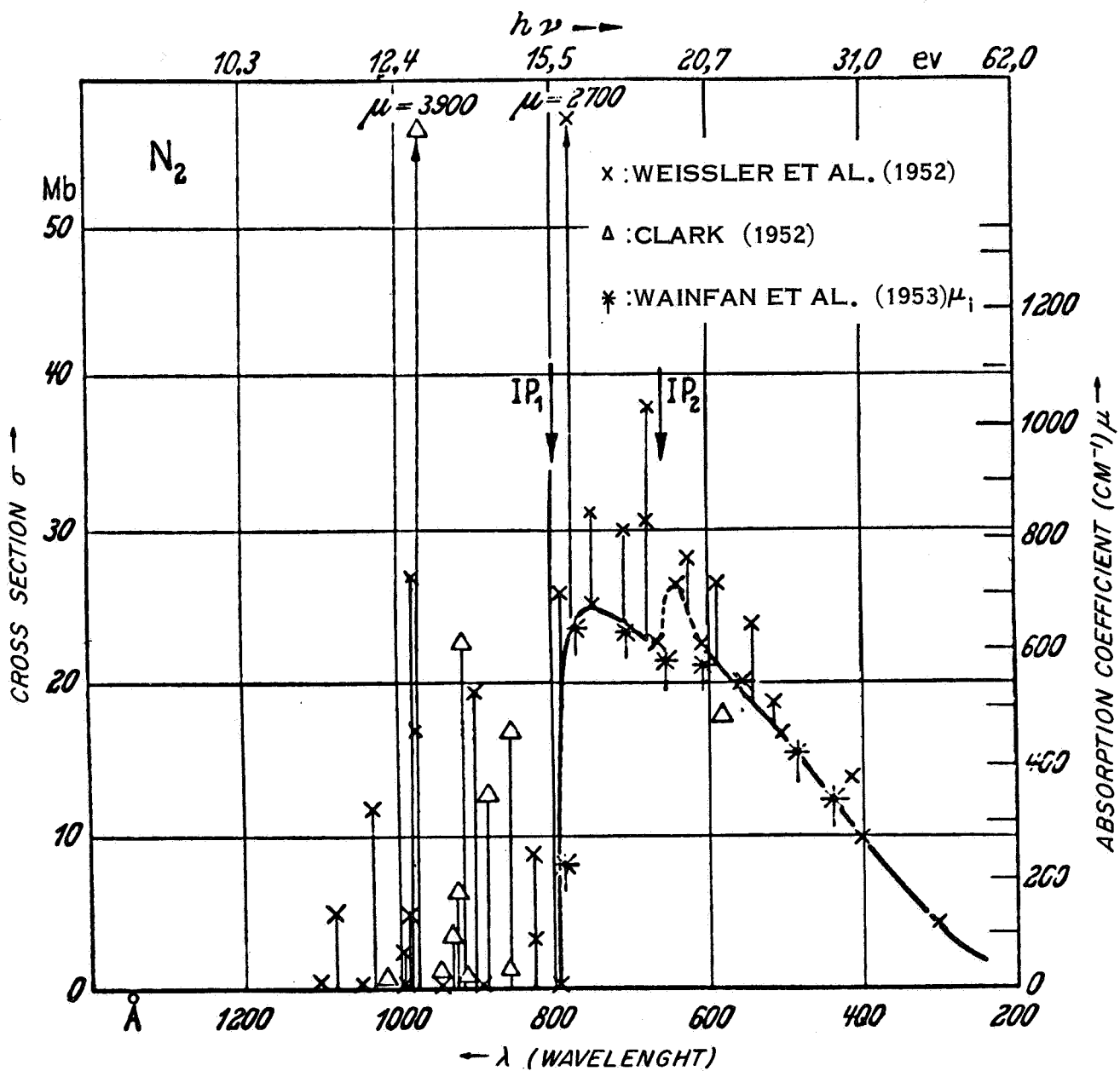


Figure 4-43 Absorption Coefficients in Nitrogen

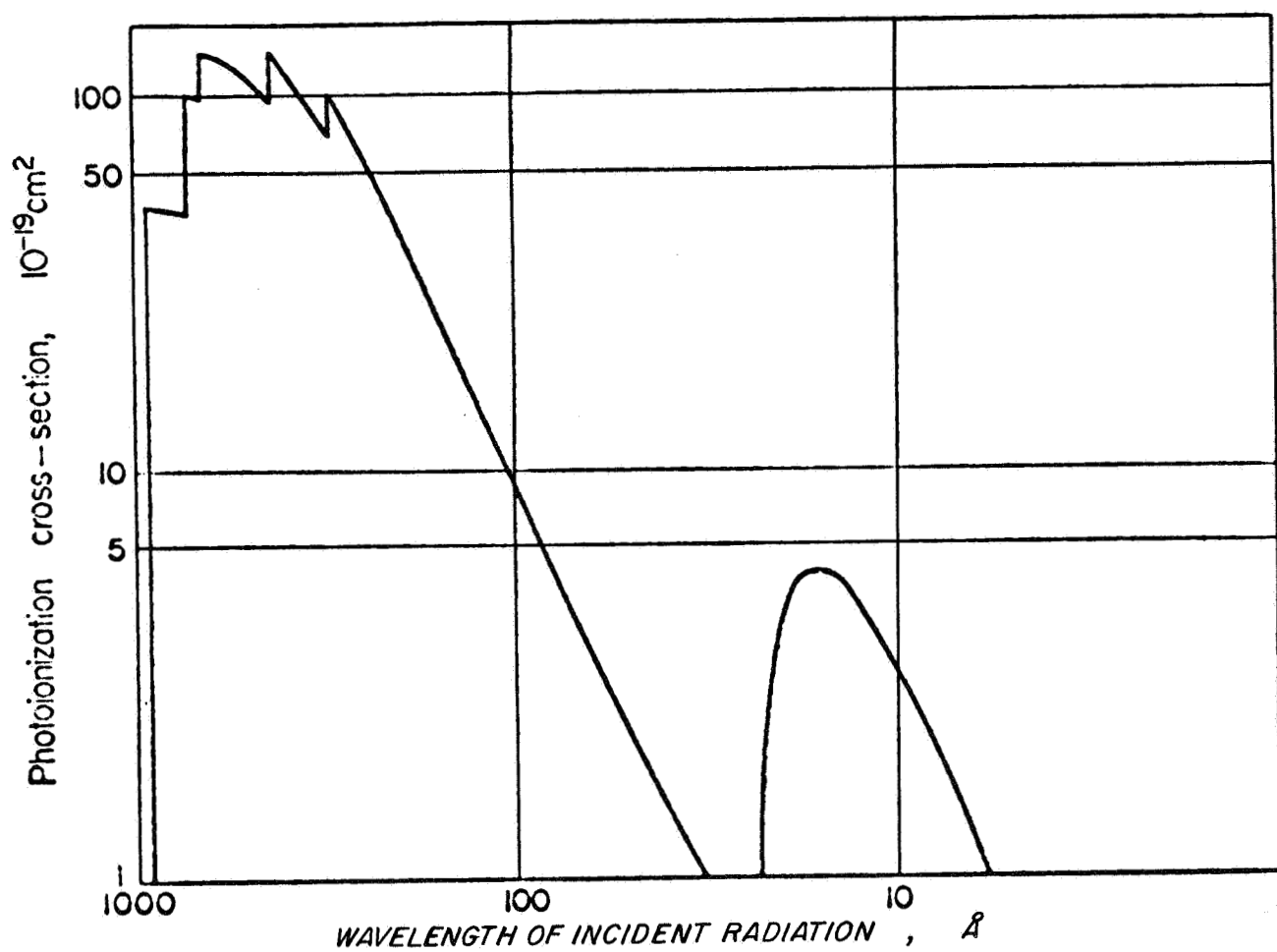


Figure 4-44 Photionization Cross-Section of Atomic Oxygen as a Function of the Wavelength of the Incident Radiation

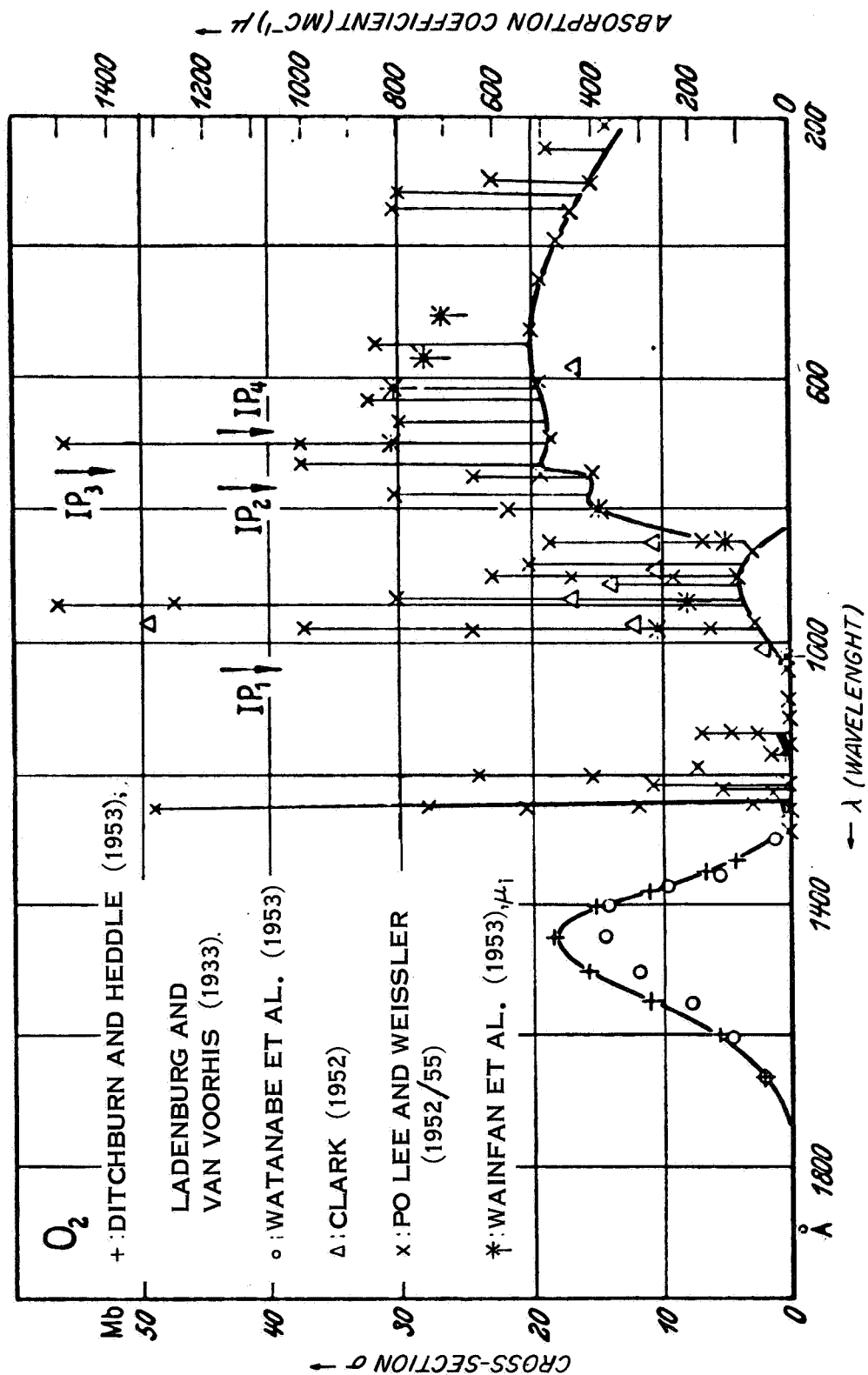


Figure 4-45 A Survey of Absorption Coefficients in Oxygen.
Note the strong resonance bands superimposed over regions of continuous absorption.

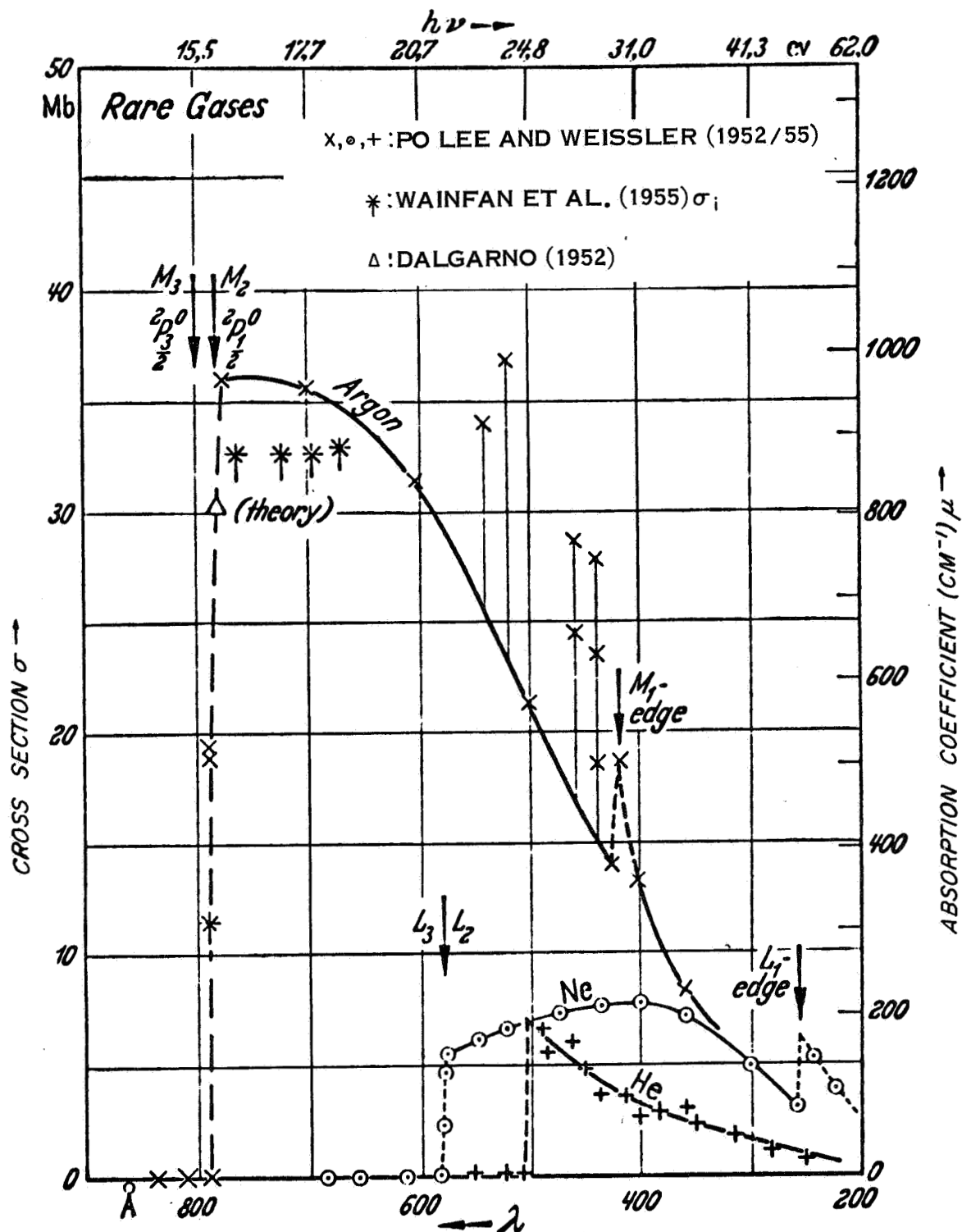


Figure 4-46 Photoionization Cross-Sections in Helium, Neon and Argon

band (see Figure 4-46). For this reason a special detection channel is provided, able to monitor the He II, Ly α (303.8 Å) line of the Sun, yielding 2.5×10^9 photon/cm²-sec at 1 a.u. Inspection of the Figures 4-41 through 4-46 shows that all constituents present comparable cross-sections at this frequency. Thus, deduction of the existence and percentage of noble gases may be obtained only after having acquired data of the other components by use of the lower frequency band.

4.4.5.3 Absorption Criteria Over an Inhomogeneous Path

The mean transmission over a spectral interval, $\Delta\nu$, for the i^{th} constituent may be expressed by

$$T_i = \frac{I_i(\Delta\nu)}{I_o(\Delta\nu)} = \frac{1}{\Delta\nu} \int_{\Delta\nu} \exp \left[- \sum_j \sigma_{ij} \int_0^L N_i d\ell \right] d\nu \quad (4.4-122)$$

where

σ_{ij} = the molecular cross-section of the i^{th} constituent corresponding to the j^{th} spectral line in the interval $\Delta\nu$ (may be assumed pressure and temperature independent)

N_i = molecular number density of the i^{th} constituent

L = the total absorptive path length.

For the case of many constituents, the total transmission in the spectral interval $\Delta\nu$ is given by their product, namely,

$$T_{\Delta\nu} = \prod_i T_i \quad (4.4-123)$$

In the proposed experiment, a number of ultraviolet channels exist (e.g., 11) and each channel monitors different groups of absorbing lines. Since there are more channels than the number of expected constituents, redundant information will be obtained and applied to the subsequent synthesis problem. For each channel, the received intensity $I_o(\Delta\nu)$ is recorded aboard the satellite at a time just before immersion of the ray path through the atmosphere of Mars. During the penetration process, the

output of each channel, $T\Delta\nu$, is simultaneously recorded every 1/2 second. The observed data will be synthesized making use of model matching techniques and the constituents, their densities, and their respective profiles will be determined.

4.4.5.4 Comments on Height Resolution in the UV Range

Although the proposed receiving aperture (collimator) observes the total solar disk, the corresponding height resolution is significantly more accurate than one might expect using simple ray analysis. This is due to the fact that the bundle of rays emerging from the upper limb of the Sun is absorbed less than those coming from the lower limb (since these rays pass through more dense atmospheric layers). The received effects of the upper and lower limbs cancel resulting in an apparent received intensity that essentially originates from the central region of the solar disk. This assumption may be shown valid for an isothermal atmosphere when the altitude is significantly larger than the scale height and the absorption is due to a single constituent. The situation may change slightly when more than one constituent is present, and the band considered involves many lines. However, attenuation versus altitude plots obtained by OSO III have offered for the Earth's atmosphere an altitude accuracy of ± 5 km, for altitudes around 200 km (Ref. 8).

4.4.5.5 Design Criteria for the Ultraviolet System

4.4.5.5.1 Introduction

Of the possible UV systems that have been flown on satellites or rockets (e.g., the Ebert spectrometer, collimating grating monochromators, concave grating spectrometers), the concave grating spectrometer is here proposed because the OSO III satellite experiment has demonstrated the advantages of monitoring the ultraviolet absorption in fixed bands during occultation (Ref. 8).

The use of a concave grating with a "grazing incidence" mounting has been flown aboard rockets (Ref. 70) and is suggested here for examining the spectrum in the band 300-1300 Å. The use of grazing incidence for these short wavelengths with reduced resolution can provide sufficient signal so that a number of spectral intervals within the band can be monitored continuously as the satellite-Sun line of sight passes through the Martian

atmosphere. In the following sections, we shall relate the physical parameters of the spectrometer with the spectrographic characteristics of the instrument.

4.4.5.5.2 Instrument Design

In Figure 4-47 the suggested UV spectrometer is presented. A concave grating of radius $R_g = 2$ meters is considered and a string of detectors, each with its own exit slit, are placed along the indicated Rowland circle. No moving slits are envisaged and the resulting spectral observation will be made over narrow wavelength intervals (e.g., $\Delta\lambda = 2 \text{ \AA}$) dispersed over the band 300-1300 \AA . The number of spectral intervals that can be observed is determined by the number of detectors that can be located along the Rowland circle. This, in turn, is a function of the dispersing power of the grating.

From the grating formula we obtain that

$$\sin \beta = \sin \alpha - \frac{m \lambda}{p} \quad (4.4-124)$$

where

m = order of interference

p = distance between rulings

α = angle of incidence (Figure 4-47)

β = angle of diffraction (Figure 4-47)

For $\lambda_{\max} = 1.3 \times 10^3 \text{ \AA}$, we have the minimum β and for $\lambda_{\min} = 8 \times 10^2 \text{ \AA}$ we have the maximum β denoted in Figure 4-47. We desire to allow $\Delta\beta = (\beta_{\max} - \beta_{\min})$ to be large so that many detectors can be placed in this interval. A plot of $\Delta\beta$ as a function of β_{\max} is shown in Figure 4-48 for the case $\alpha = 86^\circ$.

In order to keep the spectrometer pact (i.e., lateral width small) β_{\max} should be limited to angles near 60° . Assuming $\beta_{\max} = 65^\circ$, $\beta_{\min} \approx 59^\circ$, the lateral width is

$$W = R_r \sin (\alpha - \beta_{\min}) \approx 50 \text{ cm} \quad (4.4-125)$$

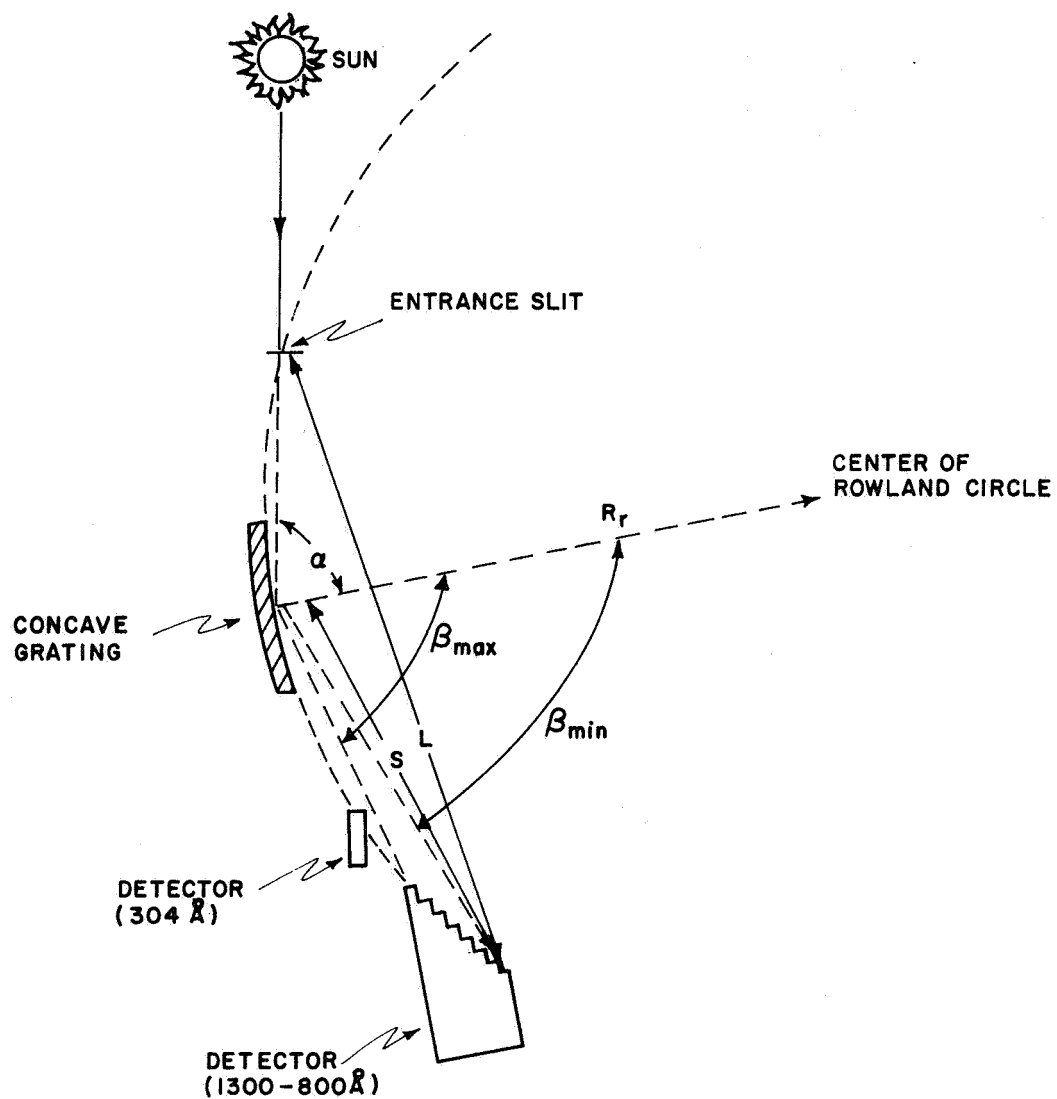


Figure 4-47 The Ultraviolet Spectrometer

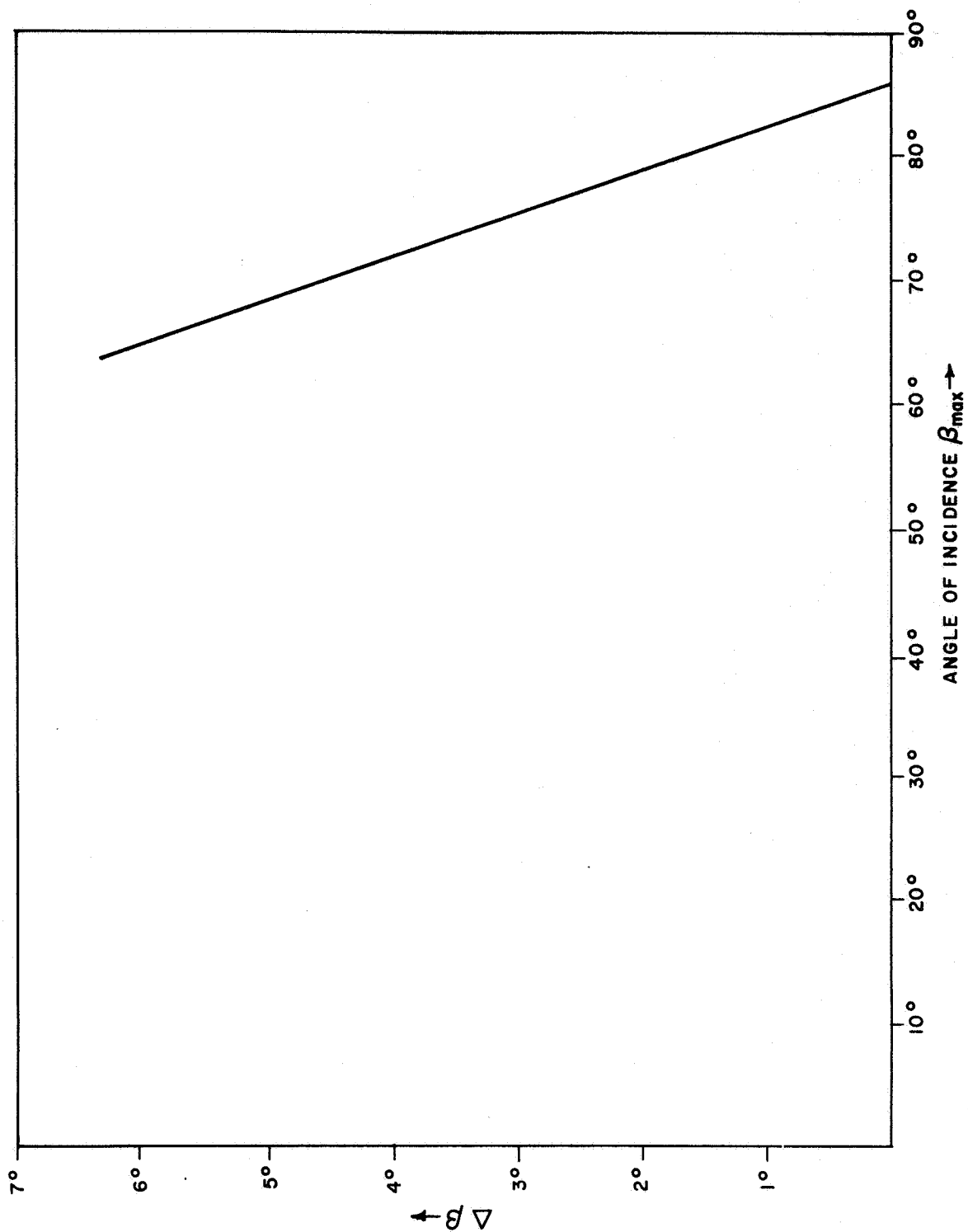


Figure 4-48 Angular Spread of Diffracted Rays in Interval
800 Å-1300 Å ($\alpha = 86^\circ$)

and the length L of the spectrometer is

$$L \approx 2R_r \sin (\alpha + \beta_{\min}) \approx 2 \text{ meters} \quad (4.4-126)$$

The angular width corresponding to a wavelength interval, $d\lambda$, is given by

$$dp = \frac{m d\lambda}{p \cos \beta} \quad (4.4-127)$$

The width of the exit slit for each detector is W_s , where

$$W_s = S d\beta \quad (4.4-128)$$

where S is the chord length depicted in Figure 4-47. Hence,

$$S = 2R_r \cos \beta \quad (4.4-129)$$

where

$$R_r = \frac{R_g}{2} = 10^2 \text{ cm} \quad (4.4-130)$$

where R_g = radius of curvature of grating.

Substituting the above into Equation 4.4-128,

$$W_s = 2R_r \frac{m}{p} d\lambda \quad (4.4-131)$$

and the exit slit width normal to S is independent of β .

The value of m/p can be computed from Equation 4.4-124. Substituting $\beta_{\max} = 65^\circ$ into Equation 4.4-124,

$$\frac{m}{p} = \frac{(\sin \alpha - \sin \beta_{\max})}{\lambda_{\min}} = 1.14 \times 10^4 \quad (4.4-132)$$

Substituting Equation 4.4-132 into 4.4-131 gives

$$W_s = 2.28 \times 10^6 d\lambda \quad (d\lambda \text{ in cm}) \quad (4.4-133)$$

The number of detectors that can be placed along the interval is determined by the width of the detectors, W_d . This width, W_d , will then determine the spacing, $\Delta\lambda$, of the resolution widths $d\lambda$ in the band, where

$$\Delta\lambda = \frac{p}{m} \frac{W_d}{2R_r} \quad (4.4-134)$$

For the assumed values of p/m and R_r , we have

$$\Delta\lambda = 44 W_d \text{ \AA} \quad (4.4-135)$$

where W_d is the detector width in cm.

4.4.5.5.3 Detector Considerations

The detector under consideration is a windowless magnetic photomultiplier developed by Wiley and Goodrich of the Bendix Corporation and adopted to UV spectroscopy by Hinteregger et al. (Ref. 74). Because of the low sensitivity to long wavelength radiation, it is not necessary to be concerned with stray light in the near ultraviolet. The multipliers have quantum yields as high as 10^{-1} at $\lambda = 800 \text{ \AA}$ and at least 10^{-2} at $\lambda = 1200 \text{ \AA}$. A background count rate of less than 1 false count/sec can be achieved (Ref. 74). Multipliers with width W_d of the order of 1 cm are presently available. Thus if $W_d = 1 \text{ cm}$,

$$\Delta\lambda = 44 \text{ \AA} \quad (4.4-136)$$

Hence, in the spectral band 1300-800 \AA at least 10 channels can be monitored.

The 303.8 \AA line may be located (for the assumed $m/p = 1.14 \times 10^4$) at a diffraction angle $\beta \approx 74^\circ$ along the Rowland circle.

It may be noted that using the data of Hall et al. (Ref. 70), a signal-to-noise ratio of 10^2 may be deduced at the detector output for an incident photon rate in the Martian atmosphere of $10^8/\text{sec-cm}^2$ (Ref. 72).

4.4.6 PHYSICAL PARAMETERS OF THE IR AND UV INSTRUMENTATION

4.4.6.1 IR Equipment

The physical parameters of the IR interferometer system are:

Volume	15 cm x 15 cm x 45 cm
Weight	9 kg
Collecting	
Mirror Area	500 cm^2
Power	15 W

4.4.6.2 UV Equipment

The physical parameters of the UV spectrometer system are:

Volume	50 cm x 20 cm x 10 cm
Weight	4.5 kg
Power	15 W

4.4.6.3 Interface and Pointing Requirements

For the IR experiment, the hole should be pointing at the center of the Sun with a pointing accuracy of ± 1 minute. This will locate the hole over a region within five solar degrees from the center part of the Sun.

In the UV experiment, the slit should pass through the central part of the Sun with an accuracy of ± 1 minute.

4.4.6.4 Telemetry Requirements

The rate of storage for both the IR and UV systems are respectively 2×10^4 and 5×10^3 bits/sec. The equipment should begin to store when the minimum altitude of the ray path is 300 km from Mars and should turn off after occultation when the minimum ray path altitude reaches that same distance. A maximum total storage capacity of 3.5 megabits per occultation is therefore required, inclusive of both the IR and UV experiments.

4.5 BANDPASS RADIOMETRIC EXPERIMENTS

4.5.1 OUTLINE

The purpose of this experiment is twofold:

a. To measure the temperature of the Martian surface by a measurement of the spectral radiance of upwelling radiation with 8 to 12 μ window of the assumed Martian atmosphere.

b. To measure the vertical temperature profile by similar radiance measurements on the long wavelength side of the 15 μ CO₂ emission band.

4.5.1.1 Surface Radiometry

4.5.1.1.1 General

Temperature-sensitive remote sensors generally operate at either microwave or infrared wavelengths, and consideration to both regions of the electromagnetic spectrum has been given for possible use on the Martian mission. However, weight, power, spatial resolution, and orbital constraints make a microwave experiment infeasible at this time and attention has been directed toward defining an infrared experiment to provide information on the surface temperature of Mars.

It is useful to review in more detail the reasons behind this choice. The microwave emission from a solid surface is given by the product of the surface emissivity and the surface temperature; therefore a single observation will not determine either quantity. However, as shown in Figure 4-49, the emissivity is dependent on the polarization of the emitted radiation and the angle of incidence, thus measurements made at different polarizations or angles of incidence enable the separation of emissivity and surface temperature. For example, a measurement made at normal incidence (incidence angle zero degrees) will give, after correcting for antenna pattern effects,

$$T_b(0) = e_n T_s,$$

where T_s is the surface temperature, e_n is the emissivity for normal incidence, and T_b is the microwave brightness temperature. A second measurement, made at some incidence angle i , will give

$$T_b(i) = e(i) T_s$$

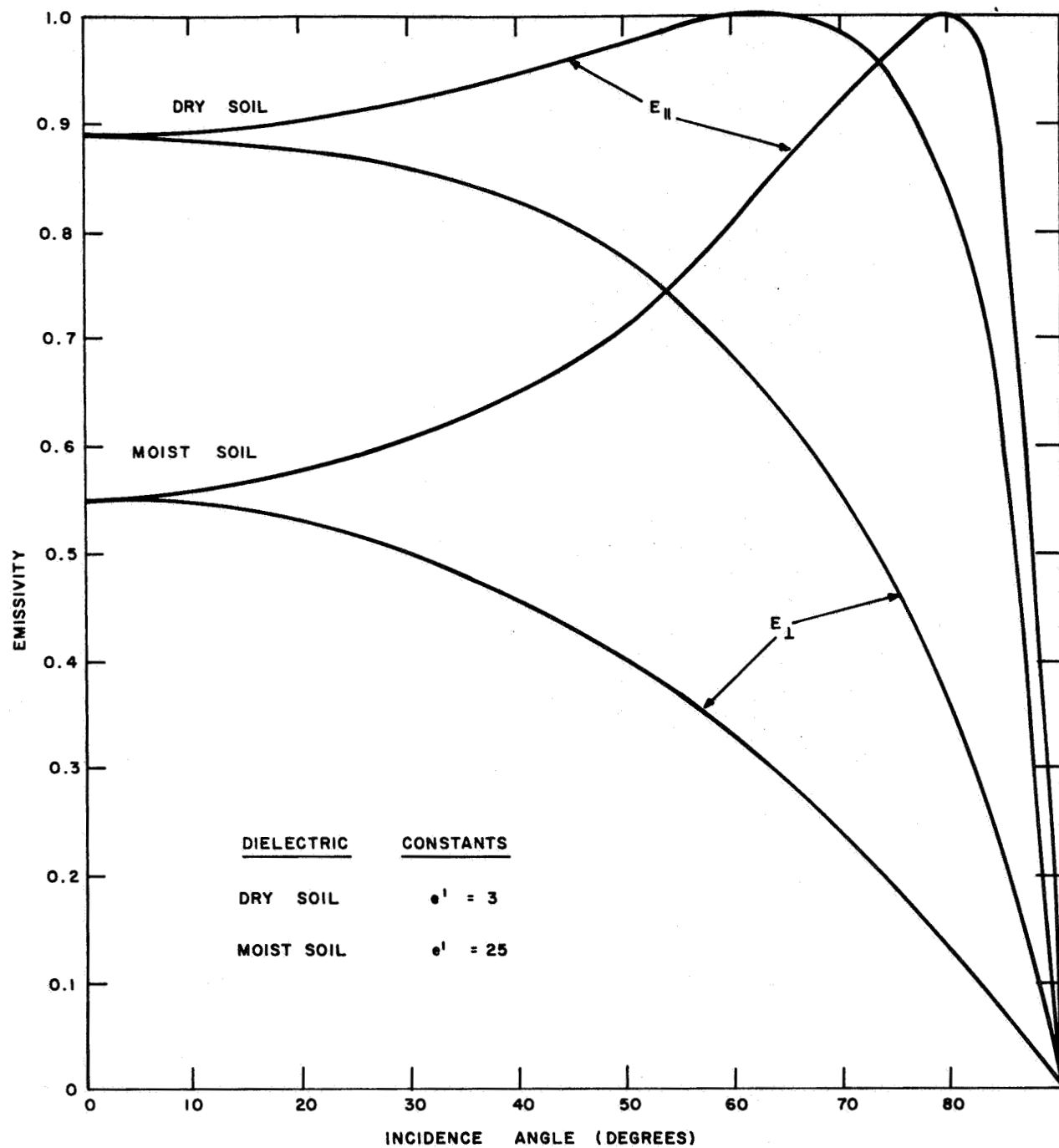


Figure 4-49 Emissivity vs. Angle of Incidence

where $e(i)$ is the emissivity for incidence angle i and for the particular polarization used for the measurement. The ratio of $T_b(0)/T_b(i)$ is independent of the surface temperature and will serve to determine the real part of the dielectric constant of the surface material. With the dielectric constant determined in this manner, the normal-incidence emissivity can be computed and the surface temperature determined from $T_b(0)$.

The method outlined above assumes that the Martian surface can be regarded as a smooth, dielectric sphere. This assumption will undoubtedly introduce errors into the results, but ground-based radar observations of Mars indicate that the planet may be generally regarded as smooth for wavelengths of 10 cm and longer. The effects of surface roughness can only be estimated by assuming a statistical model of roughness.

Note from Figure 4-49 that for polarization parallel to the plane of incidence, an angle of incidence can be found for which the emissivity is unity. This is the well-known Brewster Angle. If observations could be made at this angle, one measurement would serve to determine the surface temperature. However, the Brewster Angle cannot be specified in advance because it is a function of the dielectric constant. This is also shown in Figure 4-49 where curves are presented for both dry and wet soil.

Although the microwave observations discussed above would be of value for a spacecraft orbiting a planet at a fixed distance from the center of the planet, the experiment becomes quite unattractive for the case where the planet-vehicle distance changes by an order of magnitude, or more, during one orbit. This arises because of the necessity to know, and maintain, a given angle of incidence on the planetary surface. This can be seen by referring to the geometry of Figure 4-50. The antenna pointing angle ϕ is related to the planetary radius r_0 and the planet-vehicle distance r by the equation

$$\sin i = (r/r_0) \sin \phi$$

where i is the angle of incidence. If r is a function of time, and is to be kept constant, then ϕ must be programmed to change as the vehicle orbits the planet. Furthermore, as (r/r_0) becomes large, the finite antenna resolution of the microwave antenna will result in a large "smearing" of incident angles, and a resultant loss of accuracy in the observations. It can be easily shown

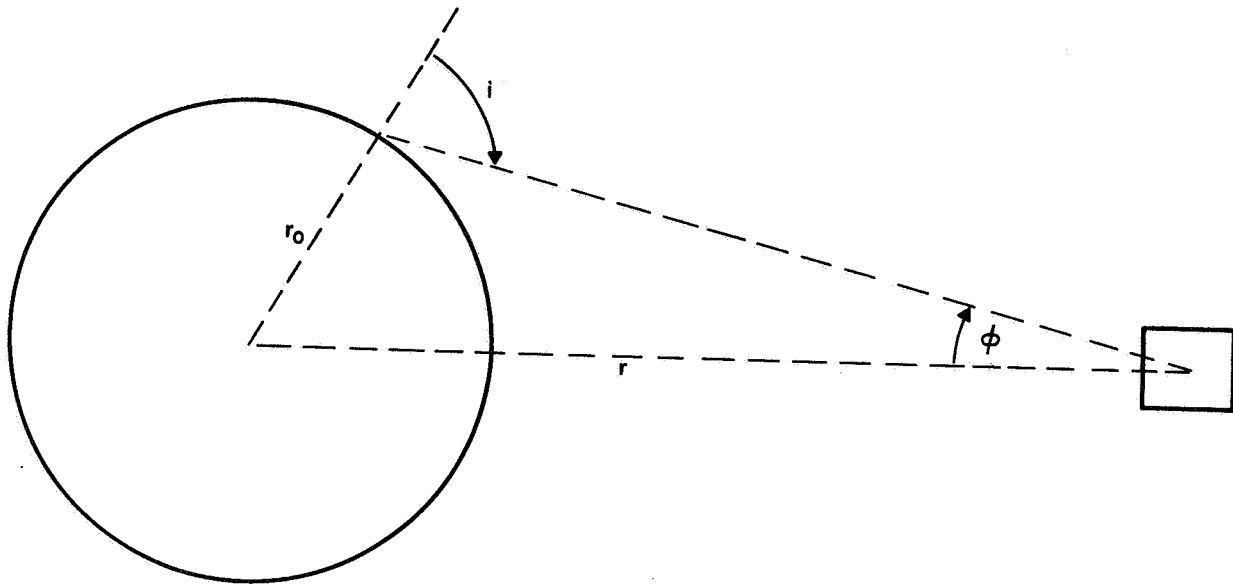


Figure 4-50 Geometry of the Radiometric Measurements

that if θ_B is the antenna beamwidth, then the range of incident angles included in the antenna beam is given by

$$\Delta i = (r/r_0) (\cos \phi / \cos i) \theta_B.$$

When r/r_0 is large, this smearing can be so large as to destroy the usefulness of the experiment. If one envisions an operating wavelength of 10 cm and an antenna diameter of 2 m, then a beamwidth of approximately 4 degrees results. However, when $r \approx 7 r_0$, which represents the extreme of the Voyager orbit, then one beamwidth will integrate, or include, a range of incident angles of approximately 50 degrees. Clearly it is impossible to speak of a unique angle of incidence and the experiment becomes meaningless. It is for this reason that the microwave experiment has not been considered in further detail as a possible Voyager experiment. These considerations would apply in general for the experimental set-up outlined here as long as highly elliptical orbits are proposed.

Also for the infrared radiation the emission from a thermal source depends on the emissivity of the surface and the temperature of the emitter. As this experiment will measure only the total emitted radiation, absolute temperatures will not be obtained. Surface temperatures may be estimated by making reasonable assumptions about the surface emissivity. Because of the nonlinearities of the Planck radiation law, surface emissivities estimated to an accuracy of five percent will enable a temperature determination accurate to one or two percent.

Ground-based infrared observations of Mars and the results of the Mariner 4 Experiments indicate that the Martian atmosphere should be highly transparent to infrared wavelengths as long as the vibration-rotation bands of CO₂ are avoided. Therefore, the sensor will respond to surface emission, except when the sensor views Martian clouds.

4.5.1.1.2 Experiment Definition

The experiment has been defined on the assumptions that the spacecraft-planet distance varies from 1000 to 20,000 km, the velocity of the subvoyager point on the surface is 4 km/sec at the distance of closest approach, and that a television camera will be trained on the planet throughout the useful life of the infrared radiometer experiment.

The experiment consists of an infrared radiometer operating in the wavelength band 8 to 10.5 microns, bore-sighted along the axis of the television camera, weighing approximately 0.5 pounds, and consuming 2.5 watts. Spatial resolution on the surface of the planet will be approximately 2 x 3 km at the distance of closest approach, assuming an integration time of 0.6 seconds. Temperature sensitivity should be approximately 2 °K. Telemetry requirements are one 8-bit word every 0.6 seconds. Provisions must be made for calibration of the radiometer. This can be accomplished conveniently by (1) viewing a small object of known temperature and emissivity, and (2) viewing cold space. Both can be done by utilizing a small, movable mirror that periodically directs the beam to view the two calibrators.

The experiment should operate continuously. In the event that the spacecraft television is not operated continuously, then consideration should be given to decoupling the two instruments and having the infrared radiometer view the subvoyager point at

all times. However, the correlation between the output of the television camera and the infrared radiometer will provide valuable information on the thermal properties of the surface. Also, the TV camera will serve to define cloud conditions in the field of view of the infrared radiometer. Correlation of the temperatures of the clouds with a temperature profile, independently determined, will provide an estimate of the height of the clouds.

4.5.1.2 Atmospheric Radiometry

A spectroscopic technique for the remote sensing of atmospheric temperature and its variations with altitude has been suggested by Kaplan, (Ref. 76) developed in a simplified form by Wark (Ref. 77) and has been used in experiments on the earth's atmosphere.

The basis of the technique is that, when examined from above a planetary atmosphere, the upwelling radiation in an optically dense spectral region originates at an altitude determined by its spectral position. The greater the optical density at the spectral point, the more likely that the corresponding radiation originates high in the atmosphere. Given a model of the atmosphere, a weighting function can be derived for each of a set of spectral regions in a molecular emission-absorption band to indicate the relative contribution to the total flux, of radiation coming from points at various altitudes.

By mathematical inversion, the atmospheric temperature profile can be recovered to a degree depending on the number and accuracy of the spectral soundings made. The ambiguity inherent in this inversion is removed by foreknowledge of the expected temperature profile. In our case, it can be measured independently during occultation by use of absorption spectroscopy. Applying this technique to the emission in the 15μ band of CO_2 for the Martian atmosphere, we would choose, by the use of fixed interference filters, six to eight spectral channels on the short wavelength side of the band. A suitable choice would be at 780, 770, 760, 740, 730, 700 and 680 cm^{-1} each with a 5 cm^{-1} spectral bandpass. This part of the band should be free of the interference from other atmospheric constituents unless NO_2 is present in much greater concentration than expected.

An experiment of this nature has been proposed by Hanel and Chaney (Ref. 78) using an interferometric spectrometer of the type considered for our own absorption spectral studies. We believe, however, that given the presence of a downward looking

radiometer, it becomes a simple matter to introduce additional filters and detectors to provide the atmospheric temperature scanning capability (Figure 4-51). The same objective and chopping optics would be used for both types of radiometry to give a capability of obtaining simultaneously a high resolution net of the temperature of the planet's surface and of the atmosphere directly above it. Calibration of the thermistor detectors and optics can be done in the same way as for the 8 - 10 μ radiometer. The final design would have to depend on the weight and power available, but if we assume that each channel has its own detector and amplifier, the additional weight would be approximately 0.25 Kg and the additional power approximately 7.5 watts.

The projected data rate is six to eight 10-bit words every second when in use.

The simplicity of this technique is purchased at the price of insensitivity to small-scale variations of the temperature profile as well as a possible major error if the prior model profile is incorrect in form. The measurement of transmission during occultation will remove this possibility. These measurements will allow the diurnal variation of the atmospheric temperature profile to be measured and correlated with the UV and IR leaking of the atmosphere.

4.5.2 EQUIPMENT DESCRIPTION - SUMMARY

Total Weight	0.5 Kg
Size	15 cm x 15 cm x 30 cm
Power Consumption	10 watts

4.5.3 POINTING REQUIREMENT - SUMMARY

Either directed to subvoyager point at all times or boresighted with television system.

4.5.4 TELEMETRY REQUIREMENTS

Data acquisition rate maximum of 9, 10 bit-words per second.

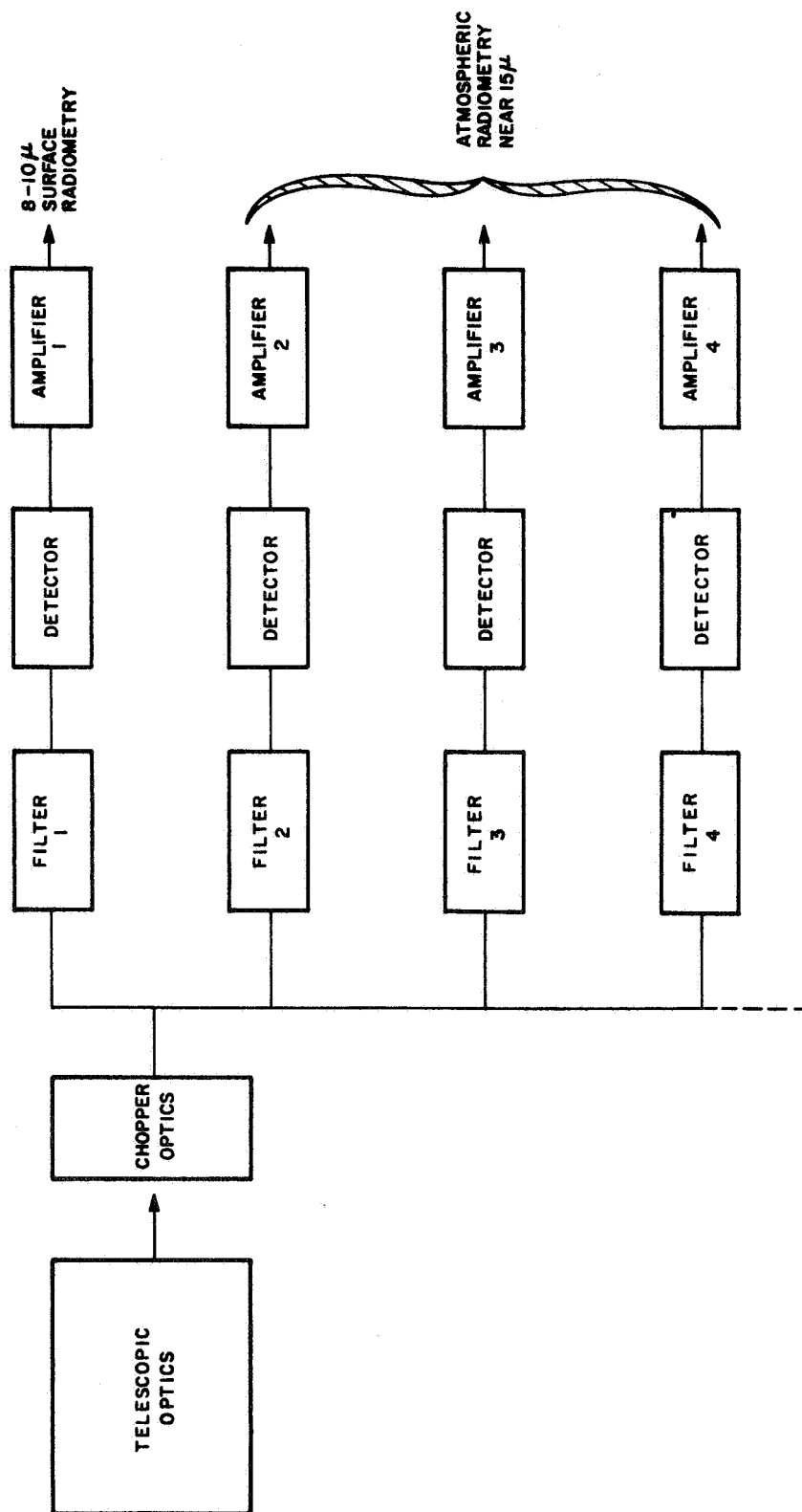


Figure 4-51 Optical Schematic for Bandpass Radiometry Experiment

4.5.5 COMMAND FUNCTIONS

- o On/off control of entire instrument
- o Possible switch to TV alignment or to subsatellite point
- o Switching between calibrate positions and viewing positions

4.6 SUMMARY OF WEIGHT, VOLUME AND PRIMARY POWER REQUIREMENTS FOR OVERALL EXPERIMENT SYSTEM

Table 4-8 summarizes the weight, volume, and primary power requirements for the overall system, inclusive of telemetry and command functions.

It is assumed that primary power is provided by the spacecraft and that the same applies to the basic telemetry and to the command subsystems.

TABLE 4-8

SUMMARY OF WEIGHT, VOLUME, AND PRIMARY POWER REQUIREMENTS FOR THE OVERALL EXPERIMENT SYSTEM

	Power (W)	Weight (Kg)	Volume (m ³)
Refractivity Experiment (M&D)	55 (67) *	17.8	0.22
Radiometric Experiment	10	0.5	0.0675
Spectrometric Experiment	32	13.50	0.025
GRAND TOTAL	97 (109)	32	0.0633

*Power consumption of 55W is for Daughter, 67W is for Mother. Although each orbiter (for redundancy reasons) contains both mother and daughter payloads, only one is energized when the system at each terminal operates.

5. DATA REDUCTION REQUIREMENTS

5.1 REFRACTIVITY DATA PROCESSING

5.1.1 COLLECTING EXPERIMENT DATA

To simulate the experiment, rays were traced using a three-dimensional double precision ray tracing computer program that incorporated the models of electron density, pressure, and temperature previously described, (subsection 4.3.3). Atmospheric and ionospheric effects were introduced to the index of refraction in the following manner.

$$\mu^2 = \frac{1 + 2\left(\frac{\mu_I^2 - 1}{\mu_I^2 + 2} + \frac{\mu_A^2 - 1}{\mu_A^2 + 2}\right)}{1 - \left(\frac{\mu_I^2 - 1}{\mu_I^2 + 2} + \frac{\mu_A^2 - 1}{\mu_A^2 + 2}\right)}$$

where μ is the combined index of refraction, μ_I is the ionospheric index of refraction:

$$\mu_I^2 = 1 - \frac{N}{12400 f^2}$$

and μ_A is the atmospheric index of refraction:

$$\mu_A = 1 + C_A \frac{P}{T}$$

N is the electron density in electrons/cc

f is the frequency in MHz

P is the pressure in dynes/cm²

T is the temperature in °K

C_A is the atmospheric coefficient of refractivity
in $^{\circ}\text{K cm}^2/\text{dyne}$

For varying frequencies, longitudes and gradients, tables are constructed that give the height of transmitter, longitude of transmitter, height of receiver, longitude of receiver, and phase delay in cycles on transmission between two points. These are the real data we expect from the experiment and the basic inputs needed for our data reduction programs.

5.1.2 DATA REDUCTION

The first problem in data reduction is to establish tables of satellite position versus phase delay.

Once these tables have been set up, they must be further broken down so that each 1 km x 300 km x 300 km cell now has five numbers associated with it: transmitter height and angle, receiver height and angle, and phase delay.

These data will be reduced in one of four ways, depending on the sharpness of the gradients and the degree of bending of the rays. This can be determined once the experiment has been performed by the values of phase delay for a given frequency and the variation from cell to cell. Table 5-1 below tells which data reduction method will be used for bending and gradient conditions.

TABLE 5-1
DATA REDUCTION METHODS

	Straight path	Appreciable bending
Mild Gradients	① Abel transform along a single vertical profile	② Model matching along a single vertical profile
Sharp Gradients	③ Abel transform along many verticals simultaneously	④ Model matching along many verticals simultaneously

Methods 1 and 2 both start from a table of transmitter and receiver positions versus phase delay. With the Abel transform technique, it is assumed that the transmission is along a straight line and the minimum height reached is that hit by the straight line connecting the transmitter and receiver. A refractivity profile is uniquely determined in straight line segments. With the model matching technique, a ray is traced through the refractivity profile that is being constructed by trial and error, an angle of take off and a refractivity slope are found that cause the ray to reach the receiver with the correct phase delay. In this case, the values are not uniquely determined but are a function of built-in tolerances. This method is more costly in computer time than the Abel transform technique.

Methods 3 and 4 generate profiles along many verticals simultaneously, filling all profiles down to a given height before the next height is attempted. In this way horizontal gradients can be accounted for.

Results with methods 1 and 2 have shown that for the 2000 MHz case the results can be obtained to within an accuracy of 5 percent with a spacing of 1 km. In the model matching case, results are found to be within 5 percent even when points are taken every 5 km or greater. Figure 5-1 and 5-2 show results for $f = 2000$ MHz and $f = 600$ MHz.

Results of method number 3 are reported in Figures 5-3 and 5-5, and the steepness of the modeled horizontal gradients are shown in Figures 5-4 and 5-6 respectively. Figure 5-4 is a model of greater steepness than any expected on Mars, while Figure 5-6 is the maximum gradient that is realistically expected; i.e., N_{\max} down from 90 percent to 10 percent in 1 hour longitude span. For the recovered profiles in Figure 5-3, the average errors amount to 43 percent for the Point A profile, 7 percent for the Point B profile, and 15 percent for the Point C profile. For the profiles in Figure 5-5, the average errors amount to 31 percent for the Point A profile, 7 percent for the Point B profile, and 7 percent for the Point C profile. The 7 percent average error should be improved considerably when model matching is employed, since ray bending does account for errors of this magnitude. The 31 percent error also can be improved upon by model matching, possibly to bring the error below the 5 percent mark. Method number 4 also has been computerized, although calculation examples are not presented here.

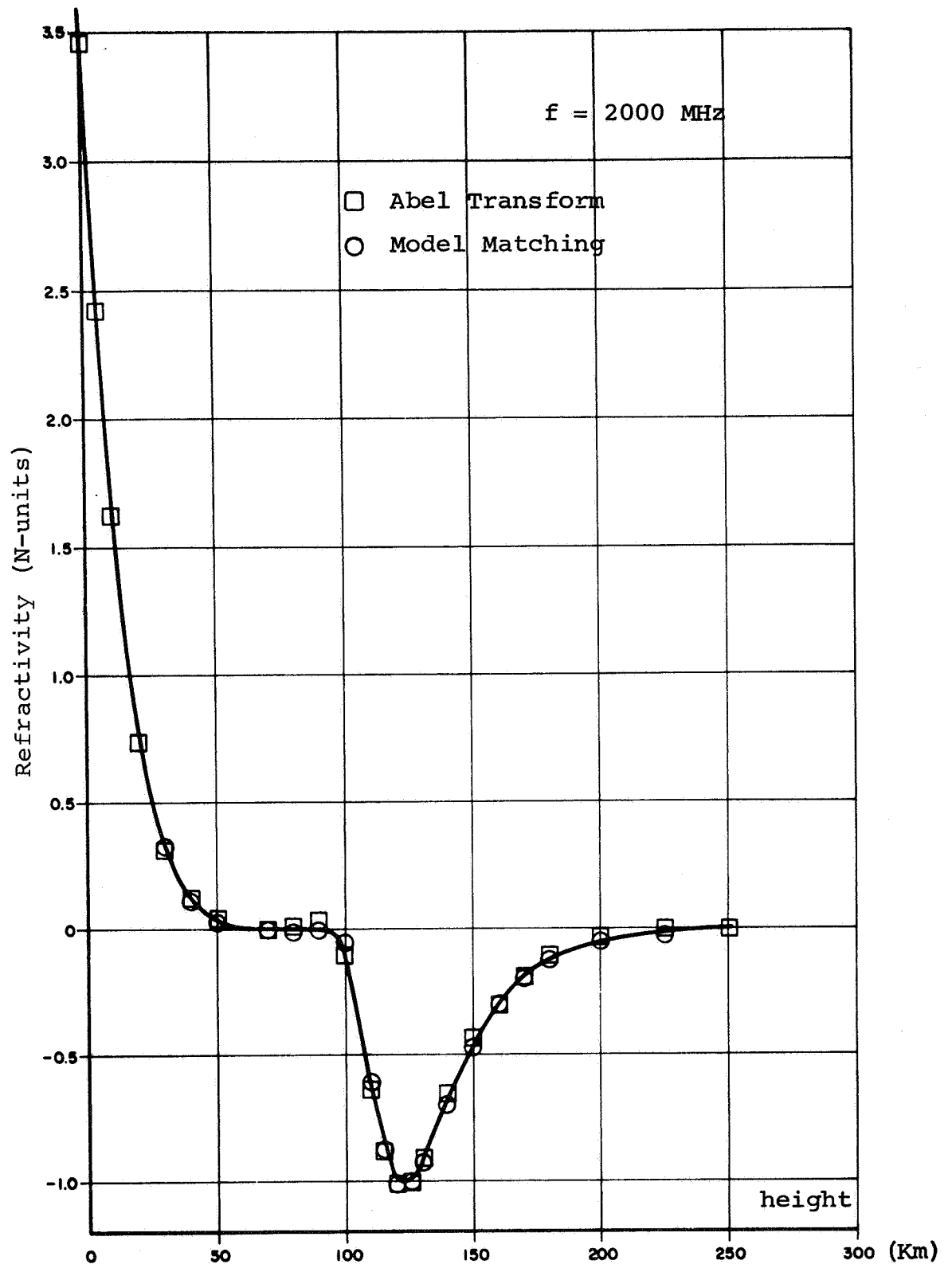


Figure 5-1 Recovered Refractivity vs. Height
($f = 2000 \text{ MHz}$)

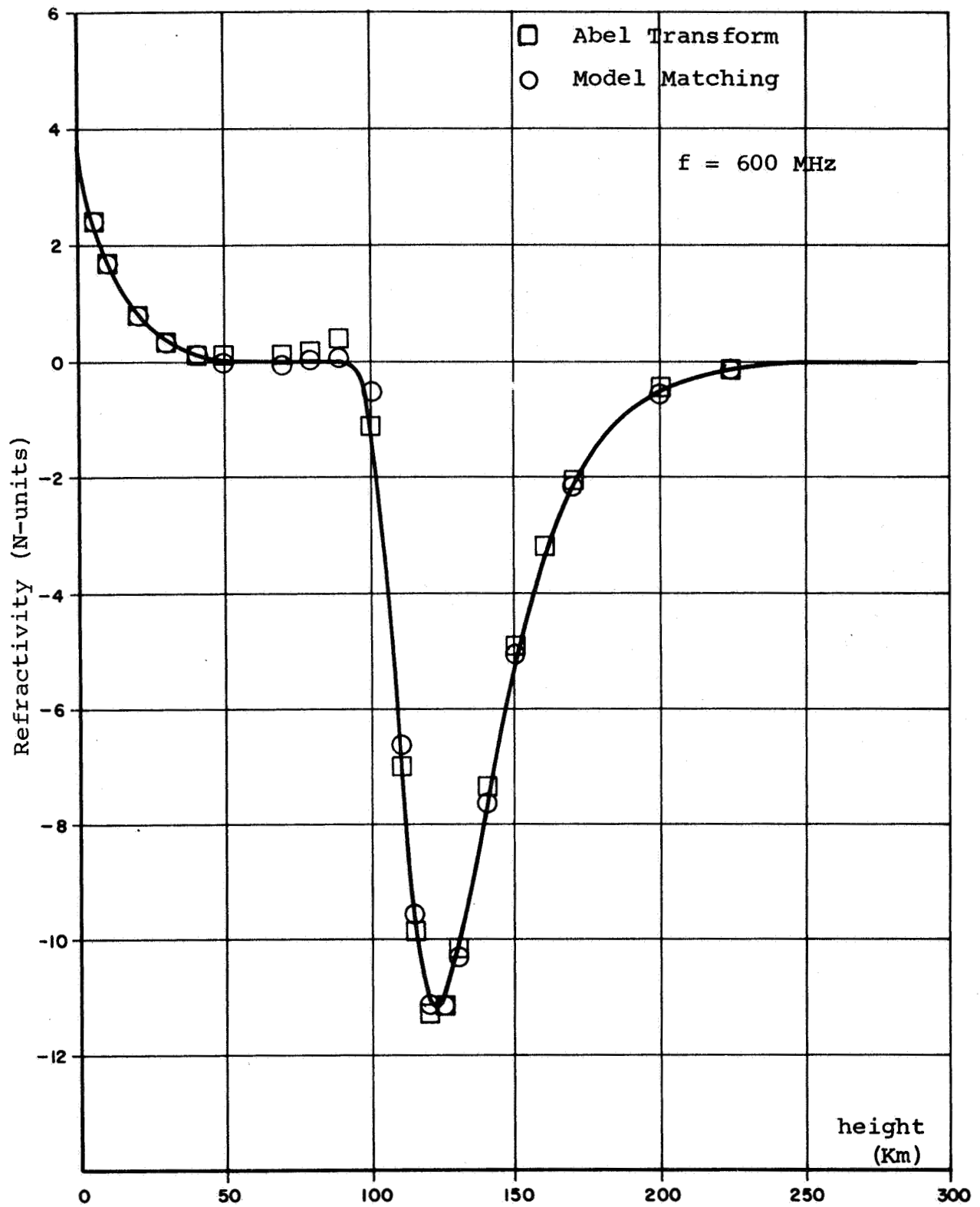


Figure 5-2 Recovered Refractivity vs. Height
(f = 600 MHz)

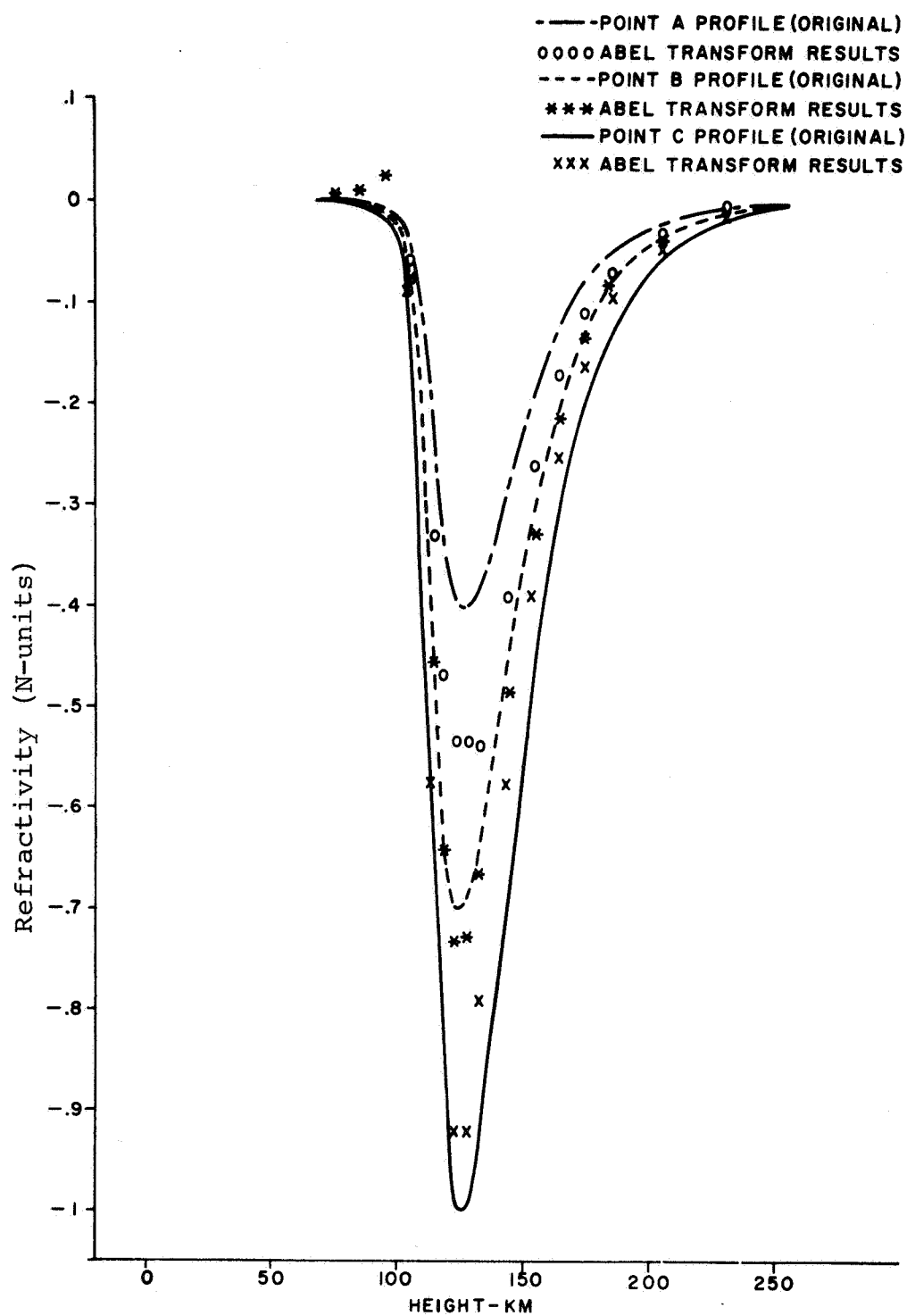


Figure 5-3 Recovered Refractivity vs. Height with Horizontal Gradient of Figure 5-4
($f = 2000$ MHz)

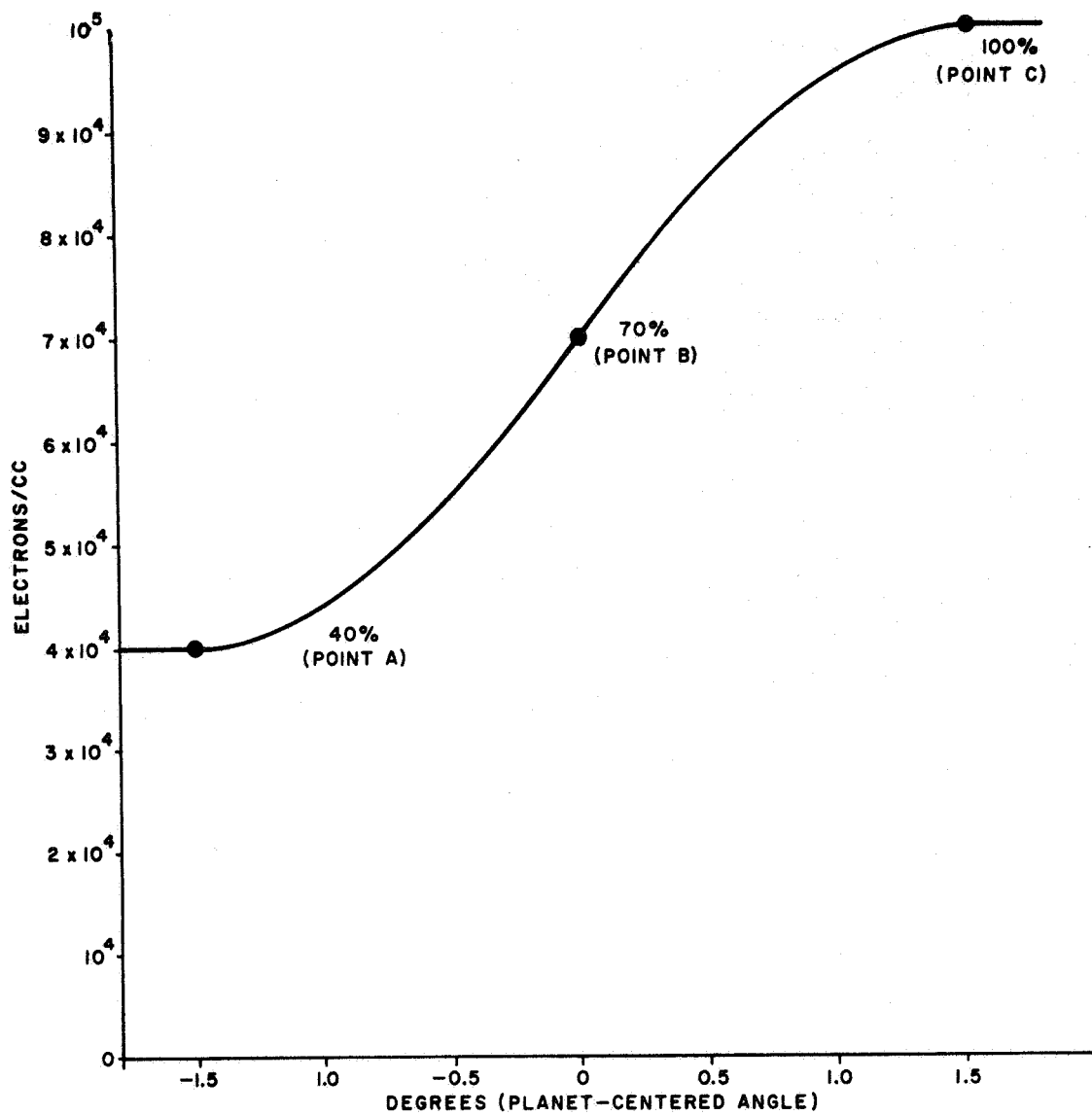


Figure 5-4 High-Steepness Model for Horizontal Gradient ($F_2 N_{\max}$ vs. Longitude)

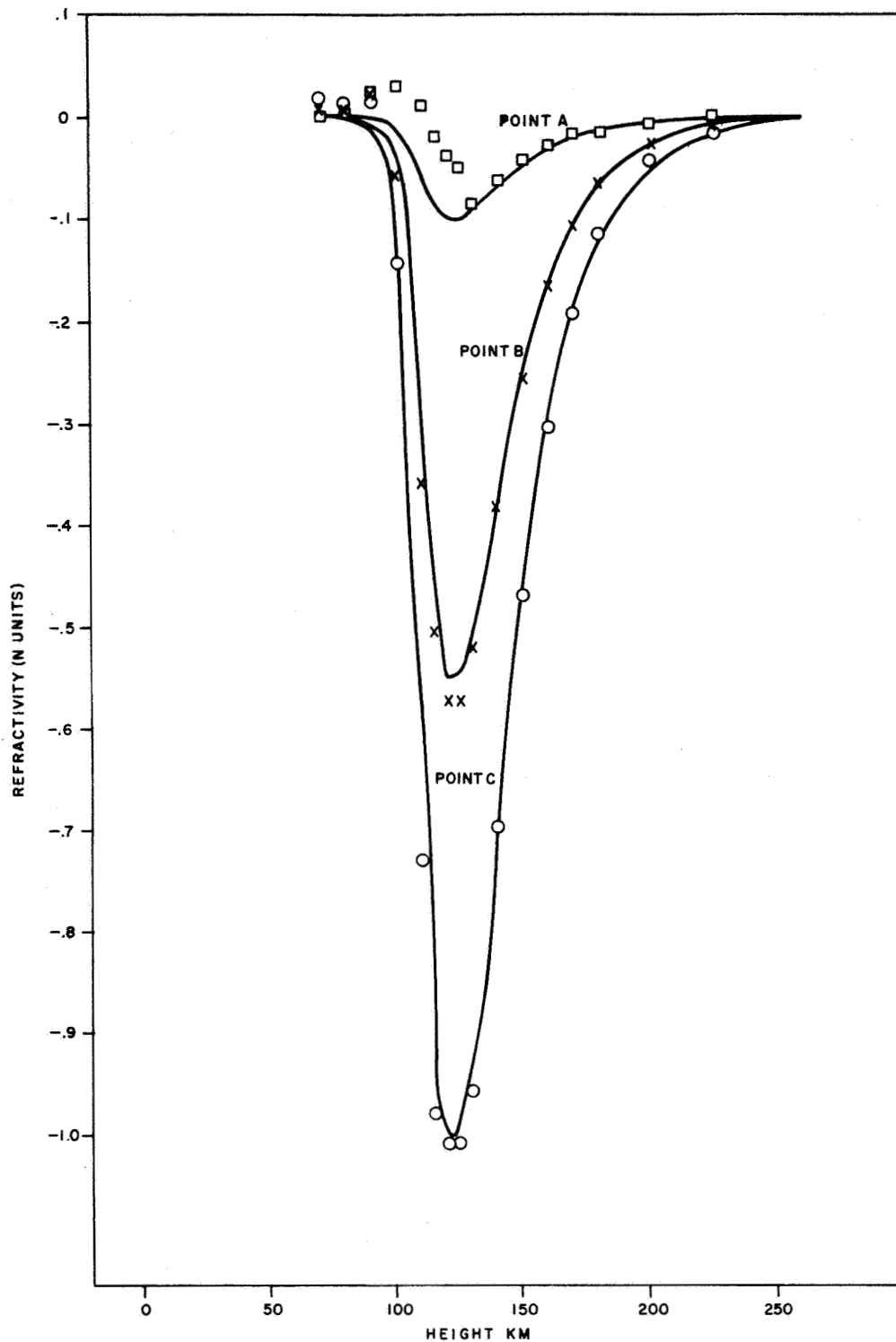


Figure 5-5 Recovered Refractivity vs. Height with
Horizontal Gradient of Figure 5-6
($f = 2000$ MHz)

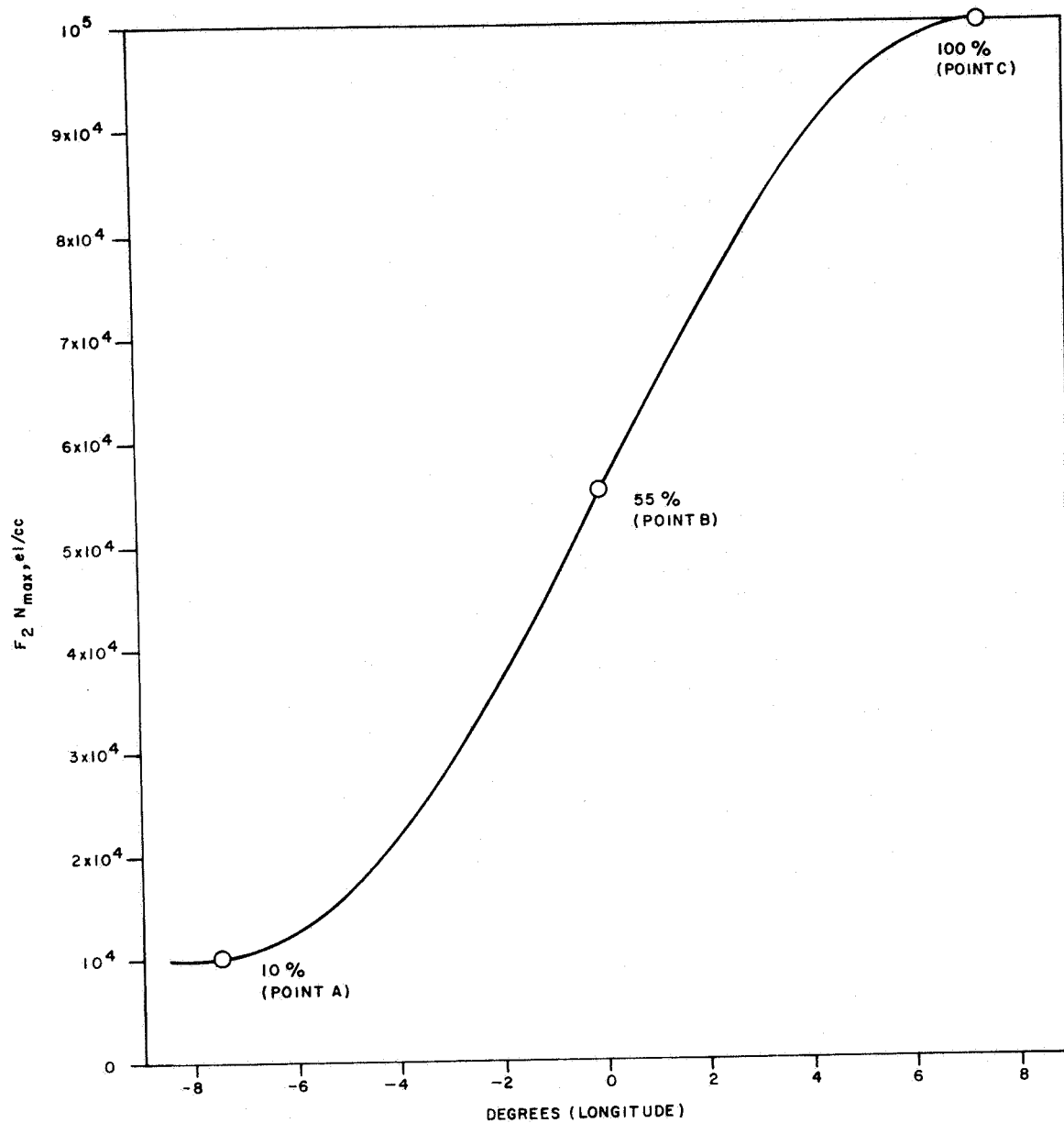


Figure 5-6 Adopted Model for Horizontal Gradient
($F_2 N_{max}$ vs. Longitude) with Realistic Steepness

Once the refractivity profiles have been determined for two frequencies, they can be separated into dispersive and non-dispersive effects, giving the atmospheric (μ_A) and the ionospheric (μ_I) indices of refraction. In the absence of magnetic field, μ_I gives a direct measurement of the electron density. On the other hand, μ_A is of limited use unless we know at least the constituents of the atmosphere and their percentages.

5.1.2.1 Abel Transform Reduction Along A Single Vertical

The observable quantities are transmitter and receiver positions versus differential phase delay. These will be converted to tables of path offset from the surface of the planet versus differential phase delay in cycles, $\Delta\phi$.

$$\Delta\phi = \frac{-f}{0.3} \left(\int_{-\infty}^{\infty} \mu(r) ds - \int_{-\infty}^{\infty} ds \right) = \frac{f}{0.3} \left(\int_{-\infty}^{\infty} (1 - \mu(r)) ds \right)$$

Where f = frequency in MHz and s = path length in km

This integral is a function of the distance of the ray from the center of the planet at the point of its closest approach to the planet's surface. By changing variables, we can write:

$$\Delta\phi(\rho) = \frac{2f}{0.3} \int_{\rho}^{\infty} \frac{(1 - \mu(r))r dr}{\sqrt{r^2 - \rho^2}} = -\frac{2f \times 10^{-6}}{0.3} \int_{\rho}^{\infty} \frac{N(r)r dr}{\sqrt{r^2 - \rho^2}}$$

Where r, ρ , and s are defined by Figure 5-7, and $N(r)$ is the refractivity in N-units.

Applying the Abel Transformation, we obtain

$$N(r) = -\frac{3 \times 10^{-5}}{\pi f r^2} \int_r^{\infty} \frac{\rho \Delta\phi(\rho) + \rho^2 \Delta\phi'(\rho)}{\sqrt{\rho^2 - r^2}} d\rho$$

If we now normalize with respect to R_0 = planet radius, this becomes

$$N(r) = -\frac{3 \times 10^5}{\pi f r^2 R_0} \int_r^{\infty} \frac{\rho \Delta\phi(\rho) + \rho^2 \Delta\phi'(\rho)}{\sqrt{\rho^2 - r^2}} d\rho$$

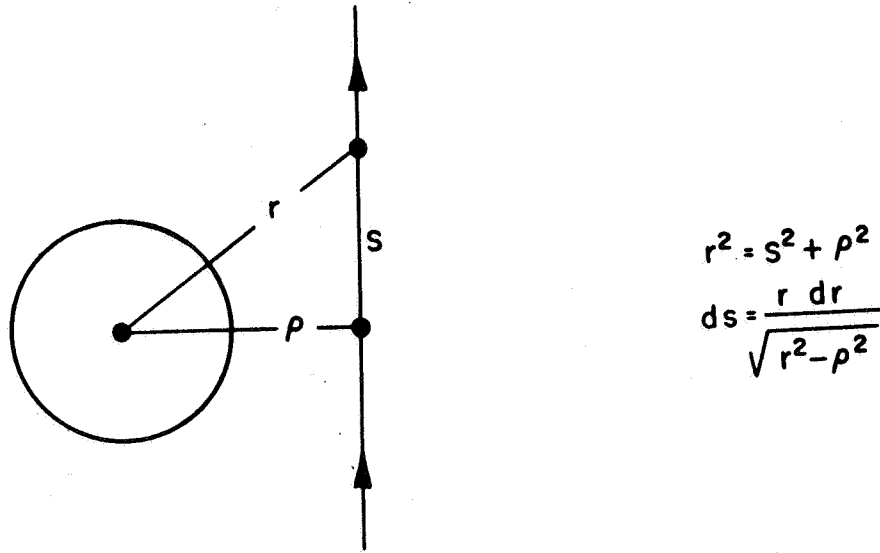


Figure 5-7 Probing Link Geometry

If we consider $\Delta\phi(\rho)$ as straight lines between input data points then

$$\Delta\phi(\rho) = a_{i,1} \rho + a_{i,2} \quad \text{where } r_i < \rho \leq r_{i+1}$$

and

$$a_{i,1} = \frac{\Delta\phi_{i+1} - \Delta\phi_i}{r_{i+1} - r_i}$$

$$a_{i,2} = \Delta\phi_i - r_i a_{i,1}$$

$$\Delta\phi'(\rho) = a_{i,1}$$

and $\rho \Delta\phi(\rho) + \rho^2 \Delta\phi'(\rho) = 2a_{i,1} \rho^2 + a_{i,2} \rho$

then,

$$N(r) = C \left\{ \int_r^{r_m} \frac{\rho \Delta\phi(\rho) + \rho^2 \Delta\phi'(\rho)}{\sqrt{\rho^2 - r^2}} d\rho + \sum_{i=m}^{n-1} \int_{r_i}^{r_{i+1}} \frac{\rho \Delta\phi(\rho) + \rho^2 \Delta\phi'(\rho)}{\sqrt{\rho^2 - r^2}} d\rho \right\}$$

Where $r_{m-1} < r \leq r_m$

and

$$C = - \frac{3 \times 10^5}{\pi f r^2 R_o}$$

or

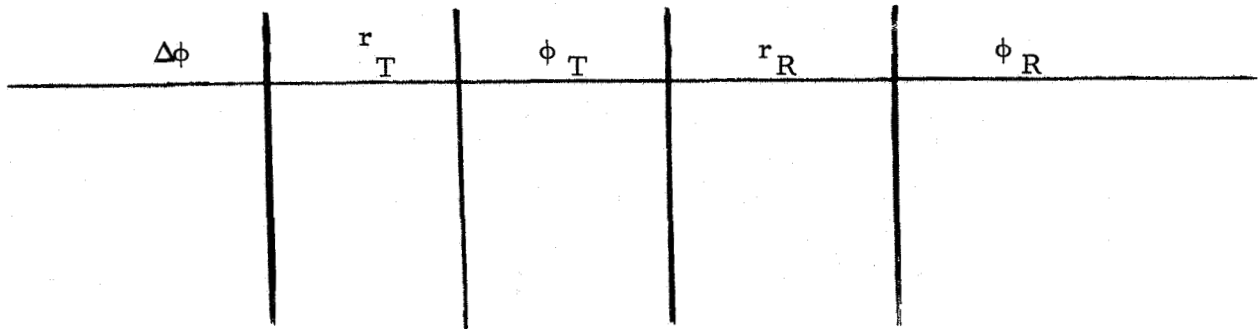
$$N(r) = C \left\{ \int_r^{r_m} \frac{2a_{m-1,1} \rho^2 + \rho a_{m-1,2}}{\sqrt{\rho^2 - r^2}} d\rho + \sum_{i=m}^{n-1} \int_{r_i}^{r_{i+1}} \frac{2a_{i,1} \rho^2 + \rho a_{i,2}}{\sqrt{\rho^2 - r^2}} d\rho \right\}$$

This is easily integrated to give $N(r)$ directly as a function of $\Delta\phi_i$

$$N(r) = C \left\{ a_{m-1,1} \left(r_m \sqrt{r_m^2 - r^2} + r^2 \log_e \left(\frac{r_m + \sqrt{r_m^2 - r^2}}{r} \right) \right) + a_{m-1,2} \sqrt{r_m^2 - r^2} + \sum_{i=m}^{n-1} \left[a_{i,1} \left(r_{i+1} \sqrt{r_{i+1}^2 - r^2} - r_i \sqrt{r_i^2 - r^2} + r^2 \log_e \left(\frac{r_{i+1} + \sqrt{r_{i+1}^2 - r^2}}{r_i + \sqrt{r_i^2 - r^2}} \right) \right) + a_{i,2} \left(\sqrt{r_{i+1}^2 - r^2} - \sqrt{r_i^2 - r^2} \right) \right] \right\}$$

5.1.2.2 Model Matching Along A Single Vertical Profile

This program reconstructs a profile of N_I , the refractivity in N-units, versus h , the height above the planet surface, given $\Delta\phi$, the phase delay in cycles, for many positions of the two orbiting satellites - one a transmitter, the other a receiver. We assume the data points we have gathered are so spaced that the minimum points of their line of sight are along a vertical. It is along this vertical that we will determine the index of refraction. We must also arrange the coordinates of the input positions of the satellites so that we may work in a plane. We then have an input table.



Where $\Delta\phi$ is the phase delay in cycles, r_T is the distance to the transmitting satellite from the center of the planet, ϕ_T is an angle of the transmitting satellite along the great circle connecting the transmitter and receiver, r_R is the distance to the receiving satellite from the center of the planet, and ϕ_R is the angle of the receiving satellite along the great circle connecting the transmitter and receiver.

We trace a ray from transmitter to receiver, assuming at first this will be a straight line. If α_0 is the angle from the radial direction of the transmitter to the line of sight between the two satellites, we compute α_0 as follows:

$$\alpha_0 = \pi - \sin^{-1} \left\{ \frac{r_T \sin(\phi_T - \phi_R)}{\overline{TR}} \right\}$$

Where

$$\overline{TR} = \left\{ r_T^2 + r_R^2 - 2r_T r_R \cos(\phi_T - \phi_R) \right\}^{1/2}$$

We stop our integration at $r = r_R$ and here $\phi = \phi_R$

If $(\phi_F - \phi_R) r_R \leq 1$, we are satisfied that the path is sufficiently close to the path actually traveled and we go on to check $\Delta\phi$. If this condition is not satisfied, we must adjust α and try again.

Solving for the Correct α :

Suppose the situation is given by Figure 5-8. We want to rotate the curve $T O' F$ about T so that if we extended $O'F$ it would pass through R . Call this angle of rotation β . To find β , we must find $\hat{T O'' R} = \hat{T O' F}$ and the $\hat{T R O''}$. The information we have to this point is r_T , ϕ_T , r_R , ϕ_R , r_F , ϕ_F , and TR . The angle $\hat{T O' F}$ is obtained as follows:

$$\overline{TF}^2 = r_T^2 + r_F^2 - 2r_T r_F \cos(\phi_T - \phi_F)$$

$$\hat{F T O} = \cos^{-1} \left(\frac{\overline{TF}^2 + r_T^2 - r_F^2}{2r_T \overline{TF}} \right)$$

Because the ray can be bent outward or inward, we must consider two cases. The difference in the argument is strictly in the sign of a few terms. For the duration of the argument, whenever two signs appear, the upper sign will refer to the case where $(\pi - \alpha) \geq \hat{FTO}$, and the lower sign will be used when $(\pi - \alpha) < \hat{FTO}$.

$$\eta = \pm(\pi - \alpha - \hat{FTO})$$

$$\hat{TFO} = \pi - \eta - |\phi_F - \phi_T|$$

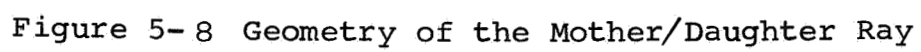
$$\chi = \pm(\alpha_F - \hat{TFO})$$

$$\hat{T O' F} = \pi - \eta - \chi$$

From this triangle we can also find $\overline{T O'}$ as follows

$$\overline{T O'} = \overline{TF} \frac{\sin \chi}{\sin \hat{T O' F}} = \overline{T O''}$$

$$\text{Then } \hat{T R O''} = \sin^{-1} \left(\frac{\overline{T O'}}{\overline{TR}} \sin \hat{T O' F} \right)$$



Then

$$\beta = \pi - \overset{\wedge}{\text{TRO}}'' - \overset{\wedge}{\text{TO}}'F$$

And

α is corrected as follows

$$\alpha = \alpha_0 + \beta.$$

This procedure is repeated if this α does not bring the point F sufficiently close to R. In no case, however, is it repeated more than 6 times. We then go on to test our $\Delta\phi$ for closeness to the inputted $\Delta\phi$.

Computing $\Delta\phi$:

As the ray is traced from the point T to the point F, the phase path length h_p is computed.

$$\text{The phase delay in km} = h_p - \overline{\text{TF}}$$

$$\text{or in cycles } \Delta\phi_c = \frac{h_p - \overline{\text{TF}}}{0.3} f$$

Where f is the frequency in MHz.

We must now compare $\Delta\phi_c$ with $\Delta\phi$ from our input table. Let $\Delta\phi_i$ be our current value from the input table and $\Delta\phi_{i-1}$ be the previous value in the input table. Then we regard $\Delta\phi_c$ as sufficiently close to $\Delta\phi$ if

$$\frac{\Delta\phi_i - \Delta\phi_c}{\Delta\phi_i - \Delta\phi_{i-1}} \leq 0.01. \text{ If this condition is satisfied we}$$

accept this portion of the refractivity profile and go on to the next entry. If the condition is not satisfied we must vary λ_i in the refractivity model.

Refractivity Model:

The refractivity profile we are trying to construct will have

the following form

$$N = \lambda_i (h - h_{i-1}) + \lambda_{c_i} \quad \text{where } h_i \leq h < h_{i+1}$$

and N is the refractivity in N-units
The index of refraction, μ , is given by

$$\mu = 1 + N \times 10^{-6}.$$

h_i = height of satellites

λ_{c_1} = refractivity at the satellite position $\approx -.001$ for 1000 km.

λ_i is varied until $\Delta\phi$ for a ray passing between the two satellites matches $\Delta\phi$ given by the experiment. The h_2 is taken as the minimum point in the transmission link, $\lambda_{c_2} \approx \lambda_1 \cdot (h_2 - h_1) + \lambda_{c_1}$, and we look for λ_2 using the next set of

satellite positions and trying to match the next value of $\Delta\phi$.

Finding λ_i :

The first λ , λ_1 , is a guess given by the input. We trace a ray with λ_1 and if $\Delta\phi_c$ does not meet the accuracy condition, we adjust λ_1 by the following scheme. Let $\lambda_1' = \lambda_1$

$$\text{If } \Delta\phi_c < \Delta\phi_1, \quad \lambda_2' = \lambda_1' / 1.1$$

$$\text{If } \Delta\phi_c \geq \Delta\phi_1, \quad \lambda_2' = 1.1\lambda_1'$$

We also save λ_1 , $\Delta\phi_c$, and α

Call them λ_1' , $\Delta\phi_c$, and α_1

Now we trace a ray with $\lambda_1 = \lambda_2'$ adjusting α as necessary. If $\Delta\phi_{c2}$ does not match our accuracy condition, we interpolate to find λ_3' and α_3 as follows

$$\lambda_3' = \lambda_1' + \frac{|\Delta\phi - \Delta\phi_{c_1}|}{|\Delta\phi_{c_2} - \Delta\phi_{c_1}|} (\lambda_2' - \lambda_1')$$

and

$$\alpha_3 = \alpha_1 + \frac{|\Delta\phi - \Delta\phi_{c_1}|}{|\Delta\phi_{c_2} - \Delta\phi_{c_1}|} (\alpha_2 - \alpha_1)$$

and we trace another ray.

We have found that a linear interpolation is preferable to higher order interpolations in most cases, since higher order interpolations lead to nonphysical answers. In the third and successive iterations we use the following approach. Set up a table of values in ascending order of λ_p so we have a table that looks like

λ	$\Delta\phi$	α
λ'_1	$\Delta\phi'_1$	α'_1
λ'_2	$\Delta\phi'_2$	α'_2
λ'_3	$\Delta\phi'_3$	α'_3

Where $\lambda'_1 < \lambda'_2 < \lambda'_3$

We do a linear interpolation with the following points.

If $|\Delta\phi - \Delta\phi'_1| < |\Delta\phi - \Delta\phi'_3|$, we interpolate using $\Delta\phi'_1$ and $\Delta\phi'_2$
Unless

- (1) $\Delta\phi'_3$ was the last value computed. In this case we would use $\Delta\phi'_1$ and $\Delta\phi'_2$ unless $(\Delta\phi'_2 - \Delta\phi)$ and $(\Delta\phi'_1 - \Delta\phi)$ are of opposite signs in which case we would use $\Delta\phi'_1$ and $\Delta\phi'_3$.

or

- (2) $(\Delta\phi'_1 - \Delta\phi)$ and $(\Delta\phi'_2 - \Delta\phi)$ are the same sign in which case we use $\Delta\phi'_1$ and $\Delta\phi'_3$

If $|\Delta\phi - \Delta\phi'_1| > |\Delta\phi - \Delta\phi'_3|$, we interpolate using $\Delta\phi'_2$ and $\Delta\phi'_3$

Unless:

- (1) $\Delta\phi'_1$ was the last value computed. In this case we would use

$\Delta\phi'_1$ and $\Delta\phi'_2$ unless $(\Delta\phi'_2 - \Delta\phi)$ and $(\Delta\phi'_3 - \Delta\phi)$ are of opposite sign in which case we would use $\Delta\phi'_1$ and $\Delta\phi'_3$

or

(2) $(\Delta\phi'_2 - \Delta\phi)$ and $(\Delta\phi'_3 - \Delta\phi)$ are the same sign in which case we would use $\Delta\phi'_1$ and $\Delta\phi'_2$.

Tracing a Ray:

To trace a ray, we are given r_T , ϕ_T , and α and we use Haselgrove's equations in two dimensions to find r , ϕ , y_r and y_ϕ where y_r and y_ϕ are the direction cosines in the r and ϕ directions respectively. Phase path length, h_p , is the independent variable.

$$\dot{r} = \frac{y_r}{\mu}$$

$$\dot{\phi} = \frac{y_\phi}{\mu r}$$

$$\dot{y}_r = \frac{1}{\mu} \frac{\partial \mu}{\partial r} + y_\phi \dot{\phi}$$

$$\dot{y}_\phi = -y_r \dot{\phi}$$

Where μ is the index of refraction.

Initially $r = r_T$, $\phi = \phi_T$, $y_r = \mu \cos \alpha$, and $y_\phi = \mu \sin \alpha$. y_r and y_ϕ are further constrained by the condition $y_r^2 + y_\phi^2 = \mu^2$

From this we obtain r_F , ϕ_F , h_p , and α_F where

$$\alpha_F = \cos^{-1}(y_r)$$

5.1.2.3 Abel Transform Along Many Verticals Simultaneously

This Abel transform program, which takes account of the horizontal gradients in the refractivity, uses the same basic approach of the program described in Section 5.1.2.1; but $a_{i,1}$ and $a_{i,2}$ must now be generated in a different manner, taking account of the value of θ , the longitude at which the path intersects a layer, as well as r , the offset distance. The input becomes a series of tables of the type shown in Section 5.1.2.2 where such

a table must be read in for each value of θ_c where θ_c is the longitude at which the path come closest to the planet surface.

The order in which the $N(r_i, \theta_j)$ is generated is as follows. All $N(r_i, \theta_j)$, $j = 1, N_\theta$ are found where $r_1 > r_2 > \dots > r_{N_2}$. This is not necessary for the Abel transform, but is used for input compatibility with the model matching techniques.

Briefly, what the method does is keep track of where a straight line intersects the spherical shells. We then interpolate between values of $\Delta\phi$ on the shell. The interpolated values are then used to solve the problem as if these values were for a spherically symmetric model. This means we must solve the problem separately for going in and out. Figure 5-9 will help to demonstrate this.

If we are solving for the value of refractivity at point E, we procede as follows:

Find

$$\Delta\phi_A = \Delta\phi(r_1, \theta_1) + \frac{\theta_A - \theta_1}{\theta_2 - \theta_1} (\Delta\phi(r_1, \theta_2) - \Delta\phi(r_1, \theta_1))$$

$$\Delta\phi_B = \Delta\phi(r_2, \theta_1) + \frac{\theta_B - \theta_1}{\theta_2 - \theta_1} (\Delta\phi(r_2, \theta_2) - \Delta\phi(r_2, \theta_1))$$

$$\Delta\phi_C = \Delta\phi(r_3, \theta_3) + \frac{\theta_C - \theta_2}{\theta_3 - \theta_2} (\Delta\phi(r_3, \theta_3) - \Delta\phi(r_3, \theta_2))$$

etc.

We then use $\Delta\phi_A, \Delta\phi_B, \dots, \Delta\phi_E$ to solve one half of the path, as in Section 5.1.2.1, and $\Delta\phi_E, \Delta\phi_F, \dots, \Delta\phi_I$ to solve the other half of the path. We thereby obtain $N(r_5, \theta_4)$.

The following algorithm describes the method in detail.

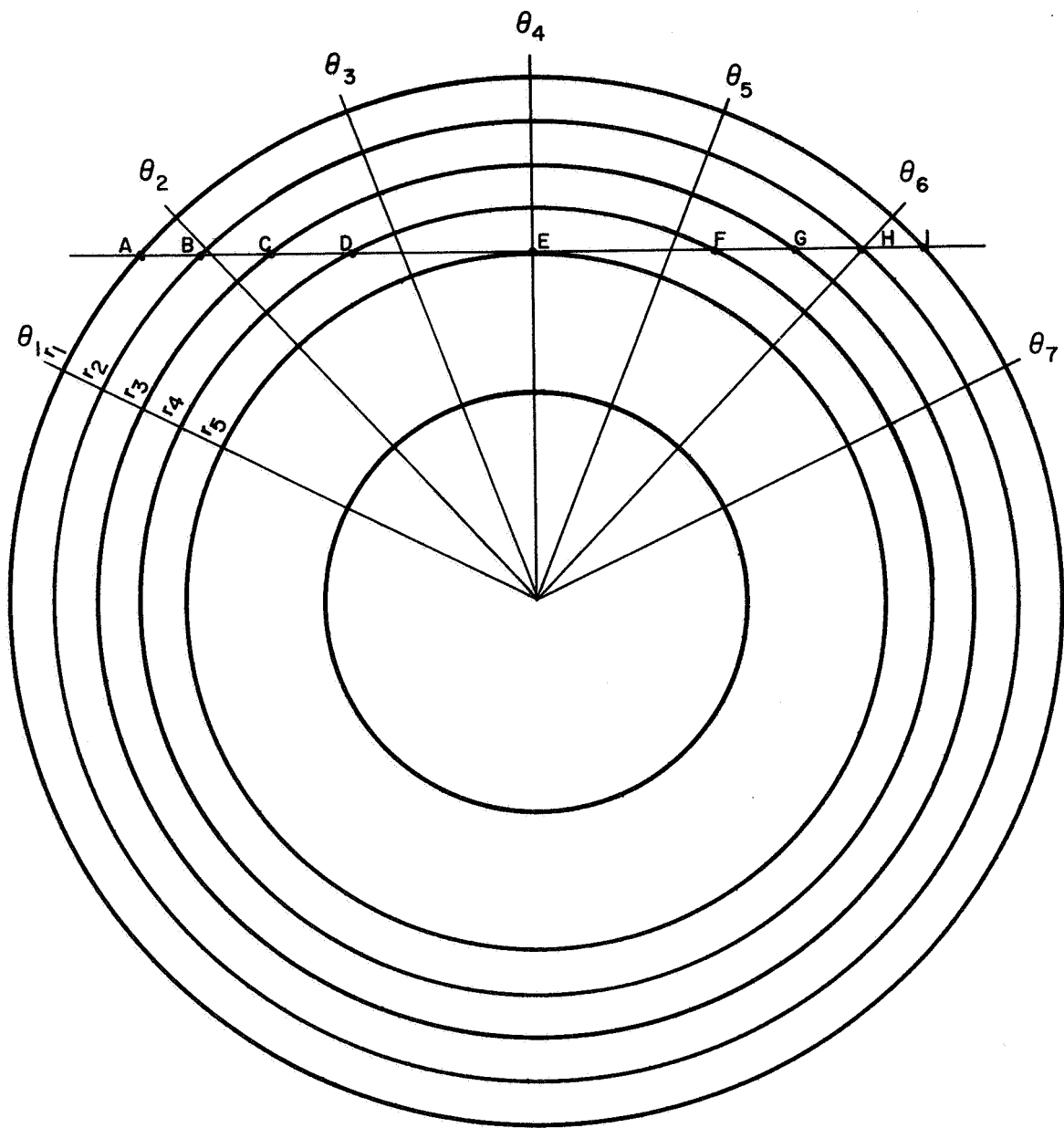


Figure 5-9 Geometry of the Profile Inversion along
Many Vertices Simultaneously by Abel
Transform

for i = 1, 2, , n_R

for j = 1, 2, , n_θ

$$\chi_t(i, j) = R_t(i, j) \sin \theta_t(i, j)$$

$$y_t(i, j) = R_t(i, j) \cos \theta_t(i, j)$$

$$\chi_r(i, j) = R_r(i, j) \sin \theta_r(i, j)$$

$$y_r(i, j) = R_r(i, j) \cos \theta_r(i, j)$$

$$C = \frac{y_t(i, j) - y_r(i, j)}{\chi_t(i, j) - \chi_r(i, j)}$$

$$R_{\min}(i, j) = R_t(i, j) \cos \left(\frac{\theta_t(i, j) - \theta_r(i, j)}{2} \right)$$

$$\rho(i, j) = \frac{R_{\min}(i, j)}{R_o}$$

$$\tau(i, j) = - \frac{0.3 \Delta \phi(i, j)}{f}$$

$$\tau_L = 0$$

$$\rho_L = \frac{R_t(i, j)}{R_o}$$

for $k = 1, 2, \dots, i-1$

$$A = R_{\min}^2(k, j)(1 + C^2)$$

$$B = 2 C R_{\min}(k, j)(y_r(i, j) - C x_r(i, j))$$

$$C = (y_r(i, j) - C x_r(i, j))^2 - R_{\min}^2(k, j)$$

$$\theta = \sin^{-1} \left(\frac{-B - \sqrt{B^2 - 4AC}}{2A} \right)$$

Find ℓ such that

$$\theta_C(\ell) \leq \theta < \theta_C(\ell + 1)$$

$$\tau_N = \tau(k, \ell) + \frac{\theta - \theta_C(\ell)}{\theta_C(\ell + 1) - \theta_C(\ell)} (\tau(k, \ell + 1) - \tau(k, \ell))$$

$$\rho_N = \rho(k, \ell) + \frac{\theta - \theta_C(\ell)}{\theta_C(\ell + 1) - \theta_C(\ell)} (\rho(k, \ell + 1) - \rho(k, \ell))$$

$$a_1 = \frac{\tau_L - \tau_N}{\rho_L - \rho_N}$$

$$a_2 = \tau_N - a_1 \rho_N$$

$$\begin{aligned} \text{sum} = \text{sum} + a_1 & \left\{ \rho_L \sqrt{\rho_L^2 - \rho^2(i, j)} - \rho_N \sqrt{\rho_N^2 - \rho^2(i, j)} \right. \\ & \left. + \rho^2(i, j) \log_e \left(\frac{\rho_L + \sqrt{\rho_L^2 - \rho^2(i, j)}}{\rho_L + \sqrt{\rho_N^2 - \rho^2(i, j)}} \right) \right\} \\ & + a_2 \left(\sqrt{\rho_L^2 - \rho^2(i, j)} - \sqrt{\rho_N^2 - \rho^2(i, j)} \right) \end{aligned}$$

$$\rho_L = \rho_N$$

$$\tau_L = \tau_N$$

$$a_1 = \frac{\tau_L - \tau(i, j)}{\rho_L - \rho(i, j)}$$

$$a_2 = \tau(i, j) - a_1 \rho(i, j)$$

$$\begin{aligned} \text{sum} = & \text{sum} + a_1 \left\{ \rho_L \sqrt{\rho_L^2 - \rho^2(i, j)} \right. \\ & \left. + \rho^2(i, j) \log_e \left(\frac{\rho_L + \sqrt{\rho_L^2 - \rho^2(i, j)}}{\rho(i, j)} \right) \right\} \\ & + a_2 \sqrt{\rho_L^2 - \rho^2(i, j)} \end{aligned}$$

$$\tau_L = 0$$

$$\rho_L = \frac{R_r(i, j)}{R_o}$$

for $k = 1, 2, 3, \dots, i-1$

$$A = R_{\min}^2(k, j)(1 + C^2)$$

$$B = 2C R_{\min}(k, j)(y_r(i, j) - C \chi_r(i, j))$$

$$C = (y_r(i, j) - C \chi_r(i, j))^2 - R_{\min}^2(k, j)$$

$$\theta = \sin^{-1} \left(\frac{-B + \sqrt{B^2 - 4AC}}{2A} \right)$$

Find l such that

$$\theta_C(l) \leq \theta < \theta_C(l+1)$$

$$\tau_N = \tau(k, l) + \frac{\theta - \theta_C(l)}{\theta_C(l+1) - \theta_C(l)} (\tau(k, l+1) - \tau(k, l))$$

$$\rho_N = \rho(k, l) + \frac{\theta - \theta_C(l)}{\theta_C(l+1) - \theta_C(l)} (\rho(k, l+1) - \rho(k, l))$$

$$a_1 = \frac{\tau_L - \tau_N}{\rho_L - \rho_N}$$

$$a_2 = \tau_N - a_1 \rho_N$$

$$\begin{aligned} \text{sum} = \text{sum} + a_1 & \left\{ \rho_L \sqrt{\rho_L^2 - \rho^2(i, j)} - \rho_N \sqrt{\rho_N^2 - \rho^2(i, j)} \right. \\ & \left. + \rho^2(i, j) \log_e \left(\frac{\rho_L + \sqrt{\rho_L^2 - \rho^2(i, j)}}{\rho_N + \sqrt{\rho_N^2 - \rho^2(i, j)}} \right) \right\} \\ & + a_2 \left(\sqrt{\rho_L^2 - \rho^2(i, j)} - \sqrt{\rho_N^2 - \rho^2(i, j)} \right) \end{aligned}$$

$$\rho_L = \rho_N$$

$$\tau_L = \tau_N$$

$$a_1 = \frac{\tau_L - \tau(i, j)}{\rho_L - \rho(i, j)}$$

$$a_2 = \tau(i, j) - a_1 \rho(i, j)$$

$$\begin{aligned} \text{sum} = \text{sum} + a_1 & \left\{ \rho_L \sqrt{\rho_L^2 - \rho^2(i, j)} \right. \\ & \left. + \rho^2(i, j) \log_e \left(\frac{\rho_L + \sqrt{\rho_L^2 - \rho^2(i, j)}}{\rho(i, j)} \right) \right\} \\ & + a_2 \sqrt{\rho_L^2 - \rho^2(i, j)} \end{aligned}$$

$$N_{i, j} = \left[\frac{\text{sum}}{2\pi R_o \rho(i, j)} \right] 10^{+6}$$

5.1.2.4 Model Matching along Many Verticals Simultaneously

This method uses the same input as the Abel transform technique (subsection 5.1.2.3) and solves for the refractivity in the same sequence (i.e., all angles for one height working from the greatest height to the planet surface). In this case, we construct a two-dimensional grid of refractivity, and the ray tracing is done using interpolated values from this grid. The elevation angle of the ray and the vertical slope of the refractivity will be found in the same manner described in subsection 5.1.2.2.

5.2 SPECTROSCOPIC DATA PROCESSING

As the ray path moves through the atmosphere of Mars, incident radiation at frequencies in both the IR and UV become absorbed in varying degrees depending upon the relative line strengths. (We assume that conditions are such that the radiation emanating from the localized regions of the sun under surveillance during the period of occultation remains substantially the same). The raw data that will be extracted from the satellite storage are the transmissivity values at frequency intervals in the IR and UV regions as a function of satellite location. This can be reduced to the transmissivity values as a function of the different ray paths defined by the minimum altitudes of these paths with Mars. The ray path bend can be obtained by the refractivity measurements.

A technique exists by which the resulting transmissivity due to absorption and its rate of change with frequency may be related to tabulated homogeneous parameters. A system of N simultaneous equations with N unknowns may be arrived at and solved using a high speed digital computer. The solutions of these equations lead to altitude profiles of constituents, density, pressure, and temperature.

5.3 RADIOMETRIC DATA PROCESSING

Position of the spacecraft and look angles toward the surface will be correlated to radiometric raw data.

Corrections will be applied to the data from the two calibrations performed periodically during the mission. This is achieved by comparing the readout values when the radiometer looks at the small target on board the Orbiter (of known temperature and emissivity) with the expected temperature reading; comparison

will also be made of the readout values when the radiometer looks toward free space with the expected temperatures.

Correlation between the radiometric data and the TV camera output will be performed in order to gain insight into the thermal properties of the surface and for cloud studies.

6. CONCLUSIONS AND RECOMMENDATIONS

The study reported here has provided the preliminary proof of the feasibility and practicality of unambiguously probing the atmosphere and ionosphere of Mars from a dual-orbiter platform.

In principle, the method is capable of mapping three-dimensionally the ionized and neutral atmosphere of the planet at all longitudes and latitudes, of performing repetitive measurements in each resolution cell, of describing accurately horizontal gradients of realistic steepness.

However, if from one standpoint, the study has resolved various issues that were interrogative marks at the beginning, it has pointed out, from another standpoint, new areas of concern that require further analysis and experimentation.

In particular, the following points deserving additional study are worth mentioning:

1. A minimization of the lock-in time of the phase-sensitive refractivity link at emersion from occultation would enhance the ability of the system of probing the lower layers of the atmosphere. A lock-in time on the order of 0.1 second would be highly desirable, owing to the high speed (on the order of a few km/sec) that characterizes the sweeping through the atmosphere of the probing path, and owing to the importance of collecting atmospheric samples near the planet's surface. This lock-in time requirement exceeds the present state-of-the-art by approximately a factor of 5.

2. The removal of geometrical doppler from the total doppler observed at emersion requires the preparation of a high-accuracy computer program for orbital mechanics calculations, of the type that MIT Lincoln Lab is preparing for the radar tracking of the planet Mercury in the forthcoming 4th test of the general relativity theory.

3. For cases (like the Earth) in which a magnetic field affects the radio waves propagation appreciably, a study is required of the phase perturbations imposed on the link by polarization behavior and its relationship to induced phase perturbations

as well as the issue of the motion of the link's terminals around their c.g.'s.

4. Phase scintillation in a medium that, like the Earth's ionosphere, exhibits this type of phenomenon must be investigated and the statistics of the induced phase instabilities evaluated.

5. The recent experience (still unpublished) of AFCRL (OSO III) and Harvard College Observatory (OSO IV) in transmission absorption spectroscopy measurements of the density of the upper layers of the Earth's atmosphere provides, from one side, a strong encouragement in developing further the method that Raytheon suggested to NASA for planetary research some time ago. Now, it can no longer be stated that the method is not acceptable because it was never tested in space. From another side, however, this experience has made clear that additional studies are needed, especially in the area of broadening the dynamic range of the probing in order to cover, with the selection of a suitable set of lines, the tremendous range of absorptions going from the outer boundary of the atmosphere down to surface levels.

6. The ability to correlate Sun occultation and mother/daughter occultation measurements belonging to the same resolution cell must be investigated with consideration given to the time dynamics of the refractive and absorptive phenomena occurring in the same cell.

For the reasons told above, a follow-up study would be desirable before a full implementation of the dual-orbiter mission is undertaken, either around the Earth or around a remote planet.

7. REFERENCES

- (1) Baum, W.A. and Code, A.D. (1953), A Photometric Observation of the Occultation of Sigma Arietis by Jupiter, *Astron J.*, 58, pp. 108-112.
- (2) Elsmore, B. (1957), Radio Observations of the Lunar Ionosphere, *Philosophical Magazine*, p. 1040.
- (3) Menzel, D. H. and DeVancouleurs, G. (1960), Results from the Occultation of Regulus by Venus, *Astron J.*, 65, p. 351.
- (4) Weisberg, H. (1963), On the Possibility of Studying Planetary Atmospheres by Observing Stellar Occultations from a Flyby Space Probe or Planetary Orbiter, *Icarus* 2, pp. 226-227.
- (5) Kliore, A. et al. (1965), Occultation Experiment: Results of the First Direct Measurement of Mar's Atmosphere and Ionosphere, *Science*, Volume 149, pp. 1243-1248.
- (6) J. V. Harrington (1965), Study of a Small Solar Probe (Sun-blazer) Part I, Radio Propagation Experiment. MIT Rep. PR-5255-5, July 1.
- (7) Landini, M. et al. (1965), Atmospheric Density in the 120-190 km Region Derived from the X-Ray Extinction Measured by the US NRL Satellite 1964-01-D, *Nature*, Volume 206, pp. 173-174.
- (8) Hinterregger, H. E., AFCRL, Private Communication.
- (9) Reeves, E. M., Harvard College Observatory, Private Communication.
- (10) Coogan, J. M. (1967), A Method for Studying Planetary Atmospheres Employing the Dual Flyby Mode, AIAA 5th Aerospace Conference, New York, N. Y., January 23-26.
- (11) Harrington, J. V. et al. (1966), Electromagnetic Measurements of Planetary Atmospheres and Ionospheres by an Orbital Pair, Raytheon IRP Report FR-66-71, March 7.

- (12) Lombardini, P. P. et al. (1967), Centimetric and Millimetric Wave Spectroscopy of Planetary Atmospheres from Orbital Pairs, Raytheon IRP Report FR-66-242, Revision A, March 1.
- (13) Harrington, J. V. et al. (1967), Mars Mariner IV Radio Occultation Experiment: Comments on the Uniqueness of the Results, Paper accepted for publication in JGR, December.
- (14) Lombardini, P. P. et al. (1965), Phase Changes in an Interplanetary Link Caused by a Perturbation on the Solar Wind, Raytheon IDP Report FR-65-465, December 22.
- (15) Curkendall, D. W. (1966), Orbit Determination of Two Spacecraft Through the Use of Earth-Based Multiple-Link Doppler Tracking Data, JPL, Contract NAS 7-100, Phase I Report.
- (16) Seddon, C. J. (1953), Propagation Measurements in the Ionosphere with the Aid of Rockets, JGR, Volume 58, No. 3, pp. 323-325, September.
- (17) Langworthy, B. M. (1967), HRT-11 Model Matching Program Raytheon Technical Memo MSD/AERO-3674, May 4.
- (18) NASA Doc. SP-3016, Venus and Mars Nominal Natural Environment for Advanced Manned Planetary Mission Program.
- (19) Fjeldbo, G. et al. (1966), Models of the Atmosphere of Mars Based on the Mariner IV Occultation Experiment, JGR, 71, No. 9, pp. 2307-2316.
- (20) Russel, R. K. (1967), Satellite Orbit Determination Accuracy Study Applicable to Voyager Trajectories, JPL Space Programs Summary, pp. 37-45, Volume III.
- (21) Mathison, R. P., (1965), Mariner Mars 1964 Telemetry and Command System, IEEE Spectrum, Volume 2, No. 7, July, pp. 76-84.
- (22) Gardner, F. M. (1966), Phase-Lock Techniques, J. Wiley and Sons.

- (23) Brooks, E. M. (1967) "Comprehensive Summary of Available Knowledge of the Meteorology of Mars and Venus" NASA Contractor Report, NACA CR-786, May.
- (24) Rea, D. G. (1965) "The Atmosphere and Surface of Mars" A Selective Review. Presented at Lunar and Planetary Seminar C.I.T., September.
- (25) Van Tassel, R. A. and Salisbury, J. W. (1965) Planetary Environments. In: Handbook of Geophysics and Space Environments. AFCRL Chapter 20.
- (26) Evans, Pitts and Kraus, "Venus and Mars, Nominal Natural Environment For Advanced Manned Planetary Mission Programs" NASA SP-3016 2nd Edition.
- (27) Owen, T., (1966a) "Recent Observations of the Photographic Spectrum of Mars - A preliminary result." In Proc., of Caltech - JPL Lunar and Planetary Conference - Sept. 13 - 18, pp 247 - 251.
- (28) Belton, M.J.S. and Hunten, D.M., (1966a). "The Abundance and Temperature of CO₂ in the Martian Atmosphere", Astrophysical J., Vol. 145, pp 454 - 467.
- (29) Spinrad, H. (1966a) "Spectroscopic Observations of Mars," Proc. of Caltech - JPL Lunar and Planetary Conf., September 13-18, 1965, pp 245-246.
- (30) Opik, E. J. (1966), "The Martian Surface," Science, Vol. 153, pp 255 - 265.

- (31) Shawhan, S. D., (1966) "Ionization Rate and Electron Density Profile for the Martian Ionosphere Based on Mariner IV Observations", 47th Annual AGU Meeting, April 19 - 22, 1966, Washington, D.C.
- (32) Marmo, F. F., Sharnanand, and P. Warneck (1965) "Ozone Distribution In the Atmosphere of Mars", Journal of Geophysical Research, Vol. 70, pp 2270 - 2272.
- (33) Shimizu, M., (1966), "A Theoretical Investigation of Cytherian, Martian and Javian upper atmospheres COSPAR, International Space Science Symposium, Vienna, May 10 - 19.
- (34) Gross, S. H., W. E. McGovern, and S. I. Rasool (1966) "Mars - Upper Atmosphere" Science, Vol. 151, pp 1216 - 1221.
- (35) Fjeldbo, G., V. R. Eshleman, A. J. Kliore, D. L. Cain, G. S. Levy, and F. D. Drake (1966b), "Preliminary Results of the Mariner II radio occultation measurements of the upper atmosphere of Mars". Proc., of Caltech - JPL Lunar and Planetary Conf., Sept. 13 - 18, pp 267 - 272.
- (36) Owen, T. (1966b), "The Composition and Surface Pressure of the Martian Atmosphere. Results from the 1965 Opposition" Astrophys J., Vol. 146, pp 257 - 270.
- (37) Adelman, B. (1966) "Altitude Variations on Mars", The Rev. of Popular Astronomy, VLX No. 540, p 20.
- (38) Gray, L. D. (1966) "Interpretation of Low Resolutions Spectro of Mars in the 2μ Region". AIAA Aerospace Sciences Meeting, New York, Jan. 24 - 26, 1966 - 12 pp.
- (39) Gray, L. D. (1966 b) "Transmission of the Atmosphere of Mars in the Region of 2μ ". Icarus, Vol 5, p 390 - 398.

- (40) Otterman, J., and F. E. Bronner, 1966, "Martian Wave of Darkening": A Frost Phenomenon? Science, Vol. 153, pp 56 - 60.
- (41) Spinrad, H., (1966b), "Resolution of CO₂ "Hot Band" in the Venus Spectrum" Astrophys J., Vol 145, pp 943 - 945.
- (42) Fjeldbo, G., W. C. Fjeldbo, and V. R. Eshleman, (1966): Models for the Atmosphere of Mars Based on the Mariner IV Occultation Experiment, Scientific Reports Nos. 2 and 15, 33 pp.
- (43) Ghosh, S. N., and Edwards, H. D. (1956), "Rotational Frequencies and Absorption Coefficients of Atmospheric Gases ", Air Force Surveys in Geophysics, No. 82, AD No. 98763, March. (Atmospherics Physics Lab, Geophysics Research Direct., Air Force Cambridge Research Center, Bedford, Mass.).
- (44) Gordy, W. (1948), "Microwave Spectroscopy", Reviews of Modern Physics, Vol. 20, No. 4, p 668.
- (45) Lombardini, P. N. Doviak, R. J. and Goldhirsh, J. (1967) "Centimetric and Millimetric Waves Spectroscopy of Planetary Atmospheres From Orbital Pairs" Raytheon Report FR-66-242, Rev. A., March.
- (46) Plass, G. N., (1952) "A Method for the Determination of Atmospheric Transmission Functions From Laboratory Absorption Measurements", Journal of the Optical Society of America, Vol. 24, No. 9, September, p 677.
- (47) Plass, G. N., (1963a), "Spectral Band Absorptance for Atmospheric Slant Paths" Applied Optics, Vol. 2, No. 5, p 515.
- (48) Stull, V. R., P. J. Wyatt, G. N. Plass, (1964), "The Infrared Transmittance of Carbon Dioxide" Applied Optics, Vol. 3, No. 2, p 243.

- (49) Burch, D. E., E. B. Singleton, and D. Williams (1962), "Applied Optics", Vol. 1, p. 359.
- (50) Kaplan, L. D , D. F. Eggers, Jr. (1956), "Intensity and Line - Width of the 15 - Micron Carbon Dioxide Band Determined by a Curve-of-Growth Method". Journal of Chem. Physics, Vol. 25, No. 5, November - pp. 876 - 883.
- (51) Plass, G. N., D. I. Fivel (1953), "Influence of Doppler Effect and Damping on Line Absorption Coefficient and Atmospheric Radiation Transfer", Astro-Physical Journal, Vol. 117.
- (52) Co-spar International Reference Atmosphere (1961), North-Holland Publishing Co., Amsterdam.
- (53) Goody, R. M., (1964), "Atmospheric Radiation" Oxford at the Clarendon Press, Great Britain, P 128.
- (54) Stull, V. R., P. J. Wyatt and G. N. Plass (1963), "The Infrared Absorption of Carbon Dioxide, Infrared Transmission Studies", Vol. III, Rept. SSD-TDR-62-127 Space Systems Division, Air Force Systems Command, Los Angeles, California.
- (55) Wyatt, P. J., V. R. Stull, G. N. Plass (1962) "The Infrared Absorptance of Water Vapor", Report SSD-TDR-62-127, Vol. II, Space Systems Division, Air Force Systems Command, Los Angeles, California.
- (56) Wyatt, P. J., V. R. Stull, G. N. Plass (1964), "The Infrared Transmittance of Water Vapor", Applied Optics, Vol. 3, No. 2, Feb., p 229 - 241.
- (57) Plass, G. N. (1963b), "Transmittance Tables for Slant Paths in the Stratosphere", Infrared Transmission Studies, Final Report, Vol. 5, Air Force Systems Command, SSD-TDR-62-127 - Vol. 5, 22 May.

- (58) Calfee, R. F., and D. Gates (1966), "Calculated Slant - Path Absorption and Distribution of Atmospheric Water Vapor", Applied Optics, Vol. 5, No. 2, Feb., pp 287 - 292.
- (59) Kirk, R. J., B. F. Watson, E. M. Brooks, and R. O'B. Carpenter, (1967), "Infrared Horizon Definition", NASA Contractor Report, NASA CR-722, April.
- (60) Plass, G. N. (1963c) "Transmittance of Carbon Dioxide and Water Vapor Over Stratospheric Slant Paths", Applied Optics, Vol. 3, No. 4, pp 479 - 482.
- (61) Loewenstein, E. V., (1966), "The History and Current Status of Fourier Spectroscopy", Applied Optics, Vol. 5, No. 4, May, p 847.
- (62) Low, M. J. D., (1967), "Subtler Infrared Spectroscopy", International Science and Technology, February.
- (63) Williams, R. A., and W.S.C. Chang, (1962), "An Analysis of the Interferometric Submillimeter Radiometer", Ohio State University Research Foundation Report No. 1093-9, July.
- (64) Born, M., and E. Wolf, (1964), "Principle of Optics" - Second revised edition, MacMillan Co., New York, p 443.
- (65) Block Engineering Co., Cambridge, Mass., Private Communication.
- (66) Jamieson, J. A., "Infrared Physics and Engineering", McGraw-Hill Co., p. 145.
- (67) Wolf, E., (1967) Editor, "Progress in Optics", John Wiley, New York, p 304.

- (68) Hall, L. A., W. Schweiger, H. E. Hinteregger, (1965), "Improved Extreme Ultraviolet Absorption Measurements in the Upper Atmosphere", Journal of Geophysical Research, Vol. 70, No. 1, p. 105.
- (69) Hall, L. A., C. W. Chagnon, H. E. Hinteregger (1967) "Daytime Variations in the Composition of the Upper Atmosphere", Journal of Geophysical Res., Vol. 72, No. 13, July, p. 3425.
- (70) Hall, L. A., K.R. Damon, H. E. Hinteregger (1963), "Solar Extreme Ultraviolet Flux Measurements in the Upper Atmosphere of August, 1961", Space Research, Vol. III, North Holland Publishers, New York, p. 745.
- (71) Garozhankin, B. N., K. I. Gringauz, N. M. Shutte (1967), "Absorption of Ultraviolet Solar Radiation in the Upper Atmosphere Near the Main Ionization Maximum, According to Measurements of Photoemission by Means of Earth Satellite", Space Research, Vol. VII, North Holland Publishers, N.Y., p. 378.
- (72) Hinteregger, H. E. (1965) "Absolute Intensity Measurements in the Extreme Ultraviolet Spectrum of Solar Radiation", Space Science Reviews, Vol. 4, p. 461.
- (73) Weissler, G. L. (1956), "Photoionization in Gases and Photoelectric Emission from Solids", Handbuch der Physik, Vol. XXI, Springer Verlag, East Germany.
- (74) Hinteregger, H. E., and L. Heroux, (1960), "Resistance Strip Magnetic Photomultiplier for the Extreme Ultraviolet", Rev., of Scientific Instruments, Vol. 31, No. 3, March.
- (75) Delgarno, A., Parkinson, D. (1960), "Photoionization of Atomic Oxygen and Atomic Nitrogen", Journal of Atmospheric and Terrestrial Physics, Vol. 18, p. 335.

- (76) Kaplan, L. D., Inference of Atmospheric Structure from Remote Radioactive Measurements, J.O.S.A., Vol. 49, p. 100A, (1959).
- (77) Wark, D. Q., On Indirect Temperature Soundings of the Stratosphere from Satellites, J.G.R., Vol. 66, p. 77, (1961).
- (78) Hanel, R. H., and Chaney, L., Doc. X-650-64-209, GSFC.
- (79) Brown and Woodward, Experimentally determined radiation Characteristics of conical and triangular antennas, RCA Review, december 1952.

APPENDIX A

TRANSMITTANCE FROM INHOMOGENEOUS PATHS OBTAINED FROM HOMOGENEOUS PATH DATA

In the following paragraphs, a technique first introduced by Plass (Ref. 47) is reviewed for which the transmittance over a nonhomogeneous path (i.e., density, pressure, and temperature vary) may be deduced by comparing fundamental physical quantities over this path with the transmittance for a homogeneous path along which the pressure and temperature is constant. This technique is particularly applicable for the cases of either "strong line absorption" or "weak line absorption." When the absorption is between these extremes, methods of interpolation may be applied.

A.1 GENERAL FORMULATION

When the path over which absorption occurs is inhomogeneous with density, pressure, and temperature, the absorption coefficient over the spectral interval, $\Delta\nu$ (resolution of spectrometer), may be expressed as

$$k_\nu(u) = \sum_{i=1}^N S_i \sigma_i[\nu, \alpha_i(u)] \quad (\text{A-1})$$

where S_i is the intensity of the i^{th} line in the spectral interval, $\Delta\nu$; σ_i is the line shape factor for the i^{th} line, which is a function of the frequency, ν , and the half-width of the line, α_i . Also, u is the mass of absorbing gas per unit area along the entire inhomogeneous path and is defined as

$$u = \int_0^{\ell} \rho_a d\ell \quad (\text{A-2})$$

where ρ_a = mass density of the absorbing gas. The summation (A-1) is taken over the N spectral lines that contribute to the absorption in the frequency interval, $\Delta\nu$. The pressure broadened half-width, α_i , at some temperature T, and pressure, P, is given by

$$\alpha_i = \alpha_{oi} (P/P_o) (T_o/T)^{1/2} \quad (A-3)$$

where α_{oi} is the half-width at some standard temperature, T_o , and pressure, P_o . (A generally accepted experimental value for the reference line half-width in the 15μ CO_2 band is $\alpha_o = 0.064 \text{ cm}^{-1}$, $P_o = 1 \text{ atm}$, $T_o = 298^\circ \text{K}$ (Ref. 50)).

The absorptance, A, over a finite spectral interval, $\Delta\nu$, is given by

$$A = \frac{1}{\Delta\nu} \int_{\Delta\nu} \left\{ 1 - \exp \left[- \int_0^u k_\nu(u) du' \right] \right\} d\nu \quad (A-4)$$

and the transmittance, T, is

$$T = \frac{I}{I_o} = 1 - A \quad (A-5)$$

where I_o and I are the incident and attenuated power densities, respectively. We shall initially confine our attention to two special cases, namely, the "strong line approximation" and the "weak line approximation". Later we shall connect these two extremes by a method of interpolation.

A.2 STRONG LINE APPROXIMATION

The strong line approximation is valid when the absorption of the incident radiation is virtually complete over frequency intervals at least several half-widths wide around the centers of the strongest lines in the band, and when these lines are

largely responsible for the absorption over the given frequency interval (Ref. 57). For this case, we shall assume that the line shape factor is Lorentz broadened and given by

$$\sigma_i(\nu, \nu_{oi}, \alpha_i) = \frac{\alpha_i}{\pi[(\nu - \nu_{oi})^2 + \alpha_i^2]} \quad (\text{A-6})$$

In the region ν close to ν_{oi} , the radiation is completely absorbed. Hence, we may neglect α_i in the denominator of equation A-6 (Ref. 53). That is, we are now interested in the behavior of the wings when $(\nu - \nu_{oi})^2 \gg \alpha_i^2$. When ν is in the vicinity of ν_{oi} , the integral in the integrand of (A-4) is insensitive to changes in the denominator of $\sigma_i(\nu, \nu_{oi}, \alpha_i)$. Hence, equation A-6 becomes

$$\sigma_i(\nu, \nu_{oi}, \alpha_i) = \alpha_i g_i(\nu, \nu_{oi}) \quad (\text{A-7})$$

where $g_i(\nu, \nu_{oi})$ is the corresponding factor in (A-6) and is only a function of the line center frequency, ν_{oi} , and the frequency under consideration, ν .

The form (A-7) is actually valid for any pressure broadened line shape, $g_i(\nu, \nu_{oi})$ (Ref. 47). Substituting equation A-7 into equation A-1 and the resulting relation into equation A-4, we obtain

$$\Delta \nu A = \int_{\Delta \nu} \left\{ 1 - \exp \left[- \sum_{i=1}^N g_i(\nu, \nu_{oi}) \int_0^u S_i(T) \alpha_i du' \right] \right\} d\nu \quad (\text{A-8})$$

The expression for the absorptance over a homogeneous path is

$$\Delta v A_H = \int_{\Delta v} \left\{ 1 - \exp \left[- \sum_{i=1}^N g_i(v, v_{oi}) S_i(T_H) \alpha_{ih} u_h \right] \right\} dv \quad (A-9)$$

where $S_i(T_H)$, α_{ih} , and u_h are the intensities, half-widths, and mass of absorbing gas per unit area for the temperature, T_h , and pressure, p_h , along a homogeneous path.

By comparing equation A-8 with equation A-9, it is apparent that the absorption over the homogeneous path and that over the inhomogeneous path are equal when the corresponding exponents in the integrand are equal. That is,

$$u_h(v) \sum_{i=1}^N g_i(v, v_{oi}) S_i(T_H) \alpha_{ih} = \sum_{i=1}^N g_i(v, v_{oi}) \int_0^u S_i \alpha_i du' \quad (A-10)$$

It may be shown that the spectral lines $S_i(T)$ may be given by the same function of temperature, so that

$$S_i(T) = s(T) S_i(T_H) \quad (A-11)$$

where $s(T)$ is a function that can be calculated from the theory of molecular spectra, and may be approximated by equation 4.4-24 when the temperature difference is small and the line intensities are not too dissimilar (Ref. 47).

Substituting equations A-3 and A-11 into equation A-10, we obtain

$$u_H(P_H T_H^{-1/2}) = \int_0^u s(T) P T^{-1/2} du' \quad (A-12)$$

where the common factor $\sum_{i=1}^N g_i(v, v_{oi}) \alpha_{ih}$ cancels out on both sides of equation A-10. It is interesting to note that where the equivalent mass of absorbing gas per unit area for the homogenous path in equation A-10 was frequency dependent, the corresponding u_H in (A-12) is not. Equation A-12 may be expressed in terms of the equivalent absorptive path length (expressed in atmosphere-cm) that gives the same absorption at a temperature T_H and pressure P_H as that over an inhomogeneous path. Substituting the following in equation A-12,

$$du = M_P N(\ell) d\ell \quad (A-13)$$

$$u_H = M_P N_H L_H \quad (A-14)$$

where

M_P = the product of the molecular weight and the proton rest mass

$N(\ell)$ = the molecular density along the inhomogeneous path

N_H = equivalent homogeneous molecular density

L_H = equivalent homogeneous path length

$d\ell$ = elemental inhomogeneous path length,

we obtain

$$u_H^* = \frac{N_H L_H}{n_O} = \frac{P_W^{-1} T_W^{1/2}}{n_O} \int_0^{\ell} S(T) N(\ell) P T^{-1/2} d\ell \quad (A-15)$$

(atm-cm)

where n_O = Loschmidt's number = $2.69 \times 10^{19} \text{ cm}^{-3}$.

A.3 WEAK LINE APPROXIMATION

The weak line approximation is valid when the absorption of each spectral line considered individually is small even near the line centers. Hence, the weak line approximation assumes the exponent in the integrand of equation A-4 is sufficiently small so that it may be replaced by the first two terms of the Taylor expansion of the exponential term. Hence, equation A-4 becomes

$$A_{\Delta\nu} = \int_{\Delta\nu} \left\{ \int_0^u k_{\nu}(u') du' \right\} d\nu \quad (\text{A-16})$$

Substituting equation A-1 into equation A-16 we obtain

$$A_{\Delta\nu} = \int_{\Delta\nu} \left\{ \int_0^u \left[\sum_{i=1}^N S_i \sigma_i [\nu, \alpha_i(u)] \right] du' \right\} d\nu \quad (\text{A-17})$$

Taking the summation out of the integrand and interchanging the order of integration, we obtain

$$A_{\Delta\nu} = \sum_{i=1}^N \int_0^u S_i(u') \left[\int_{\Delta\nu} \sigma_i [\nu, \alpha_i(u')] d\nu \right] du' \quad (\text{A-18})$$

For a homogeneous path, equation A-18 becomes

$$A_H \Delta\nu = u_H \sum_{i=1}^N S_{iH} \left[\int_{\Delta\nu} \sigma_i [\nu, \alpha_i(u_H)] d\nu \right] \quad (\text{A-19})$$

If the absorptions are to be the same, we may equate A-18 and A-19. Hence,

$$u_H \sum_{i=1}^N S_{iH} \left[\int_{\Delta\nu} \sigma_i [\nu, \alpha_i(u_H)] d\nu \right] = \sum_{i=1}^N \int_0^u S_i(u') \left[\int_{\Delta\nu} \sigma_i [\nu, \alpha_i(u')] d\nu \right] du' \quad (A-20)$$

Since the shape factor $\sigma_i[\nu, \alpha_i(u')]$ is normalized to unity (i.e. $\int_0^\infty \sigma_i[\nu, \alpha_i(u')] d\nu = 1$), if the interval of integration, $\Delta\nu$, is

large enough so that most of the absorption due to the individual lines occur within this interval, then the integrals of equation A-20 will approximate unity, resulting in

$$u_H \sum_{i=1}^N S_{iH} = \sum_{i=1}^N \int_0^u S_i(u') du' \quad (A-21)$$

If the approximation equation A-11 is valid, equation A-21 becomes

$$u_H = \int_0^u s(T) du' \quad (A-22)$$

Using the same procedure as in the strong line case, we may obtain the equivalent absorptive path length given by

$$u_H^* = \frac{1}{n_o} \frac{\sum_{i=1}^N \int_0^{\ell} s_i(\ell) d\ell}{\sum_{i=1}^N s_{iH}} \quad (\text{atm-cm}) \quad (\text{A-23})$$

or

$$u_H^* = \frac{1}{n_o} \int_0^{\ell} N(\ell) s(T) d\ell \quad (\text{atm-cm}) \quad (\text{A-24})$$

A.4 INTERPOLATION BETWEEN STRONG AND WEAK LINES

The equivalent homogeneous concentration giving the same absorption as that over an inhomogeneous path has been deduced in the preceding sections and is repeated below for both the strong line and weak line approximations.

$$P_H T_H^{-1/2} u_H^* = \frac{1}{n_o} \int_0^{\ell} s(T) N(\ell) P T^{-1/2} d\ell \quad (\text{A-25})$$

(strong line approximation)

or

$$u_H^* = \frac{1}{n_o} \int_0^{\ell} N(\ell) s(t) d\ell \quad (\text{A-26})$$

$$u_H^* \left(\sum_{i=1}^N s_{iH} \right) = \frac{1}{n_o} \sum_{i=1}^N \int_0^{\ell} N(\ell) s_i(\ell) d\ell \quad (\text{A-27})$$

(weak line approximation)

Assume that the strong line approximation is valid. A knowledge of the integrand of equation A-25 determines a specific value for the corresponding integral. The strong line assumption dictates that one and only one value of absorptance is possible in any set of tables for which the product of P_H , $T_H^{-1/2}$ and u_H^* is equal to that constant value on the right-hand side of (A-24). Hence, a certain amount of arbitrariness exists in selecting these product factors. That is, if we arbitrarily select u_H^* , the product $P_H T_H^{-1/2}$ is fixed. We desire to select the arbitrary value dictated by equation A-26. Substituting this value back into equation A-25 then determines the product $P_H T_H^{-1/2}$, and a set of tables will uniquely specify the absorptance. Hence, we have used the weak line formulation of equation A-26 to give the correct result for the strong line case.

Assume now that the weak line approximation is the truly valid case. Hence u_H^* may be determined by evaluating the right-hand side of equation A-26. A set of tables will give only one value of absorptance for the specific value of u_H^* independent of P_H or T_H . Since the answer is independent of P_H and T_H , we may substitute u_H^* into the left-hand side of equation A-24, evaluate the right hand integral and determine the product $P_H T_H^{-1/2}$. We may then examine a set of tables corresponding to the determined values u_H^* and $P_H T_H^{-1/2}$ and determine the corresponding absorptance. Since this absorptance value is independent of P_H and T_H , it is indeed the correct result. It may be noted that the absorptance for the weak line case satisfies the strong line formulation of equation A-25. Hence, use of the above procedure gives the correct absorption value and satisfies equally well both the strong and weak line limits.

In the immediate region where both the weak and strong line approximations may be somewhat in error, the result derived in this manner provides a smooth interpolation between the absorptance curves that are valid in the weak and strong line limits. Plass (Ref. 57) has used a similar technique to deduce the absorptance over slant paths in the Earth's atmosphere.

Plass (Ref. 57,60) has also used a similar technique to the one described above to deduce the transmittances over slant paths in the Earth's stratosphere. The equations he satisfied simultaneously were,

$$u_H^* = \frac{1}{n_o} \int_0^{\ell} N(\ell) d\ell \quad (\text{A-28})$$

$$P_H = \frac{1}{u_H^* n_o} \int_0^{\ell} N(\ell) P d\ell \quad (\text{A-29})$$

$$\sum_{i=1}^N S_{iH} = \frac{1}{u_H^* n_o} \sum_{i=1}^N \int_0^{\ell} S_i(\ell) N(\ell) d\ell \quad (\text{A-30})$$

The use of these equations represents a perturbation technique in which it is assumed that $s(t)$ is unity in equations A-25 and A-26, resulting in equations A-28 and A-29. The temperature variation along the path is taken into account by equation A-27. The equivalent temperature, T_H , which must be used over the homogeneous path, is chosen such that the equality of equation A-30 is valid. Hence equations A-28, A-29, and A-30 determine values of u_H^* , P_H , T_H from which the tabulated absorption may be deduced.

APPENDIX B

THE USE OF A SUBSATELLITE AS THE DAUGHTER TERMINAL OF THE ORBITING PAIR

B-1 INTRODUCTION

Certain advantages may accrue in the experiment configuration over a Voyager-to-Voyager (or equivalent orbiter-to-orbiter) experiment when a subsatellite daughter is added to each spacecraft. The following description defines these potential advantages and briefly describes the parameters of such a subsatellite, which might be accommodated in the Voyager mission to Mars.

B-2 OBJECTIVE AND JUSTIFICATION

The advantages of using an auxiliary subsatellite are the provision of greater probability of mission success due to increased redundancy at a moderate overall increase in weight; greater dynamic orbital flexibility, resulting in an increased experimental data collection rate; physical independence between Voyager and subsatellite, avoiding the problem of mutually conflicting pointing requirements between different classes of experiments. Lastly, a decision to orbit only a single Voyager would still permit the execution of the refractivity experiment.

B-2.1 ENHANCED MISSION PROBABILITY

If identical Voyagers are used, each with a subsatellite, failure of one parent vehicle or one subsatellite permits the experiment to survive. There are four possible redundant modes of operation in contrast to the case where only two Voyagers equipped with integral daughter equipment are used. In this latter case, failure in any one part of the system destroys the mission.

The penalty paid in using subsatellites is the added weight required for subsatellite structure, internal power supply, and attitude stabilization equipment - on the order of 23 kg, per Voyager.

B-2.2 DYNAMIC FLEXIBILITY

Use of a subsatellite offers the possibility of increased flexibility in the design of orbits, providing an additional degree of freedom in enhancing the scan rate of the resolution cell. The subsatellite orbit may differ from the parent Voyager and be chosen to increase the occultation occurrence rates between terminals. The net result is an increase in the ability to measure time-dependent properties of the Martian ionosphere/atmosphere.

B-2.3 SENSOR POINTING CONFLICTS

A number of related but independent experiments is planned for the Voyager. It is likely that these will impose conflicting pointing requirements. For example, Earth communications imply a directional Earth-oriented antenna; surface phenomena, will require Mars-oriented sensors such as cameras. Other experiments, such as refractivity, require vehicle-to-vehicle communications.

The physical separation of the daughter terminal of the refractivity experiment permits a degree of independence of pointing requirements and thus alleviates the conflict.

B-2.4 SINGLE VOYAGER CASE

Should it be decided to orbit a single Voyager system per launch, the refractivity experiment survives when a subsatellite is used. In the case of the integrated Voyager, the experiment is nullified.

B-3 SUBSATELLITE REQUIREMENTS

A subsatellite replacing the second Voyager in the experiment must provide one-way communication to Earth for stereo-doppler tracking purposes. It must also communicate with the mother Voyager receiving a 2000 MHz signal and returning phase-locked 500 MHz and 2160 MHz signals. The 2160 MHz signal is directed toward the Earth (Figure B-1). These communication links, and the need for solar illumination of the power cells, impose attitude requirements on the subsatellite. Three approaches to this problem have been studied:

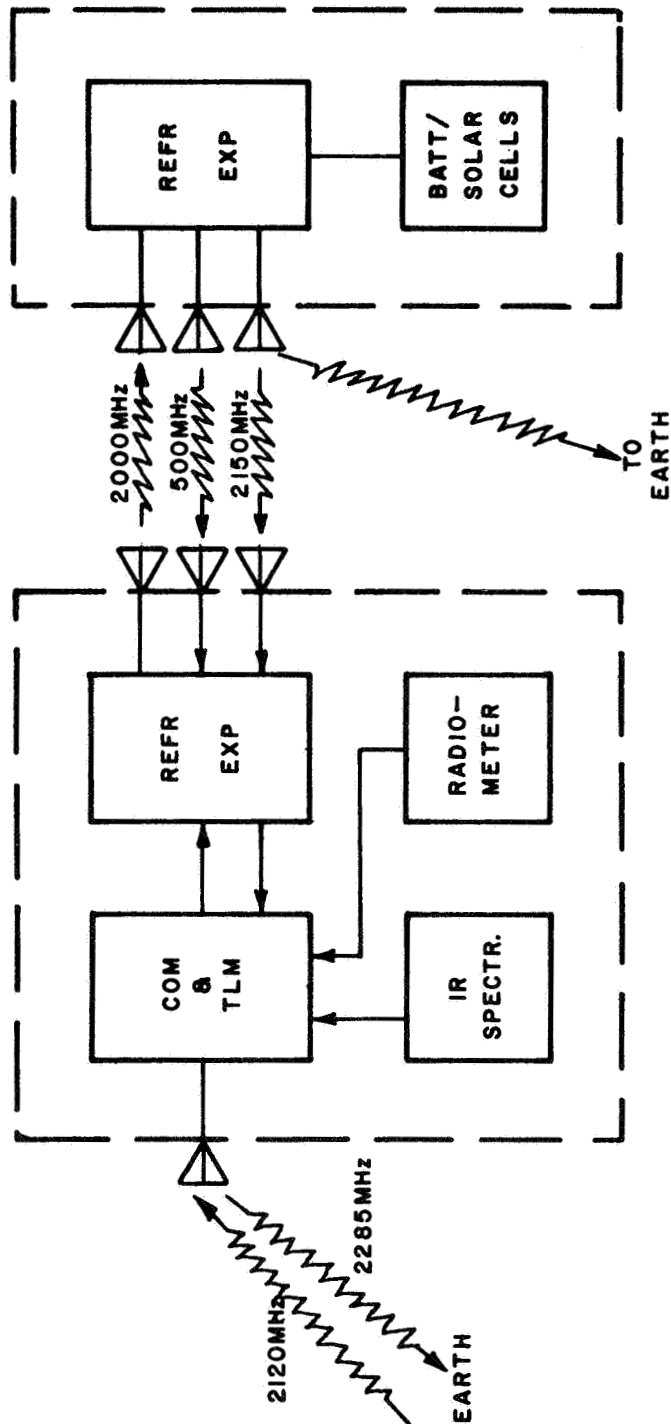


Figure B-1 Voyager-Subsatellite Configuration

1. An unstabilized subsatellite
2. A spin-stabilized satellite that covers both Earth and Voyager with a common antenna
3. A spin-stabilized satellite with separate antennas for Voyager and Earth communication link.

The major system characteristics of these candidate configurations are summarized in Table B-1.

The first system considered, the unstabilized satellite, was eliminated since fully omnidirectional antennas would require high radiated power and associated directional antennas would require complex sensing, processing and adaptive pointing mechanisms for which a high weight penalty would have to be paid.

In the second case, simultaneous use of a common antenna to communicate with both Earth and Voyager requires excessive RF power to contact Earth.

The third option appears the most satisfactory and has been chosen as the design baseline. In this case, the vehicle would be spin-stabilized with its spin axis normal to the plane of the ecliptic. This provides a constant look angle to Earth relative to the subsatellite and hence permits the use of a directive antenna for communication to Earth.

The fact that the Martian equator is inclined about 25° to the plane of the ecliptic, that the coplanar experiment is an inclined orbit, and that the orbital precession rates of Voyager and subsatellite differ, causes a constantly changing geometrical relationship between vehicles. This means that the look angles between vehicles relative to the subsatellite spin axis vary over almost the entire possible range of 180° in elevation.

TABLE B-1
POSSIBLE SUBSATELLITE SYSTEM CONFIGURATIONS

METHOD OF STABILIZATION	POINTING DIRECTION	SOLAR CELLS	# CELLS	BEAM ANGLE FOR PANCAKE ABOUT AXIS FOR EARTH	BEAM ANGLE FOR PANCAKE ABOUT AXIS TO VOYAGER	TORQUEING REQUIRED	STABILIZATION REFERENCE #1	STABILIZATION REFERENCE #2	REMARKS
Tumbling	None	Sphere	4	10° Phased Arrays Pointed Toward Receivers Based Either on Retro- Directivity or Computed From Sensed Lines	10°	None	Seen - Mars Voyager Vehicle. Angle to Earth Will In All Likelihood Require Computation		
Spin	Normal Ecliptic	Cylinder	3	> 10°	± 70°	None	Sun	Earth or Canopus	Best Possibility Second Reference Is Only Problem
	Normal Sub-Sat Orbit	Sphere	4	70°	> 10°	0.41°/Day	Mars Over a Long Period of Time		Second Choice - All Problems Have An Immediate Solution
	Normal Earth Voyager	Sphere	4	> 10°	> 10°	Variable As High As 2°/Day	From Secondary Reference - Sun Mars		Attitude Reference and Torqueing Problems Appear To Be Serious
	Sun	Plane	1	> 50° (200 Days)	180°	1 Rev/Year	Sun		Retrodirective Antenna To Parent Voyager Might Solve Voyager Link Antenna Problem
	Mars	Sphere	4	180°	180°	2 Revs/Day	Mars	Not Required	Has No Merit

These look angles require near-isotropic antennas for inter-vehicle communications but, as noted earlier, stabilization in the plane of the ecliptic permits the use of a directive antenna to Earth with some degree of gain.

B-4 SUBSATELLITE ATTITUDE CONTROL

Although we have referred to the subsatellite as being stabilized with its spin axis normal to the ecliptic, it would actually use Mars and the Sun in establishing its orientation relative to the ecliptic. Since Mars' orbit is inclined only 1.85° out of the ecliptic, for antenna orientation purposes, this can be considered to be the ecliptic plane.

The subsatellite will be spring-ejected from Voyager, after precise orientation of the latter, at a relative velocity of ≥ 10 meters/second. After ejection, spin-up will be achieved by cold gas jets mounted off-axis and tangential to the circumference of the subsatellite. Spin-up after injection minimizes the reaction on Voyager.

After spin-up, data from a subsatellite Sun sensor and Mars horizon scanner will be relayed to Earth via Voyager. In this manner, attitude errors due to Voyager misalignment, spring-ejection assymetry can be assessed and corrective impulses computed and commanded. Thereafter, periodic attitude checks will be made and corrective action commanded, if required.

B-5 SUBSATELLITE ANTENNAS

The system requirements dictate a very broad coverage. An omnidirectional azimuth with 140° elevation coverage is required. A simple antenna configuration which meets these needs is the biconical horn. Brown and Woodward (Ref. 79) measured the gain and the pattern characteristics of this antenna.

Figure B-2 shows the relative gain of the biconical antenna versus height of the antenna with the flare angle α as a parameter. For optimum results, both the gain and patterns must be taken into account. The best results can be achieved by making the length 255 electrical degrees with a flare angle of 50 to 60 degrees. At 500 MHz the antenna need not be of solid construction but can be made of thin rods to save weight.

To calculate the performance of these antennas, for example, we can choose $\alpha = 50^\circ$, $\beta = 255^\circ$; then $G = 0.75$ (with respect to the dipole). The gain with respect to the isotropic source is $.75 \times 1.64 = 1.23 = 1.75$ db. From Figure B-3 we see that the pattern is constant over a 120° vertical angle to within a db, and drops to -3 db relative to the dipole (-1.25 db relative to isotropic) for a 140° cone angle. For other values of β , the patterns are similar but exhibit greater fluctuations.

A second radiator, omnidirectional in azimuth but with higher directivity in elevation will be employed for the sub-satellite-to-Earth link, yielding a gain of 9 db. This will consist of the same helical antenna described in Section 4.3.5.3. Both antennas will be mounted on the subsatellite spin axis.

B-6 POWER REQUIREMENTS AND PRIMARY SOURCE

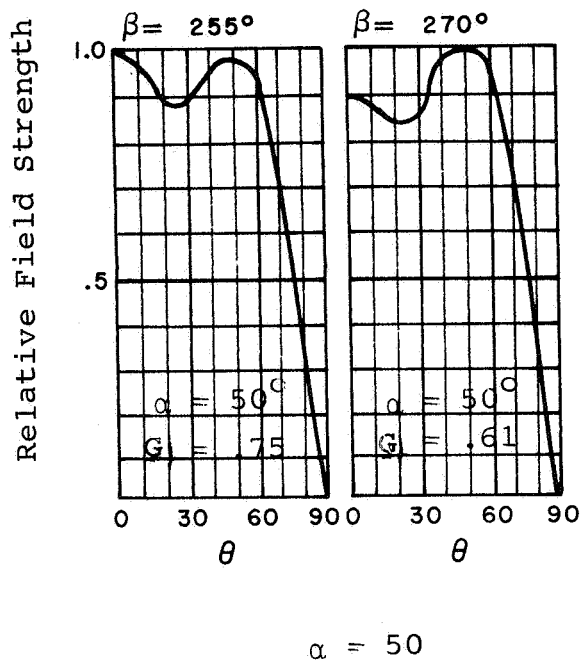
The subsatellite would be a foreshortened cylinder that would rotate about its major inertial axis. This means its spin axis orientation is fixed in inertial space. Spin rate will be 50 revolutions per minute to provide high stability.

As the experimental mission duration is designed to be three months or more, the conventional solar cell/storage battery type of electrical power supply would be used. Solar paddles are discarded since the vehicle will not be sun oriented, and since they would interfere with the radiation patterns of the quasiisotropic antennas. The solar cells are installed symmetrically around the curved peripheral surface. Taking into account a required average power drain of 60 watts, cell efficiency deterioration with time, the partial solar illumination due both to attitude and occultation, the solar cell area required is 5 m^2 .

This area can be accommodated on a cylindrical vehicle 1.2m in diameter and about 1m in height.

B-8 PRELIMINARY DESIGN

The major parameters required are summarized in Table B-2. This shows that the overall weight is 43.55kg, prime power required is 58 watts, and that the component volume is 0.078 m^3 . The actual vehicle overall volume, however, will be 1.65 m^3 as dictated by the required surface area for solar cell accommodation and the shape dictated by the use of spin stabilization.



β = Electrical Length ($^\circ$)

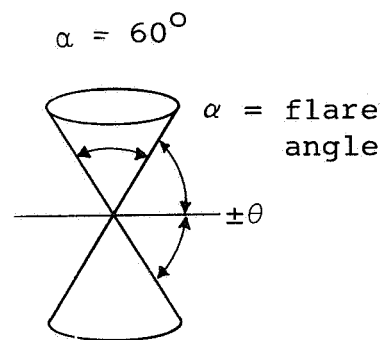
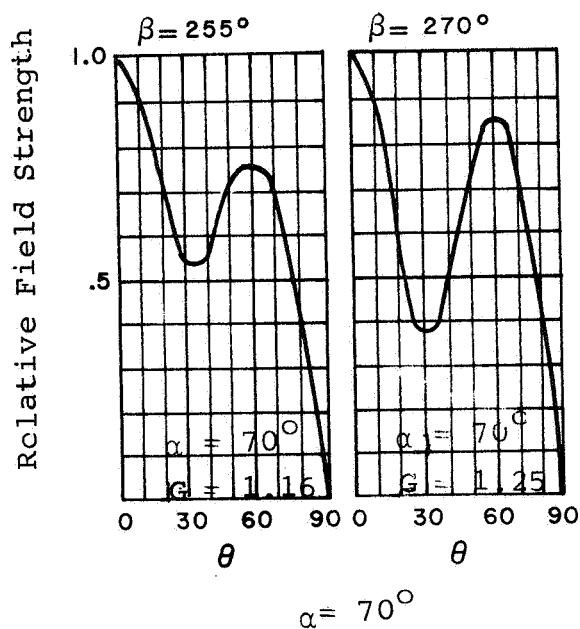
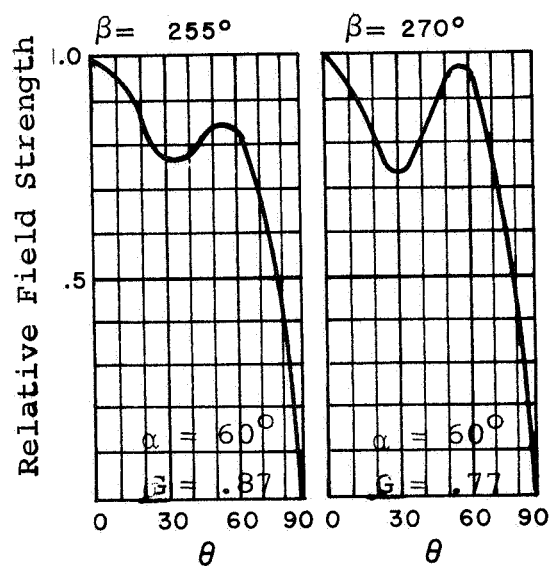


Figure B-3 Measured Field Patterns for Biconical Dipoles for Various Lengths and Flare Angles

B-9 INTERFACE REQUIREMENTS

All normal spacecraft interface requirements apply between subsatellite and Voyager. The principal factors are presented in Table B-3.

Unusually stringent requirements peculiar to Voyager are contained in Table B-4.

TABLE B-2

SUBSATELLITE

Item	Power Watts	Weight kg
Phase-Locked Loop	4	2.7
500 MHz Transmitter	5	0.68
2160 MHz Transmitter	21	1.12
Receiver	1	0.9
Solar Cells, Batteries	10	13
Attitude Sensor and Control	2	3.6
Structure and Thermal	10	11.2
Spin-up and Attitude Control Propulsion	-	3.6
Antennas	-	2.25
Communication and Command	5	4.5

TOTAL POWER 58 watts

TOTAL WEIGHT 43.55kg

TOTAL VOLUME (Components) 0.078m^3

TOTAL VOLUME (Vehicle) 1.65m^3

SHAPE - Cylindrical Diameter 1.2m

Height 1m

TABLE B-3
STANDARD INTERFACE FACTORS

Item	Subitem	Qualifications
Mechanical	Mass, Balance, Volume, Form Factor, Mounting, Separation Mechanism	Power required in flight
Thermal	Flow, Configuration, Sinks Sources	
Electrical	Energy, Voltage, Current, Frequency, Transients, Duty Cycle, Operating Cycles	
EMI		
Safety		
Data Handling	Format, Rates, Channels Storage, Coding	Governed by DSN
Sensor Pointing	Orientations, Rates, Apertures, Obscuration	Governed by DSN
Stabilization Modes	RF Power, SNR, Data Rates & Formats, Command Repertoire	
Communications		
Attitude Contamination	Propulsion, Outgassing	At Separation

TABLE B-4
SPECIAL INTERFACE FACTORS

Item	Comment
Sterilization	Bacteriological Cleanliness
Quarantine	Governs Orbital Lifetime